Experimental Characterization of the Calcium Looping Process for CO_2 Capture

Von der Fakultät Energie-, Verfahrens- und Biotechnik der Universität Stuttgart
zur Erlangung der Würde eines Doktors der Ingenieurwissenschaften (Dr.-Ing.)
genehmigte Abhandlung

Vorgelegt von

Alexandros Charitos

aus Athen, Griechenland

Hauptberichter: Prof. Dr. techn. Günter Scheffknecht

Mitberichter: Prof. Dr. Piero Salatino

Tag der mündlichen Prüfung: 04.07.2013

Institut für Feuerungs- und Kraftwerkstechnik der Universität Stuttgart

2013

Acknowledgements

The work presented within this thesis has been carried out during my employment at the Institute of Combustion and Power Plant Technology (IFK), within the time period 2005-2011. First of all, I am indebted to the federal state of Baden-Württemberg for the financial support, in terms of employment as a research scientist, provided during the above time period.

I would like to express my gratitude to Prof. Dr. techn. Günter Scheffknecht for giving me the opportunity to conduct research within the IFK, a reputable institute with unique infrastructure for demanding experimental work. Moreover, I would like to thank Professor Scheffknecht for his supervision and advice. My gratitude is extended to Prof. Dr. Juan Carlos Abanades (Instituto Nacional del Carbón, INCAR, Spanish Research Council, CSIC) for his scientific advice, guidance and cooperation, which have significantly helped the progression of this work. I would also like to thank Prof. Dr. Piero Salatino for his insight with regard to the Calcium looping process. My gratitude is expressed to Prof. Dr. Emmanuel Kakaras not only with regard to process understanding but also for motivating me throughout my studies to take up scientific challenges and pursue a doctoral degree.

In addition, I would like to thank the former and current heads of the decentralized energy conversion (DEU) department of IFK, namely Dr.-Ing. Roland Berger, Dr.-Ing. Anja Schuster and Mariusz Zieba for helping me organize my work in a constructive manner. Furthermore, I am grateful to my colleagues at DEU for their help in a variety of aspects related to my thesis. Hence, I would like to thank Ajay Bidwe, Heiko Dieter, Norman Poboß and Glykeria Varela – and especially Craig Hawthorne – for helping me enhance my understanding on process and fluidization engineering aspects, design experiments and analyze results. Moreover, the fruitful cooperation with the colleagues of INCAR-CSIC Dr. Mónica Alonso and Dr. Nuria Rodríguez is gratefully acknowledeged. Also, I would like to thank the colleagues who played a very crucial role in the design and operation of the 10 kW_{th} IFK Dual Fluidized Bed (DFB) facility, the key piece of equipment for the realization of the experimental work: Heiko Holz, Bernd Krieger, Tommy Pfeifer and Alexander Schulze. The realization of all activities was marked by the contribution of those students, who carried out their study-, Diploma- or Master's theses, under my supervision, i.e. Ajay Bidwe, Christos Christodoulou, Jens Friedrich, Giorgos Kopanakis, Loukianos Korovesis, Pinelopi Koutrouki, Aristeidis Nikolopoulos, Norman Poboß and Daniel Schlegel.

Moreover, I would like to express my gratitude and appreciation to the workshop and administration for their decisive contribution. Hence, I would like to thank Herbert Höll and Ralf Nollert for their outstanding work in constructing piece by piece the 10 kW_{th} IFK DFB facility. A special thank you goes to Renate Klein, Ursula Docter, Manfred Seitz and Marja Steinlechner for their immense help and support with regard to administrative issues.

In addition, I would like to thank my family: my late father Prof. Dr. Athanasios A. Haritos, my mother Prof. Dr. Maria Weini-Haritou, my aunt Amalia Weini and my brother Dr. Aristomenis Charitos. Their constant moral and financial support and faith have been determining factors in order for this work to be realized. Finally, I would like to express my warm “thank you” to my partner Philomena Konstantinidis, who has been a constant source of inspiration and power, which were so much needed in carrying out this work.

To my father
Prof. Dr. Athanasios A. Haritos

Table of Contents

Nomenclature

Symbols	Explanation	Unit
A_i	cross sectional area of component i	m^2
C_0	characteristic constant for a mechanical valve	-
$C_{s\ inlet\ cyclone}$	solid concentration in cyclone inlet flow	kg/m^3
D_i	diameter of component i	m
d_p	particle size	µm
$\overline{d_p}$	median particle size	µm
$(dP/dz)_i$	pressure drop gradient of component i	Pa/m
$(dX_{carb}/dt)_{reactor}$	carbonation reaction rate	s^{-1}
E_{carb}	CO_2 capture efficiency	-
E_{eq}	equilibrium CO_2 capture efficiency	µm
E_{carb}/E_{eq}	eq. normalized CO_2 capture efficiency	-
f_{active}	fraction of carbonator active particles	-
F_0	fresh molar Ca make-up flow	mol/s
F_0/F_{CO2}	fresh molar Ca make-up ratio	mol_{Ca}/ mol_{CO2}
F_{Ca}	molar Ca rate between reactors	mol/s
F_{CO2}	inlet molar flow of F_{CO2} in the carbonator	mol/s
F_{Ca}/F_{CO2}	Ca looping ratio	mol_{Ca}/ mol_{CO2}
$(F_{Ca}/F_{CO2})_{no\ cv}$	Ca looping rate ratio if no double exit loop seal with cone valve is used	mol_{Ca}/ mol_{CO2}
F_{ges}	inlet molar flow of gas other than CO_2 in the carbonator	mol/s
g	acceleration of gravity	m^2/s
G_{gi}	gas flow through component i based on its cross section	kg/m^2s
$G_{s\ cv}$	solid flow rate between reactors, controlled through cone valve, based on riser cross-section	kg/m^2s
$G_{s\ entrainment}$	riser entrainment based on its cross-section	kg/m^2s
G_{si}	solid flow through component i based on its cross-section	kg/m^2s
k_s	carbonation surface kinetic constant	s^{-1}
$k_s\varphi$	apparent rate carbonator constant	s^{-1}
L_x	length of component x	m
N	carbonation/calcination cycle number	-
N_{th}	theoretical cycle number, realized within the DFB installation	-

n_{Ca}	amount of Ca in carbonator	mol
$n_{Ca,total}$	amount of Ca in the DFB system	mol
P_i	carbonator pressure at a given axial height	mbar
t*	time needed for a particle entering the carbonator to increase its carbonate content from X_{calc} to $X_{max,ave}$	s
t*´	time needed for a fully calcined carbonator sample to increase its carbonate content to $X_{max,ave}$	s
T_{carb}	average carbonator temperature	°C
T_{calc}	regenerator temperature	°C
t_{reg}	regenerator residence time	s
TSI	Total Solid Inventory	kg
u_0	riser superficial velocity	m/s
u_k	velocity where relative riser pressure drop fluctuations level off	m/s
u_{mf}	minimum fluidization velocity	m/s
$u_{inletcyclone}$	inlet gas velocity in cyclone	m/s
U_{sl}	slip velocity between gas-solid in standpipe i	m/s
ν_i	volume fraction of gas specie i	-
ν_{eq}	volume fraction of CO_2 at equilibrium conditions	-
W_i	Inventory within component i	kg
$X_{max,ave}$	average maximum carbonation conversion	mol_{CaCO3}/ mol_{Ca}
$X_{max,N}$	maximum carbonation conversion at carbonation/calcination cycle N	mol_{CaCO3}/ mol_{Ca}
X_{calc}	average sorbent carbonate content in/after the regenerator	mol_{CaCO3}/ mol_{Ca}
X_{carb}	average sorbent carbonate content in/after the carbonator	mol_{CaCO3}/ mol_{Ca}

Greek symbols	Explanation	Unit
ε_s	solid fraction	-
ε_{mf}	voidage at minimum fluidization conditions	-
μ	gas viscosity	Pas
η_{reg}	regeneration efficiency	-
ρ_{bulk}	bulk density of suspension	kg/m^3
ρ_g	gas density	kg/m^3
ρ_s	solid density	kg/m^3
φ	gas-solid contacting effectiveness factor	-
φ_s	particle sphericity	-
τ	carbonator space time	s
τ_{active}	carbonator active space time	s

Acronyms	Explanation
BFB	Bubbling Fluidized Bed
Bub	Bubbling
CFBC	Circulating Fluidized Bed Combustor
CLC	Chemical Looping Combustion
DFB	Dual Fluidized Bed
FB	Fluidized Bed
FICFB	Fast Internally Circulating Fluidized Bed
LHV	Lower Heating Value
Mov	Moving
PSD	Particle Size Distribution
TG	Thermo-Gravimetric

Subscripts	Explanation
A	relates variables to approach A for active space time calculation
B	relates variables to approach B for active space time calculation
In reference to Figure 3.1	
atm	atmosphere
cv	cone valve
cyclone	cyclone and exit duct (from point b to point c)
double exit ls	double exit loop seal (from point e to point f)
lower ls	lower loop seal (from point l to point m)
lower st	lower standpipe (from point l to point k)
ls weir	loop seal weir
riser bottom	bottom part of riser (from point g to point a)
riser top	top part of riser (from point a to point b)
riser total	whole length of riser (from point g to point b)
upper st	upper standpipe (from point e to point d)

Abstract

Drastic reduction of CO_2 emissions is required to combat climate change phenomena. Post-combustion CO_2 capture summarizes a portfolio of technologies applicable to new and existing coal fired power plants. A competitive process of this kind is Calcium looping, which is expected to become commercial by 2020. The above statements are based on the fact that the process utilizes a Ca sorbent, its fluidized bed nature, the possibilities for process integration (including steam cycle integration) and its technological maturity. Respective attributes lead to a cost per ton of CO_2 avoided of below €20/t and an electric efficiency penalty of below 6-8 %. The Calcium looping process is carried out in a Dual Fluidized Bed (DFB) system with continuous looping of CaO, the CO_2 carrier, between two beds. The system consists of a carbonator, where CO_2 from flue gas is absorbed by CaO and a regenerator, where captured CO_2 is released. The CO_2-rich regenerator flue gas can be finally sequestered. A 10 kW_{th} DFB facility has been built and operated at the Institute of Combustion and Power Plant Technology (IFK) of the University of Stuttgart, consisting of a riser coupled with a Bubbling Fluidized Bed (BFB), having the aim of providing proof of principle and characterizing the fluid-dynamic and reactor performance interactions, occurring between boundary conditions, independent and dependent variables, which determine the CO_2 capture efficiency. Reactor performance interactions have been studied in close cooperation with Instituto Nacional del Carbón (INCAR) of the Spanish Research Council (CSIC).

Fluid-dynamic interactions have been studied mainly through investigations conducted within a scaled cold model of the 10 kW_{th} IFK DFB facility. Since the majority of independent variables influence further dependent variables through fluid-dynamic interactions, it has been important to conduct a detailed fluid-dynamic analysis. Hence, the independent variables of carbonator superficial velocity, Total System Inventory, reactor overpressure, loop seal aeration, the opening of a mechanical valve for solid circulation control between the beds and the cold model Particle Size Distribution have been varied in a systematical manner. A stable operating region, bordered by two unstable regions has been identified for the cold model carbonator riser. Moreover, the influence of the independent variables mentioned above on important dependent variables, i.e. of the carbonator riser pressure drop and its inventory, the carbonator flow structure demarcated by the pressure and solid fraction profile, the carbonator entrainment and the solid flow between the two reactors of the Calcium looping system, has been assessed. With regard to the latter

two variables empirical correlations have been attained. The results from the fluid-dynamic analysis suggest that all dependent variables could be set through variation of the independent ones. Hence, the DFB setting is proven to be an excellent reactor system for carrying out the Calcium looping process.

Reactor performance interactions include those that influence the overall carbonation rate and are not of a fluid-dynamic nature, while the respective analysis bares their name. The study of these interactions has taken place through numerous experimental runs realized within the 10 kW_{th} IFK DFB facility, utilizing its Circulating Fluidized Bed (CFB) or its Bubbling Fluidized Bed (BFB) as the carbonator, and the 30 kW_{th} INCAR-CSIC DFB facility. The latter facility and the experimental runs conducted through its utilization have been realized outside the scope of this thesis. However, the data obtained from the 30 kW_{th} INCAR-CSIC DFB facility are utilized here extensively. The result analysis examines the closure of the CO_2 carbonator mass balance expressions between (i) the CO_2 that has disappeared from the gas phase (ii) the $CaCO_3$ that is circulating between reactors and (iii) the $CaCO_3$ that is formed within the carbonator bed. Through the first mass balance, the quality of gas measurements (conducted online with use of analyzers), solid analysis (Thermo-Gravimetric, TG, tests) and manual measurements (e.g. measurement of solid flows) is confirmed. Through the second mass balance expression, the results indicate that only a slightly overstoichiometric flow of active Ca is needed, i.e. a Ca-flow that can react in the fast reaction regime, for a given CO_2 capture efficiency to be achieved. The third expression requires simplification, i.e. the replacement of the first order derivative reaction rate term with an expression that has no derivative term, prior to assessing how well it fits the experimental data. Hence, the simplification of this mass balance expression is carried out with use of two theoretical approaches (A & B), which incorporate state of the art theoretical considerations, and lead to two different carbonator models. It has to be noted that the models and approaches are based on existing literature, which partially bears the contribution of the thesis author, and are validated here. Both models are simple, i.e. they utilize the assumptions of instant mixing for the solids and plug-flow for the gas. They lead also to different carbonator active space time expressions. The active space time is for both approaches the key parameter to interpret the carbonator reactor results since it is indicative of the CaO inventory per molar flow of CO_2 participating in the carbonation reaction and of its reaction rate. Under the light of these approaches, the behavior of dependent variables included in the models is analyzed, i.e. that of the decay of the maximum carbonation conversion (known also as sorbent activity), the actual carbonation conversion in/after the regenerator and the form of the axial vol.-% CO_2 & pressure drop profiles. In addition, the effect of further dependent variables, i.e. carbonator temperature, the Ca

looping ratio and carbonator space time on the carbonator CO_2 capture efficiency is explained based on approaches A & B. Approach B, utilizing a reaction rate independent of the difference of the maximum and actual particle carbonation conversion ($X_{max,ave}$-X_{carb}), fits all experimental data sets well. This is not the case for Approach A when considering a data set resulting from operation of the 10 kW_{th} IFK DFB facility with use of its CFB as the carbonator. Hence approach B, with its respective model and active space time expression, can be considered as generic, i.e. can be applied to any carbonator. The variation of the respective active space time parameter leads to a CO_2 capture efficiency variation between 30 % and greater than 90 %. The results presented here confirm the technical viability of the Calcium looping post-combustion CO_2 capture process. They have been used for designing the current pilot-plant facility, which are scaled up 20-50 times with regard to the lab-scale facilities.

Kurzfassung

Um die Auswirkungen des Klimawandels abzumildern, ist eine drastische Reduktion von Kohlendioxidemissionen dringend notwendig. Mit der Bezeichnung Postcombustion-Verfahren werden verschiedene Technologien zusammengefasst, bei denen CO_2 nach der Verbrennung von fossilem Brennstoff aus einem Kraftwerksabgas abgeschieden wird. Diese Verfahren können sowohl bei neuen als auch bei bestehenden Kohlekraftwerken angewendet werden. Einer der wettbewerbsfähigsten Prozesse ist das Calcium Looping-Verfahren, dessen kommerzielle Nutzung bis zum Jahr 2020 erwartet wird. Die Wettbewerbsfähigkeit des Calcium Looping-Verfahrens ist durch folgende Umstände begründet: (i) Es wird ein natürliches, kostengünstiges kalziumhaltiges Sorbens verwendet, (ii) es können kommerziell verfügbare Wirbelschicht-Reaktoren zum Einsatz kommen und (iii) es besteht die Möglichkeit die Prozesswärme in den Dampfkraftprozess zu integrieren. Somit können die CO_2-Vermeidungskosten auf unter 20 €/t reduziert und der elektrische Wirkungsgradverlust auf unter sechs bis acht Prozentpunkte vermindert werden. Das Calcium Looping-Verfahren wird in einer dualen Wirbelschichtanlage durchgeführt, in der CaO als CO_2-Träger kontinuierlich zwischen zwei Wirbelschichtreaktoren zirkuliert. Das System besteht aus einem Karbonator, in dem CO_2 mit Hilfe von CaO aus dem Abgas absorbiert wird, und einem Regenerator, in dem das CO_2 freigesetzt wird. Dieser hochkonzentrierte Abgasstrom kann dann getrocknet, verdichtet und in geeigneten geologischen Formationen gespeichert werden. Am Institut für Feuerungs- und Kraftwerkstechnik (IFK) der Universität Stuttgart wurde eine 10 kW_{th} Wirbelschicht-Anlage gebaut und betrieben. Diese besteht aus einer zirkulierenden Wirbelschicht und einer gekoppelten stationären Wirbelschicht. Mit Hilfe der Versuchsanlage wurde die technische Machbarkeit des Calcium Looping-Prozesses gezeigt und die fluiddynamischen und reaktionstechnischen Abhängigkeiten charakterisiert. Die reaktionstechnischen Abhängigkeiten definieren den CO_2-Abscheidungsgrad im Karbonator und werden bestimmt durch voneinander abhängige und unabhängige Variablen. Diese wurden in enger Zusammenarbeit mit dem Instituto Nacional del Carbón des Spanischen Forschungsrats erforscht.

Die fluiddynamischen Abhängigkeiten sind mittels eines skalierten Kaltmodells der oben genannten 10 kW_{th} DFB-Anlage untersucht worden. Dabei wurden die unabhängigen Variablen, nämlich die Karbonator-Leerrohrgeschwindigkeit, die Feststoffmasse in der DFB-Anlage, der Reaktorüberdruck, die Siphon-Fluidisierung, die mechanische Ventilöffnung (welche die Feststoffzirkulation zwischen den

Wirbelschichten reguliert) und die Partikelgrößenverteilung systematisch variiert. Für die Betriebszustände des Kaltmodell-Karbonators wurde ein Bereich mit stabilen Betriebszuständen festgestellt, welcher von zwei instabilen Bereichen begrenzt wird. Darüber hinaus wurde der Einfluss der oben genannten unabhängigen Variablen auf wichtige abhängige Variablen abgeschätzt. Zu den abhängigen Variablen gehören der Druckverlust im Karbonator sowie die Karbonatorbettmasse. Auch das Strömungsprofil im Karbonator, das von seinem Druckprofil und seinem Feststoffanteilprofil gekennzeichnet ist, der Feststoffaustrag aus dem Karbonator und die Feststoffzirkulation zwischen den beiden Calcium Looping-Reaktoren gehören zu den abhängigen Variablen. Bezüglich der beiden letztgenannten Variablen wurden empirische Gleichungen aufgestellt. Die Ergebnisse der fluiddynamischen Analyse zeigen, dass alle abhängigen Variablen durch unabhängige Variablen bestimmt werden können. Somit ist die DFB-Anlage als Reaktorsystem für die Umsetzung des Calcium Looping-Prozesses bestens geeignet.

Als reaktionstechnische Abhängigkeiten gelten diejenigen, die die Karbonatisierungsrate beeinflussen und die nicht von fluiddynamischer Natur sind. Diese Zusammenhänge wurden experimentell unter Nutzung der institutseigenen Anlage und der Versuchsanlage des spanischen Forschungspartners erforscht. Die Versuche an der spanischen Anlage wurden außerhalb des Rahmens dieser Abhandlung durchgeführt. Die daraus gewonnenen Daten allerdings werden an dieser Stelle ausgiebig genutzt. Mittels der Versuchsergebnisse kann überprüft werden, inwieweit sich die CO_2-Massenbilanz des Karbonators zwischen (i) dem CO_2, welches aus der Gasphase entfernt wurde, (ii) dem $CaCO_3$, welches zwischen den Reaktoren zirkuliert und (iii) dem $CaCO_3$, welches im Karbonatorbett entsteht, schließt. Mit einer Massenbilanz kann die Qualität der Gasmessungen (online durchgeführt), der Partikelanalyse (thermogravimetrische Untersuchungen) sowie der manuell durchgeführten Messungen (zum Beispiel die Messung von Feststoffmassenströmen) bestätigt werden. Die Massenbilanz zeigt außerdem, dass ein überstöchiometrisches Angebot aus aktivem Calcium benötigt wird, um einen bestimmten CO_2-Abscheidungsgrad zu erreichen und um CO_2 im Bereich der sogenannten schnellen Reaktionsrate (fast-reaction-regime) abzuscheiden. Die Massenbilanz muss, bevor sie mit den experimentellen Daten abgeglichen werden kann, vereinfacht werden. Die Vereinfachung der Massenbilanz wird durch zwei theoretische Herangehensweisen (A und B) bewerkstelligt und führt somit zu zwei verschiedenen Karbonatormodellen. Die Herangehensweisen sowie die Modelle sind teilweise der Literatur entnommen und werden hier validiert. Die beiden Herangehensweisen führen zu verschiedenen aktiven Raumzeit-Ausdrücken. Die aktive Raumzeit, die das Verhältnis zwischen Karbonatorinventar, Sorbensaktivität und CO_2-Molenstrom beschreibt, ist der

Schlüsselparameter um die Ergebnisse des Karbonators zu interpretieren. Mit Hilfe dieser zwei Modelle und den zugehörigen aktiven Raumzeit-Ausdrücken kann das Verhalten einiger abhängiger Variablen, die in den Modellen enthalten sind, analysiert werden. Zu diesen Variablen gehören (i) die Abnahme der maximalen Kapazität zur schnellen CO_2-Einbindung, auch als Sorbens-Aktivität bezeichnet, (ii) die tatsächliche Karbonatisierung im beziehungsweise nach dem Regenerator und (iii) die Form des axialen CO_2- und Druckprofils des Karbonators. Außerdem erklären die beiden Modelle den Effekt weiterer abhängiger Variablen auf den CO_2-Abscheidungsgrad. Dabei handelt es sich um die Karbonator-Temperatur, die Ca-Looping Ratio und die Karbonator-Raumzeit. Modell B, das einen Reaktionsraten-Ausdruck benutzt, welcher unabhängig von der Differenz zwischen der maximalen und der tatsächlichen Karbonatisierung der Partikel ist, stimmt mit allen experimentellen Daten überein. Hingegen ist die Übereinstimmung der experimentellen Daten mit dem Modell A nicht in allen Fällen gültig. Die Variation der aktiven Raumzeit-Parameter führt zu einem CO_2-Abscheidungsgrad bis über 90 Prozent. Die hier gezeigten Ergebnisse bestätigen die Realisierbarkeit des Calcium Looping-Post-Combustion-CO_2-Abscheidungs-prozesses.

1 Introduction and motivation

Drastic reduction of CO_2 emissions is required due to climate change phenomena [1]. The Copenhagen accord has set an objective to balance greenhouse gas emissions to 450 ppm of CO_2 equivalent and limit temperature increase by 2°C. Subsequently, the IEA World Energy Outlook updated its 450 scenario in the 2010 edition (WEO 2010) thus defining a possible way for achieving such a goal [2].

1.1 The potential of Carbon Capture and Storage (CCS) technologies

The WEO 2010 450 scenario [2] necessitates that the power sector, which is the prime CO_2 emitter today, is largely decarbonized. Policy implementation which will discourage CO_2 intensive power generation is therefore necessary. However, since the 450 scenario also predicts an average annual increase of electricity demand of about 1.7 %, a portfolio of low carbon technologies is needed to supply capacity additions. Figure 1.1 presents the annual reduction of CO_2 emissions and of the CO_2 intensity with regard to the power sector required for the 450 scenario to be achieved. This is realized in comparison to the Current Policies scenario, also presented in the WEO 2010, which is a business as usual scenario considering policies adopted by mid-2010 [2,3].

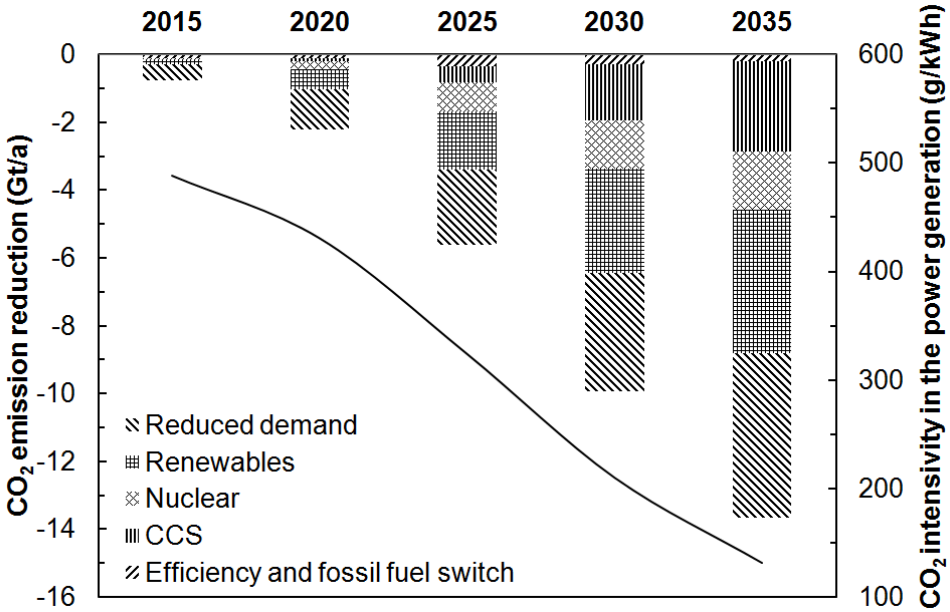

Figure 1.1: Change in world CO_2 emissions regarding power generation in the 450 Scenario compared with the Current Policies Scenario; Source: World Energy Outlook 2010 [2]

Figure 1.1 reveals the magnitude of the challenge set by the Copenhagen accord and the 450 scenario. The difference with regard to annual CO_2 emissions between the Current Policies Scenario and the 450 Scenario by the year 2035 is approximately 14 Gt/a, while significant activity is noted after 2020. Moreover, Figure 1.1 identifies the technological means for achieving the above goal. Carbon Capture and Storage (CCS) technologies include the processes developed to capture CO_2 from the exhaust of power stations and from other industrial sources, the infrastructure for handling, transporting CO_2 and storing the CO_2 in deep geological formations [4]. According to Figure 1.1, the contribution of CCS technologies to the total CO_2 emission reduction at the year 2035, when considering the 450 Scenario and Current Policies Scenario, is just under 20 %. In absolute numbers the noted reduction accounts for 2 Gt/a & 0.7 Gt/a, and is achieved through CCS application in coal and gas-fired power plants, respectively [2]. Moreover, as noted by the definition given above, CCS technologies do not only aim at CO_2 mitigation from the power generation sector. The 450 scenario projects reduced CO_2 emissions, i.e. 1.3 Gt/a, with regard to the Current Policies Scenario, as a result of CCS application in the industrial sector [2]. Industries suitable for the application of CCS include cement, oil refineries, iron and steel, gas processing chemicals and pulp and paper [4].

The European Union (EU) is amongst the key promoters with regard to the development and application of CCS technologies and has released interesting numbers with regard to the future of CCS in the EU [5]. These projections include, among others, that the maximum capacity for CCS equipped fossil fired power plants within the EU is assessed to be 190 GW by the year 2030. In such a case, 32 % of the electricity consumption of the EU would be provided from the above capacity. Furthermore, the achieved CO_2 capture efficiency of these plants is expected to be at least 85 %, while the cost per CO_2 avoided is calculated to be €35/t. It is also interesting to note that the EU, in accordance to the World Energy Outlook 2010 report, expects major deployment of CCS applications after 2020. However, an investment of €1 billion is expected until that time in related R&D research in order to improve efficiency and cost, while exploring novel technologies.

1.2 Technological options for the CO_2 capture step

The first element of the CCS chain is the CO_2 capture step and is the most energy intensive. Different options hereto have been summarized and evaluated in a recent review from Florin and Fennell [4]. Three groups of technologies have been identified [4], depending on whether the CO_2 capture takes place downstream, upstream or during fuel combustion. Thereby, a given process is classified to belong to the post-

combustion, pre-combustion or oxy-combustion technology group, respectively. Their generalized flow diagrams are given in Figure 1.2.

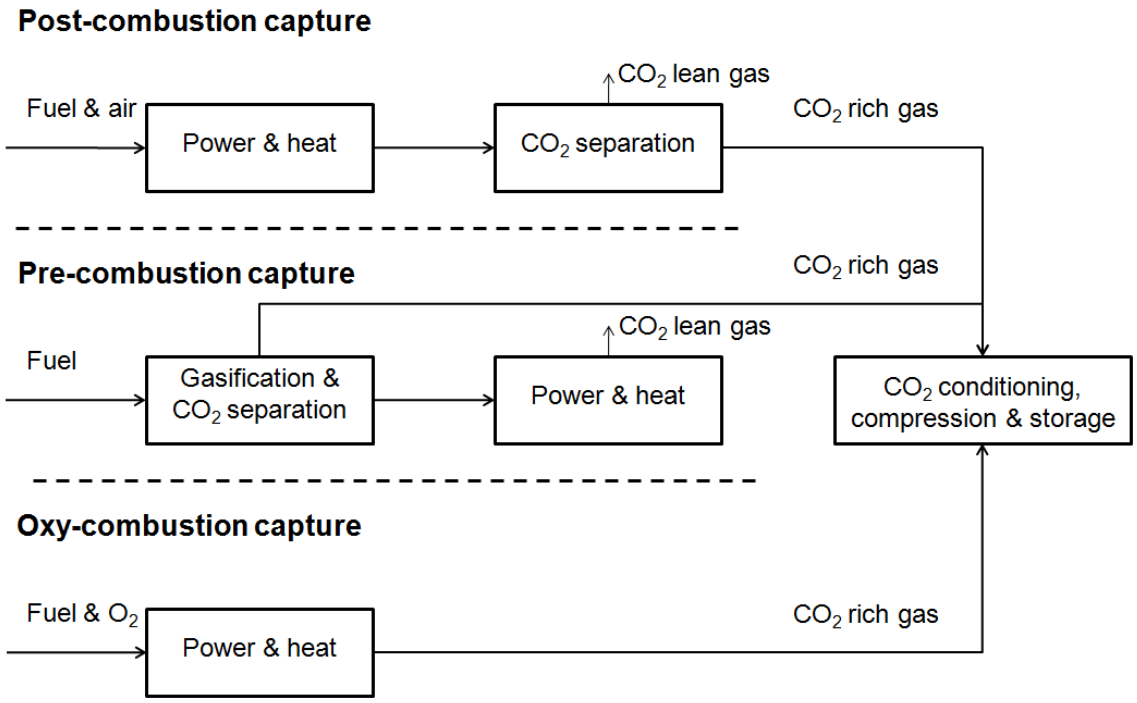

Figure 1.2: Groups of technological options for realizing the CO_2 capture step [4, 6]

With application of the post-combustion CO_2 capture option, the power generation concept of today remains largely unchanged since the CO_2 separation block becomes a further conditioning component of the flue gas path. Processes of the above technological group consider solvent scrubbing, the high temperature Calcium looping process and a series of more novel technologies, i.e. utilization of low- temperature sorbents, ionic liquids, biological capture using algae ponds or bioreactors and membrane CO_2 separation [4]. Different options for solvent scrubbing involve the use of aqueous amine and ammonium solvents, amino-acid salt solvents and potassium carbonate solvents [4]. With regard to aqueous solvent scrubbing different solvents have been proposed which include among others MEA (monoethyloamine), DEA (diethylamine), AMP (amino-methyl-propanol) [7] and suitable blends [8]. The ammonium solvent is utilized within the chilled ammonia process [9]; the process name demarcates that the CO_2 separation occurs at a much lower temperature, i.e. 0-20°C [10], in comparison to the aqueous amine solvents. On the other hand, the Calcium looping process [11], which is a high temperature process involving CO_2 absorption at 600-700°C and sorbent regeneration at above 900°C, exhibits also different schemes. Hence, the mainstream Calcium looping process takes into account combustion under an O_2/CO_2 environment with regard to sorbent regeneration, while

more advanced schemes foresee an allothermal form of heat transfer [12]. Moreover, low temperature solid sorbents is also a diverse technological field, ranging from amine impregnated sorbents to others which are K [13] or Na based [13,14].

On the other hand, the pre-combustion CO_2 capture route involves fuel gasification under pressure with CO_2 separation. The H_2 rich gas produced can be used for power generation through a combined cycle process scheme [15, 16]. Alternatively, the H_2 rich product gas can be supplied to a fuel cell, thus achieving higher overall electric efficiency values [15, 16, 17]. The most advanced process of this category is the Integrated Gasification Combined Cycle process with CCS. Other pre-combustion processes far less developed include the Limestone Enhanced Gasification of Solids (LEGS) process [16] and the Zero emission Coal Alliance (ZECA) process [17]. However, all three mentioned technologies differ in the method that the H_2 rich, pressurized gas is prepared. The IGCC process, for example, involves (i) partial oxidation of the fuel with pure O_2 (ii) shift of the syngas to CO_2 and H_2 and (iii) CO_2 separation with natural solvents, e.g. with use of the Selexol or Rectisol process [15]. On the other hand the LEGS process utilizes allothermal steam gasification with CO_2 chemi-sorption from a Ca sorbent, thus producing a H_2 rich, pressurized gas in one step [16]. The LEGS process, along with its CO_2 neutral biomass gasification counterpart, i.e. the Absorption Enhanced Reforming (AER) process, is a prime example of the Sorption Enhanced Reforming (SER) technologies. Moreover, the ZECA process utilizes a more complicated flow sheet involving the following main process steps [17]: (i) gasification of coal with a hydrogen/steam mixture to produce a CH_4 rich gas (ii) steam reforming to H_2 (driven by the CaO to $CaCO_3$ carbonation reaction) (iii) conversion of part of the H_2 to H_2O and electricity in a fuel cell (the rest is used a gasification agent in the first step). Heat integration between the steps allows up to 70 % of the fuel energy, based on the higher heating value, to be converted to electricity.

Finally, the oxy-fuel combustion processes necessitate the combustion of fuel with O_2 and in the absence of N_2. The type of the oxy-fuel process is characterized based on the form that O_2 is supplied to the combustion chamber and the method which is used for its production [4]. The conventional oxy-fuel process relies on the production of O_2 in a cryogenic Air Separation Unit (ASU) and its supply in gaseous state to the boiler [6]. This process can be further improved if the ASU is substituted by a membrane reactor for O_2 separation from air [4]. On the other hand, the Chemical Looping Combustion (CLC) process, which falls within the oxy-fuel family, necessitates the supply of oxygen in the solid state, i.e. bound within a metal oxide [4, 18].

There is no general solution with regard to which option is to be chosen in order for the CO_2 capture step to be realized [18]. For example, post-combustion technologies have an advantage when implementing CCS technology as a retrofit. This is true since pre-combustion options are not applicable in such a case, while retrofitting an existing boiler for oxy-combustion would require that the unit remains offline for a significant time [18]. In any case, the issues of (i) technological maturity of a specific CO_2 capture option at a given time, (ii) electric efficiency penalty with regard to a same capacity power unit without CCS and (iii) the costs per ton of CO_2 avoided and of electricity generation will always be amongst the most significant factors in naming the CO_2 capture option to be chosen for a specific case.

1.2.1 Technological maturity

The term ‘technological maturity’ demarcates the remaining development needed for a given process to be deployed at industrial scale. In order to quantify this aspect with regard to the different options for the CO_2 capture step, a ranking has been recently carried out [4]. The Technological Readiness Levels (TRLs) rank scheme, developed by NASA, has been utilized for this purpose. Hence, a given CO_2 capture process can by assigned a TRL value from 1-9. A TRL of 1 would mean that only basic principles have been observed, a TRL of 5 indicates that the technology or part of the technology has been validated in a working environment; while a TRL of 9 means that the technology is deployed. The result of this ranking for all post-, pre- and oxy-combustion processes to date is given in graphical form in Figure 1.3. However, Figure 1.3 is only a snap-shot of the reality at the end of 2010 and can be quickly outdated by subsequent developments.

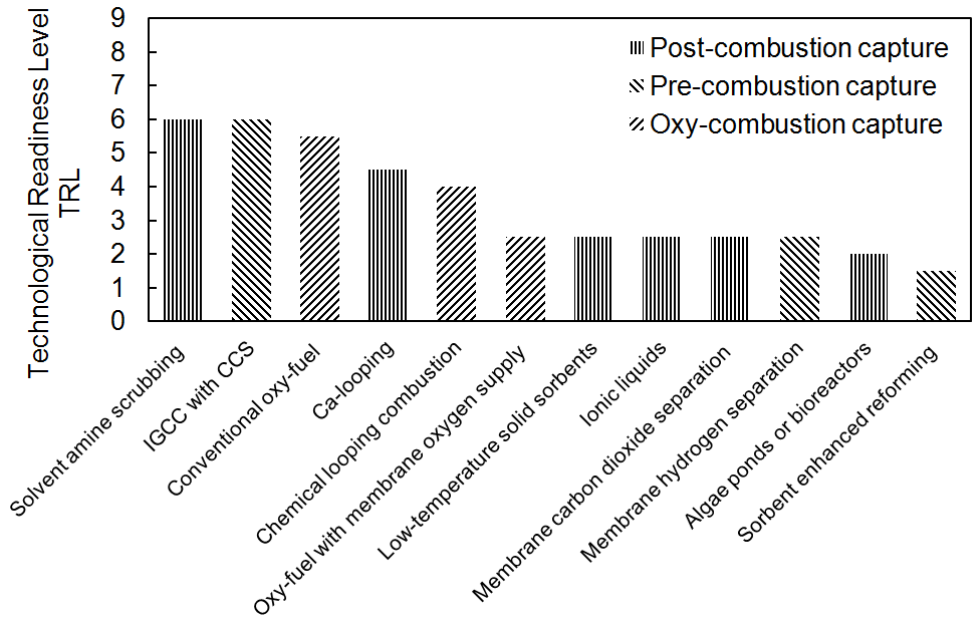

Figure 1.3: Technological Readiness Level (TRL) ranking of CO_2 capture processes [4]

Figure 1.3 postulates the leading role of amine solvent scrubbing, including the chilled ammonia process. Hence, these processes are ranked with a TRL of six. In the case of amine scrubbing, this is justified based on that this technology is established in the natural gas processing sector [4]. However, process scale-up is needed for process application to post-combustion CO_2 capture due to the associated larger flue gas flows. A number of pilot plants worldwide are investigating this key issue [19]. Examples include the following plants, both in operation and under construction, the country and capacity of which are noted in brackets: Didcot (UK, 1.2 t/d_{CO2}), PC Compostilla (Spain, 5 t/d_{CO2}), Cato (Netherlands 6 t/d_{CO2}), Niederaußem (Germany, 7.2 t/d_{CO2}), Esjberg (Denmark, 24 t/d_{CO2}), Aberthaw (UK, 50 t/d_{CO2}) and Brindsi (Italy, 60 t/d_{CO2}) [19-25]. Above installations can treat flue gases from the 100s of kW_e scale to the few MW_e scale. Moreover, a further pilot plant, located at the Staudinger power plant in Germany, has demonstrated the amino-acid salt solvent process variant [26]. As noted, the high TRL ranking is extended also to the chilled ammonia process, based on the performance of a 20 MW_e/ 54 MW_{th} facility installed at the Mountaineer power plant in the United States [27]. It is the successor of pilot plants smaller by approximately an order of magnitude located at Pleasant Prairie (USA) and Karlshamm (Sweden).

The CCS equipped IGCC power plant also exhibits an equal TRL as that of amine solvent scrubbing. This is because there is large experience with conventional IGCC plants, despite availability issues [18], while their worldwide capacity has reached 7600 MW_e by 2009 [15]. Moreover, as noted above CO_2 separation can be realized with well proven processes and is facilitated by the large partial pressures of

CO_2. Process modifications, required between a CCS equipped and a conventional IGCC plant, include adaptation of the gas-turbine to burn an almost pure H_2 gas [15].

The conventional oxy-combustion process, i.e. where gaseous oxygen from an ASU is supplied to the boiler is ranked with a TRL of 5-6. An astonishing number of promising pilot-plants in the tens of MW_{th} scale have been successfully taken into operation and are under construction. These plants utilize both Pulverized Coal (PC) and Fluidized Bed (FB) combustion technology and include the B&W (USA; 30 MW_{th}), Jupiter (USA, 20 MW_{th}), Oxy-coal UK (UK; 40 MW_{th}), Alstom-Windsor facility (USA; 15 MW_{th}), Vattenfall (Germany, 30 MW_{th}), Total-Lacq (France; 30 MW_{th}), Callide (Australia; 90 MW_{th}), Ciuden-PC (Spain; 20 MW_{th}), Ciuden-CFB (Spain; 30 MW_{th}) and Enel HP oxy (Italy; 48 MW_{th}) [28]. Above plants burn a variety of fuels from natural gas to sub-bituminous and bituminous coals. In addition, it is interesting to note that the case of the Lacq plant is an example with regard to retrofitting an air-fired boiler to an oxy-fired one [18].

Amine solvent scrubbing & chilled ammonia, the CCS equipped IGCC and the conventional oxy-fuel processes are commercially available today and are expected to see industrial application by 2015. This is demarcated by a significant amount of projects around the globe [4, 28, 29]. On the other hand, the Calcium looping and CLC are considered as CCS technology of the 2^{nd} generation [30], since they are expected to become commercial near 2020 [4]. Their development is justified based on their competitiveness to existing options; however, further progress is necessitated. The status of these 2^{nd} generation technologies is demonstrated from their respective TRL rankings, i.e. 4-5 for the Calcium looping process and 4 for CLC. With regard to the Calcium looping process, four continuous lab-scale plants were built and operated, i.e. in IFK (10 kW_{th}), INCAR-CSIC (30 kW_{th}), CANMET and the thermal institute of the Tsinghua University [31-34]. In addition, the process has been recently demonstrated in a 200kW_{th} pilot plant also at IFK [35, 36], a 1 MW_{th} facility of TU Darmstadt [37] and the larger pilot plant, i.e. the 1.7 MW_{th}, located in La Pereda, Spain [38]. All of the above Calcium looping facilities are discussed in further detail in section 2.2. On the other hand, CLC can be considered as quite developed for natural gas combustion; however, application for solid fuels still remains a challenge. In the case of atmospheric natural gas combustion, the biggest facility to date is a 120 kW_{th} facility located at the TU Vienna [39]. It is interesting to note that although a pressurized natural gas CLC facility would have the advantage of implementing a combined cycle power generation concept, the atmospheric CLC concept is still more competitive than any other oxy-fuel natural gas combustion concept [40]. In the case of in-situ solid fuel combustion, within a CLC facility, demonstration has not exceeded lab-scale [41]. Particular challenges involve fuel conversion and separation of ash-char-metal particle

mixtures. Moreover, application for syn-gas combustion coming from a gasifier would most likely be feasible if both gasifier and CLC unit are under pressure [40]. However, design of pressurized DFB facilities still remains a technological challenge.

1.2.2 Costs and Electric effiency penalty

In a recent review, Rubin et al. [42] states that the application of state of the art CCS technology on new coal combustion plants and gasification plants may increase the cost of electricity by 60-80 % and by about 30-50 %, respectively. According to the same authors, this translates to a cost of electricity for new combustion plants with CCS of $40-70/MWh and a cost of CO_2 avoided of $60-80/$t_{CO2}$. Furthermore, these authors provided a table (reproduced in Table 1.1a) listing representative values of the efficiency of the power generation technologies with and without application of the different major CCS process types. On the other hand, Table 1.1b reports energy efficiency and efficiency penalties of coal fired and IGCC plant simulations found within recent literature. Table 1.1b provides a picture of values that are reported with regard to the Calcium looping technology and how these compare to the major capture processes. However, it has to be noted that Table 1.1b should not be used for detailed comparison since the assumptions behind the studies may vary significantly.

Table 1.1a: Representative values of power plant efficiency and CCS penalty* [42]

Power plant & capture system	Net plant efficiency* (%) without CCS	Net plant efficiency* (%) with CCS)	Additional energy input (%) per net kWh output	Reduction in net kWh output (%) for fixed input
Existing subcritical pulverized coal, post-combustion capture	33	23	43	39
New supercritical pulverized coal, post-combustion capture	40	31	29	23
New supercritical pulverized coal oxy-combustion capture	40	32	25	20
New IGCC (bituminous) pre-combustion capture	40	33	21	18
New natural gas comb. cycle, post-combustion capture	50	43	16	14

* All efficiency values are based on the higher heating value of the fuel. Individual studies, reporting values around the above ranges, are given within Rubin et al. [42]

Table 1.1b: Indicative efficiency and efficiency penalty values found in recent literature

Capture system	Base case power plant	Net plant efficiency (%) no CCS**	Net plant efficiency (%) with CCS**	CO_2 capture Efficiency (%)
Amine (MEA) scrubbing & chilled ammonia	522 MW_e existing supercritical power plant firing bituminous coal [43] (with MEA)	41.1	31.9 (-9.2)	90.0
	788 MW_e supercritical power plant firing hard coal [44] (with MEA)	42.2	31.6-32.8 (-9.4-10.6)	90.0
	800 MW_e Hitachi supercritical coal power plant [45] (with MEA)	46.9	35.4-37.4 (-9.6-11.3)	90.0
	408 MW_e Nordjyllandsvaerket state of the art coal heat and power plant [46] (with chilled ammonia)	47.9	38.7 (-9.2)	90.0
IGCC with CCS	485.19 MW_e Shell gasifier using coal with 8 % moisture (a.r.) and 28.5 % volatiles [47]	46.6	37.1 (-9.5)	90.8
	448.97 MW_e Siemens gasifier using coal with 8 % moisture (a.r.) & 28.5 % volatiles [47]	43.1	36.0 (-7.1)	92.4
Oxy-fuel combustion	555.3 MW_e supercritical power plant (based on 600°C technology) firing Kleinkopje coal [48]	45.9	36.4 (-9.5)	90.2
	605.9 MW_e supercritical power plant (based on 700°C technology) firing Kleinkopje coal [48]	50.1	39.9 (-10.2)	90.2
Calcium looping	1052 MW_e state of the art coal power plant. Total power of original & Calcium looping plant: 1533 MW_e [49]	45.6	39.2 (-6.4) Cement credits lead to 0.86 points penalty reduction [50]	80.0 in carbonator & 88.0 after regenerator exit ****
	450 MW_e (net) state of the art coal power plant. Total power of original and Calcium looping plant: 622 MW_e [51]	44.9	37.0 (-7.9) Cement credits lead to 2.92 points penalty reduction [50]	85.0 in carbonator & 88.7 after regenerator exit****
	350 MW_e existing subcritical plant firing low rank high sulphur lignite. Total power of original & Calcium looping plant: 831.8 MW_e [52]	36.0 (41.4)***	32.9 % (-8.5) Cement credits lead to 0.50 points penalty reduction [50]	90.0 in carbonator & 96.3 after regenerator exit****

** All efficiency values are based on the lower heating value

*** The efficiency in brackets corresponds to the average efficiency of the existing plant and of a state of the art supercritical plant having the same fuel input as the added Calcium looping plant

**** The overall capture efficiency will be lower.(> 90 %) of the given value after the regenerator due to further CO_2 losses, occurring during CO_2 rich gas conditioning, escaping with non-condensable gases (e.g. [48]).

Although, a detailed comparison on the basis and assessments of the different studies is beyond the scope of this thesis a number of points can be addressed. Of particular help, with regard to the Calcium looping related works is the review of Romano et al. [50]. The first observation with regard to Table 1a and 1b is that the Calcium looping process exhibits generally a lesser efficiency penalty than the main post-combustion technology of amine scrubbing. This is mainly associated with heat recovery options existing in the first case and absent in the latter. The CO_2 capture efficiency after the regenerator is higher than that of the carbonator due to that the CO_2 related to fuel combustion and fresh sorbent calcination within the regenerator is also captured. The difference between the CO_2 capture efficiency after the regenerator and that of the carbonator depends on the heat requirements assigned to the regenerator and the foreseen make-up flow need. The overall CO_2 capture efficiency is lower than the "after the regenerator" values reported in Table 1.1b since further losses of CO_2 occur during conditioning which escape along with non-condensable gases (N_2, O_2, NO, etc.) [28, 48]. The overall CO_2 capture efficiency of the Calcium looping plant can be approximated when taking into consideration the CO_2 capture efficiency after the regenerator with the CO_2 capture efficiency of a state of the art oxy-fuel unit [48]. Considering the above, in combination with the fact that CCS technology deployment is expected after 2020, Calcium looping may play an important role in the post-combustion CO_2 capture field in less than a decade. Moreover, the potential utilization of the calcined purge material leads to a significant improvement in terms of the efficiency penalty, since then the calcination of the fresh $CaCO_3$ is not to be considered as an energy penalty [50]. Using the terminology of Romano et al. [50] the resulting efficiency penalty reduction is termed in Table 1.1b also as credits to the cement industry. The work of Martínez et al. [52] underlines that the Calcium looping process is particularly valuable as a retrofit option. This is true, since the retrofit plant can be equipped with a highly efficient supercritical steam cycle, thus allowing the new power generation unit, i.e. existing power plant & Calcium looping plant to operate at acceptable efficiency. Hence, the work of Martínez et al. (one case examined by the authors summarized briefly in Table 1.1b) shows that an existing plant of 36 % net efficiency, when equipped with a Calcium looping plant incorporating its own highly efficient steam cycle can operate as a single power generation unit at an efficiency of 32.9 %. This should not be misleading in terms of efficiency penalty, since the latter is calculated using as a reference efficiency value (i.e. 41.4 % for the case from the work of Martínez et al. [52]) that is equal to the average of the net efficiency of the existing plant (i.e. 36 %) and that of a state of the art supercritical plant (i.e. 45 %) having the same fuel input as the Calcium looping system. Moreover, Calcium looping is competitive to oxy-fuel combustion and IGCC with CCS systems, as can be seen by the electric efficiency values predicted through

the studies of Table 1.1b. The work of Abanades et al. [53] is of particular interest since it provides direct comparison between the Calcium looping and the conventional oxy-fuel processes at same conditions. Within their work, it is demonstrated that a state of the art air fired power plant equipped with a Calcium looping facility will always exhibit a better electric efficiency than a same power output oxy-fuel system. This is true since in the air fired power plant equipped with a Calcium looping system case only a fraction of the total fuel is burnt under oxy-fired conditions, whereas in an oxy-fired combustor all the fuel is burnt in such a modus. The resulting 2-3 times bigger oxygen stream in the latter case justifies the worse efficiency of the oxy-fired system caused by the operation of the energy intensive Air Separation Unit (ASU). Moreover, according to the same work [53], the advantage of Calcium looping is retained over oxy-fuel combustion also when considering capital cost. The authors justify this based on the fact that the cost of an oxy-fired power plant is significantly higher than a conventional plant [53, 54]. Hence, since a conventional plant equipped with a Calcium looping unit is in terms of scale and power production a 50-70 % conventional plant and a 30-50 % oxy-fuel plant, such a system is cheaper than a 100 % oxy-fired unit. The added cost considered for building a carbonator unit with regard to the Calcium looping application does not change the above picture.

Finally, it is interesting to note that the cost of electricity production with Calcium looping application has been reported to correspond to CO_2 avoidance costs of €18.6/t [55] and $15.5/t (authors provide also a worst case and best case value, which are equal to $8.3/t and $36.6/t respectively) [53]. These values are relatively low with regard to the range reported in the review of Rubin et al. [42]. The electricity production costs have been reported equal to €48/MWh [51] and €41/MWh [55], which correspond to the lower range of Rubin et al. [42] for new combustion plants with CCS. As mentioned, the overall feasibility of the Calcium looping process, noted by respective values, is justified based on a number of attributes, e.g. (coupling of the process with a steam cycle, utilization of a cheap and available sorbent), which are analyzed in a dedicated section below.

1.3 The Calcium looping process schematic

The Calcium looping process is depicted schematically in Figure 1.4. It comprises a Dual Fludized Bed (DFB) system with continuous looping of CaO and was conceived by Shimizu et al. in 1999 [11]. A percentage of the incoming CO_2 molar flow (F_{CO2}) is absorbed by the carbonator inventory (n_{Ca}). This percentage is termed as the CO_2 capture efficiency (E_{carb}) and is the metric of carbonator operation. Hence, a CO_2 lean flue gas is produced. The CO_2 captured is transferred in the form of

$CaCO_3$ to the regenerator with the solid flow (F_{Ca}). The sorbent is calcined to a great extent in the regenerator at temperatures above 900°C and recirculated back to the carbonator for further CO_2 capture. A make-up flow (F_0) of $CaCO_3$ is necessary to compensate for the decay of the maximum carbonation conversion of the sorbent [56]. The energy required for regeneration of the sorbent is supplied from oxy-fuel combustion of a C-fuel, while other more cost-effective alternatives have been proposed [12].

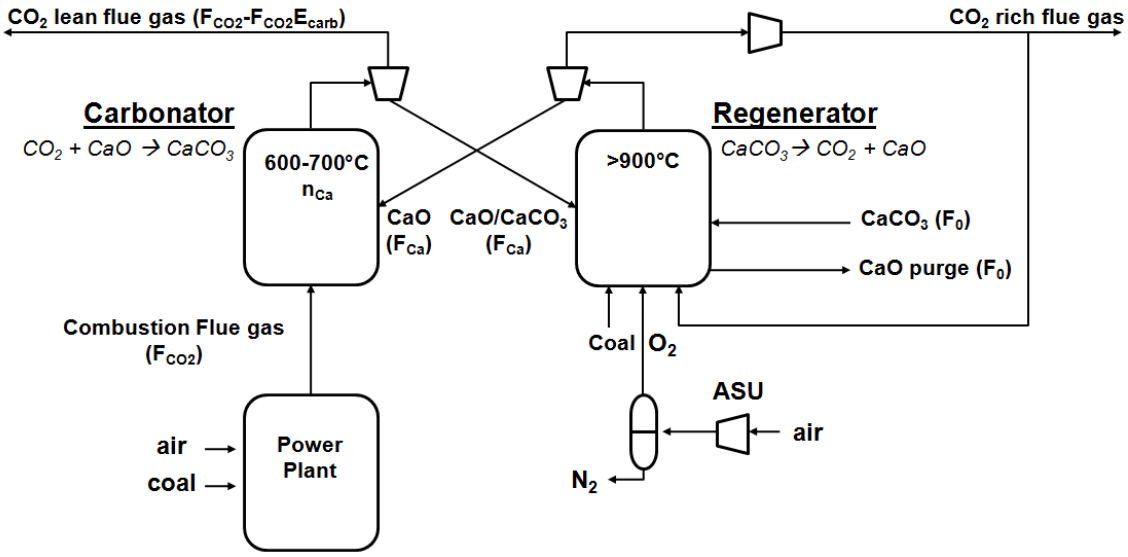

Figure 1.4: The Ca- looping process schematic; ASU: Air Separation Unit

The energy spent in the regenerator is recovered with use of a high efficiency steam cycle configuration [49, 51, 52]. Eventually, a CO_2 rich stream can be produced from the regenerator which is suitable for storage after compression and conditioning. However, CaO circulation between two fluidized beds and its use as a CO_2-carrier has been realized before CO_2 capture became an issue, i.e. during the CO_2 Acceptor process in the 1960-70s for syngas production [57]. Today, the scheme of Figure 1.4 is also considered for gasification applications, using brown coal or biomass, in order to produce a hydrogen rich syngas and/ or a CO_2 stream suitable for sequestration. In the case of coal the process is named, as already mentioned, LEGS (Limestone Enhanced Gasification of Solids) [16] and in the case of biomass AER (Absorption Enhanced Reforming) [58]. With regard to the AER process, results have been reported on an industrial scale (8 MW input) [59].

1.4 Objectives and related tasks

The continuous Calcium looping process had been a paper concept at the time that this work started in 2005, being tested only in Thermo-Gravimetric Analyzer (TGA) equipment, e.g. [60], and batch reactors [61]. Although, such studies continue to produce important information [62], the in depth gas-solid fluid dynamic and reactor performance analyses, with use of continuous lab-scale equipment, were considered a necessity in order to provide proof of principle and to characterize the process. Hence, conducting these two types of analyses, with regard to the Calcium looping system of Figure 1.4, is the thesis objective. The role and significance of gas-solid fluid-dynamic analysis and reactor performance analysis is further highlighted in Figure 1.5, in a simplified manner.

1. **Gas-solid fluid-dynamics analysis:** Hereby, the aim lies in understanding the gas-solid fluid-dynamic interactions within the different parts of a Calcium looping reactor facility, i.e. carbonator, regenerator and solid circulation system and identifying a facility operating window. Thereby, the establishment of the link between parameters that an operator can change manually (independent variables, e.g. carbonator velocity and solid circulation valve opening) and parameters that are a result of fluid-dynamics interactions is sought out.
2. **Reactor performance analysis:** Boundary conditions and independent variables define dependent ones. This happens, besides fluid-dynamic interactions, also through interactions related to: (i) carbonation reaction rate (ii) sorbent properties, (iii) the combustion process within the regenerator and (iv) steam cycle integration. It is the further combinations of dependent variables that define the CO_2 capture efficiency of the carbonator, as depicted in Figure 1.5. These are of a “reactor performance” nature and to an extent of a fluid-dynamic one. Steam cycle integration interactions and those related to the combustion process in the regenerator have not been studied in the frame of this thesis. However, all other non-fluid-dynamic interactions leading to the derivation of the CO_2 capture efficiency are included within the scope of the reactor performance analysis conducted here. The main objective of this task is to describe these interactions by validating a simple yet efficient carbonator model, despite simplifications.

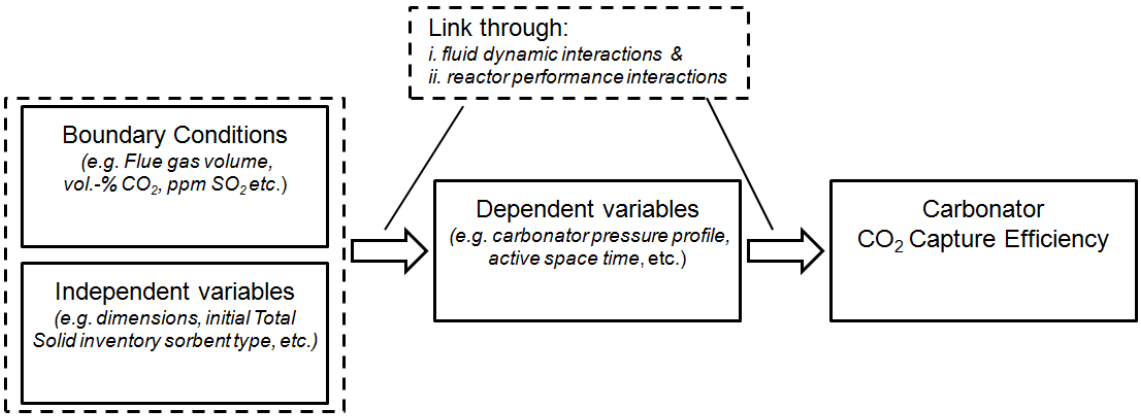

Figure 1.5: Calcium looping variables and interactions

The list of tasks chosen in order for the above objectives to be met is generally outlined below. Thereby, the aim is to provide insight with regard to the approach taken and not to describe in detail the scope of work performed. In addition, the list below is considered to exhibit a further merit, i.e. that it can be considered as a generic path for scaling-up novel fluidized bed processes from paper concepts to lab-scale. However, it is not the first time that such a pathway has been adopted. Suitable references hereto come from other DFB processes, i.e. the CLC process [63] and the biomass steam gasification Fast Internally Circulating Fluidized Bed (FICFB) [64] process.

1. **Basic engineering of the continuous 10 kW_{th} IFK DFB facility:** This task involved carrying out basic engineering with regard to the above unit. This was realized by bringing together information related to Ca chemistry and fluidization engineering. The resulting product has been a preliminary facility design draft.
2. **Scaled cold model testing:** Constructing a fluid-dynamically scaled cold model of the above draft, through utilization of the Glicksman simplified criteria, resulted into two benefits. Firstly, the 10 kW_{th} IFK DFB facility design was further evolved according to observations. Secondly, the experimental campaigns conducted at the cold model provided a large experimental data base, which was used for achieving the objective of realizing an in-depth fluid-dynamic analysis.
3. **Detailed engineering, building and commissioning of the 10 kW_{th} IFK DFB facility:** This task has been the most time intensive. Moreover, it has been a multidisciplinary task. Hence, project management and detailed engineering with use Computer Aided Design (CAD) were carried out within the scope of this thesis, while the construction, on-sight assembly, electrical installation,

automations and software programming were performed through the work of colleagues, which are mentioned by name in the acknowledgement section. Facility commissioning has been also an arduous task that paved the way for the task of the reactor performance analysis to be met.

4. **Realization of experimental campaigns, result analysis and comparison with results from other DFB systems:** The successful experimental campaigns, conducted with use of the 10 kW_{th} Dual Fluidized Bed facility have been the basis for realizing the task of reactor performance analysis. Their realization required process and fluidized bed understanding, as well as technical support with regard to the facility. Result analysis involved the creation of simple programs which allowed quick evaluation of quite large data sets. However, it has been the combined assessment of the 10 kW_{th} IFK DFB results with those of the 30 kW_{th} DFB facility of INCAR-CSIC, produced outside the scope of thesis, which led to the fulfilment of the reactor performance analysis task. Hence, in a large number of cases IFK and INCAR-CSIC lab-scale data sets are presented together. The common conclusions reached are validated by a simple reactor model, despite the differences of experimental conditions and equipment. Hence, the above methodology has been considered sufficient for achieving the reactor performance analysis/ characterization objective.

1.5 Overview and outline

The following chapters have the goal to comprehensively present the state of the art with regard to theory and process developments, to describe the experimental methodology and to discuss and summarize the results obtained within the conducted fluid-dynamic and reactor performance analyses. Moreover, the thesis annex contains details with regard to the 10 kW_{th} IFK DFB facility and its scaled cold model, while all obtained data are presented in tabular form, thus allowing for independent researchers to validate their own modeling approaches (as has already been the case [65, 66]). A brief overview of the content of each chapter is given below.

Chapter 2 deals with the state of the art and provides the necessary information required to understand design, operational aspects and experimental results. Firstly, an analysis with regard to the process attributes, responsible for the rapid development of the Calcium looping process, is carried out. These include the utilization of a Ca sorbent, the process fluidized bed nature and the ability of recovering process heat to produce additional power. Furthermore, the experimental installations which have appeared in Europe, Canada and the P.R. of China are proof of the successful

development and are discussed separately. Subsequently, aspects of sorbent chemistry and the carbonation reaction are analyzed. These include the reaction equilibrium, the different carbonation rate regimes and the decay of the sorbent maximum carbonation conversion. They are then coupled with the mass balance expressions of the continuous facility system, already presented in Figure 1.4. Based on the above, two simple carbonator models, available through state of the art literature, and respective active space time parameter expressions are postulated thus providing a link between Calcium looping facility operating parameters and the CO_2 capture efficiency. At this point, all Calcium looping variables are divided into boundary conditions, independent variables and dependent variables, thus setting the stage for the next chapters discussing their fluid-dynamic and reactor performance related interactions. Finally, the simplified scaling relationships of Glicksman are introduced in order to provide the relevant theory for defining the 10 kW_{th} Calcium looping DFB facility fluid-dynamic interactions through respective cold model measurements.

Chapter 3 presents the operating principle of the 10 kW_{th} IFK DFB facility by presenting its scaled cold model. The bulk of the experimental results included here, have been derived with use of this apparatus. Specific focus is given to the gas-solid flow patterns occurring within the DFB reactor system. Subsequently, the application of the Glicksman scaling laws is analyzed, thus justifying scaled cold model dimensions and operating conditions. Data acquisition techniques and parameter variation range are also explained. Moreover, experimental closure of the facility pressure balance equations is demonstrated. These equations are the main tool required for analyzing the link noted in Figure 1.5, i.e. that between operator choices and parameters resulting from fluid-dynamic interactions. As a next step, a number of aspects are highlighted with regard to the heart of the facility, i.e. the cold model carbonator riser. Firstly, a stable operating region, bordered by two unstable regions is presented. In addition, the cold model riser pressure profile, solid fraction profile, solid flow structure and their variation with respect to operational parameters have been analyzed in order to draw conclusions with regard to axial inventory allocation and gas-solid contacting which are important criteria for the CFB carbonator's CO_2 capture efficiency. Finally, empirical correlations are provided regarding the cold model riser entrainment and the solid looping rate between the two beds.

Chapter 4 characterizes carbonator performance and in that context touches upon issues related to the regenerator as well. Experimental results presented within this chapter originate from steady state operation of both the 10 kW_{th} IFK (utilizing its CFB or its BFB as the carbonator) and the 30 kW_{th} INCAR-CSIC facilities. In that sense, both facilities are schematically presented, while experimentally derived parameters and measuring techniques are defined. Also here, the methods of

measurement, the parameter variation range, as well as simplifications met are stated and analyzed. High CO_2 capture efficiency steady state operation is presented and demarcates process stability and potential. Moreover, the reasonable closure of carbon mass balance expressions established for both facilities adds confidence with regard to the quality of the analysis conducted. Thereby, a necessary condition for the capture of a given molar flow of CO_2 has been established, implicating the active flow of Ca supplied to the carbonator. Sorbent deactivation and regeneration efficiency both influence the carbonator CO_2 capture efficiency and are linked to process variables. Subsequently, the riser pressure profile of the actual 10 kW_{th} IFK DFB facility is demonstrated, while a brief comparison to scaled cold model predictions is carried out, thus validating the latter despite a few discrepancies which are noted. The carbonator riser axial CO_2 profile, measured here for the first time, indicates that the carbonator is a plug-flow reactor with regard to the gas, thus justifying such a modeling approach. Moreover, the effect of three key carbonator variables, i.e. carbonator temperature, Ca looping ratio and carbonator space time on the CO_2 capture efficiency are presented and explained based on the two theoretical approaches postulated in Chapter 2. Subsequently, the respective model and active space time expressions are plotted against all available experimental data sets. As a result, an approach is found which correlates well with all experimental data sets included in this work. The contents of this chapter confirm the technical viability of the Calcium looping post-combustion CO_2 capture process.

Since conclusions derived from the fluid-dynamic analysis and reactor performance analysis are presented in Chapter 3 and 4, respectively; **Chapter 5** presents a brief outlook. It summarizes on the one hand why Calcium looping could become a prominent post-combustion CO_2 capture technology and explains how this work can be of further aid to process development. The annex includes in tabular form all obtained results as well as geometrical details of the 10 kW_{th} IFK DFB facility and its cold model. The goal is to provide a complete package of information to independent researchers who would like to validate their modeling approaches based on the experimental data presented here. Finally, the literature list is considered to provide significant sources with regard to three scientific fields, i.e. (i) CCS technology and respective policy, (ii) fluid dynamics of FB and especially DFB systems and (iii) chemistry & reactor engineering of the Calcium looping process.

2 State of the art

In this chapter, the attributes of Calcium looping, which justify that the technology is considered a major CO_2 capture option, are presented first. Moreover, a detailed overview and analysis of Calcium looping facilities existing worldwide has been conducted. In addition, basic elements of sorbent theory, system mass balance-reactor modeling and variable categorization are discussed. Finally, the Glicksman simplified scaling laws are presented since they represent the connection between the 10 kW_{th} IFK DFB facility and its cold model.

2.1 Attributes of the Calcium looping process

The attributes of the Calcium looping process explain the moderate electric efficiency penalty values and the low cost per ton of CO_2 avoided, i.e. < €20/t_{CO2}, noted in sub-section 1.2.2. They are associated to (i) the Ca sorbent and its properties, (ii) the process fluidized bed nature and the potential for process integration and (iii) the ability to couple process heat with a highly efficient supercritical steam cycle.

2.1.1 Utilization of the Ca sorbent

Limestone is well geographically distributed and is a low cost material exhibiting a cost of approximately \$10/t_{CaCO3} [67]. After water, limestone is the cheapest industrial chemical [40]. This is an advantage over Chemical Looping Combustion which utilizes synthetic and more expensive sorbents [40] as well as over low temperature sorbents proposed for post-combustion applications [68]. Moreover, the CaO purge removed for the DFB system is by no means “waste material”. Possible uses include cement clinker production and SO_2 capture in FB combustors. The potential for utilization of the Ca purge from the cement industry becomes apparent when considering that (i) the calcination reaction is responsible for 60 % of the energy input required for cement production [69], (ii) CO_2 emissions from cement plants account for 5 % of the global CO_2 emissions [69] and (iii) cement production grew from 594 Mt in 1970 to 2200 Mt in 2005 [1] and is predicted to increase more. On the other hand use of the Ca purge for SO_2 capture during fluidized bed combustion has been suggested since large pores, formed during particle carbonation/calcination cycling, are less subject to pore blockage during sulfation [70]. Therefore, used Ca

from a Calcium looping facility is a better sorbent than a freshly calcined limestone in terms of SO_2 capture.

Finally, the Ca sorbent allows for post-treatment and pre-treatment in order to counteract its main disadvantage, i.e. the deactivation of sorbent CO_2 carrying capacity from 17.8 mol/ kg_{CO2} to less than 1 mol/ kg_{CO2} with increasing carbonation/calcination cycles [71]. Anthony has summarized and evaluated possible options hereto which include (i) the use of additives (ii) sorbent hydration, (iii) thermal pre-treatment and made an assessment with regard to the use of synthetic sorbents [71]. According to his review, the use of additives (e.g. Na_2CO_3 and NaCl) is to be considered with skepticism in terms of effectiveness. Moreover according to the same publication, sorbent hydration has proven to improve sorbent performance on the one hand but on the other hand induces a predisposition to fracture of the treated particles thus making the particles unsuitable for fluidized bed applications. In addition, thermally activated samples have shown enhanced activity for over 1000 cycles without loss in mechanical stability. Finally, synthetic Ca sorbents are also recognized as a possible future option provided that the price differentials with regard to the natural sorbents remain in the range of $50-100/t or less [71].

2.1.2 Fluidized bed nature and potential for process integration

A prime reason facilitating the scale up of Calcium looping process is that it is based on fluidized bed technology and benefits from several related developments. Hence, standard knowledge related to fluid-dynamics and FB combustion, facilitates efforts during design and operation of a Calcium looping facility. Particular aspects involve the CFB carbonator, the CFB regenerator and the solid circulation system. The carbonator design is considered to be not so far from that of an air-fired CFB Combustor (CFBC), since their operating conditions are similar [72]. Moreover, since operation of the regenerator reactor necessitates oxy-fuel combustion, related progress is driven both from air-fired CFBC knowledge, as well as developments in the independent field of oxy-fired CFBC units [53] which is growing rapidly [73]. Finally, existing information regarding standpipe operation, mechanical and non-mechanical valves [74] provide technical solutions for designing a solid circulation system between the carbonator and the regenerator [72]. With regard to this issue, the operation of other DFB facilities, e.g. dedicated for CLC [63] and the Fast Internally Circulating Fluidized Bed (FICFB) [64], is also of significant aid.

Besides being an add-on technology to a given power plant, as any post-combustion technology is, the Calcium looping process exhibits a further unique feature in terms of process integration, i.e it can also be used as an SO_2 scrubber. SO_2

capture applies for both the SO_2 contained in the flue gas and that produced in the regenerator. Thereby, the need for a Flue Gas Desulfurization (FGD) unit may be overall eliminated. This statement is supported by findings on sulfation rates for particles expected in a Calcium looping system, i.e. having gone through a number of carbonation/calcination cycles and exhibiting a $CaSO_4$ conversion of below 5 % [75]. However, in order to evaluate such an option, the effect of sulfation on the Ca sorbent must be better understood, since the formation of $CaSO_4$ reduces the ability of the sorbent to capture CO_2 [70, 76]. In any case, the $CaSO_4$ conversion of the Calcium looping facility inventory, which is the key measure controlling the sulfation impact on CO_2 capture, can be controlled through adjustment of the Ca make-up and purge flow (F_0), shown in Figure 1.4.

2.1.3 Steam cycle process coupling

The matter at hand is also a matter of process integration; however, it is discussed separately because of its importance. Steam cycle coupling of the Calcium looping process is the prime reason behind the process cost effectiveness. Hence, the energy spent in the regenerator, in order to heat the solids to calcination temperature and for the endothermic calcination reaction to take place, is recovered in the carbonator with use of a high efficiency steam cycle. A good example for realizing such a task is supplied by Hawthorne et al. who have suggested a possible steam cycle configuration, shown in Figure 2.1, for a state of the art 1052 MW_e coal-fired power plant [49]. Since, the electric efficiency and CO_2 avoidance costs from this work are already summarized in sub-section 1.2.2, the focus of this passage is more to pinpoint the sources of heat recovery and energy sinks, while quantifying the respective amounts.

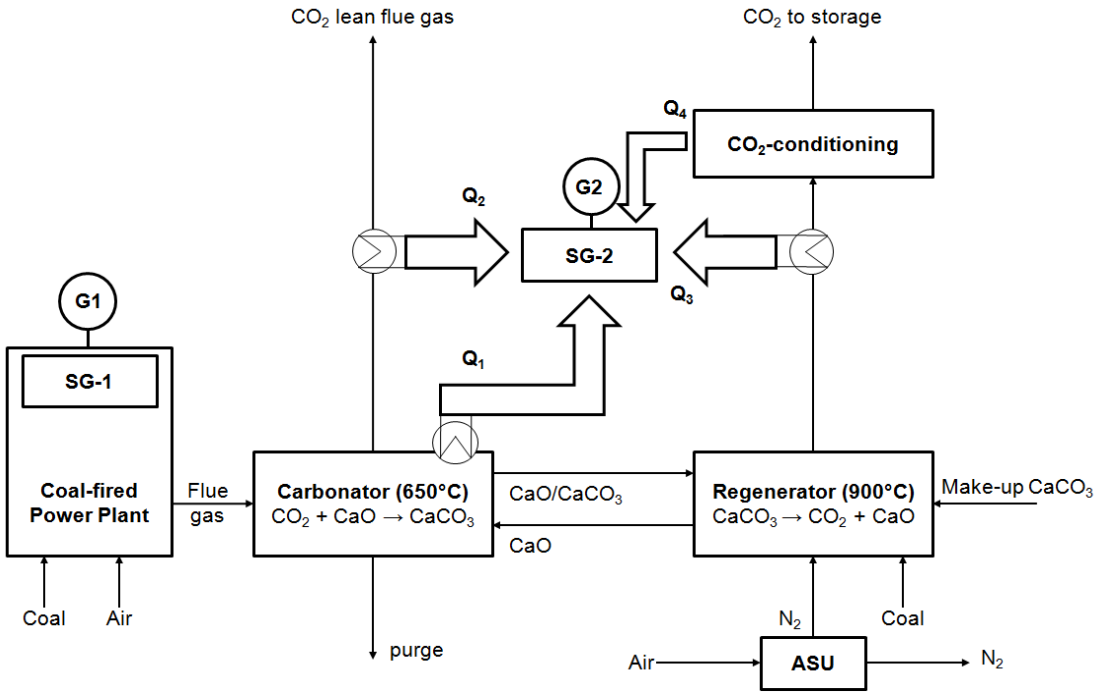

Figure 2.1: The Calcium looping process schematic [49]; SG: Steam Generator, ASU: Air Separation Unit

In the schematic of Figure 2.1, power is considered to be produced by two independent steam cycles, i.e. one for the original power plant and one for the Calcium looping facility. Hence, with regard to the latter facility heat is extracted for the purpose of steam generation from the carbonator (Q_1), through gas flows exiting the carbonator (Q_2) and regenerator (Q_3) at their respective temperatures and during CO_2 conditioning (Q_4). Moreover, Hawthorne et al. suggested that the evaporator surfaces are placed in the carbonator, while re-heat and superheat surfaces are positioned in the convective back-pass of the carbonator and the regenerator. In addition, it has been shown that the heat release taking place during CO_2 compression can be used in the economizer. Major energy sinks are on the one hand the CO_2 compression and on the other the operation of the Air Separation Unit ASU. Values for the energy streams Q_1-Q_4 as well as the two energy sinks mentioned are supplied in Table 2.1 [49].

Table 2.1: Heat sources and sinks in a Calcium looping system coupled with a steam cycle [49]

Heat source	Gas Flow	Temperature in/out	Power
Carbonator boiler (Q1)	-	650°C/ 650°C	960 MW_{th}
Carbonator convection pass (Q2)	860 kg/s	650°C/ 370°C	280 MW_{th}
Regenerator convection pass (Q3)	397 kg/s	900°C/ 370°C	264 MW_{th}
Economizer at CO_2 compression (Q4)	397kg/s	140°C/ 50°C	120 MW_{th}
Electric Consumption – CO_2 compression	N. A.	N. A.	128 MW_e
Electric Power Consumption – ASU	N. A.	N. A.	115 MW_e

There is a clear margin of optimization for the energy integration of the Calcium looping process. This can be achieved with use of alternative concepts with regard to heat supply in the regenerator reactor [12], thus eliminating the energy consumption related to the ASU. The most convincing of these concepts is a three fluidized bed reactor system where solids from an air-fired CFBC are used to allothermally heat the regenerator reactor [77].

2.2 Overview of experimental facilities worldwide

As noted, the technological maturity of a process is determined by the number and scale of existing facilities and their respective results. Facilities dedicated to the Calcium looping process are listed in Table 2.2. Basic characteristics of these units, i.e. (i) their nominal capacity and dimensions, (ii) the carbonator, regenerator reactor type (BFB or CFB) & respective fluidization regime, (iii) the solid circulation system utilized and (iv) published achievements realized up to now, are listed below. A number of these facilities have been (or are planned to be) operated for other processes, i.e. absorption enhanced reforming (AER) biomass steam gasification [78], CLC [37, 79] and in the case of the IFK pilot-scale facility for oxy-fuel combustion.

The scale of a facility determines the role that a given facility can undertake. Pilot scale facilities, i.e. in the range of 200 kW_{th} to 1.7 MW_{th}, are more realistic than lab-scale facilities since e.g. they utilize process heat to achieve required temperatures as opposed to the electrical heating of the lab-scale ones. Both types are important for process scale-up; lab-scale facilities have advantages with regard to sorbent characterization and the realization of parametric studies, while pilot scale units are more suited for long duration experiments under close to industrial conditions. Regarding the reactor type, experimental facilities utilizing CFB reactors are more close to industrial application conditions than those utilizing BFB ones. This is because CFB reactors allow a higher gas throughput, better gas-solid contacting and reaction efficiency [74]. However, the removal of carbonation heat has been considered to be easier in BFB carbonator reactors due to their larger reactor volume [80]. With regard to the solid circulation systems, facilities which utilize a loop-seal and a solid circulation control valve (e.g. cone valve, L-valve, screw feeder) are more realistic than others which do not. The above components are established in the field of fluidization engineering and thus are expected to see action in Calcium looping facilities of bigger scale. Finally, with regard to the work performed so far in this kind of facilities, the following can be claimed. Firstly, cold model studies characterizing reactor fluid-dynamics have been adopted as a tool in the case of many of the facilities listed below [32, 72, 81, 82]. Moreover, all lab-scale facilities have conducted parametric studies and have reached CO_2 capture efficiency values of above 90 % [31-

34]. In addition, the IFK 200 kW_{th} facility has been the first pilot-scale facility to carry out such a study and demonstrate a CO_2 capture efficiency of above 90 % and close to the equilibrium, under steady state conditions [35, 36]. The facility of TU Darmstadt has recently presented its first continuous results, demonstrating a CO_2 capture efficiency of 80 % at approximately 650°C [37]. In addition, the 1.7 MW_{th} Hunosa facility has also demonstrated process operation exhibiting a CO_2 capture efficiency of above 90 % [38]. Finally, the data from the 10 kW_{th} IFK and the 30 kW_{th} INCAR-CISC facilities have been used to take the analysis one step further, thus leading to carbonator model validation [34, 83, 84]. Finally, studies have focused also on sorbent issues, i.e. kinetic aspects of used sorbents [85], attrition [31, 33, 35 86] and re-activation methods of sorbents first utilized in a Calcium looping system [87, 88].

Table 2.2:Calcium looping experimental facilities & related work

Host & scale	Utilized reactor types	Solid circulation	Work performed
10 kW_{th} IFK	CFB as carbonator or regenerator (h: 12.4 m & Ø 70 mm) BFB as regenerator or carbonator (h: 3.2 m & Ø 114 mm)	Loop seals and cone valve system	Cold model study [72] Parametric study Max. E_{carb}: 93 % [33] CFB carbonator model validation [83, 84] reactivity analysis [85]
30 kW_{th} INCAR-CSIC	CFB as carbonator (h: 6. 5 m & Ø 100 mm) CFB as regenerator (h: 6.2 m & Ø 100 mm)	Loop seal system	Parametric study Max. E_{carb}: 97 % [34] CFB carbonator model validation [34, 83, 84] Attrition study [86]
75 kW_{th} * CANMET *refers to el. heater capacity	MB or BFB as carbonator (Ø 100 mm) CFB as regenerator (h: 5 m & Ø 100 mm)	Pneumatic line valve system	Parametric study Max. E_{carb}: > 98 % [31] Reactivation studies with spent Ca [87, 88]
10 kW_{th} Tsinghua	BFB as carbonator (h: 1 m & Ø 149 mm) BFB as regenerator (h: 1 m & Ø 117 mm)	Injection nozzle-riser, cyclone-downcomer system	Cold model study [32] Parametric study Max. E_{carb}: approx 95 % [32]
200 kW_{th} IFK 1st configuration	BFB or turbulent CFB as carbonator (h: 6 m & Ø 330 mm) CFB as regenerator (h: 10 m & Ø 210 mm)	Loop seals and L-valve system	Cold model study [81] Process demonstration and parameter variation. Max. E_{carb}: > 90 % [35]
200 kW_{th} IFK 2nd configuration	CFB as carbonator (h: 10 m) CFB as regenerator (h: 10 m & Ø 210 mm)	Loop seals and two cone valves system	Cold model study [82] Preliminary results [89]
1MW_{th} TU Darmstadt	CFB as carbonator (h: 8.7 m & Ø 600 mm) CFB as regenerator (h: 11 m & Ø 400 mm)	Loop seals and screw feeder system	Batch mode experimentation [90] Process demonstration Max. E_{carb} 80 % [37]
1-1.7 MW_{th} La PeredaHunosa	CFB as carbonator (h: 15 m) CFB as regenerator (h: 15 m)	Double exit loop seal system with adjustment between exits	Process demonstration. Max. E_{carb}: > 90 % [38]

2.3 Aspects of sorbent particle chemistry and mechanical stability

Aspects of sorbent chemistry that are dealt with in this section are necessary for understanding the Calcium looping process and analyzing the experimental results presented in subsequent sections. With regard to the sorbent chemical behavior, these include the carbonation-calcination equilibrium, the carbonation reaction regimes, corresponding rate expressions and the decay of the sorbent maximum carbonation conversion. These attributes have been extensively investigated within the last decade, especially through carbonation/ calcination cycling of a particle sample within a Thermo-Gravimetric Analyzer (TGA) [91, 92]. Experiments of this kind have reached a carbonation/calcination cycle number (N) of 500 [92]. On the other hand, particle mechanical stability has been evaluated based on the sorbent attrition behavior, as derived from batch BFB, CFB and continuous DFB experiments [86, 93].

2.3.1 The carbonation-calcination equilibrium

The volume fraction of CO_2 allowed by the equilibrium with regard to the carbonation-calcination reaction ($CaO+CO_2 \leftrightarrow CaCO_3$) is a function of temperature and is given by Equation (1) [94]. Equation (1) is represented graphically in Figure 2.2 for a temperature interval of 600°C-900°C. Below 550°C, the kinetics of carbonation have been shown to be inadequate for CO_2 capture applications [31].

$$v_{CO\,2,eq} = 4.137 \cdot 10^{7}\, exp\left(\frac{-20474}{T}\right) \qquad (1)$$

The equilibrium CO_2 volume fraction increases with increasing temperature. Taking into account that flue gases from a coal fired power plant have a CO_2 volume fraction around 15 %, a temperature range of 600°C-700°C can be considered for realization of the carbonation reaction. This is true, since the values of the equilibrium CO_2 volume fraction, within the above temperature range, lie between 0.3 % and just above 3 %, hence allowing for a CO_2 conversion in the range of 76.6 % to 97.5 %. With regard to the calcination reaction, temperatures of above 875°C must be considered, according to Figure 2.2, in order for the reaction to proceed at volume fractions of CO_2 greater than 70 % which are expected in oxy-fired regenerator reactors.

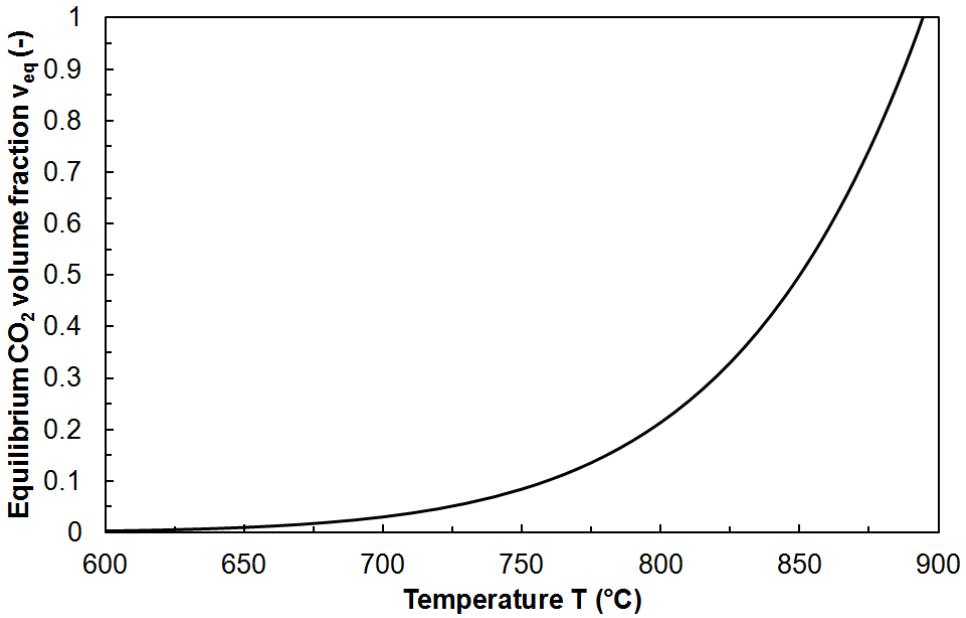

Figure 2.2: Equilibrium partial pressure of CO_2 with with regard to the carbonation-calcination reaction ($CaO+CO_2 \leftrightarrow CaCO_3$) for the temperature range of 600°C-900°C

2.3.2 The fast and slow carbonation reaction regime

The carbonation reaction proceeds through two successive reaction regimes, i.e. the fast and slow reaction regime, irrespective of the influence of the carbonation/calcination cycle number (N) [92]. Both reaction regimes are presented in Figure 2.3, where the carbonation conversion (X_{carb}) of a CaO particle sample is plotted against time with use of Thermo-Gravimetric Analyzer (TGA). The X_{carb} of a particle or sample is defined as the ratio of $CaCO_3$ mol and total Ca mol contained in that sample or particle. Hence, the X_{carb} is expressed in mol_{CaCO3}/ mol_{Ca}. The fast and slow reaction regimes are demarcated through their different slopes in Figure 2.3. During the fast reaction regime, the reaction is limited from surface kinetics only, while during the slow reaction regime it is diffusion controlled [92]. The carbonation conversion value of a particle, or sample of particles, exhibiting a given value of N, at which the reaction regime shifts from the fast to the slow reaction regime, is termed as the maximum carbonation conversion $X_{max,N}$. The relatively abrupt transition between the two reaction regimes has been linked to the formation of a $CaCO_3$ product layer having a critical thickness of 50 nm [94]. The $X_{max,N}$ is graphically derived, as shown in Figure 2.3 for cycle 4 of the Swabian Alb limestone. Hence the $X_{max,4}$ is shown to be slightly higher than 0.15 mol_{CaCO3}/ mol_{Ca}. Based on the reaction rate values of the two regimes, only the fast reaction regime can be considered for technical application.

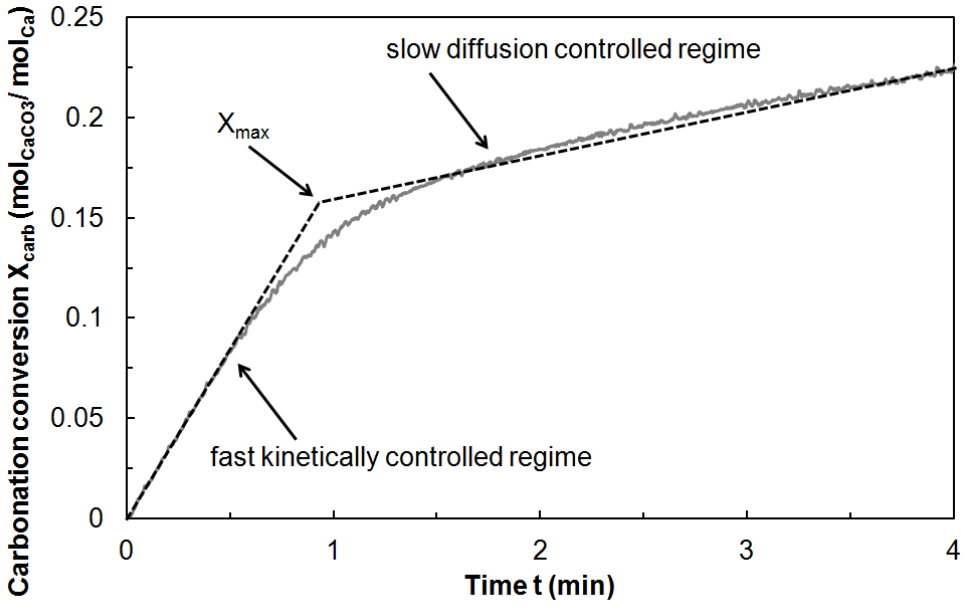

Figure 2.3: Fast and slow carbonation reaction regime; limestone Swabian Alb, cycle number N: 4.

Two equations have been considered to mathematically express the reaction rate of the fast reaction regime and are given by Equation (2) and (3). Subscripts A and B distinguish variables that are dependent on the equation used.

$$\left(\frac{dX}{dt}\right)_A = k_{sA}(X_{max,N} - X_{carb})(v_{CO2} - v_{eq}) \tag{2}$$

$$\left(\frac{dX}{dt}\right)_B = k_{sB} X_{max,N} (v_{CO2} - v_{eq}) \tag{3}$$

Both reaction rate expressions consider the reaction rate to be of first order with regard to the difference of the actual and equilibrium CO_2 volume fraction. The expression of Equation (2) further considers that the reaction rate is proportional to the difference of ($X_{max,N}$-X_{carb}), i.e. that of the maximum carbonation conversion and the actual carbonation conversion. This expression postulates that the carbonation rate decreases, while the actual carbonation conversion increases. Furthermore, it is consistent with experimental data on carbonation reaction rates reviewed by Bathia and Perlmuter and more recently by Grasa et al. [95]. On the other hand, the expression of Equation (3) takes into account that the reaction rate is only dependant on the limestone constant (k_{sB}), the maximum carbonation conversion ($X_{max,N}$) and the difference of the actual and equilibrium CO_2 partial pressure. However, the reaction rate is taken to be irrespective of the actual carbonation conversion (X_{carb}). Equation (3) constitutes an oversimplification of the reaction rate model at particle level, but has shown to be consistent with some data series reported from TG studies [96, 97].

2.3.3 Decay of the maximum carbonation conversion

The maximum carbonation conversion ($X_{max,N}$) of natural limestones decreases with each carbonation-calcination cycle [60, 91, 96]. This decay is expressed through Equation (4) for the "average" limestone [91]. The expression is derived through carbonation-calcination cycling of a variety of sorbents up to a cycle number of 500.

$$X_{\max,N} = \frac{1}{\frac{1}{1-X_R} + kN} + X_R, X_R = 0.075 \,\&\, k = 0.52 \tag{4}$$

The symbols k and X_R are constants. The X_R is termed as the residual activity, since the maximum carbonation conversion can never become smaller than X_R, even after an infinite number of carbonation-calcination cycles. The k and X_R values for the typical limestone have been found equal to 0.52 and 0.075 respectively. Equation (4) is plotted in Figure 2.4, which shows that the $X_{max,N}$ decay is steep over the first 20 cycles. Subsequently, values of $X_{max,N}$ converge slowly to the value corresponding to the residual activity, X_R. The decay of $X_{max,N}$ with increasing number of cycles (N) is a result of particle sintering of the internal pore structure [56, 60, 91]. In other words, the calcination step during carbonation/calcination cycling is known to cause shrinkage of smaller pores and enlargement of macropores. Therefore, the overall particle specific surface area decreases, thus leading to declining values of $X_{max,N}$.

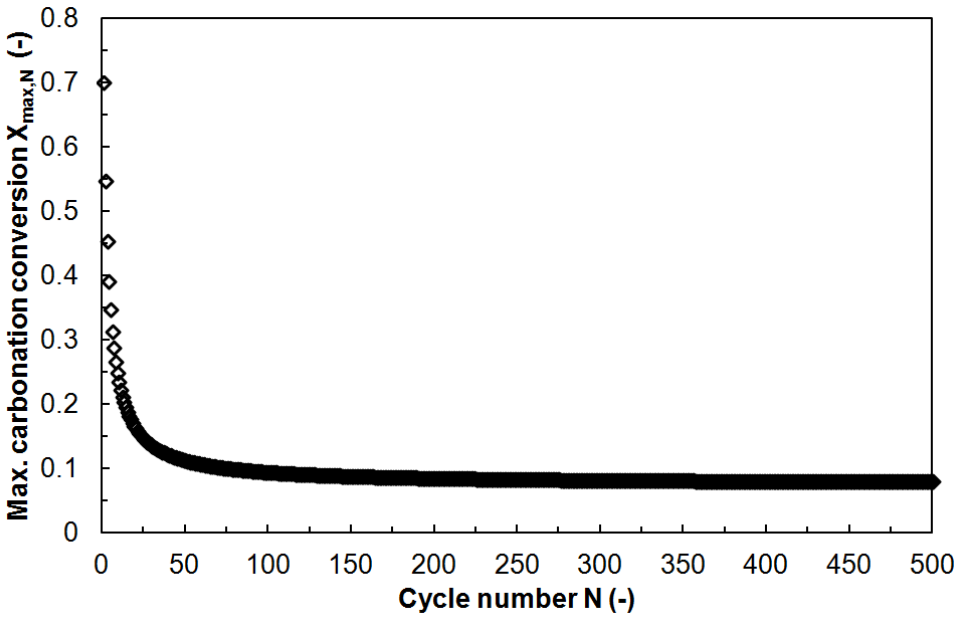

Figure 2.4: Maximum carbonation conversion $X_{max,N}$ decay over 500 cycles [91]

2.3.4 Attrition behaviour

Scala et al. have classified attrition phenomena distinguishing between primary fragmentation, attrition by abrasion and secondary fragmentation [98]. The extent of attrition is dependant mainly on limestone type and primary fragmentation seems to be the most significant mechanism [99]. Primary fragmentation occurs during the initial carbonation-calcination cycles [31, 86, 100] due to the thermal shock and the internal overpressure caused by CO_2 generation [101]. Furthermore, it has been also linked to the mechanical stresses that accompany the above procedure, and hence to the fluidization conditions [93]. Therefore, primary fragmentation is minimal for a BFBC in comparison to a CFBC. González et al. [86], performed sorbent calcination of limestone in the 30 kW_{th} INCAR-CSIC DFB system, consisting of two CFB risers, and reported reduction of the average particle diameter from the initial sizes of 130/180 μm to around 90 μm which can probably be attributed to the combination of primary fragmentation and mechanical stresses. However, after the first carbonation/calcination cycles have been completed, attrition is rather attributed to abrasion and secondary fragmentation which is related to impact stresses experienced in various regions of a fluidized bed, e.g. at the jetting region of the distributors, or walls and internals. Hence, moderate changes were reported in the particle size distribution, within the previously mentioned study [86], after the initial carbonation-calcination cycles had been completed. On the other hand, during experimentation at the CANMET lab-scale facility (see Table 2.2), significant amount of attrition has been reported also during cyclic steady state operation leading to 60 % of the initial bed material being collected in the cyclones after 25 carbonation-calcination cycles [31]. Recent DFB experiments at lab- and pilot scale reported attrition values of 2 $wt.\%h^{-1}$ and 5 $wt.\%h^{-1}$, respectively [33, 35].

2.4 Calcium looping reactor system theory

In order to utilize the knowledge with regard to particle chemistry presented above, it is important to examine the Calcium looping DFB facility as a whole. A number of important aspects are revealed through the carbon mass balance equations, including the amount of active Ca flow needed between the reactors and the carbonator design equation. The simplification of the latter equation allows, on the one hand, the derivation of an engineering variable that characterizes the CO_2 capture efficiency, while on the other, allows for a simple carbonator model. Moreover, in order to aid the discussion around fluid-dynamic and reactor performance analysis, all Calcium looping variables are categorized to boundary conditions, independent and dependent variables. Finally, the Glicksman simplified scaling criteria are introduced,

explaining how fluid-dynamic interactions measured in the cold model can be transferred to the actual unit.

2.4.1 Carbon molar balance with regard to a Calcium looping facility

Carbon enters the Calcium looping system in the following forms: (i) as CO_2 contained in the flue gas entering the carbonator, (ii) as $CaCO_3$ contained in the fresh limestone make-up stream and (iii) as fuel supplied to the regenerator [12]. Assuming complete fuel conversion, carbon exits the system almost completely in the form of CO_2. A minor percentage corresponding to not captured flue gas CO_2 is emitted to the atmosphere through the carbonator. The rest exits the facility through the regenerator in the form of a CO_2 rich off-gas. The carbon molar balance of the whole Calcium looping system is presented in detail with the help of Figure 2.5 below [11, 12].

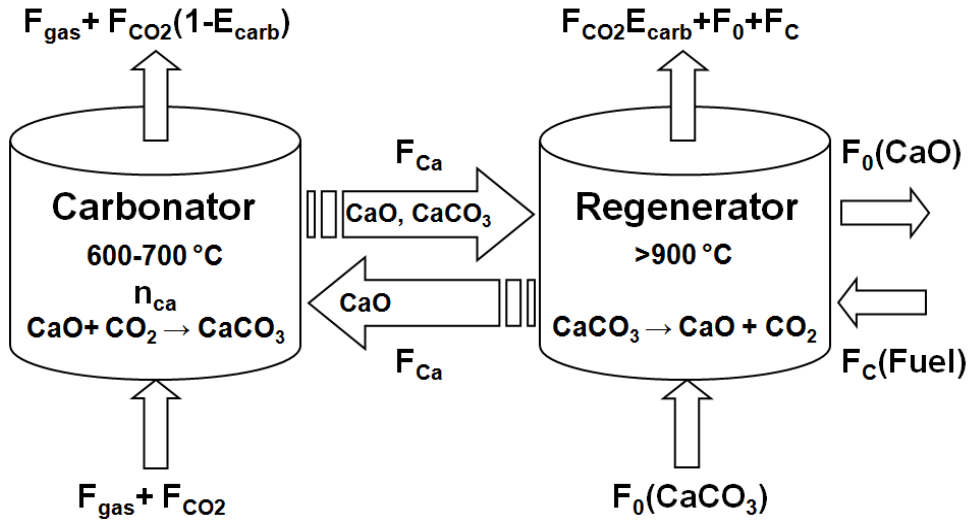

Figure 2.5: Schematic representation of the Calcium looping CO_2 mass balance [11, 12]

A percentage of the molar flow of CO_2 ($F_{CO2,in}$) entering the carbonator is chemi-absorbed from its Ca inventory (n_{Ca}) reacting at a reaction rate $(dX/dt)_{carb}$. This percentage, termed as the carbonator CO_2 capture efficiency, represents the most important metric of the Calcium looping system performance and is given in Equation (5). Thereby, a reduced CO_2 flow stream $F_{CO2,out}$ is emitted to the atmosphere.

$$E_{CO2} = 1 - \frac{F_{CO2,out}}{F_{CO2,in}} \tag{5}$$

The molar flow of CO_2 captured in the carbonator is transferred to the regenerator in the form of $CaCO_3$ contained in the Ca flow (F_{Ca}) looping between the reactors.

Therefore, the carbonation conversion value of F_{Ca} is higher at the carbonator exit than at its inlet ($X_{carb} > X_{calc}$). The molar flow of CO_2 exiting the regenerator constitutes from the CO_2 captured in the carbonator ($F_{CO2}E_{carb}$), the CO_2 emitted from the first calcination of the $CaCO_3$ make-up flow (F_0-F_0X_{calc}) and that produced from the combustion of the molar flow of carbon (F_c) contained in the regenerator fuel. Furthermore, a small amount of carbon leaves the system in the form of $CaCO_3$ (F_0X_{calc}) contained within the purge flow. Based on the above analysis, the following carbon mass balance equations can be postulated. Equations (6) and (7) express the equality between (i) the molar flow of CO_2 disappearing from the gas phase, (ii) the rate of formation of $CaCO_3$ within the carbonator bed and (iii) the increase of $CaCO_3$ mol contained in the Ca looping rate (F_{Ca}) after the carbonator exit [84, 97].

$$F_{CO2} \cdot E_{carb} = n_{Ca} \cdot \left(\frac{dX_{carb}}{dt} \right) \tag{6}$$

$$F_{CO2} \cdot E_{carb} = F_{Ca} \cdot (X_{carb} - X_{calc}) \tag{7}$$

A further mass balance consideration, based on the stoichiometry of the carbonation reaction, is postulated by the inequality of Equation (8). It expresses that in order to obtain a certain CO_2 capture efficiency value (E_{carb}), a slightly over-stoichiometric active flow of Ca, i.e. which can react in the fast reaction regime, must be supplied to the carbonator with regard to the molar flow of CO_2 being captured when considering that value of E_{carb} [34, 84].

$$F_{CO2} \cdot E_{carb} < F_{Ca} \cdot (X_{\max,ave} - X_{calc}) \tag{8}$$

The average maximum carbonation conversion ($X_{max,ave}$) is the average of the $X_{max,N}$ values of the individual particles. Hence, $X_{max,ave}$ is also expressed in mol_{CaCO3}/ mol_{Ca}. The variance of the $X_{max,N}$ values is related to the different history of the particles within the Calcium looping system. This becomes apparent when taking into account that sorbent particles are not uniformly exposed to sintering related parameters, e.g. number of times cycled between the reactors or residence times spent within the regenerator. In a Calcium looping DFB system utilizing a continuous limestone make-up flow stream (F_0), such as that of Figure 2.5, the $X_{max,ave}$ value remains constant. Recently, appropriate equations have been developed and link the $X_{max,ave}$ with the ratio F_0/F_{Ca} value only [102, 103]. Furthermore, Equation (8) underlines the importance of regenerator operation. This is true since the term corresponding to the active molar flow of Ca supplied to the carbonator, i.e. $F_{Ca}(X_{max,ave}$-$X_{calc})$, is dependent on the carbonation conversion of the solids exiting the regenerator (X_{calc}). Hence, the Ca looping rate required (F_{Ca}) can be minimized when the regenerator operates at

conditions leading to an X_{calc} value equal to zero. This is important since the Ca looping rate has been linked as a primary parameter influencing the heat requirements [104] in the regenerator and to operational cost [53]. In a large scale Calcium looping system, there will always be a trade-off between the need to achieve a X_{calc} value close to zero (full calcination) and the requirements of high temperatures and/or low partial pressures of CO_2 needed in the calciner to achieve such objective. This is particularly interesting when considering that the latter two regenerator parameters have also been associated to the $X_{max,ave}$ decay [91, 105, 106]. With the help of the mass balance of Figure 2.5, the regenerator efficiency (η_{reg}) is defined in Equation (9) [103, 107] based on the actual carbonation conversion of the incoming (X_{carb}) and exiting (X_{calc}) Ca molar stream (F_{Ca}). It expresses the fraction of the $CaCO_3$ entering the regenerator that is calcined to CaO. Hence, an η_{reg} value of 1 corresponds to complete sorbent regeneration, while a value of 0 demarcates that calcination is absent.

$$\eta_{reg} = 1 - \frac{X_{calc}}{X_{carb}} \tag{9}$$

2.4.2 Simplified mass balance and active space time expressions

The carbon mass balance of Equation (6) is the fundamental carbonator reactor design equation. It can be further simplified in order to provide a one equation carbonator model, when assuming that the carbonator reactor is a plug flow reactor with regard to the gas and deciding upon two aspects, i.e. (i) which percentage of the carbonator particles react with CO_2 in the fast reaction regime and (ii) which reaction rate expression is appropriate to be used, i.e. Equation (2) or Equation (3). The postulation of such a reactor model, after validation, establishes the link between most dependent parameters and the CO_2 capture efficiency, as shown in Figure 1.5, and therefore is the key issue with regard to reactor performance analysis. Furthermore, answering the two aspects noted above leads to a definition regarding the characteristic carbonator parameter of active space time, which has been shown to be the prime engineering variable that unlocks a comprehensive carbonator design procedure [89]. The importance of the active space time parameter is manifested in that it expresses both the carbonator inventory per molar flow of CO_2 and the reaction rate of that inventory. Two theoretical approaches have been utilized throughout this work in order to attain a simplified expression of Equation (6), i.e. a carbonator model, and an active space time expression that fits with experimental data, namely approach A & B. Hence, the use of subscripts A & B, already present in Equations (2) and (3), is expanded to distinguish between symbols that are dependent on the type of the approach used and those not used.

Approach A assumes that the carbonator reactor operates with a bed, where all particles are able to react with CO_2 in the fast reaction regime and have the same average characteristics. These include a carbonate content (X_{carb}) and the average maximum carbonation conversion ($X_{max,ave}$). The expression of Equation (2) is considered within this approach, which postulates that the particle reaction rate is proportional to the ($X_{max,ave}$-X_{carb}). Therefore, combining the assumption that all particles react with CO_2 and the rate expression of Equation (2), Equation (6) can be simplified to the expression given below [34, 83, 84].

$$E_{carb} = k_{sA} \varphi \tau \, (X_{\max,ave} - X_{carb})(\overline{\nu_{CO2}} - \nu_{eq}) \tag{10}$$

Where τ symbolizes the parameter of space time defined as the ratio of the moles of Ca present in the carbonator and the molar flow of CO_2 entering the reactor and φ is the gas-solid contacting effectiveness factor which has been defined elsewhere [34]. Based on Equation (10), the parameter of active space time $\tau_{active,A}$ has been defined as the product of the space time and the reaction rate term of ($X_{max,ave}$-X_{carb}) [33, 34, 61, 83, 84, 102], and is given in Equation (11).

$$\tau_{active,A} = \tau \, (X_{\max,ave} - X_{carb}) \tag{11}$$

Approach B makes the assumption that only a fraction, f_{active}, of the particles of CaO with a sufficiently short residence time is active in the bed and can react in the fast reaction regime [84, 97, 107, 108]. In addition, it postulates that the particles belonging to this fraction react with a reaction rate, given by the expression of Equation (3), which, as noted, is irrespective of the carbonation conversion of the particle as long as $X_{carb}<X_{max,ave}$. Taking into consideration the assumption that only a fraction of the carbonator particles react in the fast reaction regime and the reaction rate expression of Equation (3), Equation (6) can be rearranged to the form of Equation (12) [84, 107, 108].

$$E_{carb} = k_{sB} \varphi \tau \, f_{active} X_{\max,ave} (\overline{\nu_{CO2}} - \nu_{eq}) \tag{12}$$

The expression of Equation (12) has the advantage of facilitating a link between the average activity of the carbonator solids with their residence time distribution in the bed (see also Alonso et al [97] for a detailed description of the model). This is because the fraction of active particles, f_{active}, reacting in the fast reaction regime corresponds to the fraction of particles with a residence time below a critical reaction time t* [84, 97, 107, 108]:

$$f_{active} = 1 - e^{\left(-t^* / n_{Ca}/F_{Ca}\right)} \tag{13}$$

where t* is the time required for a sorbent particle at the average concentration of CO_2 in the bed to increase its carbonate content from X_{calc} to $X_{max,ave}$, after which the reaction rate becomes zero. The t* is given by Equation (14) [84, 97, 107, 108].

$$t^* = \frac{X_{\max,ave} - X_{calc}}{(dX/dt)_{reactor}} = \frac{X_{\max,ave} - X_{calc}}{k_{sB}\varphi X_{\max,ave}(\overline{v_{CO2}} - v_{eq})} \quad (14)$$

Since regenerator particles exhibit a residence time distribution, the X_{calc} of particles entering the regenerator will also vary. However, all particles are considered to exhibit the average value of X_{calc}. The same applies for the average maximum carbonation conversion where all particles are considered to exhibit the average value of $X_{max,ave}$. To highlight further the concept of t* a graphical representation, taken from the work of Alonso et al. [97], is shown in Figure 2.6.

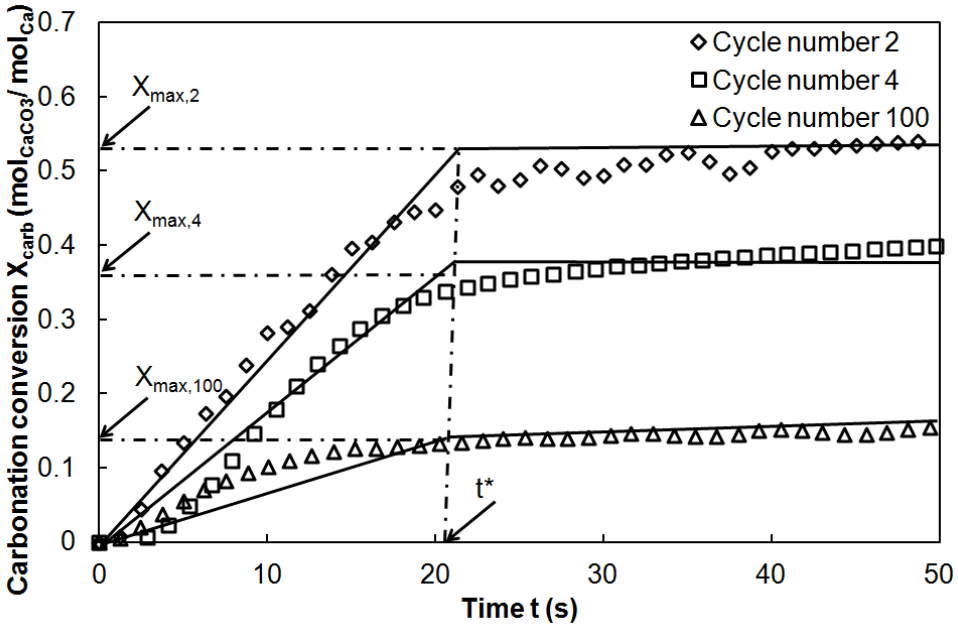

Figure 2.6: Scheme of the kinetic model of Equation (3), adopted to describe the progress of carbonation with time for different cycle number. Schematic used for the definition of t* [97]

The particles have undergone 2, 4 and 100 carbonation/calcination cycles in a TG; therefore, the symbol $X_{max,N}$ is used instead of $X_{max,ave}$, X_{calc} is equal to 0 and φ is equal to 1. The solid lines correspond to the kinetic model postulated in Equation (3), i.e. constant reaction rate for a given cycle until X_{carb} equals $X_{max,N}$ after which the reaction rate becomes equal to 0. The fact that the t* is the same for the three data sets, despite that they correspond to different cycle number and $X_{max,N}$ values, is consistent with Equation (14) since the $X_{max,N}$ is cancelled out when X_{calc} is equal to 0.

Based on the mass balance expression of Equation (12) and Equations (13), (14), the active space of this approach can be defined below [84, 107, 108]:

$$\tau_{active,B} = (f_{active}\tau)X_{\max,ave} \quad (15)$$

Where the product $f_{active}\tau$ is the space time of sorbent particles reacting in the fast reaction regime, while the $X_{max,ave}$ is the key parameter defining their reaction rate.

2.4.3 Boundary conditions, independent and dependent variables

Calcium looping variables are divided into boundary conditions, independent and dependent variables, as shown in Figure 1.5. Boundary conditions represent the system design basis. Independent variables can be directly set by the designer/ operator without the control loop implementation. Variables termed as dependent result from boundary conditions and interactions occurring between independent variables. It is reactor performance interactions and fluid-dynamic interactions of dependent variables that define the CO_2 capture efficiency. This is graphically shown in Figure 1.5. The three variable types are listed in Tables 2.3-2.5. These tables reference equations presented in this chapter with the purpose to further reveal the mechanism that the respective variables influence the CO_2 capture efficiency of the Calcium looping system.

Table 2.3: Calcium looping boundary conditions

Variable	Relevant to:	Influence through:
Flue gas molar flow of CO_2 (F_{CO2})	Whole DFB system	Dimension definition
Flue gas ppm concentration of SO_2		Sorbent $CaSO_4$ conversion
Regenerator fuel composition (C,H,S, ash, H_2O)		(i) Regenerator partial pressure of CO_2 and steam (ii) ash generation (iii) Sorbent $CaSO_4$ conversion
Flue gas vol.-% of CO_2 (v_{CO2})	Carbonator	Carbonation rate through Equation (10) and (12)
Flue gas vol.-% of steam		Carbonation rate [109]

Parameters which belong to the boundary conditions category are associated with the flue gas of the original power plant and the fuel available for the regenerator. Most likely, the actual plant and the regenerator will use the same fuel. The molar flow of CO_2 (F_{CO2}) is the parameter used for expressing in a specific sense the most important Calcium looping parameters, i.e the space time (n_{Ca}/F_{CO2}), active space time (see Equations (11) & (15)), the Ca looping ratio (F_{Ca}/F_{CO2}) and the make-up flow of fresh limestone (F_0/F_{CO2}). Hence, it will have the most important influence on the

dimensions of the whole DFB system which must accommodate flows and inventory. The inlet vol.-% of CO_2 and steam in the flue gas influence the carbonation rate. The first has an influence in the average vol.-% of CO_2, as shown in Equations (10) & (12), while the second has been shown to have a catalyzing effect on the carbonation rate [109]. In addition, sorbent sulfation will be influenced both by the SO_2 in the flue gas and that released from fuel combustion in the regenerator. Besides SO_2 release in the regenerator, fuel consistency plays a further role in that the C, H_2 and moisture content influences the partial pressure of CO_2 in the regenerator. Finally fuel consistency influences the rate of generated ash within the regenerator reactor.

Table 2.4: Calcium looping independent variables

Variable	Relevant to:	Influence through:
Aeration of non-mechanical valves	Whole DFB system	Fluid-dynamic interactions
Facility dimensions		
Initial Particle Size Distribution (PSD)		
Initial Total Solid Inventory		
Opening of mechanical valves		
Sorbent type		Sorbent properties: (i) Kinetic (X_{max} decay, k_s) (ii) Attrition properties
Carbonator velocity	Carbonator	Fluid-dynamic interactions
Heat transfer influence measure		steam cycle integration & fluid-dynamic interaction
Fuel dosing	Regenerator	Fluid-dynamic interactions & through the combustion process
O_2 supply in the regenerator		
% of recirculated off-gas		
Limestone make-up flow (F_0)		$X_{max,ave}$ [102, 103] $CaSO_4$ conversion

Independent variables include those that can be set by choice from the facility designer or operator and are shown in Table 2.4. It becomes apparent that very few carbonator related parameters can be set directly. Furthermore, Table 2.4 indicates that nearly all included parameters are of fluid-dynamic nature. Parameters defined as such influence system performance through fluid-dynamic interactions. Fluid-dynamic interactions themselves are discussed during the analysis of the scaling theory within the next section and are experimentally demonstrated in Chapter 3. Independent variables that are not “fluid-dynamic” are the properties of the limestone used associated with its type and the sorbent make-up flow. In the first case, the system is influenced mainly through mechanical and kinetic sorbent properties, while in the

latter it is influenced (i) through the noted effect of make-up flow on the sorbent average maximum carbonation conversion and (ii) through its effect on the average sorbent $CaSO_4$ conversion. In addition, heat transfer from the carbonator can be controlled with use of fluid-dynamic measures, e.g. use of an external heat exchanger with regulation of solid flow through it by means of a valve, and non fluid-dynamic measures, such as the area of the evaporator tubes that can be installed within the carbonator reactor. Regenerator parameters related to the combustion process influence the system through the reaction itself, the produced ash and the related heat release. However, independent regenerator variables influence the Calcium looping system in a fluid-dynamic sense since regenerator combustion is closely tied to the reactor velocity.

Most of the dependent variables are included in Equations (5-15) and are summarized in Table 2.5 below. Thereby, their role in influencing the CO_2 capture efficiency becomes apparent and is not further commented on within this passage. Variables of Table 2.5 that are not present in the above equations influence other dependent variables that are. This is realized through fluid-dynamic interactions and through the regenerator performance. Variables of the first type are the actual Total Solid Inventory (TSI), PSD of the Calcium looping facility, reactor pressure profiles and entrainment rates. The actual PSD and TSI may deviate from that of the feed limestone due to attrition phenomena and due to the inclusion of fuel ash in the Calcium looping system. In addition, the carbonator pressure profile influences the overall gas-solid contacting effectiveness factor (φ) of the carbonator reactor [72, 107]. Moreover, the carbonator or/and regenerator entrainment rate may define fully the Ca looping ratio (F_{Ca}/F_{CO2}) or its maximum value depending on the DFB setting utilized (see Table 2.2). Regenerator variables associated with the reactor atmosphere influence the regenerator efficiency and therefore the X_{calc} thus influencing the CO_2 capture efficiency, also. The residence time influences the CO_2 capture efficiency also by influencing the X_{calc} [107]. The validation of the interdependence postulated through Equations (5-15), which are included in Table 2.5 is realized within Chapter 4. The isolated effect of some dependent variables, i.e. carbonator temperature, F_{Ca}/F_{CO2}, space time, the average maximum carbonation conversion, on the CO_2 capture efficiency is also demonstrated in the same chapter.

Table 2.5: Calcium looping dependent variables

Variable	Relevant to:	Influence through:
Actual carbonation conversion in/after the carbonator (X_{carb})	Whole DFB system	Equations (7, 9, 10, 11)
Actual carbonation conversion in/after the regenerator (X_{calc})		Equations (7, 8, 9, 14)
Actual Particle Size Distribution (PSD)		Fluid-dynamic interaction
Actual Total Solid Inventory (TSI)		
Average Maximum carbonation conversion ($X_{max,ave}$)		Equations (8, 10, 11, 12, 14)
Ca looping ratio (F_{Ca}/F_{CO2})		Equations (7, 8, 13)
Axial pressure profile	Carbonator	Fluid-dynamic interaction through influence of φ
Average CO_2 vol.-%		Equation (10, 12, 14)
Entrainment (G_s)		Fluid-dynamic interaction through influence of F_{Ca}/F_{CO2}
Equilibrium CO_2 vol.-%		Equation (10, 12, 14)
Fraction of active particles (f_{active})		Equation (12, 13, 15)
Gas-solid contacting effectiveness factor (φ)		Equation (10, 12, 14)
SO_2 capture efficiency		Influence of k_s
Sorbent surface kinetic constant (k_s)		Equation (10, 12, 14)
Space time (τ)		Fluid-dynamic interactions & steam cycle integration
Temperature (T_{carb})		Equation (1)
Time for X_{calc} to increase to $X_{max,ave}$ (t*)		Equation (13, 14)
Velocity	Regenerator	Fluid-dynamic interaction
Entrainment		
Partial pressure of CO_2		Calcination rate
Partial pressure of steam		
Regeneration efficiency		Equation (9)
Residence time		Regeneration efficiency
SO_2 release and capture		Calcination rate
Temperature		

2.4.4 Fluid-dynamic interactions-scaling theory

Equations (1-15) are an effort to approach reactor performance interactions happening within the Calcium looping system and especially within the carbonator.

The fluid-dynamic interactions, mentioned in Table 2.4 and Table 2.5 for the Calcium looping system of Figure 2.5, occur generally within fluidized bed systems. Their qualitative and quantitative description is a broader topic which can be approached through (i) semi-empirical models (e.g. [110]), (ii) Computational Fluid Dynamic (CFD) calculation models [111, 112], or (iii) application of the scaled cold model theory [113]. The scaled cold model theory is applied within this work and allows analysis of a reactor concept experimentally under ambient conditions. It is a practical tool both before and after building the actual process facility, especially for novel processes, since it is often quicker to set-up and run than a CFD model and more accurate than semi-empirical models. The latter is true since semi-empirical models may have been derived under deviating experimental conditions in comparison to the application at hand. Moreover, the study of the fluid-dynamics of a reactor system is often more practical in a cold model, through application of the scaled cold model theory, rather than through the operation of the actual plant since the cold model allows flexibility in testing a large number of operating scenarios and allows visualization of the solid flow pattern. The scaled cold model theory as well as the independent and dependent variables it connects are shown in Figure 2.7.

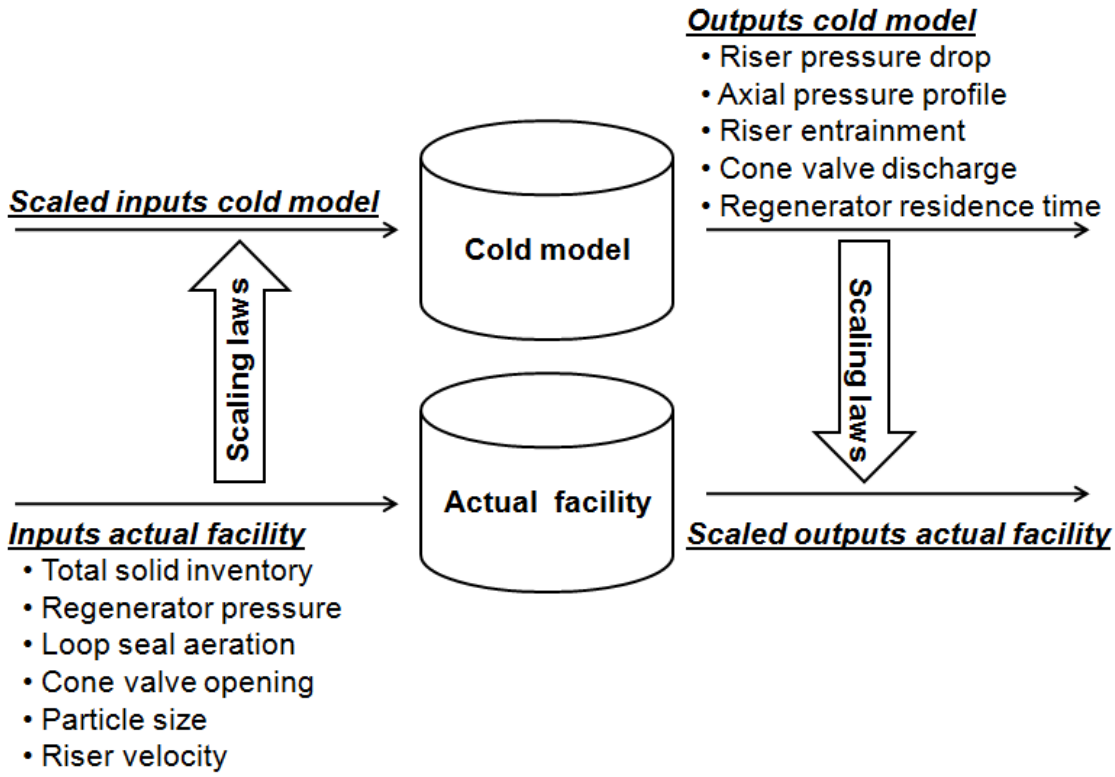

Figure 2.7: The scaled cold model theory

The scaled cold model theory principle postulates that fluid-dynamic similarity is achieved between an actual process fluidized bed facility and its cold model, operating

at atmospheric temperature and pressure, when a certain set of non-dimensional parameters are kept equal between them. This scientifically justifies the use of a scaled cold model in order to study the fluid-dynamic interactions of the actual process facility. The non-dimensional parameters which have to be kept same are listed below in Equation (16) and constitute the Glicksman simplified scaling criteria. Scaling of the pressure drop term (ΔP_x) has been shown in [114].

$$\frac{u_o^2}{gL_x}, \frac{\rho_s}{\rho_g}, \frac{u_o}{u_{mf}}, \frac{L_1}{L_2}, \frac{G_{sx}}{\rho_s u_o}, \frac{\Delta P_x}{\rho_s g D_x}, \phi, PSD \qquad (16)$$

Hence, the scaled cold model theory can be applied as follows to a Calcium looping facility and by analogy to any other reactor concept. Firstly, a value range is specified with regard to the operator defined fluid-dynamic variables of Figure 2.7. This is realized based on fluidization engineering considerations and good engineering judgement. For example, if a CFB carbonator is planned for, it is reasonable to expect an operating velocity of 3-6 m/s in contrast to a BFB unit, which would normally operate below 1 m/s. After this task is fulfilled the next step is to apply the scaling criteria in order to calculate the input values for the same variables that are to be applied to the scaled cold model. Through cold model experimentation, the respective dependent parameters listed in Figure 2.7 are measured and include reactor pressure drops, axial pressure profiles, entrainment, valve discharge values and particle residence time values. Finally, with use of the scaling laws of Equation (16) and simple considerations above cold model measurements can be transformed to the necessary actual facility dependent variables, i.e. (i) the F_{Ca}/F_{CO2} ratio, (ii) the carbonator space time, (iii) the carbonator axial solid fraction profile & gas-solid contacting, (iv) reactor entrainment values and (v) the regenerator residence time.

Regarding the set-up of a scaled cold model utilizing the criteria of Equation (16), it is useful to note that they allow for a free choice of the geometrical ratio (L_1/L_2) to be used for downscaling actual plant dimensions with regard to the cold model. In addition, free choice of only one further parameter included within the six ratios of Equation (16) is possible. This, in practical terms, means that the type of gas, having a given set of gas density (ρ_g) and viscosity (μ) values, or the solid density (ρ_s) of the particles to be used in the cold model can be chosen freely. However, after this choice is met, all other parameters are set in order for the six ratios of Equation (16) to have equal values between the cold model and the actual process facility. An additional requirement for proper scaling is that the sphericity of the cold model particles should be equal to that of the actual facility, while the relationship of their PSDs should be the same as that of their median particle size. Moreover, two further considerations must be taken into account. Firstly, the cold model and actual facility

particles must belong in the same Geldart classification category and secondly, the operating regime of the two facilities must be the same. Finally, good care must be taken that no extra forces are exerted upon the particles of the cold model that are not present in the actual facility. These forces are typically related to electrostatic forces, which can be avoided by good grounding of the cold model unit.

With regard to the Calcium looping process, the theory of fluid-dynamic scaling has been applied here for the first time and results are presented extensively in Chapter 3 with regard to the 10 kW_{th} IFK DFB facility. Subsequent application involved scaled cold model experimentation with regard to the two configurations of the 200 kW_{th} IFK facility [81, 82] However, other DFB processes related to power generation, e.g. Chemical Looping Combustion (CLC) and the Fast Internally Circulating Fluidized Bed (FICFB) steam gasification process, have employed scaled cold model experimentation extensively to assist in reactor design [64] and to study hydrodynamic aspects of operation. For example, scaled cold model testing has been applied to a two interconnected fluidized bed air biomass gasification concept [115]. Regarding CLC, a number of scaled cold models have been operated. Hence, results from CLC cold models representing 300 W_{th} [116], 10 kW_{th} [63], 60 kW_{th} [116], 120 kW_{th} [117], pressurized 2 MW_{th} [116] and 30 MW_{th} [118] CLC units have been published. Scaled cold models have also been utilized, with regard to the FICFB process, to develop suitable designs for 10 kW_{th}, 100 kW_{th} plants as well as for the scale-up of these systems to the 8 MW_{th} CHP Guessing plant [64]. Regarding the Guessing plant, cold model predictions proved to be sufficiently accurate when compared to real plant data [64] and recent cold model studies have also been published [119, 120]. The above cold model studies focused on demonstrating the suitability of the actual plants and on optimizing the reactor geometry, solid looping rate, gas leakage between reactors, bed mass and solid residence time. In addition, cold model testing has been used to validate fluid-dynamic models [121, 122].

3 Fluid-dynamic analysis through scaled cold model operation

Table 2.4 and Figure 2.7 list independent variables that affect the Calcium looping system through fluid-dynamic interactions. They are varied systematically with use of a scaled cold model of the 10 kW_{th} IFK DFB facilty. In the paragraphs below, details regarding the experimental setting are provided, while a facility specific pressure balance analysis is presented as a powerful tool before proceeding to result interpretation.

3.1 Experimental setup and procedure

The cold model of the 10 kW_{th} IFK DFB facility and its gas-solid flow pattern is presented first. Moreover, the application of the scaling theory of sub-section 2.4.4 is explained. Finally, aspects regarding parameter variation and data acquisition are highlighted.

3.1.1 Cold model 10kW_{th} DFB facility description

The cold model DFB system is shown in Figure 3.1. All dimensions of the cold model are downscaled by a factor of 2.33 from the 10 kW_{th} IFK Calcium looping DFB system. The cold model riser carbonator is 5.3 m high and has a diameter of 30 mm, while the cold model BFB has a diameter of 49 mm. The implemented riser exit is categorized as “abrupt” [123], since it is inclined downwards with respect to the horizontal direction. Solids are entrained through the different regions of the riser (1-3) and are separated by the cyclone separator (4). The riser entrainment subsequently proceeds to the double exit loop seal (6) via the upper standpipe (5) of the DFB system. The double exit loop seal used in this facility is essentially a typical loop seal with an orifice at its bottom. The size of the opening of the orifice is controlled by a cone valve (7), thus controlling the solid looping rate ($G_{s\ cv}$) through the orifice. The weir (8) of the loop seal sends the solids back to the riser, while the cone valve discharge leads to the BFB (9). The absolute pressure of the BFB (P_{BFB}) is controlled through a pressure control valve (10). Variation of the P_{BFB} is applied as an additional way of controlling the solid looping rate, since the P_{BFB} is the pressure on the discharge side of the cone valve. Solids proceed through the BFB overflow (11) to the lower loop seal (13) via the lower standpipe (12) and from there back to the riser, thereby closing the solid loop of the DFB system. The return legs of the double exit

and lower loop seals enter the riser at a slightly elevated position with regard to the distributor.

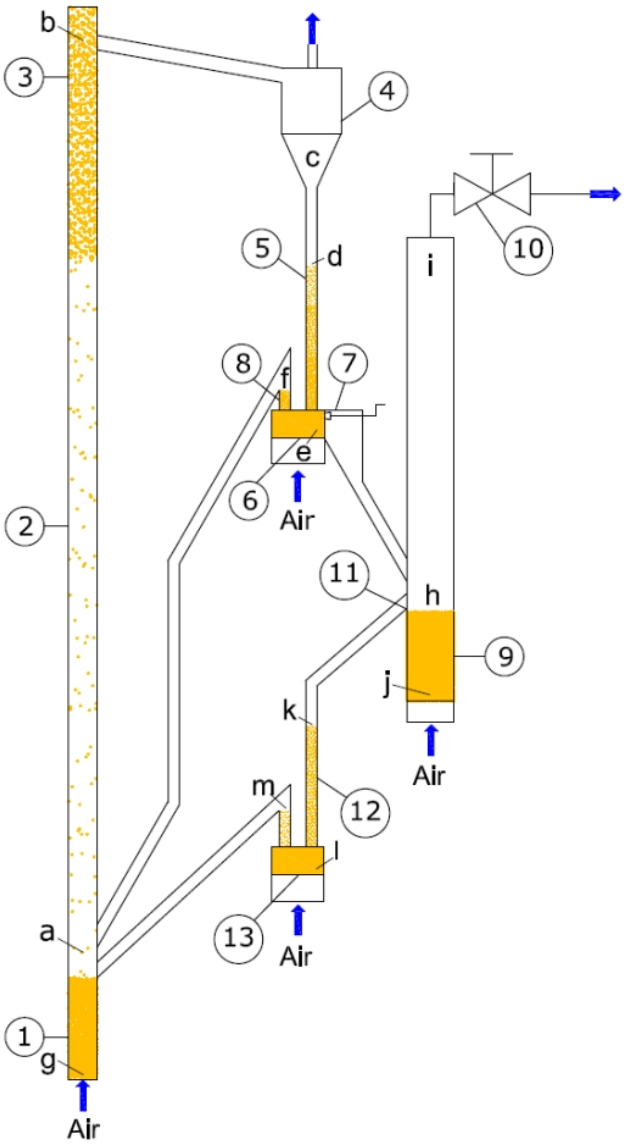

Figure 3.1: Cold model schematic; 1- dense region; 2- lean core-annulus region; 3- riser exit region; 4- cyclone; 5- upper standpipe; 6- double exit loop seal; 7- cone valve; 8- weir; 9- BFB; 10- BFB pressure control valve; 11- BFB overflow; 12- lower standpipe; 13- lower loop seal

The use of a cone valve, included in Figure 3.1, has been applied in some CFBC designs for controlling the solid flow to an external heat exchanger so as to operate the CFBC at the desired temperature [74]. However, another option that has also been proposed for controlling the solid looping rate ($G_{s\,cv}$) involving a loop seal and an L-valve [124]. Successful implementation with regard to this solid split application has been noted in the 1st configuration of the 200 kW_{th} IFK DFB facility and its cold model (see Table 2.2) [35, 81].

3.1.2 Application of the scaled cold model theory

Basic dimensions and operating conditions of the cold model and the 10 kW_{th} IFK DFB facility are given in Table 3.1. They are chosen in order to satisfy the ratios of the Glicksman simplified scaling criteria given in Equation (16).

Table 3.1: Basic values of cold model and 10 kW_{th} Calcium looping DFB facility [72]

Value	Unit	Cold model	10 kW_{th} IFK DFB
Length of the riser (L_{riser})	m	5.3	12.4
Diameter of the riser (D_{riser})	m	0.030	0.071
Gas density (ρ_g)	kg/m^3	1.188	0.369
Gas viscosity (μ)	Pas	18 E-6	39 E-6
Mean particle size ($\overline{d_p}$)	mm	142/230	419/687
Solid density	kg/m^3	5700	1800
Superficial velocity (u_0)	m/s	u_0	$1.53u_0$
Riser entrainment ($G_{s\ entrainment}$)	kg/m^2s	$G_{s\ entrainment}$	$0.486\ G_{s\ entrainment}$
Riser Pressure drop (ΔP_{riser})	mbar	ΔP_{riser}	$0.747\ \Delta P_{riser}$
Inventory (W_{riser})	kg	W_{riser}	$4.186 W_{riser}$

The gas-solid mixture chosen to simulate the hot flue gas-Ca flow was air and ZrO_2. The particle size for the 10 kW_{th} Calcium looping DFB has been chosen to be coarse and of the Geldart B classification since such particles exhibit greater gas permeability and much lower resistance to gas flow in comparison to Geldart A particles [125]. The latter aspect was believed to be of particular importance for the current small scale application with regard to the fluidization behaviour in the standpipes and loop seals. However, a limitation in the effort to conduct proper scaled experiments may be the existence of phenomena related to wall effects since the diameter of the riser is small and equal to 30 mm.

3.1.3 Data acquisition and range of parameter variation

The cold model utilizes LabVIEW® as the data acquisition system. Pressure drops within the cold model were measured with the use of 16 pressure transducers. The riser entrainment ($G_{s\ entrainment}$) and solid looping rate ($G_{s\ cv}$) were measured through stopping the aeration of the corresponding loop seal and measuring the particle bed height accumulation in the standpipe over a given period of time. The Total Solid Inventory (TSI) has been varied between 2.24 to 3.95 kg. The absolute pressure of the BFB freeboard (P_{BFB}) was varied up to 80 mbar through a pressure control valve. The opening of the orifice of the cone valve (A_{cv}) was set manually.

3.2 Facility pressure balance loops analysis

The pressure balance equations are used in this work as a tool for explaining the operation of the cold model DFB system and, hence, independent and dependent variable interactions. Two loops exist in the DFB facility, namely the a-b-c-d-e-f-a loop, atmosphere-i-h-k-l-m-a-b-c-atmosphere loop and are explained with the help of the letter symbols in Figure 3.1. Letters d and k in Figure 3.1 represent the point which is reached by particle bed height in the standpipes. For the a-b-c-d-e-f-a loop and the atmosphere-i-h-k-l-m-a-b-c-atmosphere loop, the pressure balance equations are given by Equation (17) and Equation (18), respectively.

$$(P_a - P_b) + (P_b - P_c) + (P_c - P_d) + (P_d - P_e) + (P_e - P_f) + (P_f - P_a) = 0 \tag{17}$$

$$\begin{aligned}&(P_{atm} - P_i) + (P_i - P_h) + (P_h - P_k) + (P_k - P_l) + (P_l - P_m) + (P_m - P_a) + \\ &+ (P_a - P_b) + (P_b - P_c) + (P_c - P_{atm}) = 0\end{aligned} \tag{18}$$

Figure 3.2 demonstrates a pressure map of the DFB system, whereby the pressure drop in terms of Equation (17) and Equation (18) are illustrated by joining respective points with lines although atmospheric pressure is omitted from the diagram.

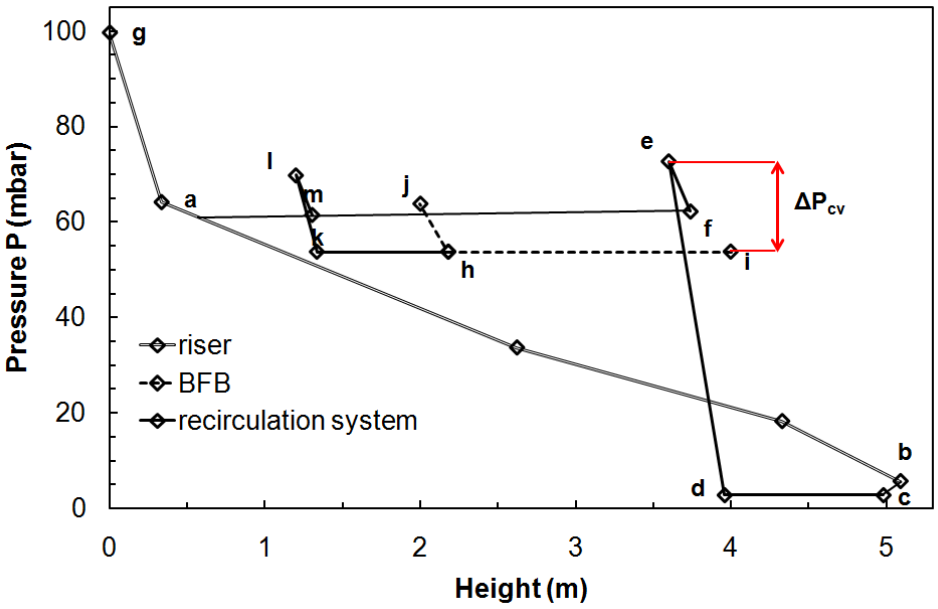

Figure 3.2: Pressure map of the cold model DFB system; TSI= 2.94 kg, u_0= 2.76 m/s, $\overline{d_p}$ = 142µm, P_{BFB}= 54 mbar

The terms (P_c-P_d), (P_f-P_a), (P_h-P_k) and (P_m-P_a) are equal to zero since the solids experience free fall between the respective points. Moreover, (P_i-P_h) is considered also

to be equal to zero due to the very low presence of solids in the BFB freeboard. Pressure at points e and l (bottom of the standpipes) exhibit the maximum values in the pressure loops represented in Equation (17) and Equation (18), thus making solid circulation and gas sealing possible. Equation (17) and Equation (18) can be rewritten by linking their pressure drop terms with the corresponding facility components and rearranging terms, as given in Equation (19) and Equation (20), respectively.

$$\Delta P_{upperst} = \Delta P_{cyclone} + \Delta P_{risertop} + \Delta P_{doubleexitls} \tag{19}$$

$$\Delta P_{lowerst} + (P_{BFB} - P_{cyclone}) = \Delta P_{cyclone} + \Delta P_{risertop} + \Delta P_{lowerls} \tag{20}$$

The $\Delta P_{riser\ top}$ is the pressure drop between the entrance point of the loop seal return legs to the riser (point a) and the exit of the riser (point b). The total riser pressure drop ($\Delta P_{riser\ total}$) is the pressure drop between the distributor (point g) and the riser exit (point b). Moreover, the pressure drop of the bottom part of the riser (point g to point a) is termed as $\Delta P_{riser\ bottom}$. The $\Delta P_{riser\ top}$, $\Delta P_{riser\ total}$ and $\Delta P_{riser\ bottom}$ are given in Equation (21).

$$\Delta P_{riser\ top} = \frac{W_{riser\ top}\, g}{A_{riser}}, \Delta P_{riser\ total} = \frac{W_{riser\ total}\, g}{A_{riser}}, \Delta P_{riser\ bottom} = \frac{W_{riser\ bottom}\, g}{A_{riser}} \tag{21}$$

The P_{BFB} represents the pressure of points i, h and k set at will with use of the pressure control valve. For the example, for the run of Figure 3.2, the P_{BFB} was set equal to 54 mbar. The absolute pressure of the cyclone ($P_{cyclone}$) is the pressure existing at point c. The term $\Delta P_{cyclone}$ represents the pressure drop through the cyclone and the duct connecting the riser exit to the cyclone (point b to c). Cyclone pressure drop has been shown to be a function of the inlet gas velocity squared [126] and, hence, of the riser velocity. However, recent studies have also included the solid concentration term of the inlet gas stream, e.g. [127]. Therefore, the $\Delta P_{cyclone}$ can be expressed by Equation (22).

$$\Delta P_{cyclone} = f\left(u^2_{inlet\ cyclone,}\, C_{s\ inlet\ cyclone}\right) \tag{22}$$

The pressure drop through the loop seals (ΔP_{ls}) (point e to point f for the double exit loop seal and point l to point m for the lower loop seal) is described with use of two terms [128]. The first represents the pressure drop through the length of the weir ($L_{ls\ weir}$). The second represents the pressure drop through the horizontal slit of the loop seal, which is a function of the solid flow ($G_{s\ ls}$) through it. The ΔP_{ls} is given in Equation (23).

$$\Delta P_{ls} = (1-\varepsilon_{mf})\rho_s g L_{ls\,weir} + f(G_{s\_ls}) \tag{23}$$

The pressure drop through the standpipe (point e to point d for the upper standpipe and point l to point k for the lower standpipe) is given in Equation (24) as the product of the standpipe pressure gradient $\left(\frac{dP}{dz}\right)_{st}$ and the length of the particle bed within the standpipe (L_{st}) [129]. The standpipe pressure gradient is given by the modified Ergun equation, shown in Equation (24). The $\left(\frac{dP}{dz}\right)_{st}$ is a function of the slip velocity (U_{sl}), given by Equation (25), between the gas and solid flow in the standpipe:

$$\Delta P_{st} = \left(\frac{dP}{dz}\right)_{st} L_{st} = \left(\frac{150\mu(1-\varepsilon_s)^2}{(\phi dp)^2 \varepsilon_s^2}|U_{sl}| + \frac{1.75\rho_g(1-\varepsilon_s)}{(\phi dp)\varepsilon_s}|U_{sl}|^2\right)L_{st} \tag{24}$$

Where U_{sl} is equal to:

$$U_{sl} = -\frac{G_{g\,st}}{\rho_g \varepsilon_s} + \frac{G_{s\,st}}{\rho_s(1-\varepsilon_s)} \tag{25}$$

The terms $G_{g\ st}$ and $G_{s\ st}$ represent the flow of gas and the solids respectively per unit area of the standpipe and are both positive in the downwards direction. The maximum gradient is reached when the slip velocity (U_{sl}) equals the minimum fluidization velocity and is given in Equation (26).

$$\left(\frac{dP}{dz}\right)_{st} = (1-\varepsilon_{mf})\rho_s g \tag{26}$$

In addition, a pressure difference is established through the orifice of the cone valve (ΔP_{cv}), which is illustrated in Figure 3.2 and is dependent on the P_{BFB}. The solid looping rate through the cone valve ($G_{s\,cv}$) can be predicted from the Jones-Davidson correlation for mechanical valves [130], as described by Equation (27). The solid looping rate is shown in Equation (27) to be a function of the product of the square root of the pressure drop through the cone valve (ΔP_{cv}) and the area available to the solid flow (A_{cv}). The solid looping rate is expressed per unit area of the riser cross section for easier comparison with the riser entrainment ($G_{s\ entrainment}$).

$$G_{scv} = \frac{C_o A_{cv} \sqrt{2\rho_{bulk} \Delta P_{cv}}}{A_{riser}} \quad (27)$$

In Equation (27), C_o is a constant equal to 0.55 [130].

3.3 Results and discussion

An analysis of stable and unstable cold model riser operating regions is performed and results are transfered to the actual 10 kW_{th} IFK DFB facility. The variation of the total riser pressure drop, pressure drop profile, entrainment and cone valve discharge with variation of independent variables, i.e. TSI, riser velocity (u_0), loop seal aeration-(u_{ls}), regenerator pressure (P_{BFB}) and PSD is of interest. This is because the $\Delta P_{riser\ total}$, pressure profile, entrainment & cone-valve discharge define the carbonator space time (τ), gas solid contacting factor (φ) and the Ca looping ratio (F_{Ca}/F_{CO2}). The importance of understanding the above fluid-dynamic interactions becomes apparent when considering that the latter three parameters influence the CO_2 capture efficiency prominently, i.e. through Equations (7, 8, 10, 12, 13)

3.3.1 Operating window of the cold model riser

The cold model riser pressure drop ($\Delta P_{riser\ total}$) is plotted against the riser velocity (u_0) in Figure 3.3a and Figure 3.3b, for runs conducted with a $\overline{d_p}$ of 142 μm and 230 μm respectively, TSI being a variable. Three regions of operation can be identified, i.e. the region of stable riser operation bordered by a slugging region at lower velocities and a region of unstable riser operation at higher velocities. The region of stable operation is limited by a minimum and maximum stable riser velocity, which increases with the TSI for both particle sizes. The minimum and maximum stable operation velocities are represented by solid lines. The constant space time (τ) line, included in Figure 3.3a and Figure 3.3b and represented by a dashed line, depicts the combinations of cold model riser velocities and riser pressure drop that simulate operation of the carbonator of the 10 kW_{th} DFB facility with a space time of 20 min. Runs above the dashed line can be considered somewhat realistic in order for CO_2 capture efficiency of above 80 % to be achieved without necessitating too high F_{Ca}/F_{CO2} or F_0/F_{CO2} ratios [33, 102]. When utilizing the cold model riser velocities of Figure 3.3a and Figure 3.3b, to predict those of to the 10 kW_{th} DFB facility carbonator, through the scaling laws of Equation (16), it is shown that stable operation can be achieved for velocities ranging from 3.5-5.3 m/s. Hence, the carbonator of the 10 kW_{th} Calcium looping DFB facility is predicted to operate at velocities similar to a CFBC [131], thus

facilitating reactor design. Furthermore, the stable riser operation regions for cold model experiments conducted with both mean particle sizes ($\overline{d_p}$) overlap to a large degree, as shown in Figure 3.3a and Figure3.3b, leading to the conclusion that variation in mean particle size does not affect hydrodynamic stability. Moreover, increasing the TSI for both $\overline{d_p}$ results in an increase of the riser pressure drop which is explained by Equation (21), as more inventory is available in the riser.

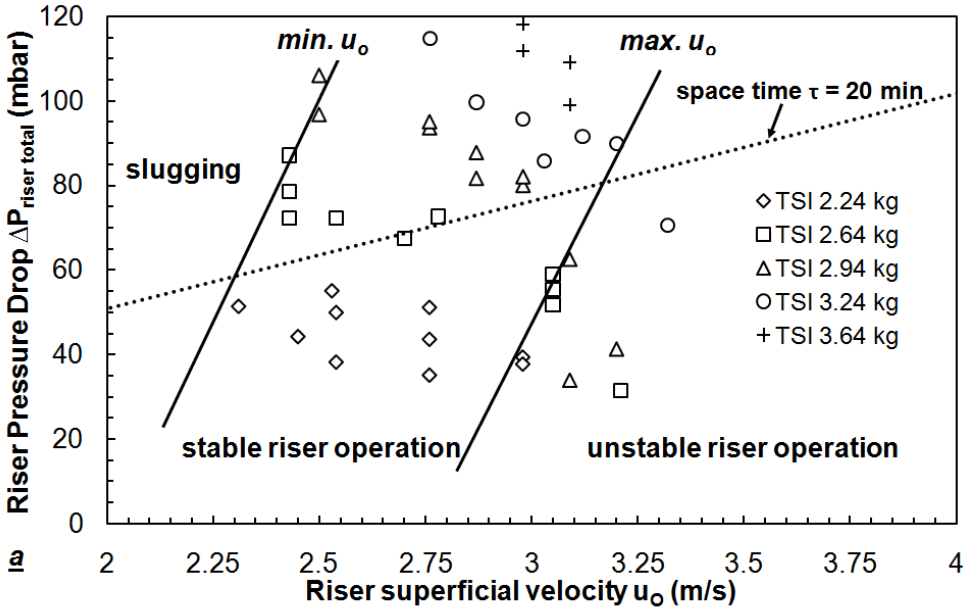

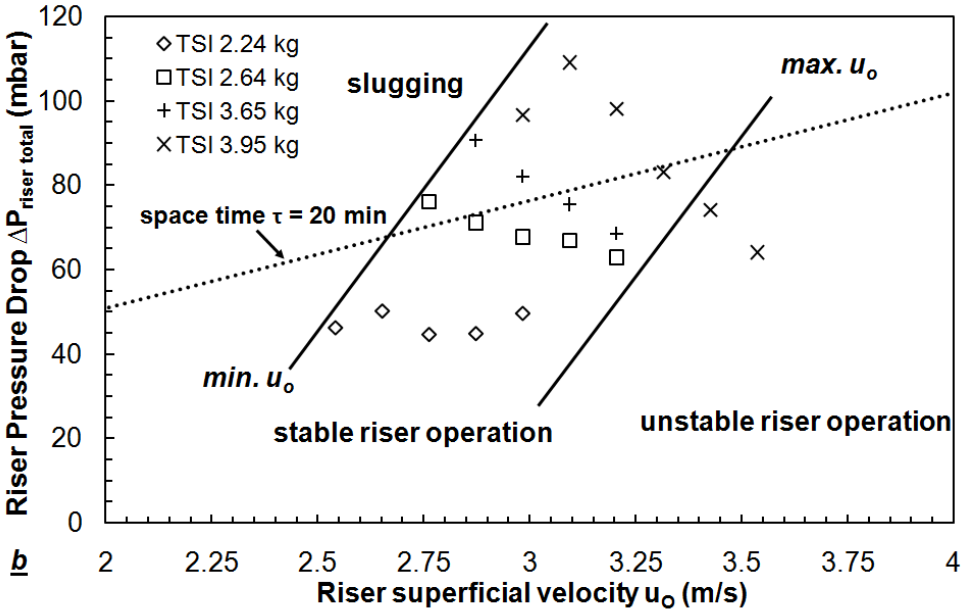

Figure 3.3a: Operational regions for cold model runs conducted with a $\overline{d_p}$ of 142 µm

Figure 3.3b: Operational regions for cold model runs conducted with a $\overline{d_p}$ of 230 µm

Below and in the vicinity of the minimum riser velocity in Figure 3.3a and Figure 3.3b, slugging phenomena are observed and are attributed to high riser pressure drop fluctuations and the small diameter of the riser. In Figure 3.4, the relative pressure fluctuation, defined as the ratio of the standard deviation of the riser pressure drop $\sigma(\Delta P_{riser\ total})$ and its mean value ($\Delta P_{riser\ total}$), is plotted against the riser superficial velocity for stable runs conducted with a mean particle size of 142 μm.

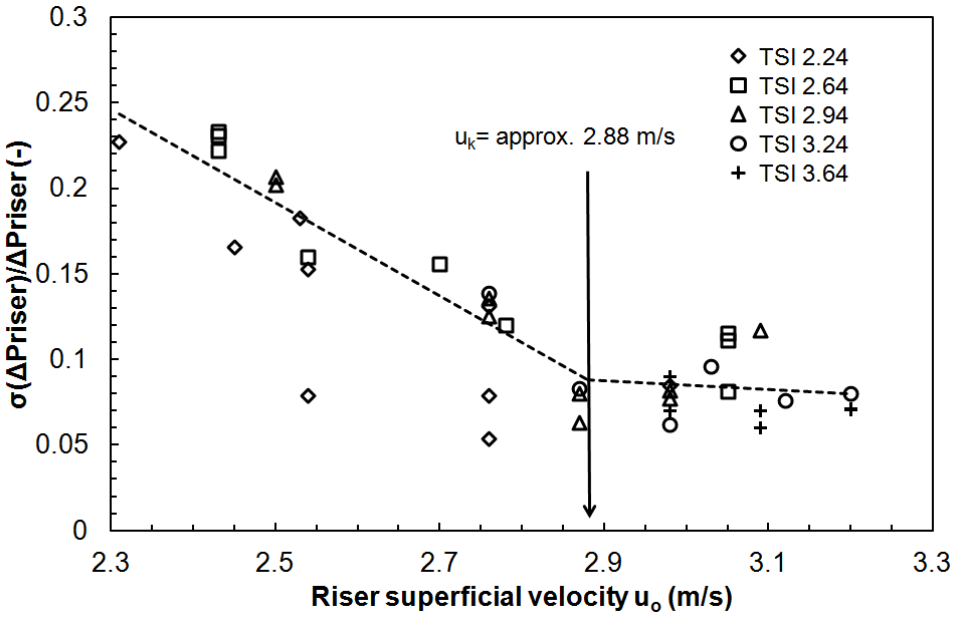

Figure 3.4: Relative pressure fluctuations for cold model runs utilizing a $\overline{d_p}$ of 142 μm

It is apparent that a great number of these runs have been conducted at a riser superficial velocity below the characteristic velocity u_k, which is identified in relevant review publications as the velocity after which relative pressure fluctuations level off [132, 133]. The value of u_k is found to be approximately equal to 2.88 m/s for the runs plotted in Figure 3.4. Despite the literature controversy [132, 133] around the meaning of u_k, it has been linked to solid transport [134]. The riser entrainment noted in the vicinity of u_k in this work was found to be in the order of 30 kg/m^{2}s. A further decrease of velocity below u_k leads to an increase of pressure fluctuations, as shown in Figure 3.4 as also noted in literature [132, 133]. The existence of a minimum riser velocity in this work, which is lower than u_k, is therefore defined as the minimum velocity where pressure fluctuations in the riser do not lead to inability of the loop seals to provide sealing. Hence, at even lower velocities, the gas from the riser takes a direct shortcut through the loop seal to the cyclone and stack resulting in an operational breakdown [128]. Since an increment of pressure drop leads to an increment of the absolute value of the riser pressure fluctuation at a given velocity, the

minimum riser velocity increases with increasing riser pressure drop and hence TSI, as already noted in Figure 3.3a and Figure 3.3b, respectively.

Above the maximum velocity the riser operation becomes unstable in a different manner which is rarely found in literature [128]. The behaviour of the DFB system in this region is illustrated in Figure 3.5 when plotting the $\Delta P_{upper\ st}$, $\Delta P_{riser\ top}$, ΔP_{cv} and $\Delta P_{riser\ bottom}$ against time for a typical run above the maximum riser velocity of Figure 3.3a.

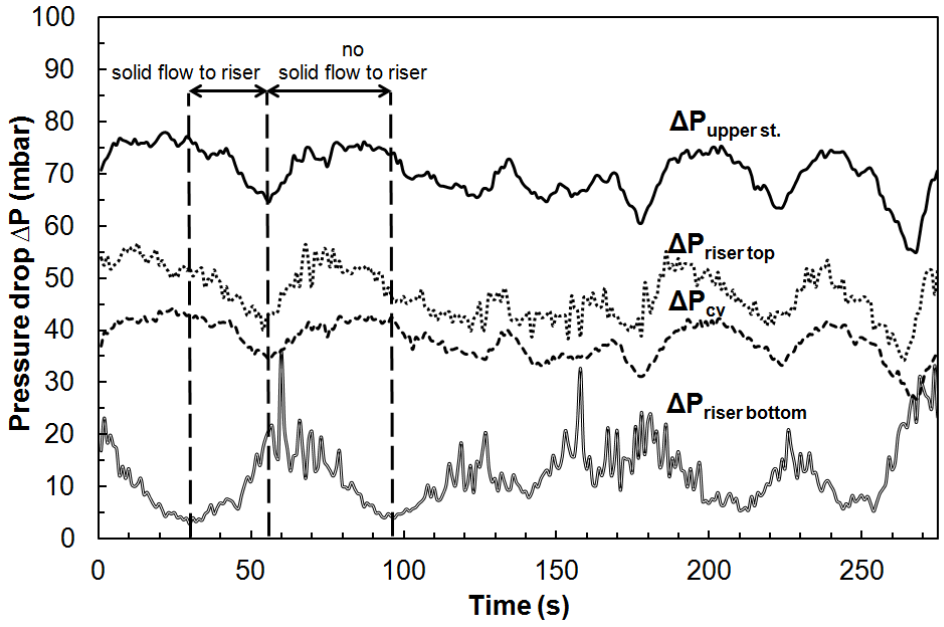

Figure 3.5: Variation of pressure drop terms vs. time within the unstable riser operation region; TSI= 2.64 kg, u_0= 3.05 m/s, $\overline{d_p}$ = 142 µm, P_{BFB}= 37 mbar

All pressure drop terms of Figure 3.5 exhibit a sinusoidal pattern with respect to time, while the phenomenon is periodic. Visual observation suggests that the pressure drop at the bottom part of the riser ($\Delta P_{riser\ bottom}$) decreases in Figure 3.5 when solid flow from the double exit loop seal to the riser stops and inventory is transferred from the bottom part of the riser (point g to a in Figure 3.1) to the upper part (point a to b) of the riser and the upper standpipe until a local minimum is reached. Solid flow consecutively commences suddenly and in a vigorous manner and $\Delta P_{riser\ bottom}$ increases until a local maximum is reached. The $\Delta P_{riser\ bottom}$ exhibits an opposite sinusoidal pattern compared to the pressure drop of the upper standpipe ($\Delta P_{upper\ st}$) and of the top part of the riser ($\Delta P_{riser\ top}$), representing the transfer of mass from the bottom part of the riser to the upper standpipe and the upper part of the riser. The variation in $\Delta P_{upper\ st}$ with time results in a variation in the pressure drop through the cone valve (ΔP_{cv}), which follows a similar trend due to the cone valve location. The system

behavior illustrated in Figure 3.5 can be explained in the following manner. The second term of Equation (23), is related to the solid flow through the loop seal ($G_{s\ double\ exit\ ls}$). An increment in riser velocity beyond the maximum velocity shown Figure 3.3a. and Figure 3.3b for a given TSI results in an increased riser entrainment ($G_{s\ entrainment}$) value that cannot be recycled through the double exit loop seal since the pressure drop through the double exit loop seal ($\Delta P_{double\ exit\ ls}$), included in Equation (23), is insufficient to push the solids through the loop seal. Therefore, the particle bed height in the upper standpipe ($L_{upper\ st}$) increases, while solid flow through the loop seal ($G_{s\ double\ exit\ ls}$) ceases thereby causes the riser inventory to drastically decrease. However, an increase in the particle bed height of the upper standpipe ($L_{upper\ st}$) leads to an increase in the upper standpipe pressure drop ($\Delta P_{upper\ st}$), as shown in Equation (24). In turn, this leads to an increase in the pressure drop through the double exit loop seal ($\Delta P_{double\ exit\ ls}$), as shown in Equation (19). Therefore, solid accumulation in the loop seal standpipe stops and solid flow through the double exit loop seal suddenly commences at a high rate when the height of the upper standpipe generates a sufficient pressure drop. The riser can be restored to stable operation at a given velocity by increasing TSI, as shown in Figure 3.3a and Figure 3.3b, since more inventory is made available to the upper standpipe and hence the capacity of the double exit loop seal to recycle the required $G_{s\ double\ exit\ ls}$ increases. This type of sinusoidal operation is of course undesirable in the 10 kW_{th} Calcium looping DFB facility. Sinusoidal variation of the pressure drop terms $\Delta P_{riser\ bottom}$, $\Delta P_{riser\ top}$ leads also to variation in riser pressure drop and likewise to variation in riser inventory, see Equation (21) and therefore by definition carbonator space time ($\tau = \frac{n_{Ca}}{F_{CO2}}$). In addition, variation in the ΔP_{cv} leads to variation in the cone valve discharge ($G_{s\ cv}$), as shown in Equation (27), and therefore by extension to the actual process, to variation in the Ca looping ratio (F_{Ca}/F_{CO2}). Operation with a slowly fluctuating carbonator space time and molar sorbent looping ratio may result in fluctuating carbonator CO_2 capture efficiency.

3.3.2 Pressure, solid fraction profile and riser flow structure

A typical axial pressure drop profile and the corresponding solid fraction profile of the cold model riser, representing the carbonator, are shown in Figure 3.6.

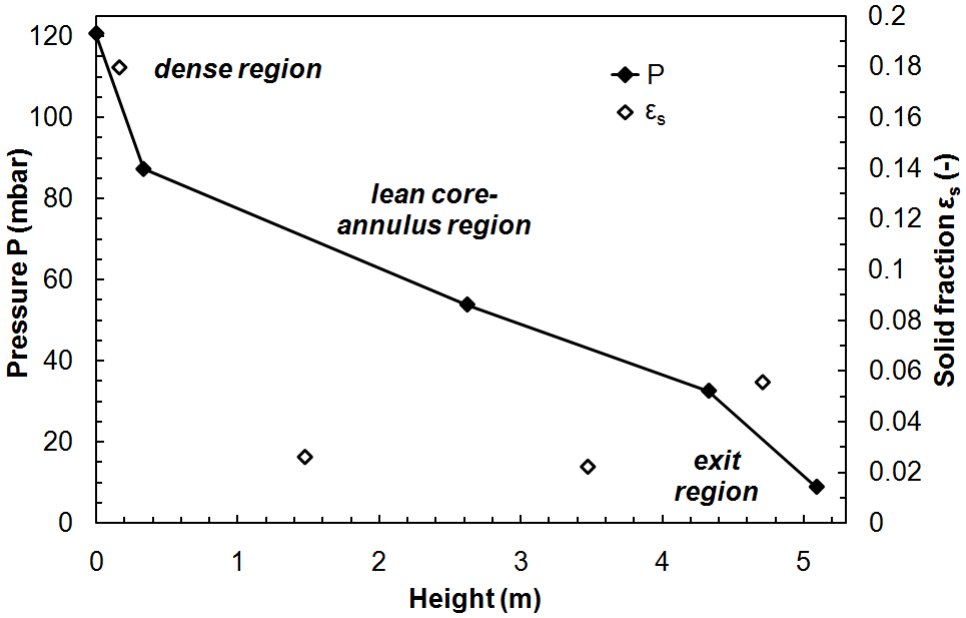

Figure 3.6: Typical pressure drop profile and ε_s profile, hydrodynamic regions of the cold model riser; TSI= 3.64 kg, u_0= 2.98 m/s, $\overline{d_p}$ = 142μm, P_{BFB}= 66 mbar

The solid fraction ε_s profile observed is "C-shaped". Three distinct fluid-dynamic regions, namely the dense region, the lean core-annulus region and the riser exit region are observed with increasing riser height and are characterized by their different pressure drop gradients and ε_s values. The allocation of the riser inventory between the different regions is important from a process point of view due to the different gas-solid contacting they exhibit. This would lead to different local φ factors in the actual carbonator unit and hence to an influence of the CO_2 capture efficiency through Equations (10) and (12). The solid fraction (ε_s) of the exit region is explained because of the "abrupt" riser exit utilized and the small scale of the riser [74]. Such a densification effect at the riser exit can be obtained also at large scale, only if a suitable constriction is applied to the flow [74]. The exit region and the lean region of the carbonator were observed to exhibit a core-annulus structure. The core-annulus structure mentioned has been previously observed for velocities above u_k [134] and has been used for CFB modeling applications also regarding Geldart B solids, e.g. [102, 110, 121]. A comparison of the flow structure predicted from the cold model, that of the actual carbonator riser of 10 kW_{th} facility and of a typical CFBC is presented later on within Chapter 4 (see sub-section 4.3.3.1).

3.3.3 Independent variable influence on the riser profiles

The pressure drop profile and solid fraction profile of Figure 3.6 are representative for all experiments in a qualitative way, while their exact form depends

mainly on independent variables. In Figure 3.7, 3.8 and 3.9 the effect of Total Solid Inventory, BFB freeboard absolute pressure (P_{BFB}) and double exit loop seal aeration ($u_{0double\ exit\ ls}$) on the riser pressure drop, pressure drop profile, and solid fraction profile of the cold model riser is illustrated, respectively.

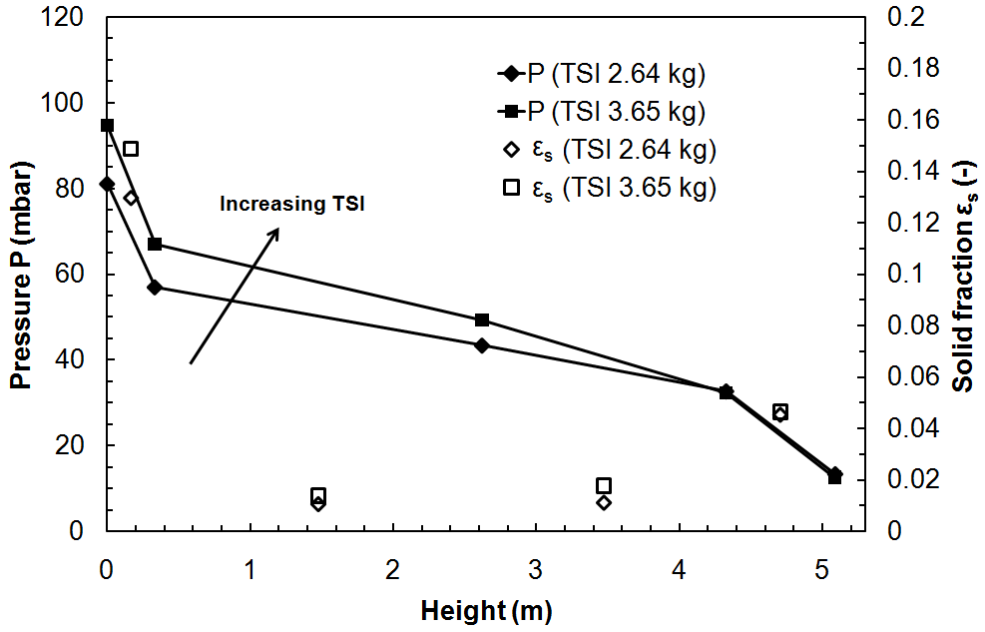

Figure 3.7: Effect of Total Solid Inventory (TSI) on the pressure drop profile and ε_s profile of the cold model riser; u_0= 2.98 m/s, $\overline{d_p}$ = 230 µm, P_{BFB}= 38 mbar

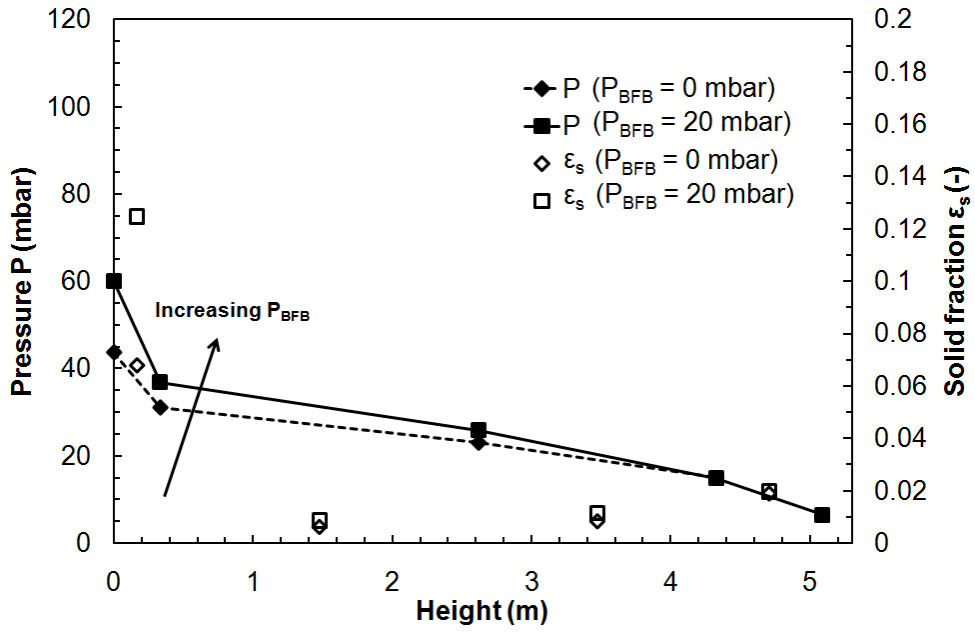

Figure 3.8: Effect of the pressure of the BFB (P_{BFB}) on the pressure drop profile and ε_s profile of the cold model riser; TSI= 2.24 kg, u_0= 2.54 m/s, $\overline{d_p}$ = 142µm

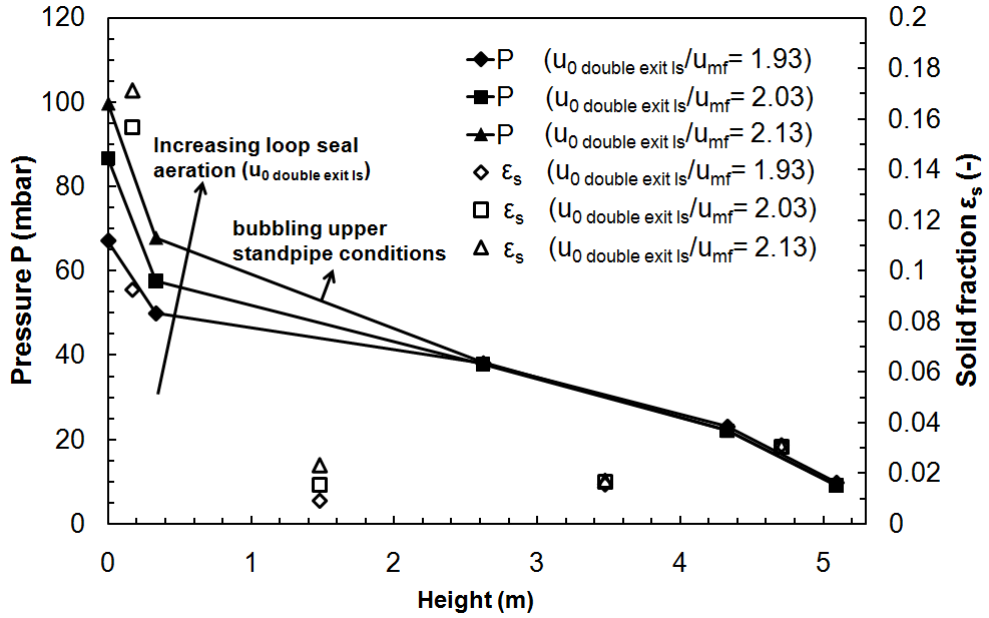

Figure 3.9: Effect of the double exit loop seal aeration ($u_{0double\ exit\ ls}$) on the pressure drop profile and ε_s profile of the cold model riser; TSI= 3.65 kg, u_0= 2.87 m/s, $\overline{d_p}$ = 230 μm, P_{BFB}= 37 mbar

An increase of any of the above parameters leads to an increase in the riser pressure drop, as shown in Figure 3.7, 3.8 and 3.9, because the riser inventory increases through Equation (21), although this occurs through different mechanisms. An increment in TSI is distributed between the riser and the standpipes according to the pressure balance expressions of Equations (19) and (20), thereby resulting in an increase of the riser pressure drop. Furthermore, when the P_{BFB} is increased, the pressure drop of the lower standpipe ($\Delta P_{lower\ st}$) decreases so that Equation (20) can be satisfied. The latter is realized through a decrease in the lower standpipe height ($L_{lower\ st}$), as given in Equation (24), and hence the lower standpipe inventory. This inventory is distributed among the riser and upper standpipe according to Equation (19) and Equation (20), thus increasing the $\Delta P_{riser\ total}$. In addition, an increase in the double exit loop seal aeration ($u_{0double\ exit\ ls}$) results in an increase in the slip velocity in the upper standpipe ($U_{sl\ upper\ st}$), as shown in Equation (25), since the gas flow travelling upwards in the upper standpipe increases. Therefore, the pressure gradient of the upper standpipe $\left(\frac{dP}{dz}\right)_{upper\ st}$ also increases, as given in Equation (24), provided that the upper standpipe is operating under moving bed conditions. Since $\Delta P_{upper\ st}$ is equal to the product of $\left(\frac{dP}{dz}\right)_{upper\ st}$ and $L_{upper\ st}$, as given in Equation (24), the latter has to decrease so as for the term $\Delta P_{upper\ st}$ to satisfy Equation (19). Therefore, inventory from the upper standpipe is distributed between the lower standpipe and the riser and the riser pressure drop ($\Delta P_{riser\ total}$) increases. When the

standpipe reaches bubbling conditions, as given by $\frac{u_{0\,double\,exit\,ls}}{u_{mf}} = 2.13$ in Figure 3.9, the maximum value of the standpipe gradient $\left(\frac{dP}{dz}\right)_{upper\,st}$ is attained, as given by Equation (26). A further increase in the $u_{0double\ exit\ ls}$ has no influence on the $\left(\frac{dP}{dz}\right)_{upper\,st}$ or on the inventory allocation in the DFB system. The increase in riser inventory caused by increasing TSI, P_{BFB} or $u_{0double\ exit\ ls}$ has a similar effect on the pressure drop profile and solid fraction profile of the riser, as shown in Figure 3.7, 3.8 and 3.9, respectively. The added inventory accumulates mainly in the dense region and lean core-annulus region of the bed, as shown by their increasing solid fraction values and pressure drop gradients. However, no change is noted regarding the exit region although it comprises approx. 20% of the riser length. Since, the solid fraction of the exit region does not change, the riser entrainment remains also unaffected. For example, the riser entrainments for the three runs shown in Figure 3.7 are almost equal and have a value of approximately 30 kg/m^{2}s. However, as summarized recently [135], two types of contrasting observations exist with respect to riser pressure drop and solid fraction profile regarding the effect of adding inventory at a given constant riser velocity and entrainment. The first type points out that the respective profiles remain unchanged, while the second type demonstrate that the solid fraction of the dense bed increases, while the solid fraction of the upper dilute region remains constant. The experiments conducted in our study tend to agree more with the second observation type, although only the solid fraction in exit region remains unchanged.

The effect of the riser velocity on the riser pressure drop, the pressure drop through the cyclone ($\Delta P_{cyclone}$) and the pressure drop of the different fluid-dynamic regions of the cold model riser is presented in Figure 3.10.

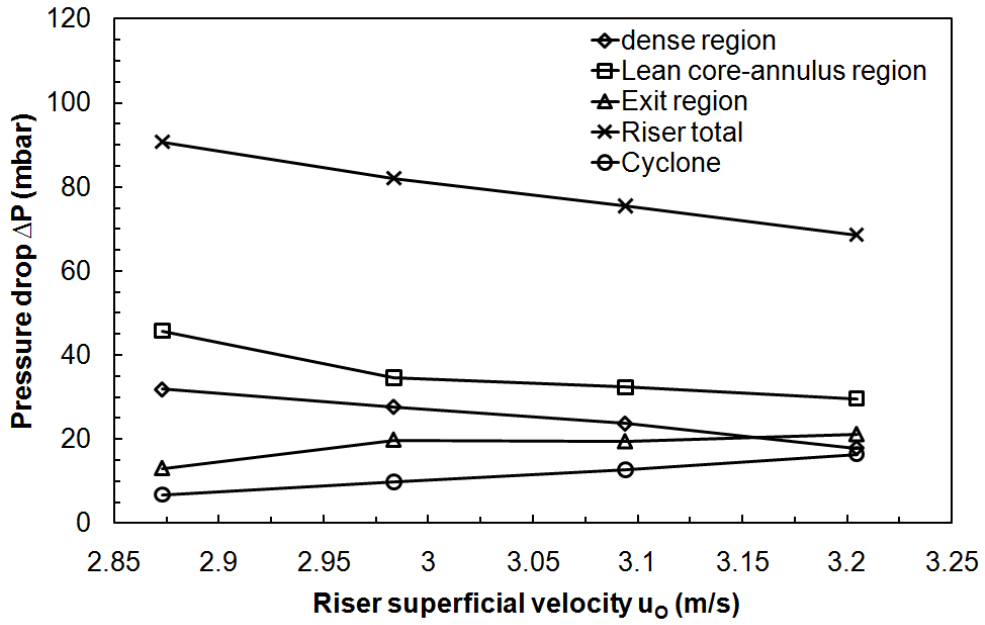

Figure 3.10: Effect of riser u_0 on the $\Delta P_{riser\ total}$, $\Delta P_{cyclone}$ and on the pressure drop of the different hydrodynamic regions of the cold model riser; TSI= 3.65 kg, $\overline{d_p}$ = 230 µm, P_{BFB}= 39mbar

Increasing riser velocity leads to an increasing $\Delta P_{cyclone}$, as predicted from Equation (22). The increase in $\Delta P_{cyclone}$ with riser velocity causes both the pressure drop of the upper standpipe ($\Delta P_{upper\ st}$) and of the lower standpipe ($\Delta P_{lower\ st}$) to increase in order to drive the solid flows through their respective loop seals (see Equation (19) and (20)). This is realized in both standpipes by increasing their particle bed heights (L_{st}), as shown in Equation (24). Therefore, the riser inventory and consequently the riser pressure drop decrease. The decrease in riser pressure drop with increasing velocity is noted for runs conducted with constant TSI and mean particle size, as also shown in Figure 3.3a and Figure 3.3b. The pressure drop in the dense and lean core-annulus region decrease with increasing riser velocity, while the pressure drop of the exit region increases. This data is in general agreement with Namkung et al. [136], who while conducting experiments with constant riser entrainment, have shown that dense bed solid fraction decreases with increasing velocity and that the solid fraction of the exit region increases to a saturation point. In this work, it can be concluded that the transfer of inventory from the riser to the standpipes with increasing velocity occurs only from the dense and lean region. Simultaneously, inventory is transferred internally to the exit region of the riser due to the increasing carrying capacity of the flow.

In order to assess the effect of mean particle size, the riser pressure drop profile and solid fraction profile are plotted in Figure 3.11 for two runs conducted with a different mean particle size of 142 µm and 230 µm respectively. The runs of

Figure 3.11 have been conducted with same riser velocity and approximately the same riser pressure drop.

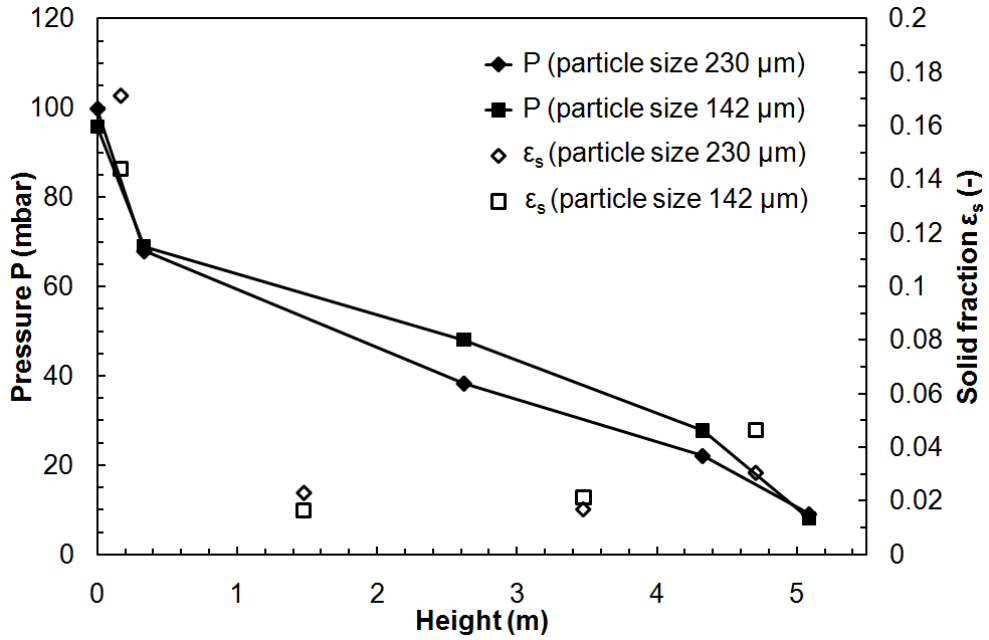

Figure 3.11: Effect of the mean particle size ($\overline{d_p}$) on the pressure drop profile and ε_s profile of the cold model riser at constant u_0 and $\Delta P_{riser\ total}$; u_0= 2.87 m/s, $\Delta P_{riser\ total}$ = 90 mbar

For the run conducted with $\overline{d_p}$ of 230 µm, larger pressure gradients and solid fraction values are noted in the dense region and in the lower part of the lean core-annulus region of the riser in comparison to the run conducted with a $\overline{d_p}$ of 142 µm. The situation is reversed in the upper part of the lean core annulus region and the exit region of the riser. Hence, it can be concluded that increasing mean particle size in the DFB system leads to an increased accumulation of inventory in the lower region of the riser due to the increased inertia of coarser particles.

3.3.4 Riser entrainment

The riser entrainment in the DFB system of Figure 3.1 represents the maximum solid looping rate ($G_{s\ cv}$) between riser and BFB that can be attained at a given operating condition. Hence, the entrainment must always be enough in order to allow for the design F_{Ca}/F_{CO2} to be established. In the case of the 10 kW_{th} IFK DFB facility this range is chosen wide, i.e. 5-20. The riser entrainment is plotted against riser velocity in Figure 3.12a and Figure 3.12b for the runs conducted with a mean particle size of 142 µm and 230 µm, respectively.

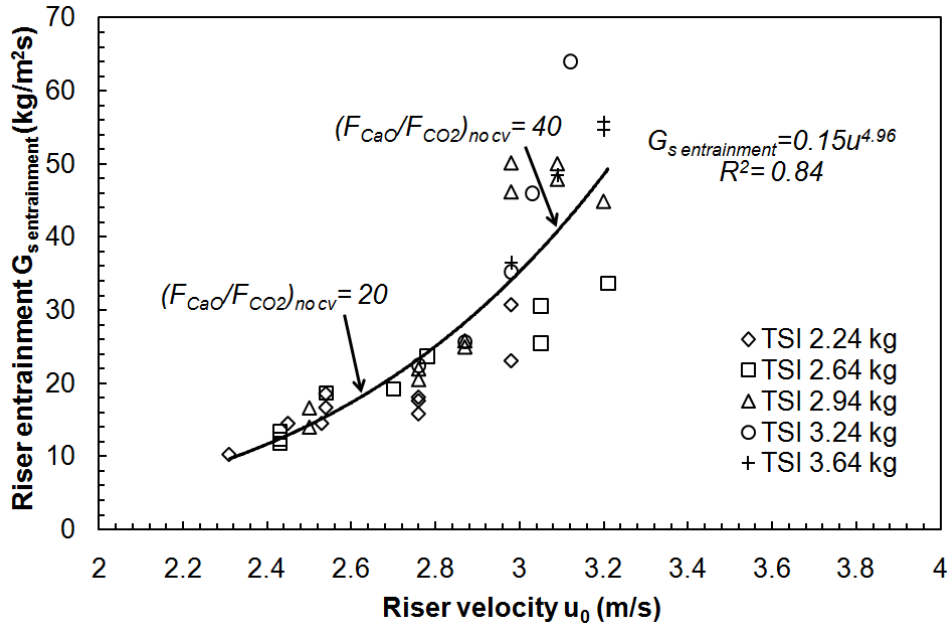

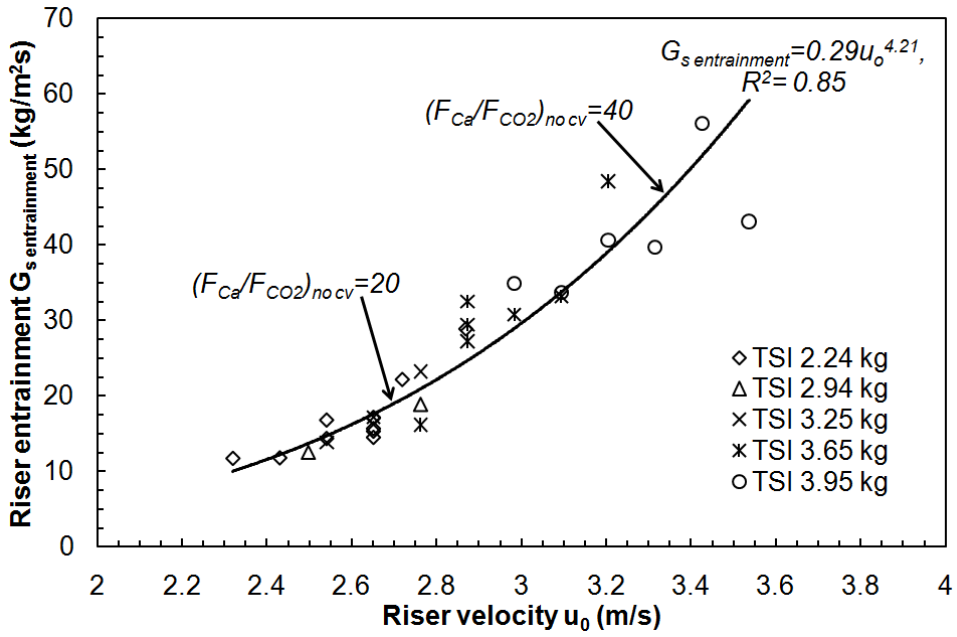

Figure 3.12a: $G_{s\ entrainment}$ against riser u_0 for runs conducted with a $\overline{d_p}$ of 142 μm

Figure 3.12b: $G_{s\ entrainment}$ against riser u_0 for runs conducted with a $\overline{d_p}$ of 230 μm

The Equation (28) and Equation (29), shown below, fit the data of Figure 3.12a and Figure 3.12b, respectively, with a good fit and correlate the riser entrainment, for each mean particle size, with the riser velocity only. Moreover, Equation (28) and Equation (29) are represented with solid lines in Figure 3.12a and Figure 3.12b, respectively.

$$G_{s\ entrainmen\ t} = 0.15u_o^{4.96}, R^2 = 0.84\ for\ \overline{d_p} = 142\,\mu m \quad (28)$$

$$G_{s\,entrainmen\ t} = 0.29u_o^{4.21}, R^2 = 0.85\ for\ \overline{d_p} = 230\,\mu m \quad (29)$$

An analogous correlation for riser entrainment as a function of riser velocity has been shown in many studies, e.g. [63, 116]. However, most of these studies also show that riser entrainment has a strong dependence on riser inventory. In this study however, the riser inventory, which is proportional to the TSI of the DFB system, has a limited effect on the riser, as shown in Figure 3.12a and Figure 3.12b. Such an effect is mainly noted at higher velocities, while it is insignificant for lower velocities. The limited TSI effect on the riser entrainment can be explained in that the gas flow has a given carrying capacity and also that the riser height is sufficient enough to store additional bed inventory in the middle and lower part of the riser without affecting the solids fraction at the exit. The riser entrainment for experiments conducted at a given u_0 with a $\overline{d_p}$ of 230 µm is less than for the experiments conducted with a $\overline{d_p}$ of 142 µm, as shown in Figure 3.12a and Figure 3.12b, due to the increased inertia of the coarser particles.

A further possibility to predict the riser entrainment in a continuous manner has been given by previous studies which have correlated the riser entrainment to various pressure drop terms in the CFB loop, e.g. [137]. Here, the riser entrainment was plotted against the pressure drop of the exit region ($\Delta P_{exit\ region}$) of the riser, as shown in 3.13. The $\Delta P_{exit\ region}$ is the pressure drop of the riser segment before the exit of the cold model riser, having a total length of 0.75 m. Equation (30) fits the data of Figure 3.13 well and correlates the $G_{s\ entrainment}$ to the $\Delta P_{exit\ region}$.

$$G_{s\,entrainment} = 2.65\Delta P_{exit\,region}^{0.87}, R^2 = 0.82 \quad (30)$$

The $\Delta P_{exit\ region}$ is expressed in mbar in Equation (30). Equation (30) matches the data of 3.13 well at lower riser velocities, while more deviation exists at higher riser velocities. This deviation is mainly attributed to of the increased error when visually measuring the riser entrainment at the higher riser velocities. Equation (30) has an advantage in comparison to Equation (28) and Equation (29) in defining the riser entrainment since Equation (30) does not include the mean particle size.

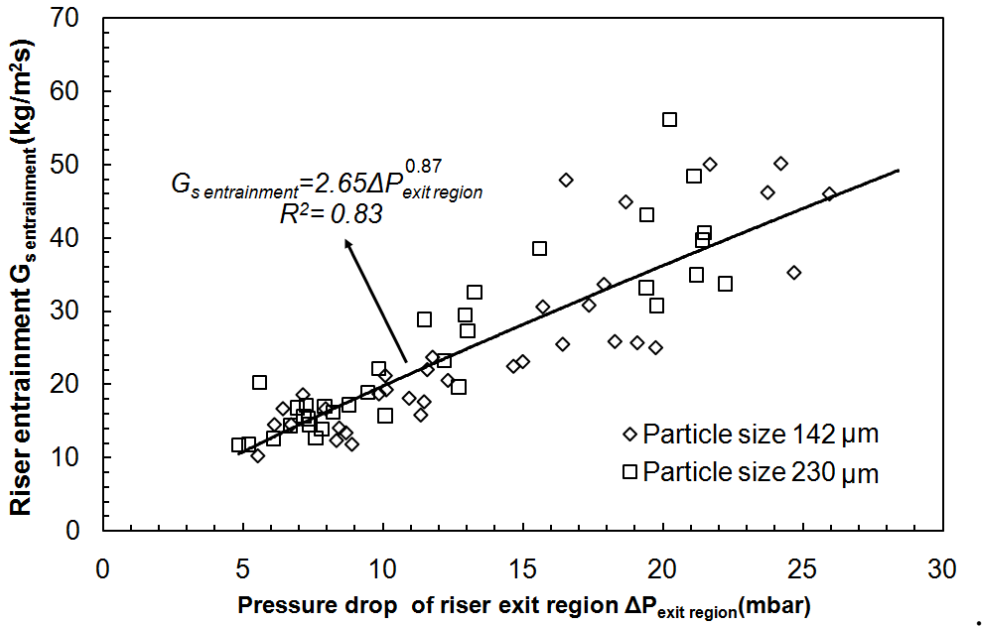

3.13: $G_{s\ entrainment}$ against $\Delta P_{exit\ region}$ for all runs with a $\overline{d_p}$ of 142 μm and 230 μm

From Figure 3.12a and Figure 3.12b, it can be derived that the double exit loop seal with use of a cone valve, shown in Figure 3.1, is necessary for the 10 kW_{th} Calcium looping DFB system in order to control the molar sorbent looping ratio (F_{Ca}/F_{CO2}) between the carbonator and the regenerator. It is shown that the cold model riser entrainment, for a riser velocity above 2.6 m/s for both mean particle diameters, exceeds the value of 17 kg/m^{2}s. Combining the above cold model data with the scaling factors of Equation (16), the conclusion is reached that the 10 kW_{th} IFK DFB riser carbonator will exceed 8 kg/m^{2}s at a velocity of 4 m/s. If the double exit loop seal with use of a cone valve were not to be used, the riser entrainment would be identical to the solid looping rate, since the entire solid flux would be directed to the BFB regenerator. Therefore, the riser entrainment would define the molar sorbent looping ratio as $(F_{Ca}/F_{CO2})_{no\ cv}$. Therefore, at carbonator velocity above 4 m/s in the 10 kW_{th} Calcium looping DFB facility, the molar sorbent looping ratio would exceed 20 and would exceed 40 at around 5 m/s for both simulated particle sizes, as noted in Figure 3.12a and Figure 3.12b. Since the regenerator operates at approximately 900°C and the carbonator at 650°C, such high solid looping rates between the two reactors would require the addition and removal of large amounts of heat, leading to temperature control problems in the 10 kW_{th} IFK DFB system and exceed the noted desired range of 5-20. Hence, the implementation of the double exit loop seal with use of a cone valve, as a solid looping rate control mechanism, is needed.

3.3.5 Solid looping rate and operation of the cone valve

The solid looping rate through the cone valve ($G_{s\ cv}$), based on the riser cross section, has been plotted against the product of the area available for solid flow (A_{cv}) and the pressure drop through the cone valve (ΔP_{cv}) in Figure 3.14.

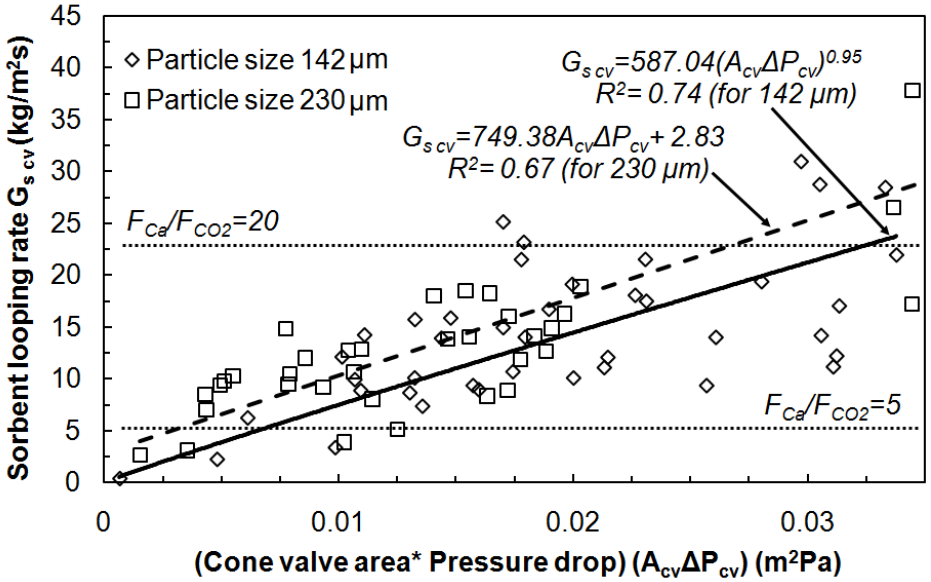

Figure 3.14: $G_{s\,cv}$ vs. the product of A_{cv} and ΔP_{cv} for all runs with a $\overline{d_p}$ of 142 μm and 230 μm

The data of Figure 3.14 are fitted with use of Equation (31) and Equation (32) for each respective median particle size used during experimentation.

$$G_{s\,cv} = 587.04\left(A_{cv}\Delta P_{cv}\right)^{0.95}, R^2 = 0.74,\ for\ \overline{d_p} = 142\,\mu m \tag{31}$$

$$G_{s\,cv} = 749.38\,A_{cv}\Delta P_{cv} + 2.826, R^2 = 0.67,\ for\ \overline{d_p} = 230\,\mu m \tag{32}$$

Obtained equations are linear with a satisfactory fit and the effect of the mean particle size is limited. However, Equation (31) and (32) are of a different form than anticipated from the Jones-Davidson correlation of Equation (27), since the ΔP_{cv} term is raised to the power of 1 and not to the power of 0.5. However, a correlation linking pressure drop and solid flow linearly, as in Equation (31) and (32), has been observed in literature when correlating the solid flow through a rectangular slit of a loop seal [128]. More recently, Grieco and Marmo [142] suggested that both the model of Equation (27) and the model of reference [128] are insufficient to describe solid flow through a valve when the perimeter to area ratio is high (corresponds to a slightly open valve) and they proved this by varying the opening of a butterfly valve to control solid flow through the return leg of a CFB. They justified their claim based on the

interactions (border effects) of the flow and the walls in the restricted section of the orifice. They showed, through model validation, that the solid flow in such a case is linear to the pressure drop, while all other model parameters are of a geometrical nature. Hence, the linear trends of Figure 3.14, Equation (31) and Equation (32) are justified since the available area for flow is only the lower part of the annulus between the cone and the orifice of the upper loop seal wall (see Figure 3.1). To support the above it should be noted that the annulus area that has been varied, during experimentation here, lies between 5.3-8.2 mm^2. However, larger cone valves have shown a solid flow dependency with the ΔP_{cv}, when raised at the power of 0.5 [82], as anticipated by the Jones-Davidson model. Finally, assuming that the carbonator of the 10 kW_{th} DFB system is operating at 5 m/s and the flue gas CO_2 vol. % is 15, the desired sorbent looping ratio range of 5-20 is shown in Figure 3.14. Since the cone valve discharge-solid looping rate ($G_{s\ cv}$) can be controlled through the cone valve so that the Ca looping ratio lies in the desired range.

3.4 Conclusions of the fluid-dynamic analysis

Fluid-dynamic analysis with use of a scaled cold model of the 10 kW_{th} IFK DFB facility has been carried out with the aim of establishing an operating window for the riser and studying respective interactions. Such interactions have been shown to occur between specific independent and dependent variables. Parameters of the first type include the Total Solid Inventory (TSI), riser velocity regenerator pressure, loop seal aeration, and PSD-median particle size. Parameters of the second type include cold model carbonator riser pressure drop, the axial pressure profile, riser entrainment and the cone valve discharge. The latter variables define through simple transformations further dependent variables which are crucial for defining the CO_2 capture efficiency, i.e. space time, the gas-solid contacting factor φ and the Ca looping ratio. Variation of all the independent parameters has shown that the specific 10 kW_{th} IFK DFB and DFB systems in general are capable of carrying out the Calcium looping process and achieving high CO_2 capture efficiencies. The most important findings include that a region of stable operation, bordered by a minimum and maximum velocity, exists for the cold model riser. At a given TSI, slugging is observed below the minimum riser velocity, while unstable operation is observed above the maximum velocity resulting in variation of riser pressure drop and solid looping rate with respect to time. Predicted operation velocities and total pressure drops of the 10 kW_{th} IFK DFB carbonator have shown to be 3.7-5.3 m/s and 22-90 mbar, respectively. Moreover, a dense region, lean core-annulus region and exit region have been observed within the cold model riser, while the solid fraction profile is found to be C-shaped. All independent parameters noted above influence the allocation of the inventory in the DFB system as well as

between the different riser regions, as observed through the riser pressure drop and solid fraction profiles. The riser entrainment was found to correlate to only riser superficial velocity for a given particle size and was not influenced by TSI. Predicted entrainment values to the 10 kW_{th} IFK DFB carbonator were in the range of 5-30 kg/m^2s. Furthermore, the pressure drop of the riser exit region has proven to be a good operational indicator of the riser entrainment value. The high riser entrainment values (typical of all CFBs) necessitate the use of mechanism for controlling the sorbent looping rate, such as the double exit loop seal with a cone valve as utilized in this facility. In this manner, the Ca looping rate can be adjusted to the desired value (5-20) through variation of the area available to the solid flow through the orifice of the cone valve and the pressure drop through the cone valve. Finally, the fluid-dynamic behavior derived through cold model experimentation presented within this chapter is compared, within section 4.3.3.1 of the next chapter, with respective data derived from the operation of the actual 10 kW_{th} IFK DFB facility.

4 Carbonator reactor performance analysis

Results from two Calcium looping facilities are presented and extensively analyzed within this chapter. These involve the 10 kW_{th} IFK DFB facility and the 30 kW_{th} DFB INCAR-CSIC facility. Design, operation and analysis regarding the first facility has been conducted within the scope of this thesis, while all above aspects of work regarding the latter facility have been conducted independently [34, 138].

4.1 Experimental facilities and methods

Brief descriptions of the 10 kW_{th} IFK and the 30 kW_{th} INCAR-CSIC facilities are given below. Subsequently, the parameter variation range and the differences between the two facilities are presented. Finally, the equipment-methods utilized in order to measure process parameters are discussed.

4.1.1 The 10 kW_{th} IFK DFB facility.

The 10 kW_{th} IFK DFB Calcium looping facility consists of a 12.4 m high, 70 mm diameter riser, a 114 mm diameter Bubbling Fluidized Bed (BFB) and is presented schematically in Figure 4.1. Moreover, the different components of the facility are numbered in detail. As noted, all of the 10 kW_{th} IFK DFB facility dimensions are 2.33 times up-scaled with respect to the cold model, presented in Figure 3.1. Furthermore, the two units exhibit exactly the same solid flow pattern [33, 72]. Two modes of operation are possible when utilizing the 10 kW_{th} IFK facility, both of which have been realized within this work. The first involves operating the riser as the carbonator and the BFB as the regenerator [84]. This mode is consistent with the fluid-dynamic analysis conducted in Chapter 3. Moreover, it provides realistic information with regard to the performance of the riser carbonator, which is the reactor type to be used industrially. The second mode involves switching the roles of the two reactors, i.e. utilizing the BFB as the carbonator and the riser as the regenerator, and has the advantage that carbonator space time can be varied almost independently of other process conditions [33]. This second mode of operation is particularly interesting when extended to suit another DFB process related to biomass gasification, namely the AER process [58, 78], whereby CO_2 capture is carried out in a BFB gasifier and calcination is carried out in an air blown regenerator. This mode of operation is depicted in Figure 4.1.

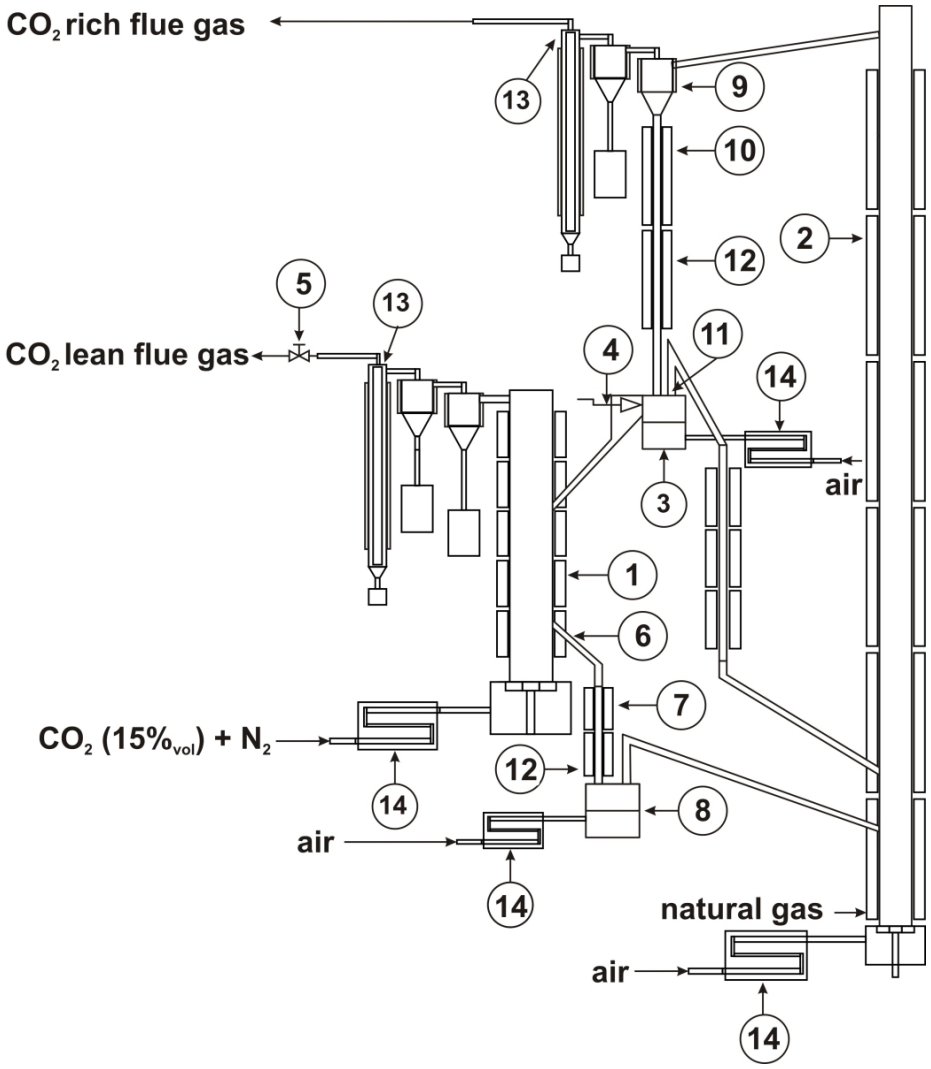

Figure 4.1: Scheme of the 10 kW_{th} IFK DFB facility operating with the riser as the carbonator and the BFB as the regenerator; (1) BFB regenerator (or carbonator), (2) riser carbonator (or regenerator), (3) double exit loop seal, (4) cone valve, (5) pressure control valve, (6) BFB overflow, (7) lower standpipe, (8) lower loop seal, (9) cyclone, (10) upper standpipe, (11) loop seal weir, (12) quartz standpipe segments, (13) candle filters, (14) electrical gas pre-heaters [33]

The reactor used as the carbonator is fluidized with CO_2 and N_2, while the other serving as the regenerator is fluidized with air or oxygen enhanced air (O_2 vol.-% 40). In addition, the loop seals are both fluidized with air. All inlet flows are controlled with dedicated mass flow controllers (MFCs) except those of the loop seals, which are controlled through rotameters. Moreover, all inlet flows are heated through dedicated electrical pre-heaters. The carbonator temperature range is between 600°C and 700°C, while that of the regenerator lies above 850°C. The desired temperature levels of the reactors and of the solid recirculation system are maintained through the operation of electrical heaters. Natural gas is supplied both to the riser and BFB, when serving as the regenerator, since heat requirements associated with calcination exceed the corresponding heater capacity. Moreover, the outlet carbonator and regenerator flows

proceed through two cyclones and a candle filter for fines removal before being emitted to the atmosphere. Finally, the quartz standpipe segments located both above the upper and lower loop seals of Figure 4.1 are utilized for measurements of solid flows, i.e. riser entrainment and cone valve discharge, respectively. In order to do so, the same methodology as in the case of the scaled cold model of Chapter 3 is applied.

4.1.2 The 30 kW_{th} INCAR-CSIC DFB facility

The INCAR-CSIC facility is shown in Figure 4.2 and consists of two circulating fluidized bed reactors: a carbonator and an air-fired regenerator [34, 138, 139]. The height of the carbonator and the regenerator is 6.5 m and 6.0 m, respectively. Moreover, both reactors have a 0.1 m internal diameter. In addition, the flue gas entering the carbonator is synthetically pre-mixed and consists of air and carbon dioxide. The carbon dioxide reacts with active calcium oxide coming from the regenerator at temperatures between 600 and 700 °C. The formed calcium carbonate is regenerated in the CFB regenerator at temperatures between 800 and 900 °C. The mixture of gases and solids leave the risers through the primary cyclones from where the solids fall through a vertical standpipe to bubbling fluidized bed loop seals. The loop seals are aerated with air and solids flow over them towards an inclined standpipe that directs them to the other reactor. The first 2.5 m of the risers and the loop seals are surrounded by electric ovens. Heat requirements in the regenerator in addition to electrical heating are covered by air-fired combustion of coal or biomass [138]. In order to extract solid samples for further analysis and measure entrainment rates a bypass of solids is located below the loop seals which divert solids to a dead volume for a certain period of time. Moreover, quartz glasses are located in the standpipe between the loop seals and the risers and are used for visual confirmation that the solid circulation rate remains stable [34, 138, 139].

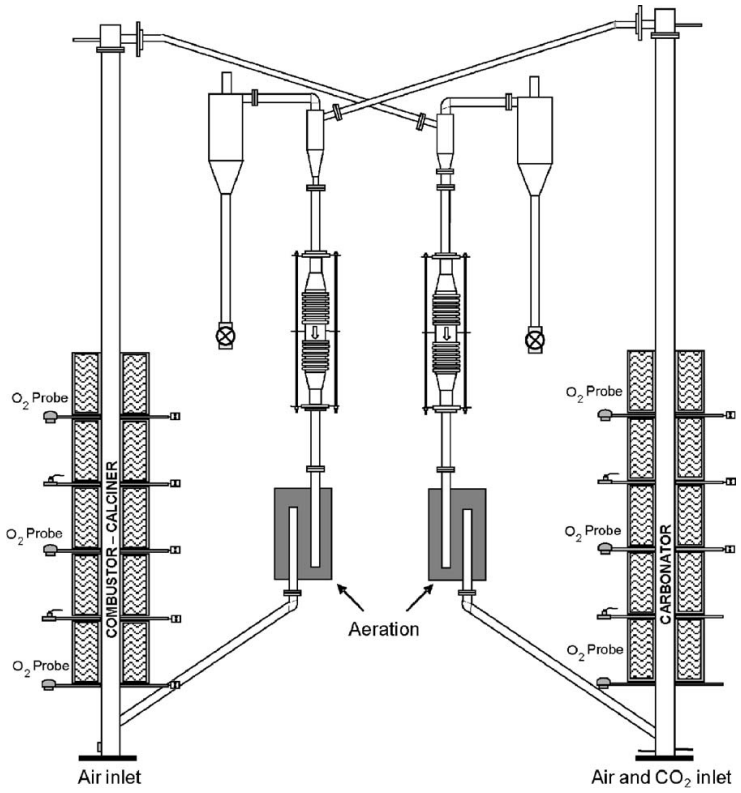

Figure 4.2: 30 kW_{th} DFB test facility at INCAR- CSIC [34, 138, 139]

4.1.3 Parameter variation & experimental setting comparison

Variables directly set during experimentation are, following the definitions of sub-section 2.4.3, either boundary conditions or independent parameters. These variables have been listed in Tables 2.3 and 2.4, while their variation range is given in Table 4.1 for three experimental settings. The first two involve the different modes of operation of the 10 kW_{th} IFK DFB facility, i.e. with use of its CFB or BFB as the carbonator (see Figure 4.1), while the third corresponds to the 30 kW_{th} INCAR-CSIC facility (see Figure 4.2). Table 4.1 can be used in conjunction with Tables 2.3 and 2.4. Hence, both the variation range and related theoretical implications of a given parameter, i.e. the way and location that it influences the system, can be understood at a glance. Moreover, Table 4.1 includes additionally the PSD of pre-calcined material used in the experiments. This is considered necessary because in all cases during the lab-scale experimentation presented here, the limestone is pre-calcined. Hence, most of the attrition occurs before the experimentation starts, i.e. during pre-calcination, as explained in sub-section 4.3.4.

Table 4.1: Parameters directly set during experimentation & range [33, 34, 83, 84, 107]

Variable	Unit	IFK (CFB)	IFK (BFB)	INCAR-CSIC
Boundary conditions				
Flue gas molar flow of CO_2 (F_{CO2})	mol/h	88-163	34-98	20-324
Flue gas vol.-% of CO_2	%	11-16	13-60*	3-25
Fuel used in the regenerator	N.A.	CH_4	CH_4	Coal (low ash & S) or biomass
Independent variables				
Related to the whole DFB system				
Initial median Particle size (d_{50})	mm	170/350	350	130/180
Initial Total Solid Inventory	kg	10-15	10-15	20-30
Loop seal velocity	m/s	Multiples of U_{mf}	Multiples of U_{mf}	Multiples of U_{mf}
Opening of mechanical valves	m^2	Adjusted to a F_{Ca}/F_{CO2} value	Adjusted to a F_{Ca}/F_{CO2} value	N.A.
Sorbent type	-	Swabian Alb limestone	Swabian Alb limestone	Two North Spanish limestones
Related to the carbonator				
Height	m	12.4	0.5	6.5
Diameter	m	0.071	0.114	0.100
Carbonator velocity	m/s	4.0-6.0	0.5-1.2	1.5-3.5
Heat transfer influence measure		El. heating & heat loss	El. heating & heat loss	El. heating & heat loss
Related to the regenerator				
Fuel dosing	kg/h	Adjusted to a T_{calc} value	Adjusted to a T_{calc} value	Adjusted to a T_{calc} value
O_2 vol.-% in the regenerator feed	%	40	40	21
Limestone make-up flow (F_0)		Batch addition	Batch addition	Batch addition

* Details of the IFK(BFB) setting runs with a CO_2 vol.-% of above 16.5 are included in Annex D; however, their analysis is beyond this thesis scope

With regard to the boundary conditions adopted for experimentation, the following can be noted. The inlet molar flow of CO_2 within the carbonator reactor is greater within the INCAR-CSIC unit since its carbonator cross sectional area is double than that of the IFK riser carbonator. Moreover, both CFB carbonators exhibit higher CO_2 throughput than when operating the IFK unit with use of the BFB as the carbonator due to the lower superficial velocity associated with the bubbling regime. The inlet vol.-% of CO_2 values utilized during experimentation with use of the 10 kW_{th} IFK facility are typical to the respective flue gas CO_2 vol.-% of coal and lignite fired

power plants. In the INCAR-CSIC case the above variable was varied within a wider range, i.e. 3-25 vol.-% of CO_2. Moreover, the fuel utilized in the regenerator has been natural gas for the IFK experimental settings and coal or biomass for the INCAR-CSIC one.

With regard to independent variables relevant to the whole DFB setting, the TSI of pre-calcined limestone utilized for facility operation in the IFK case has been in the range of 10-15 kg, while that of INCAR-CSIC is slightly larger. Moreover, loop seal fluidization had the purpose of pass through solid circulation in both facilities, while in the INCAR-CSIC case it has also an F_{Ca}/F_{CO2} regulatory function along with riser fluidization. In the IFK experimental settings the cone valve opening has been used in order to control the F_{Ca}/F_{CO2} as already explained in Figure 3.1 and 4.1. The 10 kW_{th} IFK facility has used two particle size distributions (PSDs) of a pre-calcined German limestone from the Swabian Alb region when operating under the IFK (CFB) experimental setting. Their average particle sizes were 350 μm and 170 μm. During experimentation with use of the BFB carbonator only the coarser PSD, i.e. that having a median particle size of 350 μm, has been utilized. INCAR-CSIC has carried out experiments using two different limestones from the North of Spain that presented very similar chemical behaviors with an average original particle size of 130 and 180 μm. Moreover limestones utilized by IFK and INCAR-CSIC differ with regard to their Ca purity, i.e. the North Spanish limestones are of higher purity (98 %) than that of the Swabian Alb limestone (94 %) [33, 86]. Figure 4.3 shows the decay of their maximum carbonation conversion ($X_{max,N}$) with increasing cycle number (N) as recorded with use of the INCAR-CSIC TG analyzer under same carbonation-calcination conditions. It is apparent that the decay of the $X_{max,N}$ of the German limestone is slightly more pronounced than that of the Spanish limestones [84]. Further differences can be noted between the three data sets examined. The superficial velocity within the three carbonator units is quite different, i.e. 0.5-1.2 m/s for the IFK BFB, 1.5-3.5 m/s for the INCAR-CSIC riser and 4.0-6.0 m/s for the IFK riser. Taking into account the different diameters of these reactors, too, two aspects can be highlighted. The first is that the flow of synthetic flue gases entering the INCAR-CSIC carbonator could have been produced by a firing system of 30 kW_{th}, while the corresponding firing system for the IFK riser would have been in the 10-15 kW_{th} range, while that for the BFB carbonator would have been equal to 10 kW_{th} or lower. The second aspect is that carbonators operate in neighbouring fluidization regimes, namely the bubbling (IFK (BFB)), turbulent (INCAR-CSIC) and the fast fluidization regime (IFK (CFB)). This can be identified in the fluid-dynamic regime map of Bi and Grace [140].

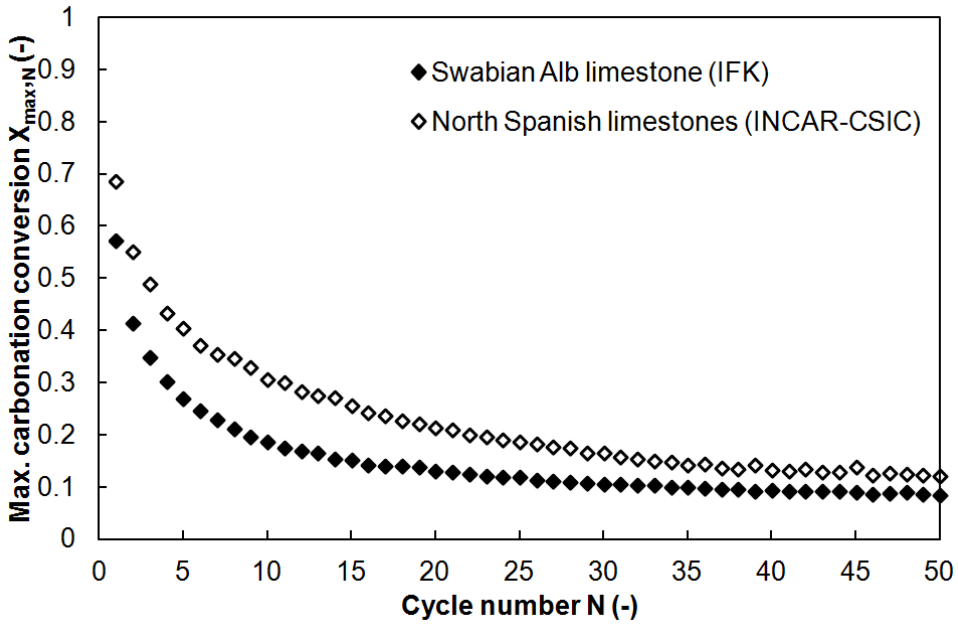

Figure 4.3: Decay of the maximum carbonation conversion, $X_{max,N}$ against the carbonation/calcination cycle number, N, for the Spanish limestones used by INCAR-CSIC and the German limestone used by IFK; carbonation conditions: 10% vol. CO_2 in air at 650ºC, calcination conditions: 10% vol. CO_2 in air at 950ºC [84]

Operation of the regenerator was conducted under oxygen-enriched conditions for the IFK case. The O_2 vol.-% of the inlet gas was 40 vol.-%. Achieving a two times higher oxygen concentration than that of air was of particular significance when operating with the BFB as the regenerator, i.e. with use of the IFK (CFB) setting. This is due to the fact that enough heat release could be achieved, while the BFB velocity did not exceed the bubbling fluidization regime range. In the INCAR-CSIC case, the regenerator was operated under air-fired mode. Full oxy-fuel regeneration foreseen for industrial Calcium looping systems has not been yet tested in these lab-scale systems.

4.1.4 Measurement techniques and respective parameter range

Since dependent variables, listed in Table 2.5, cannot be directly set without a control loop they have to be measured. Their values are derived from steady state operation periods. Such a period is defined as the situation where temperatures, pressure drops, inlet gas flows and outlet gas phase concentrations (e.g. carbonator CO_2 outlet concentration) remain constant for a time period of at least 15 minutes for both reactors of the DFB system. Table 4.2 lists the range of parameters measured or calculated after measurements, while the text below describes the measurement method. Table 4.2 has similar structure as Table 2.5 allowing the connection of the variable range with its theoretical implications. Moreover, respective measurements allow an assessment of fluid-dynamic interactions occurring within the 10 kW_{th} IFK

DFB facility itself. Measurement methods include following types (i) gas-analysis, (ii) temperature & pressure, (iii) manual and (iv) sample analysis analysis measurements.

Gas analysis measurements are conducted with use of gas analyzers and concern the carbonator, regenerator gas and the carbonator inlet gas. In the IFK case, the outlet carbonator gas CO_2 concentration is measured continuously through an ABB Advance Optima 2020 continuous gas analyzer, measuring CO_2 (0-30 vol-%) and O_2 (0- 29 vol-%) [33]. Measurements with the same analyzer at different carbonator axial positions are also possible in order to obtain a respective CO_2 profile [84]. On the other hand, the inlet CO_2 concentration is measured, with use of a sample bag which is passed through the carbonator off-gas analyzer, thus confirming the MFC flow indications. In addition, the outlet CO_2 concentration of the regenerator is also measured in the IFK case through an ABB EasyLine 3020 continuous gas analyzer, measuring CO_2 (0-100 vol-%) and O_2 (0-100 vol %). Since, the carbonator is fluidized with CO_2 and N_2, measured O_2 within the carbonator off-gas allows an exact estimation of the amount of air entering the carbonator through the two loop seals, as shown in Figure 4.1. In the INCAR-CSIC case continuous measurements of CO_2, CO and O_2 are possible from different parts of the installation. Moreover, the facility is equipped with zirconia oxygen probes to measure local O_2 concentration due to the fact that aeration in the loop seal can reach 20 % of the total flow of gas entering the risers and there is uncertainty about the path of this aeration gas [34, 138, 139]. Measurements of the outlet CO_2 vol.-% allow calculation of the average CO_2 vol.-% within the carbonator, the range of which is noted in Table 4.2. Pressure measurements are conducted with use of transducers. Such measurements allow the calculation of reactor inventories, as shown in Equation (21), and therefore the calculation of carbonator space time and the regenerator residence time. Moreover, pressure drop measurements allow the derivation of carbonator pressure profiles, as has been performed in the IFK case. Temperature measurements are conducted with use of thermocouples. They allow the calculation of the average reactor temperatures and the equilibrium CO_2 vol.-% as shown from Equation (1). Manual measurements involve solid flows, i.e. reactor entrainment and solid looping rates and the flow of fines escaping the Calcium looping facility. Measurement of the first two mentioned flows, leading to F_{Ca}/F_{CO2} derivation, has already been described within sub-sections 4.1.2 and 4.1.3. The measurement of the flow of fines escaping is realized by weighing material collected from secondary cyclones and filters. It is used for calculation of the actual facility TSI at a given moment and to quantify attrition. For the latter task, PSD measurements of the raw material, the pre-calcined material, used material after experimentation and of the fine flow exiting the system is necessary.

Table 4.2: Parameters measured during experimentation & range

Variable	Unit	IFK (CFB)	IFK (BFB)	INCAR-CSIC
Related to the whole DFB system				
Actual carbonation conversion in/after the carbonator (X_{carb})	mol_{CaCO3}/ mol_{Ca}	0.05-0.19*	0.03-0.21	0.02-0.33
Actual carbonation conversion in/after the regenerator (X_{calc})	mol_{CaCO3}/ mol_{Ca}	0.02-0.15	0-0.05	0.02-0.31
Average maximum carbonation conversion ($X_{max,ave}$)	mol_{CaCO3}/ mol_{Ca}	0.07-0.17	0.14-0.34	0.10-0.30
Ca looping ratio (F_{Ca}/F_{CO2})	mol_{Ca}/ mol_{CO2}	3-20	5-15	5-10
Related to the carbonator				
Axial pressure profile	N.A.	C-shaped	Linear	Not measured
Average CO_2 vol.-%	%	4.9-10.9	5.1-32.9	2.1-16.7
Entrainment ($G_{s\ entrainment}$)	kg/m^2s	15-20	-	1-4
Equilibrium CO_2 vol.-%	%	0.86-1.00	0.56-16.57	0.11-4.79
Fraction of active particles (f_{active})	-	0.04-0.73	0.28-0.71	0.02-0.78
Gas-solid contacting effectiveness factor (φ); average value	-	0.8	0.2	> 1
Sorbent surface kinetic constant (k_s)	s^{-1}	0.26	0.26	0.33
Space time (τ)	h	0.32-0.60	0.41-1.41	0.02-0.81
Temperature (T_{carb})	°C	646-652	651-786	570-720
Time for X_{calc} to reach $X_{max,ave}$ (t*)	s	12.0-126.2	188.6-303.3	3.1-125.5
Related to the regenerator				
Velocity	m/s	0.5-1.2	5-6	1.5-3.5
Entrainment	kg/m^2s	-	15-20	1-4
Partial pressure of CO_2	bar	< 0.3	< 0.3	< 0.3
Regeneration efficiency	%	0.15-0.97	0.61-0.98	0.04-0.94
Residence time		1-5 min	1-5 min	1-5 min
Temperature (T_{calc})	°C	900	850-900	900

* The fact that the X_{carb} the upper range exceeds that of the $X_{max,ave}$ denotes the sensitivity of respective measurements

The properties of the samples removed from the carbonator and the regenerator, i.e. X_{carb}, X_{calc}, k_{sA}, k_{sB} and $X_{max,ave}$, are determined through TG analysis tests [33, 34, 84]. Derivation of X_{carb} and X_{calc} is rather simple and is conducted through a weight measurement of a sample prior to and after full calcination. The $X_{max,ave}$ is derived according to its definition (see subsection 2.3.2) as is demonstrated in Figure 4.4, i.e. through determining the conversion point at which the reaction rate of a given sample

shifts from the fast to the slow reaction regime. Finally the k_{sB} is also defined from Figure 4.4 and Equation (3) when (i) substituting $X_{max,N}$ with $X_{max,ave}$ and (ii) approximating the reaction rate term with the ratio of $X_{max,ave}$ and t*´ which is the time needed for the sample of Figure 4.4 to reach $X_{max,ave}$ from a zero conversion value. The k_{sA} is calculated in the same way the only difference being that Equation (2) is used to describe the reaction rate. The definition of $X_{max,ave}$ and k_s values has been conducted after full calcination of the original samples coming from the IFK (CFB) and INCAR-CSIC experimental settings. This is also the reason behind the use of the symbol t*´ instead of t* in Figure 4.4, where t* corresponds to the original samples taken from the carbonators and t*´ to the same samples after full calcination. Full calcination of the samples has been realized since X_{carb} has been found too close to $X_{max,ave}$ for a large number of samples, especially in the case of the IFK (CFB) setting, thus making it difficult or impossible in some cases to estimate a k_s values from the original sample removed from the carbonator. Hence, the $X_{max,ave}$ derived from the IFK (CFB) and INCAR-CSIC settings is smaller than the value of the original sample because the natural trend of sorbent deactivation with increasing number of cycles. However, this difference can be ignored due to the typically low values of $X_{max,ave}$. In contrast to the IFK (CFB) and INCAR-CSIC experimental settings, the $X_{max,ave}$ of the IFK (BFB) setting has been derived from the original sample. The fact that samples from the IFK (CFB) exhibit an X_{carb} that is closer to $X_{max,ave}$ than the samples of the other experimental settings can be explained from the larger carbonator particle residence times of this experimental setting, as can be derived from Table 4.2. The TG analyses required for the above measurements have been conducted from INCAR-CSIC in Spain for samples coming from the IFK (CFB) and INCAR-CSIC experimental settings. Fewer samples related to the IFK (BFB) experimental setting have been analyzed from the Technical University of Munich (TUM).

At this point it is useful to comment upon the measured entrainment rates listed in Table 4.2 and on the parameter range associated with the regenerator reactor of the three experimental settings. Commenting upon the range of all other parameters of Table 4.2 is omitted in this sub-section since this is performed through the analysis presented in the following sections and sub-sections. The different fluidization regimes at which the carbonators operate justify the large differences in riser entrainment values, i.e. no entrainment for the IFK (BFB) carbonator, 1-4 kg/m^2s for the INCAR-CSIC carbonator and 15-20 kg/m^2s for that of the IFK (CFB) experimental setting. Differences in the entrainment rates of the regenerator reactors are explained in the exact same way. However, in the case of the carbonator reactors the differences in their entrainment rates underline the differences in their axial pressure profiles (see 3.13) and therefore differences in their gas-solid contacting quality. Moreover, the

differences in the entrainment rates between the IFK facility riser and the risers of the INCAR-CSIC facility justify the design decision to include or not an internal solid circulation loop (see Figures 4.1 and 4.2). Hence, in the case of INCAR-CSIC the $G_{s\ entrainment}$ provides for suitable F_{Ca}/F_{CO2} values and therefore a solid split mechanism is not needed. On the other hand, in the case of the IFK settings the F_{Ca}/F_{CO2} value would go up to 40, if no solid split mechanism had been utilized, as has been predicted from cold model experimentation (see Figure 3.12a and 3.12b).

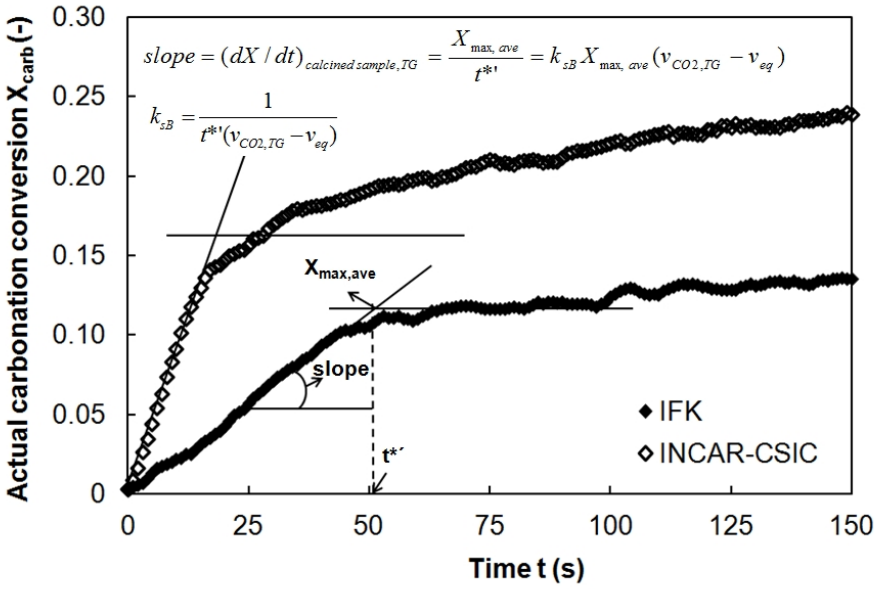

Figure 4.4: Average maximum carbonation conversion ($X_{max,ave}$) and reaction constant, k_{sB}, derivation for a calcined INCAR-CSIC and IFK sample removed from the CFB carbonators during operation; carbonation conditions: 10 vol.-% CO_2 in air at 650ºC [84]

Although the regenerator (calciner reactor) is not the primary focus of this thesis, it is worth to note that the regenerator conditions, shown in Table 4.2, can influence the carbonator reactor performance, not only through the obvious impact on calcination conversion, but trough the possible deactivation phenomena influencing the sorbent maximum carbonation conversion. Calcination atmosphere and temperature are similar in the three experimental settings, i.e. the partial pressure of CO_2 is below 0.3 bar, while the regeneration temperature has been around 900°C. Finally, the residence time within the regenerator which is crucial for sorbent regeneration has been in the range of 1 to 5 minutes in all cases.

4.2 Steady state Dual Fluidized Bed operation

Realization of DFB operation in the 10 kW_{th} IFK and the 30 kW_{th} INCAR-CSIC DFB systems of Figure 4.1 and 4.2 proved to be very straightforward. Achieving a steady state is met with relative ease and the only intervention after some hours of operation is the addition of small amounts of limestone to maintain a constant reactor inventory since some is lost over time due to attrition. Data from hundreds of hours of steady state operation have been achieved with use of the 10 kW_{th} IFK facility and the 30 kW_{th} INCAR-CSIC facility, respectively. They are utilized for discussion and extracting conclusions within the sections below. An example of a 2 h steady state, utilizing the 10 kW_{th} IFK facilty and its BFB as the carbonator, is shown in Figure 4.5. The reactor temperature and inlet CO_2 volumetric percentage are 660 °C and 15 vol-%, respectively. Since the outlet CO_2 volumetric percentage is below 1 %, the resulting CO_2 capture efficiency (E_{carb}) is constantly above 90 %. Fresh pre-calcined bed material and excess bed material, removed from the DFB system during solid sampling, were occasionally added to the carbonator, as shown in Figure 4.5. The input of this "cold" bed material resulted in dips in the carbonator temperature and led to CO_2 capture efficiencies as high as 97 %.

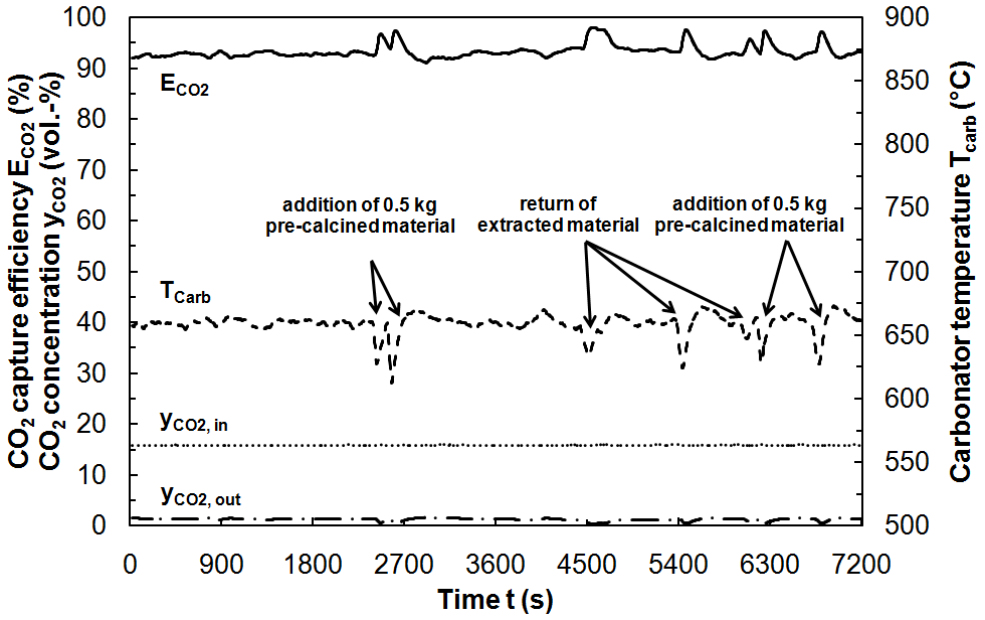

Figure 4.5: Example of a high CO_2 capture efficiency (E_{carb}) steady state: carbonator temperature (T_{carb}), inlet and outlet vol.-% of CO_2 (ν_{CO2}) and E_{carb} are plotted vs. time at a space time (τ) of 1.41 h and a Ca looping ratio (F_{Ca}/F_{CO2}) of 16.8 with use of the BFB as the carbonator

4.3 Results & Discussion I: Mass balances closure and variable behavior

The experimental closure of the carbon mass balances with regard to the carbonator supports the credibility of the results and allows for the extraction of important conclusions. This is straightforward in the case of Equations (7) and (8), since the product $F_{CO2}E_{carb}$ is known through gas analysis, F_{Ca} is measured manually and the solid properties of $X_{max,ave}$, X_{carb} and X_{calc} are derived through the TG analysis of sub-section 4.1.4 for every steady state. On the other hand, the degree to which the experimental data agree with the carbonator design mass balance equation, i.e. Equation (6), cannot be demonstrated directly but through its simplified expressions of Equation (10) and Equation (12). Since, it is considered reasonable that a number of aspects related to the right hand side of these expressions are discussed first, the respective fitting of the experimental data is carried out within section 4.5.

The right and left hand side of the CO_2 mass balance postulated in Equation (7) are plotted against each other in Figure 4.6, after being divided by the respective carbonator cross-section, for experiments conducted at the facilities of IFK and INCAR-CSIC. Points from the 10 kW_{th} IFK DFB facility have been achieved with use of both experimental settings, i.e. utilizing both the riser and the BFB as the carbonator during different experiments. The term of $F_{CO2}E_{carb}/A_{carb}$, represents the cross-section specific rate of CO_2 disappearance from the gas phase, while that of $F_{Ca}(X_{carb}-X_{calc})/A_{carb}$ expresses the cross-section specific rate of $CaCO_3$ increment within the Ca flow (F_{Ca}) after the reactor exit. The majority of the points fall in the vicinity of the 45° line thus demonstrating the accuracy of the gas-solid analysis performed leading to a good closure of the carbon mass balance. This is particularly true for the experiments conducted at the 10 kW_{th} DFB facility with use of the BFB carbonator, while somewhat greater deviation exists in the other data sets utilizing a riser carbonator. This is explained based on the larger sorbent flows circulating between the beds in the case of riser carbonator experiments and the associated difficulties with the manual measurement of the F_{Ca} parameter. The CO_2 capture rates are the largest in the case of the IFK experiments utilizing the riser as the carbonator, followed by those conducted at INCAR-CSIC, while experiments conducted at the IFK BFB carbonator exhibit the lowest CO_2 capture rates. This is justified based on that the three carbonators operate at fluid-dynamic regimes which correspond to different operating velocities, as shown in Table 4.1. A number of experiments, realized with the IFK carbonator riser operating in the fast fluidization regime, have achieved high CO_2 capture rates per unit cross-section of the riser which are closer to what is expected for large-scale application, i.e. > 6 mol/m^2s.

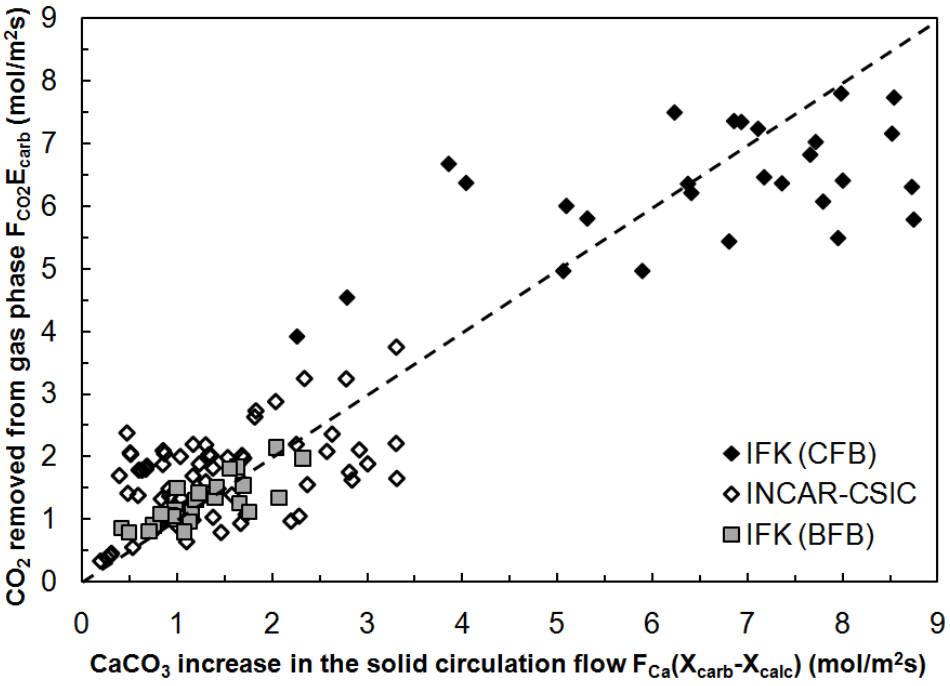

Figure 4.6: Experimental comparison between the CO_2 removed from the gas (mol/m^{2}s) in the carbonator and the $CaCO_3$ formed (mol/m^{2}s) in the solid circulating stream for IFK and INCAR-CSIC facilities; graphical representation of Equation (7) for all experiments

The validity of the experimental results is further expressed through plotting the two terms of the inequality of Equation (8) in Figure 4.7, after a minor rearrangement of terms, as has also been shown by Rodríguez et al. [34]. The variable of the x-axis, $F_{Ca}(X_{max,ave}-X_{calc})/F_{CO2}$, represents the active flow of CaO per mol of CO_2 entering the carbonator. The inclined line in Figure 4.7 represents the theoretical case where the two sides of Equation (8) would be equal and hence the supply of active Ca and the CO_2 captured would be of stoichiometric proportion. Since most of the points, from all three experimental settings, lie close to the solid line, Equation (8) is adequately fulfilled. Points on the left of the line do not conform to Equation (8) and can be explained based on the errors in the determination of the Ca looping ratio (F_{Ca}/F_{CO2}) and problems of representativeness of the solid samples analyzed. Experimental points having an E_{carb} value which deviates significantly from the equilibrium value, depicted in Figure 4.7 through the horizontal line, despite having $F_{Ca}(X_{max,ave}-X_{calc})/F_{CO2}$ greater than E_{eq} correspond to steady states where there is insufficient Ca inventory or where gas-solid contacting limitations become significant. For points where the $F_{Ca}(X_{max,ave}-X_{calc})/F_{CO2}$ is smaller than E_{eq}, the CO_2 capture efficiency is mainly limited from the quantity of active CaO flow entering the carbonator, as indicated from the inclined line. Such situations can occur due to low Ca looping ratio values (F_{Ca}/F_{CO2}), low $X_{max,ave}$ and low regeneration efficiency and hence high X_{calc} values. The behavior of these two last variables is analyzed in sections 4.3.1 and 4.3.2 below.

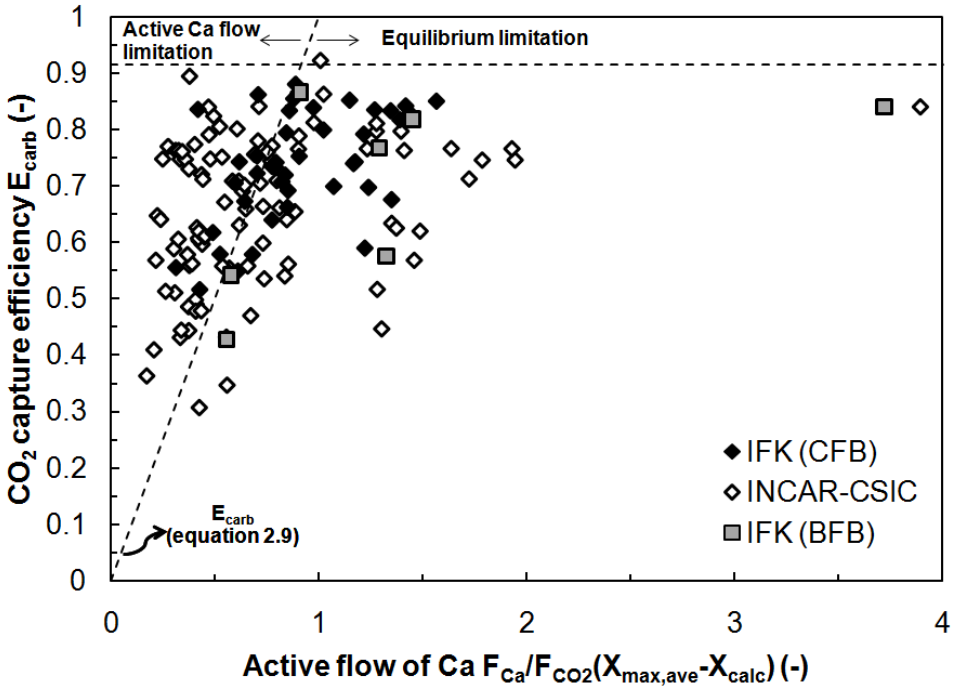

Figure 4.7: The equilibrium normalized CO_2 capture efficiency vs. the active molar flow of Ca per mol of incoming CO_2; graphical representation of Equation (8) for all experiments

4.3.1 Decay of the average maximum carbonation conversion ($X_{max,ave}$)

The estimation of the reaction rate term of the design Equation (6) uses experimentally determined values of the sorbent activity, $X_{max,ave}$, as shown in Equations (10) and (12) that are different for each sample. Through experimental derivation of the $X_{max,ave}$ values, the difficulty of their estimation through a particle population balance in these small facilities is overcome. As experiments progress in time, there is a gradual drop in the maximum average carbonation conversion of the material due to particle deactivation, related to the increasing number of carbonation-calcination cycles that the average particle has experienced in the system. In future large scale facilities the average activity will not change with time due to the continuous supply of fresh limestone, which is absent in the experiments conducted here. As noted, appropriate equations for the calculation of $X_{max,ave}$ in such systems have been recently proposed [102,103]. The evolution of the $X_{max,ave}$ during the course of long duration experiments, when using the IFK (CFB) and the INCAR-CSIC setting is presented in Figure 4.8.

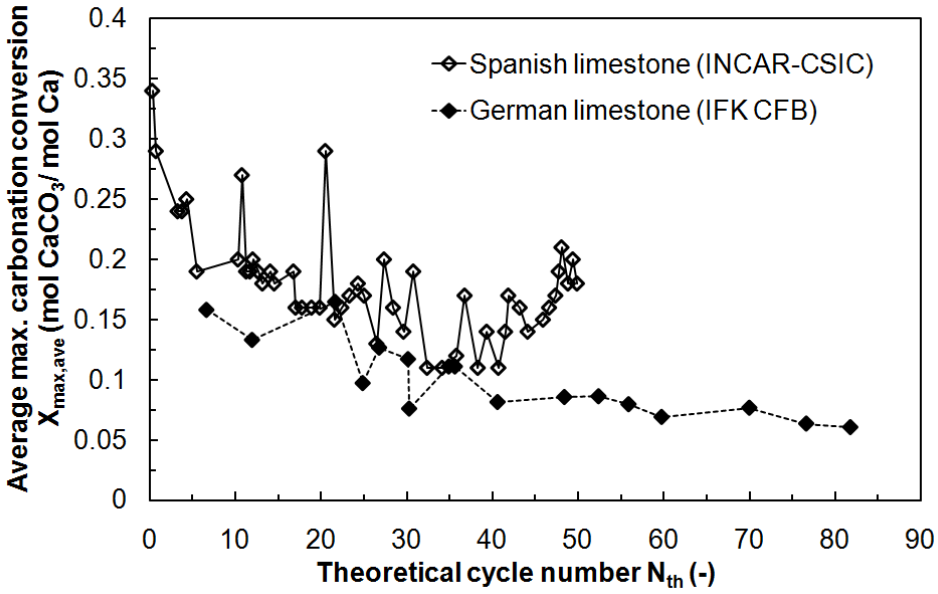

Figure 4.8: The decay of the average maximum carbonation conversion ($X_{max,ave}$) with increasing theortical cycle number (N_{th}) for steady states with carbonator temperature (T_{carb}) of 650°C, regenerator temperature (T_{calc}) of 900°C, an inlet vol. CO_2 concentration (ν_{CO2}) of 11.4 vol.-% (IFK) and 16.5 vol.-% (INCAR-CSIC) , and a regenerator residence time (t_{reg}) of 1-5 min.

Moreover, the theoretical number of cycles (N_{th}) is plotted in the x-axis and is given in Equation (33).

$$N_{th} = \int_0^t \frac{F_{CO2} E_{carb}(t)}{n_{Ca,total} X_{ave}} dt \qquad (33)$$

Where $E_{carb}(t)$ represents the instantaneous CO_2 capture efficiency, while $n_{Ca,total}$ stands for the total inventory in the DFB system. Since the $X_{max,ave}$ is measured at different time points, its value is considered constant between these points. The product, $F_{CO2}E_{carb}(t)$, is calculated through gas analysis, while the total calcium moles are known through measurements of the initial bed inventory and of the solids extracted from the system at different time points. The N_{th} expresses how many times the moles of CO_2 captured could carbonate the bed inventory ($n_{Ca,total}$) up to its average maximum carbonation conversion ($X_{max,ave}$). For a given theoretical cycle number, the INCAR-CSIC limestone samples exhibit slightly better average maximum carbonation conversion than that of IFK. This can be attributed to the better deactivation characteristics of the INCAR-CSIC limestone in comparison to that of IFK, as shown in Figure 4.3. Two further remarkable conclusions can be drawn from the same figure. The first is that it has been impossible in both installations to conduct experiments with highly active CaO, i.e. having a maximum carbonation conversion greater than 0.3 mol $CaCO_3$/mol Ca, as has been recorded during the TG experiments of Figure 4.3. Clearly, it is quite challenging to maintain the activity of the material during the first

calcination of the limestone batch. This was already noted in experiments conducted in batch mode [61] where it was speculated that the long times required for calcination of the initial limestone batch (hours) resulted in a higher effective carbonation/calcination number for the sorbent particles. The above speculation is reinforced when considering that the residence times utilized for pre-calcination of the initial batch of solids were in the range of a few hours for both INCAR-CSIC and IFK. The second is that the residual activity attained by the solids as the theoretical cycle number increases, shown in Figure 4.8, is remarkably close to the one measured in the TG test of Figure 4.3. Hence, in both Figure 4.3 and 4.8, the residual activity is around 0.1 and 0.07 mol $CaCO_3$/mol Ca for the INCAR-CSIC and IFK case, respectively. High values of CO_2 capture could be maintained also when operating with values of $X_{max,ave}$ close to the residual activity provided that the Ca looping ratio (F_{Ca}/F_{CO2}) was such, in order to account for a product of $F_{Ca}/F_{CO2}X_{max,ave}$ approximately equal or greater than 1, as indicated in Figure 4.7. Finally, the positive deviation of the $X_{max,ave}$ decay curve in the case of INCAR-CSIC, observed at a theoretical number of cycle of above 30, is attributed to the addition of 1 kg batches of fresh pre-calcined or used sorbent recovered from the secondary cyclones, as a result of primary cyclone malfunctions [86].

4.3.2 Dependence of the X_{calc} on regenerator operation

The carbonation conversion of the particles in/after the regenerator (X_{calc}) is linked to the regeneration efficiency (η_{reg}), as shown in Equation (9), and is influenced from regenerator conditions. An X_{calc} value close to zero is important for carbonator operation since it minimizes the Ca looping ratio for a given active flow of Ca, as shown in Equation (8), and increases the reaction rate of the carbonator bed, (see Table 2.5). For a constant regenerator temperature (T_{calc}) and partial pressure of CO_2 ($p_{CO2,calc}$), the regeneration efficiency, and hence the $X_{calc,}$ has been found to correlate to a single parameter as shown in Figure 4.9 and 4.10, respectively. Its definition is given through the ratio of the carbonation conversion of the particles entering the regenerator (X_{carb}) and the residence time of the average particle within the reactor (t_{reg}) [107].

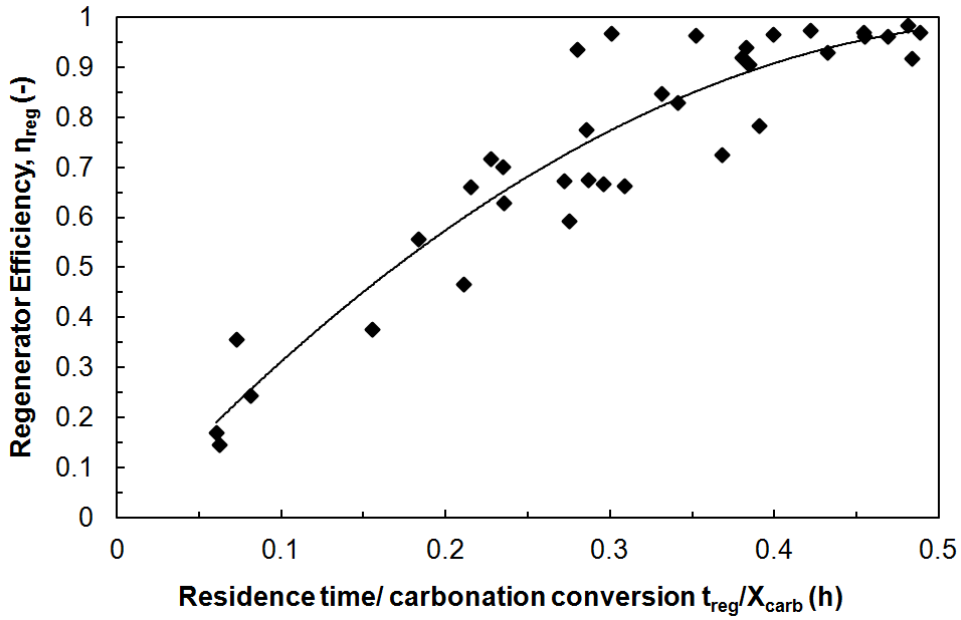

Figure 4.9: Regenerator efficiency (η_{reg}) against the characteristic parameter of t_{reg}/X_{carb} ; t_{reg}= 900°C, p_{co2}< 0.3 bar, d_p= 100-300 µm and d_p= 300-600 µm

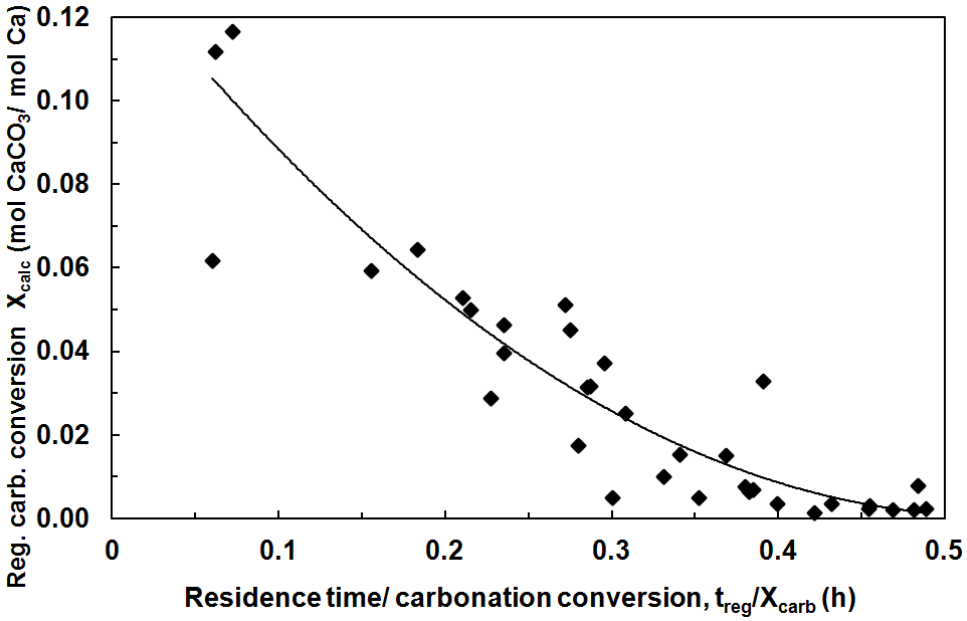

Figure 4.10: Actual carbonation conversion in/after the regenerator against the characteristic parameter of t_{reg}/X_{carb} ; t_{reg}= 900°C, p_{co2}< 0.3 bar, d_p= 100-300 µm and d_p= 300-600 µm

The regenerator efficiency increases, while the corresponding X_{calc} value decreases, when the ratio t_{reg}/X_{carb} is increased. This trend can be physically explained based upon that an increment of the (t_{reg}/X_{carb}) results to an increasing level of difficulty imposed on the regenerator reactor in order to fulfill its task. This is true since increasing the carbonation conversion X_{carb} of the incoming particle stream increases the quantity of

the $CaCO_3$ to be regenerated. On the other hand, reducing the average residence time of the particle in the regenerator, limits the exposure of the particle to calcination conditions. Although the η_{reg} and X_{calc} correlates with the t_{reg}/X_{calc} ratio well, it is unfortunate that regenerator conditions (see Tables 4.1 and 4.2) are different than those in industrial Ca looping regenerators working under oxy-fuel conditions, i.e. partial pressure of CO_2 above 0.7 bar and a regenerator temperature >900°C. However, two important messages can be derived from Figures 4.9 and 4.10: (i) that t_{reg}/X_{calc} may provide a similarly good but quantitatively different correlation under oxy-fuel conditions and (ii) the conditions of experimentation are those of an air-fired regenerator, close to the respective unit found in Ca looping processes for gasification applications such as the AER process [59, 78]. In such a case,a t_{reg}/X_{carb} > 0.4 h is expected to lead to almost full regeneration. Hence, according to Figures 4.9 and 4.10, a sorbent particle with a typical X_{carb} value of 0.1 mol_{CaCO3}/ mol_{Ca} will achieve an $\eta_{reg} \rightarrow 1$ and a $X_{calc} \rightarrow 0$ after 2.4 min. Such a residence time is easily accommodated in an FB regenerator, as suggested in the Calcium looping schematic of Figure 1.4 [11].

4.3.3 Axial pressure & CO_2 profiles

The carbonator Ca solid inventory, n_{Ca}, is a dependent variable of primary importance for carbonator operation, as shown by Equation (6). As noted, when there are no other solids in the system, other than CaO or $CaCO_3$ (as is the case in the experiments at INCAR-CSIC and IFK), it can be estimated from the pressure drop measurements in the reactors, as shown in Equation (21), and the carbonate content measured during the analysis of solid samples. The carbonator riser solid loadings have been in the range of 200-500 kg/m^2 and 560-1170 kg/m^2 for the INCAR-CSIC and the IFK (CFB) setting, respectively. This corresponds to a pressure drop between 20-49 mbar for the INCAR-CSIC carbonator riser and 55-115 mbar for the IFK one. In the case of the IFK (BFB) setting, corresponding ranges of the above variables for the BFB carbonator reactor are lower, i.e. 183-397 kg/m^2 and 18-39 mbar.

In the case of the riser carbonators, the distribution of the n_{Ca} is not uniform, as indicated already in Chapter 3. Due to this reason and based on that the carbonation reaction rate decreases as CO_2 is captured, the local CO_2 capture efficiency will vary with carbonator height as indicated by Equation (6). As noted, in the case of experiments conducted with the IFK (CFB) setting, it has been possible to determine the axial pressure profile and axial CO_2 profile along the riser carbonator, as shown in Figure 4.11.

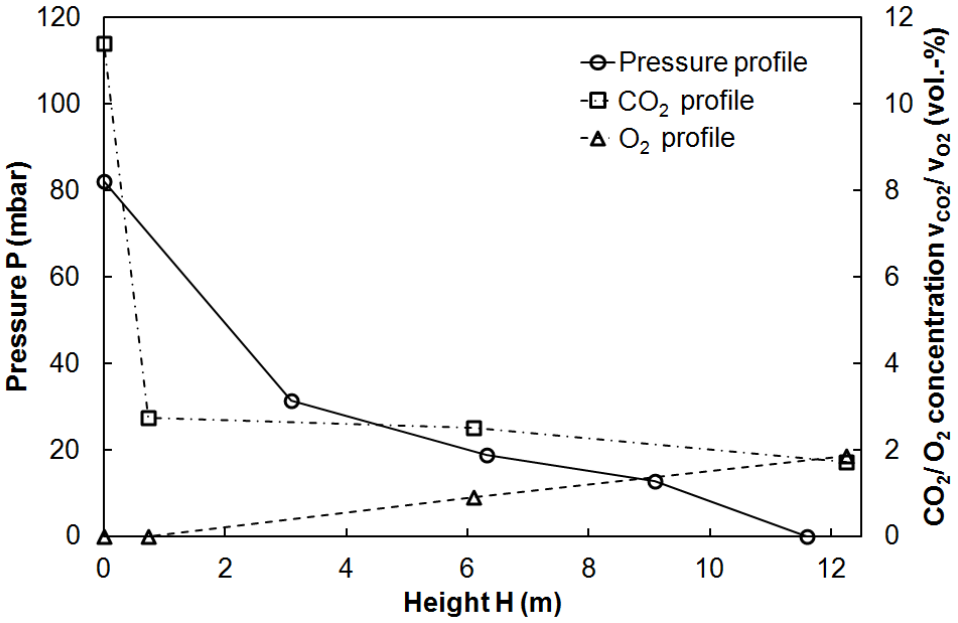

Figure 4.11: Pressure profile, axial CO_2, O_2 profile for the IFK carbonator riser. Conditions: inlet CO_2 concentration 11.4 vol.-% (rest N_2), O_2 source is air from the loop-seals entrances at 1 and 1.2 m, median particle size ($\overline{d_p}$) 340µm, superficial velocity 5.9 m/s, temperature 650°C, Ca looping ratio16.7, $X_{max,ave}$ 0.065 mol $CaCO_3$/mol Ca, CO_2 capture efficiency 0.84 and equilibrium normalized CO_2 capture efficiency 0.93

The distinct fluid-dynamic regions, also noted when analyzing the cold model riser profiles presented in Chapter 3, are demarcated by their different pressure drop gradients and solid fraction values (ε_s). The lean core-annulus region, exhibits a pressure drop gradient of ca. 3.1mbar/m corresponding to a solid fraction between 0.01-0.02. As is typical for this region the pressure drop gradient and therefore the solid fraction is higher at the bottom than at its top. At the top of the riser, the exit region is observed, having an increased pressure drop gradient and solid fraction value approximately equal to 5 mbar/m and 0.03, respectively. This densification of the solid flow at the top of the riser is due to its abrupt riser exit. As noted, this fluid-dynamic region is typical for small scale risers and is absent in large scale systems, unless a significant constriction is applied to the flow [74]. The dense region, located at the bottom of the riser exhibits the highest pressure drop gradients and solid fraction values. The dense region is contained within the first 3 m, as indicated by the corresponding measurement. The exact border of the dense region has not been obtained, since this would require a greater number of pressure measurements within this section. Assuming the typical solid fraction value of 0.2 for the dense region, its height is found equal to 1.2 m. Based on the same reasoning, the dense region height can reach values of above 2 m, when operating the riser with high solid loadings, i.e. > 1000 kg/m^2. As indicated by the axial CO_2 profile of Figure 4.11, the CO_2 vol.-% reduces from 11.40 % at the carbonator entry to 2.74 % at an axial riser height of only

0.73 m, i.e. within the dense bed region. When taking into account a total of 32 IFK steady states, conducted with axial CO_2 profile measurements, it can be noted that the CO_2 capture efficiency realized in the first 0.73 m of the dense region is always greater than 80 % of the total carbonator CO_2 capture efficiency. Hence, it is clear that the dense region plays the biggest role in terms of CO_2 capture. However, the importance of the lean-core annulus and exit regions must not be underestimated. Taking into account the axial CO_2 profile of Figure 4.11, it must be noted that the reduction of the CO_2 vol.-% from 2.5 % (measured at a riser height of 6 m) to 1.7 % (measured at the riser exit) corresponds to a CO_2 capture efficiency increase of 5.8 %, between these two axial heights. Therefore, the fluid-dynamic regions above the dense region can be considered as the polishing step in order to bring the CO_2 capture efficiency close to the equilibrium value, provided that there is enough active CaO in the reactor, as in the case of Figure 4.11. Furthermore, since the loop seals of the IFK facility and pressure measurement ports have been supplied with air, while the carbonator is fluidized with N_2 and CO_2, O_2 is detected in the carbonator riser at small percentages, i.e. < 2%. The O_2 vol.-% at the carbonator off-gas is higher than that measured at 6 m because of the mixing of the riser gas with air travelling up the standpipe. Additional reasons can be found in that pressure port purge air enters the riser at different axial points and that CO_2 capture is taking place between the height of 6 m and the riser exit. No O_2 is measured at 730 mm, since the loop seal return leg entrances come into the riser at axial heights of 1 and 1.2 m. Combining the above observations, which indicate that no gas back-mixing takes place, with the good match of the CO_2 profile with the pressure profile supports the assumption that the carbonator riser can be considered as a plug-flow reactor for the gas.

In contrast to Figure 4.11, the solid fraction within the BFB carbonator can be considered constant between the distributor and the solid overflow located at 0.5 m. Above this height, the freeboard starts which can be considered solid free. The variation of the solid fraction with carbonator velocity is depicted in Figure 4.12. Since the BFB is equipped with an overflow the change in solid fraction leads to a proportional change in the solid inventory, n_{Ca}. Other than this interdependence, the BFB carbonator n_{Ca} does not depend on any other parameter, thus allowing for almost independent space time setting through variation of the molar flow of CO_2 (F_{CO2}) entering the carbonator.

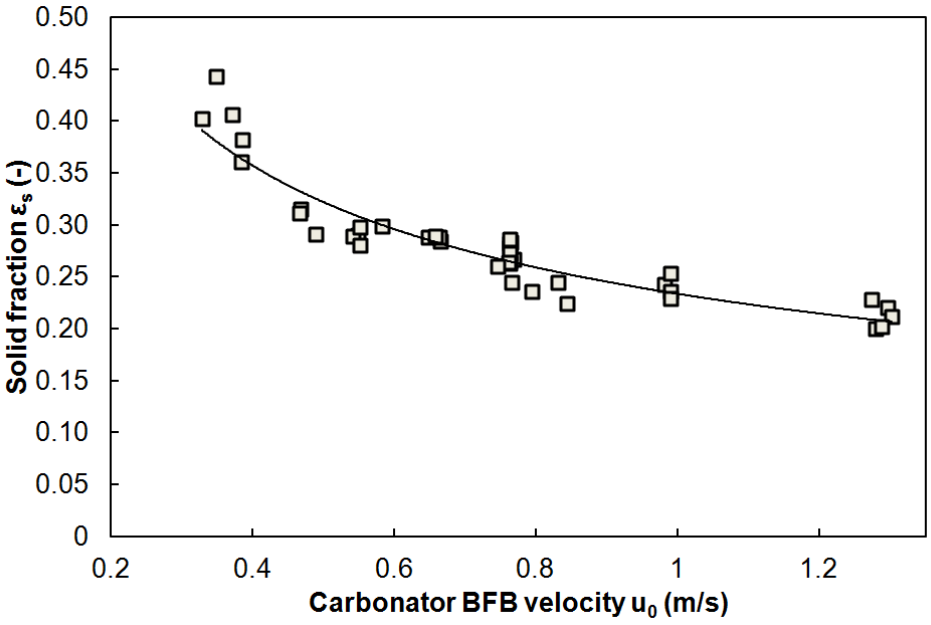

Figure 4.12: BFB carbonator solid fraction variation against superficial velocity (u_0) for all IFK(BFB) experiments

At the velocity of 0.4 m/s the BFB carbonator exhibits a solid fraction near 0.4 which is typical for the bubbling fluidization regime. Velocity increment resulted in decreasing solid fraction values, which followed the trendline of Figure 4.12 to a satisfying extent. This can be explained based on the well documented fact that bubble size increases with increasing superficial velocity [74]. At 0.8 m/s the solid fraction of 0.3 reported still seems reasonable for a BFB reactor; however the solid fraction of approximately 0.2 measured at a velocity of 1.2 m/s indicates that the fluidization behavior of the reactor approaches that of the turbulent regime. As expected for a BFB reactor, little carryover has been measured, occurring at the higher velocity values of Figure 4.12.

4.3.3.1 10 kW_{th} IFK DFB facility & cold model comparison

The successful operation of the carbonator riser presented above, when operating under the IFK (CFB) setting, and the fluid-dynamic analysis of Chapter 3 allow for a brief comparison between the cold model and the actual 10 kW_{th} IFK DFB riser carbonator profiles and operation. The cold model predictions were verified in the 10 kW_{th} IFK DFB facility with regard to the following aspects:

i. **Riser operating velocity range:** The applied riser velocity in the 10 kW_{th} IFK DFB facility was in the range of 4-6 m/s, as shown in Table 4.1. The predicted

riser operating velocity obtained through cold model experimental results of Figure 3.3a and 3.3b and the scaling criteria of Equation (16) was 3.5-5.3 m/s.

ii. **Total Solid Inventory (TSI) required for facility operation:** The actual TSI was 10-15 kg, as given by Table 4.2. The range predicted from the cold model was 9-16 kg, as also shown from Equation (16) and Figures 3.3a, 3.3b.

iii. **Riser flow structure:** In both units the riser flow structure has been shown to be of the dense, lean core-annulus, exit region flow structure type, as shown in Figure 3.6 and 4.11. Table 4.3 notes the ranges of the measured solid fractions of the three fluid-dynamic regions for the cold model and actual IFK (CFB) setting carbonator riser in comparison to the equivalent values expected in a CFBC. However, the accuracy of these values is to be treated with some caution since, as can be easily understood, the mounting positions of the pressure transducers does not necessarily coincide with the region borders.

Table 4.3: Comparison of ε_s of cold model, 10 kW_{th} IFK DFB and CFBC riser

Value	Dense bed region	Lean core-annulus region	Exit region
Cold model riser	0.1-0.22	0.01-0.025	0.01-0.07
10 kW_{th} IFK DFB riser	in the range of 0.2*	0.01-0.02	0.02-0.03
Commercial CFBC [131]	< 0.2	< 0.01	

* An exact determination was not possible since the pressure transducer connection points do not coincide with region limits. Value given is plausible based based on the pressure drops measured.

The values listed in Table 4.3 show that similar ε_s values are expected with regard to the dense bed region in all cases. However, the assessed dense bed height of the actual carbonator, i.e. around 2 m for a riser pressure drop of a 100 mbar, is slightly higher than that predicted, i.e. below 1.5 m, from cold model visual observations. The ε_s value for the lean-core annulus region is similar for the actual 10 kW_{th} riser carbonator and its cold model. Values measured within these units are significantly higher than those of a CFBC. This can be explained to a point due to the difference of scale and in that the carbonator riser is operated with high pressure drop during IFK experimentation. The noted deviation with regard to the ε_s values of exit region between the actual 10 kW_{th} IFK DFB carbonator riser and its cold model is not clearly understood. However, this is considered to be a deviation of minor significance, since the exit region is absent in large-scale units, as is shown in Table 4.3, and is limited in length. Hence, the difference between the 10 kW_{th} IFK DFB facility and its cold model can be summarized in that for a given carbonator loading cold model predictions involved a higher solid density in the

exit region and a “shorter” dense region. Therefore, it can be claimed that a high degree of similarity is present between the flow structures of the 10 kW_{th} IFK carbonator riser and its cold model. In addition, when comparing the common aspects between the fast fluidized CFB carbonator and the CFBC combustor, i.e that (i) operating velocities are similar, (ii) particle sizes are similar and of the Geldart B size, (iii) a dense bed-lean core-annulus, exit region exists, and despite that the carbonator has a lean core-annulus region of higher solid density, it can be claimed that CFBC and fast fluidized CFB carbonator fluid-dynamics exhibit a high degree of resemblance. Therefore, as noted, CFBC design is a basis for CFB carbonator design.

iv. **Effect of carbonator inventory on its pressure profile:** The increment of mass availability within the carbonator results by definition to an increment of riser pressure drop, as shown by Equation (21). The effect of doing so with use of the IFK 10 kW_{th} DFB carbonator riser is presented in Figure 4.13. The pressure profiles depicted in Figure 4.13 have been recorded for runs realized under different carbonator inventories and same other conditions.

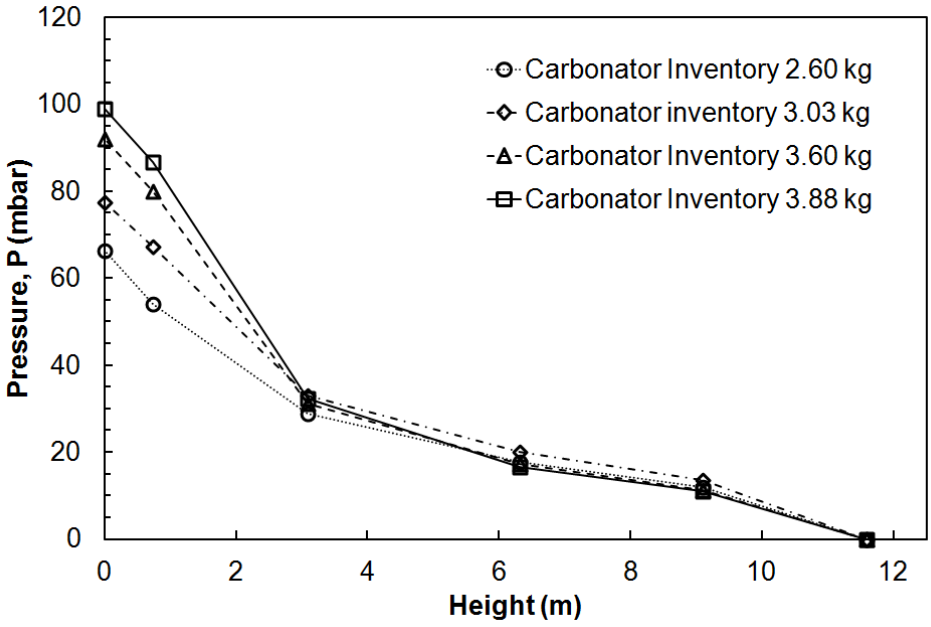

Figure 4.13: Effect of carbonator inventory (mass availability) on riser pressure profile; u_0= 5.75 m/s, $\overline{d_p}$ = 340 μm

The pressure drop readings between the axial section 3.09-12.13 m, as shown in Figure 4.13, remain practically unchanged. However, the increment of the riser pressure drop causes an increase of the pressure drop within the axial section 0-3.09 m of the same magnitude, as can be seen in Figure 4.13. The mechanism of

mass accumulation in the dense bed of the riser carbonator when increasing $\Delta P_{riser\text{-}carb}$ can be summarized in that the height of the dense bed is increased. All aspects of the above behavior are in agreement with the cold model predictions, as is evident from Figures 3.7-3.9. A further common aspect between the cold model and the 10 kW_{th} facility can be extracted from Figure 4.13. Since, the pressure near the exit of the carbonator, i.e. at a riser height of 9 m, does not change with increasing carbonator inventory, it can be claimed, as depicted in 3.13, that the latter parameter does not significantly affect the riser entrainment either. This is also in agreement with cold model experimentation as is demonstrated in of Figures 3.12a and 3.12b.

v. **Effect of carbonator velocity on its pressure profile**: The effect of velocity on the riser pressure profile of the 10 kW_{th} IFK DFB facility is presented in Figure 4.14 for two runs conducted with different superficial velocities, i.e. 5.12 m/s and 5.98 m/s while other parameters were kept constant.

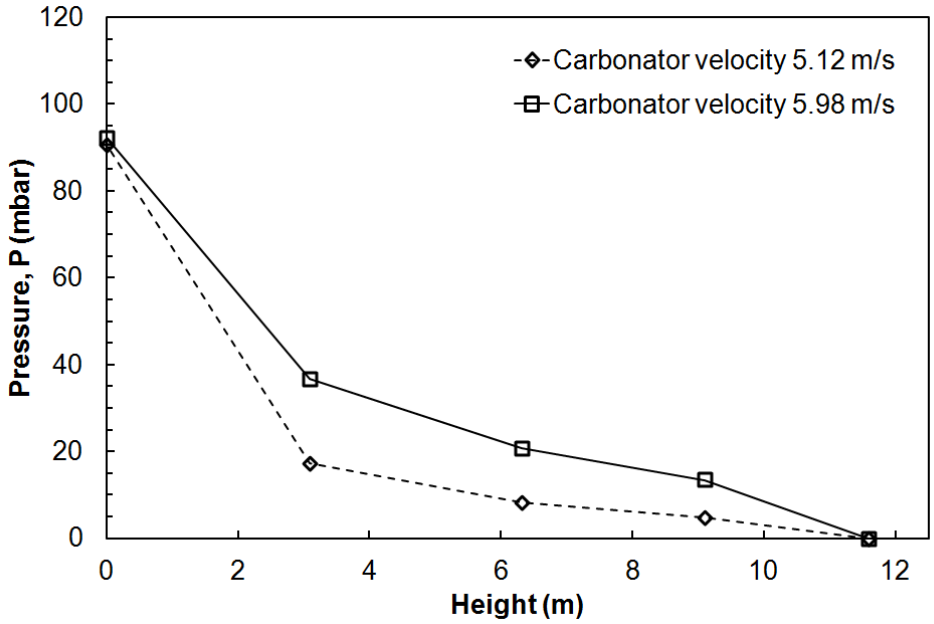

Figure 4.14: Effect of carbonator velocity on riser pressure profile; $\overline{d_p}$ = 340 μm, carbonator inventory= 3.6 kg, T_{carb}= 650°C

As shown in Figure 4.14 by increasing the velocity for the same reactor pressure drop, higher pressure drop gradients are obtained in the lean core-annulus and exit regions. The opposite is true for the axial section 0-3.09 m above the distributor, which is the region that incorporates the dense bed. Such a trend has been predicted from cold model experimentation, as is shown in

Figure 3.10. The increment of the pressure drop- solid fraction at the exit region of is a clear indicator that the riser entrainment increases (see 3.13), as has been also the case for cold model experiments which are shown in Figures 3.12a and 3.12b.

vi. **Functionality of the cone valve:** Although an empirical correlation of the sort presented in Figure 3.14 was not attained during the operation of the 10 kW_{th} IFK DFB facility the cone valve opening proved an excellent independent variable used to set the value of the dependent variable of F_{Ca}/F_{CO2}.

The common aspects between the cold model and the 10 kW_{th} IFK DFB facility listed above, despite minor deviations, support the role of the cold model as a tool for studying and predicting actual facility fluid-dynamic interactions. However, two aspects of operation with regard to the 10 kW_{th} IFK DFB carbonator riser exhibit significant deviations in comparison to the cold model and are listed below.

i. **Carbonator riser entrainment:** The riser entrainment has been shown to be 15-20 kg/m^2s for the 10 kW_{th} IFK DFB carbonator, while cold model predictions presented values up to 30 kg/m^2s, as shown in Figure 3.12a and 3.12b.This is despite the fact that a significant number of runs, with use of the 10 kW_{th} IFK DFB facility, were realized at around 6 m/s, i.e. at a higher velocity than the corresponding predicted cold model operating window, and with finer PSDs. This is attributed to the noted overestimation of the pressure drop and solid fraction of the exit region during cold model experimentation. These parameters are directly linked to the entrainment, as shown in Figure 3.13.

ii. **Slip-stick flow pattern in the upper standpipe:** Slip-stick phenomena were always present within the upper standpipe of the 10 kW_{th} IFK DFB facility. They were visually observed through the quartz glass the location of which is shown in Figure 4.1. The magnitude of the phenomena was far less in the upper standpipe of the cold model than in that of the actual 10 kW_{th} IFK DFB facility. Such phenomena have been linked to a critical value of the second term of the right hand side of Equation (25) which corresponds to the actual solids downflow velocity within the standpipe [74, 141]. According to the investigations of Bidwe et al. if the corresponding value of this velocity is below 0.025 m/s in a standpipe slip-stick phenomena are not present [141]. During experimentation with the 10 kW_{th} IFK DFB facility the actual solid downflow velocity range has been 0.032-0.043 m/s thereby justifying their existence. Beyond this range the slip stick phenomena resulted to blocking of the riser cyclone and led to tripping the facility.

4.3.4 Attrition measurement results & proposed improvement

As noted, the attrition behavior impacts the system by influencing the actual PSD and therefore the reactor pressure profiles. This in turn, depending on the DFB setting, may influence the carbonator gas-solid contacting factor (φ) and the n_{Ca} through the impact of attrition on TSI distribution (see Equation (19) and (20)). Moreover, in the case where the flow of fines exiting the system, as a combined result of attrition rate and cyclone efficiency, is larger than the make-up flow needed to uphold a desired $X_{max,ave}$ value; than attrition phenomena dictate the value of the F_0/F_{CO2} ratio. During experimentation with use of the 10 kW_{th} IFK DFB facility, sorbent attrition is characterized by comparing the Particle Size Distribution (PSD) of: a) the raw $CaCO_3$, b) the CaO after the first pre-calcination, and c) the bed material after 8 h of operation, as shown in Figure 4.15. The results of Figure 4.15 are the outcome of a day of experimentation with use of the IFK (BFB) setting. However, these results are representative of all 10 kW_{th} IFK DFB experiments, utilizing prior BFB sorbent pre-calcination. Average pre-calcination residence time was in the range of 1 h, while the corresponding fluidization gas was air. As shown in Figure 4.15, the median particle size (dp_{50}) reduced from 340 μm to 325 μm, after the first pre-calcination. More significant attrition was observed after 8 h of operation with 20% of the total material collected from the DFB system (including secondary cyclones and candle filters) being below 125 μm. The median particle size was further reduced to 300 μm, while 16% of the material was collected outside the DFB loop. The rate of material lost to the secondary cyclone and filter due to attrition is found to be 2 wt.-%/h.

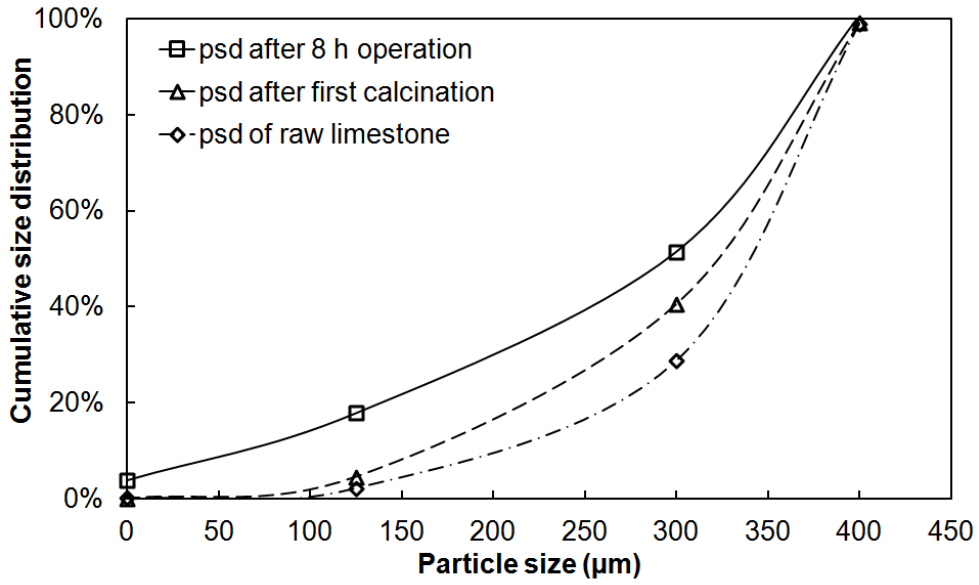

Figure 4.15: Particle size distribution (PSD) of initial limestone, of material after first pre-calcination and after 8 h of operation.

Sorbent attrition was not found to be a significant problem during experimentation with use of the 10 kW_{th} IFK DFB facility. The mean particle size was reduced only by 5 %, during pre-calcination, as a result of primary fragmentation. However, the fine particles potentially entrained from the BFB used for pre-calcination, were not included in this calculation. In conclusion, the moderate attrition during pre-calcination noted in the 10 kW_{th} IFK DFB facility may be associated either to the type of limestone used, or the mild mechanical stresses associated with bubbling fluidization pre-calcination conditions or both. An added reason may be that sorbent pre-calcination was never complete. During continuous cyclic carbonation-calcination steady state operation primary fragmentation is expected to be of less significance since the sorbent conversion of the carbonator solids is typically below 15 %. In this work the limestone make-up flow required to compensate for the reported attrition rate of 2% wt./h, obtained during continuous cyclic carbonation-calcination operation, corresponds to a make-up ratio (F_0/F_{CO2}) of 0.04. A significantly higher value of F_0/F_{CO2}, equal to 0.085, has been considered feasible for maintaining sorbent activity during operation of an industrial-scale Calcium looping facility operating with a carbonator CO_2 capture efficiency of 80% [49]. Therefore, the attrition values reported from the 10 kW_{th} IFK DFB facility do not represent a process limitation.

The attrition results presented in the text above may be combined with results from the DFB systems mentioned in sub-section 2.3.4, i.e. the results from (i) the 30 kW_{th} INCAR-CSIC DFB facility, (ii) the 1st configuration of the 200 kW_{th} IFK DFB facility and (iii) the CANMET DFB facility. All facilities indicate high primary fragmentation when the first calcination is carried out in a CFB calciner. Results from the 30 kW_{th} INCAR-CSIC DFB facility indicate that CFB pre-calcination leads to a rapid median particle size drop which stabilizes after primary fragmentation is completed. The 1st configuration of the 200 kW_{th} IFK DFB facility, utilizing continuous calcination of the make-up flow in a CFB calciner reports a drop of 150 μm after a week of experimentation and quantify the rate of solids leaving the system to be equal to 5 % wt./h. [35] The CANMET DFB unit also shows significant attrition during CFB pre-calcination; surprisingly high attrition rates are maintained throughout operation which could be explained based on limestone or facility specific reasons. Therefore, based on the observations of Scala et al. [93], i.e. that the extent of primary fragmentation is linked to the mechanical stresses that accompany it, and on the findings of Calcium looping pilot plants mentioned above, it seems potentially feasible to add a BFB pre-calcination reactor to the Calcium looping flow sheet. Such a reactor could be placed between the $CaCO_3$ silo and the BFB regenerator of Figure 1.4. Such a setting may lead to a Calcium looping system exhibiting less attrition since: (i) the limestone is expected to undergo minor particle size changes

during its pre-calcination and (ii) the calcined product will be partially sintered, as that of Figure 4.8 for N_{th}= 0, and therefore mechanically stronger. The Calcium looping setting incorporating a pre-regeneration reactor is proposed for further investigation to scientifically prove its merit and is given in Figure 4.16.

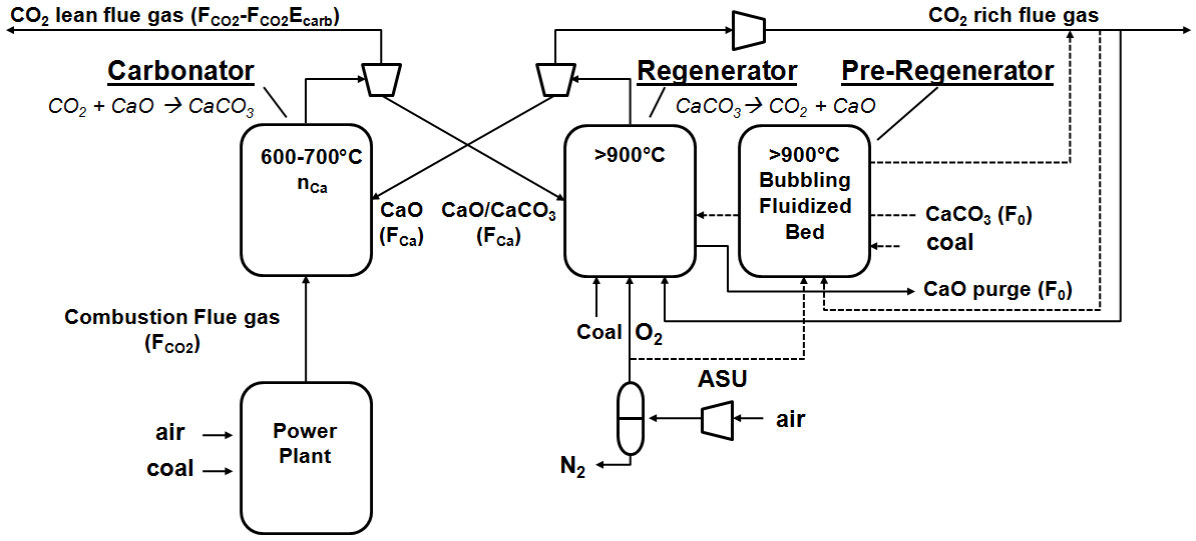

Figure 4.16: Calcium looping system with pre-calcination unit for attrition reduction

4.4 Results & Discussion II: Variable effect on the CO_2 capture efficiency

In this section, the effect of individual dependent variables on the CO_2 capture efficiency is demonstrated. Varied parameters include carbonator temperature (T_{carb}), the Ca looping ratio (F_{Ca}/F_{CO2}) and the carbonator space time (τ). Observed trends are discussed based on the parameter interdependence postulated by the two theoretical approaches A & B presented in sub-section 2.4.2. Parameter variation has been conducted with use of the IFK (BFB) experimental setting.

4.4.1 Effect of temperature

The carbonator temperature (T_{carb}) is increased between three consecutive steady states in Figure 4.17, while utilizing the BFB of the 10 kW_{th} IFK facility as the carbonator. The equilibrium CO_2 capture efficiency (E_{eq}), derived from Equation (1), is plotted for every steady state and decreases with increasing carbonator temperature. In all 3 steady states, the Ca looping ratio (F_{Ca}/F_{CO2}) was kept at significantly high values (> 14) in order to achieve the maximum possible CO_2 capture efficiency. The measured CO_2 capture efficiency (E_{carb}) and the calculated equilibrium CO_2 capture efficiency corresponding to the measured carbonator temperature (E_{eq}), are compared in Figure 4.17 and demonstrate good agreement. The lowest steady state temperature

characterized in this study was 630°C and it resulted in the highest steady state CO_2 capture efficiency measured, equal to 93 %.

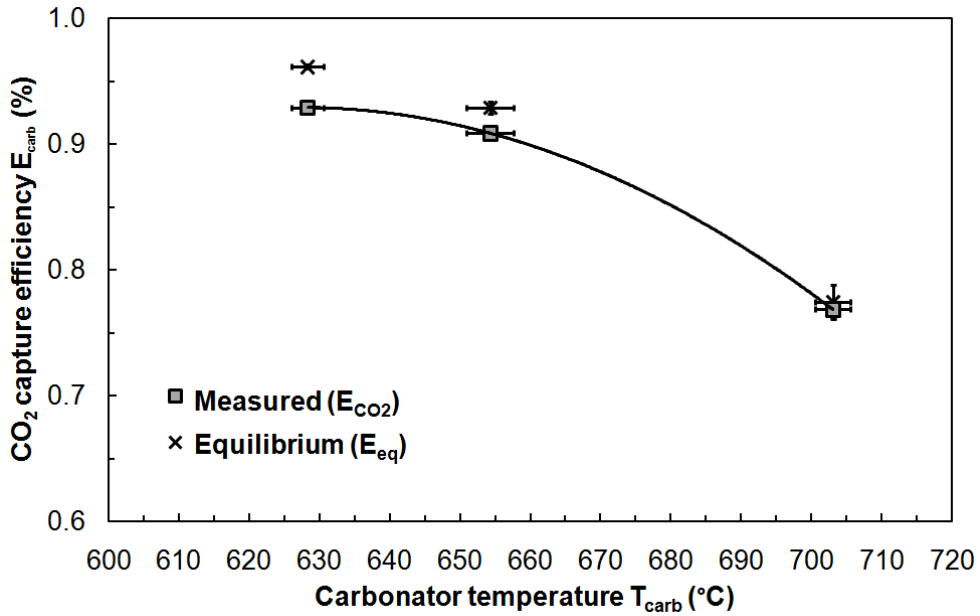

Figure 4.17: CO_2 capture efficiency (E_{carb}) and equilibrium CO_2 capture efficiency (E_{eq}), vs. carbonator temperature (T_{carb}) for steady states with an inlet vol. CO_2 concentration (ν_{CO2}) of 15 vol.-%, a space time (τ) of 0.55 h, and a Ca looping ratio (F_{Ca}/F_{CO2}) >14

The trend of decreasing CO_2 capture efficiency with increasing carbonator temperature observed during steady state operation in Figure 4.17 is explained based on Equation (1). Moreover, the explanation is independent of the type of the theoretical approach used, i.e. A or B. Hence, decreasing T_{carb} leads, according to Equation (1) to an increase of the equilibrium CO_2 vol.-% (ν_{eq}). As a result the carbonation reaction rate decreases (see Equations (2) and (3)) and therefore the CO_2 capture efficiency value decreases also, as expected from the simplified mass balance carbonator model expressions of approach A, Equation (10), and approach B, Equation (12). In any case, the measured data suggests that for a given temperature, the CO_2 capture efficiency can approach its equilibrium value provided that the calcium bed is satisfactorily active.

4.4.2 Effect of Ca looping ratio F_{Ca}/F_{CO2}

As observed from Figure 4.17, temperature influences the CO_2 capture efficiency. Therefore, in order to properly compare different steady states which may occur at slightly different temperatures, the equilibrium-normalized CO_2 capture efficiency (E_{carb}/E_{eq}) is hereby introduced as a metric which quantifies the reactor

performance in comparison to the optimum allowed by thermodynamic chemical equilibrium. Figure 4.18 plots the equilibrium-normalized CO_2 capture against the Ca looping ratio for three steady states which were conducted consecutively.

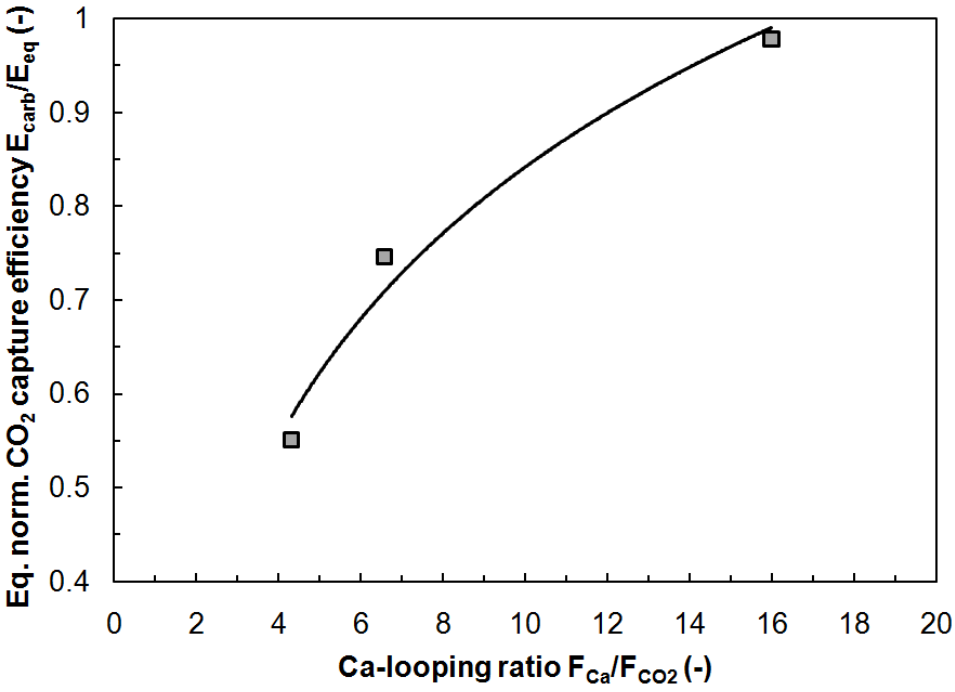

Figure 4.18: Equilibrium-normalized CO_2 capture efficiency (E_{carb}/E_{eq}) vs. Ca looping ratio (F_{Ca}/F_{CO2}) for steady states with an inlet vol. CO_2 concentration (ν_{CO2}) of 15 vol.-%, a carbonator temperature (T_{carb}) of 660 °C, and a space time (τ) of 0.47 h

Increasing the value of the F_{Ca}/F_{CO2} ratio has been the result of successively adjusting the independent parameter of cone valve opening (see facility sketch of Figure 4.1), while other process conditions were kept constant. The $X_{max,ave}$ is also considered constant, despite not being measured for these steady states, since they were conducted consecutively and within a short period of time. Therefore, the increment of N_{th} is not considered to be significant, thus justifying the assumption of constant $X_{max,ave}$ between the three steady states with use of Figure 4.8. The trend of Figure 4.18 shows that for the respective experimental conditions, the E_{carb}/E_{eq} increases from around 0.55 to almost 1 when the F_{Ca}/F_{CO2} is increased from 4 to above 16. The explanation of the above statement depends on the theoretical approach adopted, i.e. A or B.

According to approach A, which utilizes the reaction rate expression of Equation (2), an increase in F_{Ca}/F_{CO2} leads to an increase of the carbonation rate of the whole carbonator inventory (n_{Ca}). This occurs through the decreasing values of the average carbonation conversion of the carbonator bed (X_{carb}) when the F_{Ca}/F_{CO2} is increased. The X_{carb} reduces during the three steady states of Figure 4.18 from

0.12 mol_{CaCO3}/mol_{Ca} (when F_{Ca}/F_{CO2}= 4) to below 0.11 mol_{CaCO3}/ mol_{Ca} (when F_{Ca}/F_{CO2}= 6) and below 0.06 mol_{CaCO3}/ mol_{Ca} (when F_{Ca}/F_{CO2}> 16). The X_{carb} behavior can be understood based on Equation (7) and on that the particle residence time within the carbonator decreases when increasing the F_{Ca}/F_{CO2}. Moreover, decreasing X_{carb} values lead to an increasing values of active space time, $\tau_{active,A}$, shown in Equation (11). Finally, an increment of $\tau_{active,A}$ leads to an increment of the CO_2 capture efficiency, as shown from the simplified mass balance-carbonator model expression of Equation (10). Alternatively, when considering the interdependence scheme of theoretical approach B, the trend of Figure 4.18 is justified based on that the increase of the F_{Ca}/F_{CO2} leads to the increase of the active bed fraction (f_{active}) of the carbonator inventory (n_{Ca}) reacting at a constant reaction rate, as shown in Equation (13). An increase of the f_{active} leads to increasing values of active space time ($\tau_{active,B}$), as given Equation (15). Hence, the increase in the CO_2 capture efficiency can be explained by the $\tau_{active,B}$ increase, as shown in the simplified mass balance- carbonator model of Equation (12). Finally, it should be stated that the effect of F_{Ca}/F_{CO2} variation on the $X_{max,ave}$ [102, 103] has not been defined due to the nature of the experiments conducted within this work. In these experiments the F_{Ca}/F_{CO2} and $X_{max,ave}$ variables have been decoupled, i.e. are independent from one another. Future experiments realizing long duration steady states and utilizing a make-up flow of fresh limestone, absent here, would be suitable to define the interdependence between these variables.

4.4.3 Effect of space time (τ)

Figure 4.19 plots the equilibrium-normalized CO_2 capture efficiency against the Ca looping ratio for three series of steady states conducted under different values of space time within the BFB carbonator: 0.32 h, 0.47 h and 0.78 h. Space time variation was achieved by varying the BFB carbonator velocity from 0.5 m/s to 1.2 m/s while maintaining a constant CO_2 inlet concentration of 15 vol-%. For experiments conducted under constant space time, the trend stated in the previous section, namely that the increase of the Ca looping ratio results in an increase in the carbonator equilibrium-normalized CO_2 capture efficiency, holds true. However, for the same Ca looping ratio, the space time has a significant influence on the equilibrium-normalized CO_2 capture efficiency, as shown in Figure 4.19. For example, at Ca looping ratio values from 5 to 8, the equilibrium-normalized CO_2 capture efficiency obtained when operating at a space time of 0.78 h is 1.5 to 2.2 times higher than when operating at a space time of 0.32 h. At higher Ca looping ratio values, the difference in equilibrium-normalized CO_2 capture efficiency between different space times becomes less significant until at a Ca looping ratio of 15, the CO_2 capture efficiency values reached

are close to equilibrium values irrespective of the space times characterized in this study.

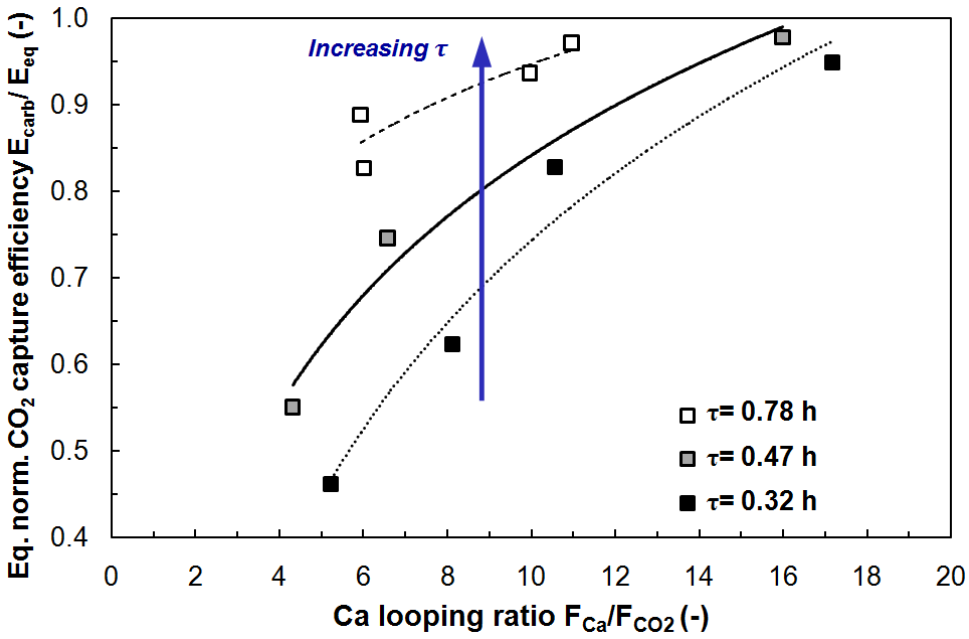

Figure 4.19:. Equilibrium-normalized CO_2 capture efficiency (E_{carb}/E_{eq}) against the. Ca looping ratio (F_{Ca}/F_{CO2}) for steady states with an inlet vol. CO_2 concentration (ν_{CO2}) of 15 vol.-%, a carbonator temperature (T_{carb}) of 660 °C, and varying space time (τ)

The effect of space time (τ) on the equilibrium-normalized CO_2 capture efficiency has also been predicted from previous modeling efforts [97, 102]. It is further explained in that an increase of space time essentially means an increase in the bed inventory in the carbonator (n_{Ca}) for a constant molar inlet flow of CO_2 (F_{CO2}). Hence, an increase of space time leads to a direct increase of active space time, as shown from respective expressions of both theoretical approaches A & B, i.e. Equations (11) and (15), respectively. Hence, an increase of active space time leads to an increase of CO_2 capture efficiency, as expected from the respective simplified mass balance-model expressions of the two approaches, i.e. Equations (10) and (12). The lower range of Ca looping ratios (5 to 8 mol Ca per mol CO_2 fed) characterized in this study always resulted in lower CO_2 capture efficiencies compared with those resulting from higher Ca looping ratios. As explained in the previous sub-section this is due to lower overall bed reactivity of the bed exhibited in such a case. Hence, the effect of space time on the CO_2 capture efficiency is more pronounced at lower Ca looping ratios than at higher ones, as shown in Figure 4.19.

4.5 Results and discussion III: Model & active space time validation

Both Equation (10) of approach A and Equation (12) of approach B are carbonator reactor models that link dependent Calcium looping variables with the CO_2 capture efficiency. The respective active space time expression, i.e. Equation (11) for approach A and Equation (15) for approach B, is the key parameter of these models. It is indicative of both the sorbent inventory and the reaction rate of that inventory. For a given carbonator reactor operating at given fluidization conditions, limestone type, temperature and inlet CO_2 Vol.-%, the active space time is the single parameter determining the CO_2 capture efficiency. In the sections below the simplified mass balance model expressions of Equation (10) and (12) are fitted to the data of the three experimental settings of Tables 4.1 and 4.2. The aim of this exercise is to judge their validity, obtain the most suitable active space time expression from the two given in Equation (11) and (15) and therefore obtain a clear understanding of the interdependence between dependent Calcium looping variables and reactor performance.

4.5.1 Approach A: Data fitting to Equation (10)

The equilibrium normalized CO_2 capture efficiency is plotted against the active space time expression of Equation (11), $\tau_{active,A}$, in Figure 4.20.

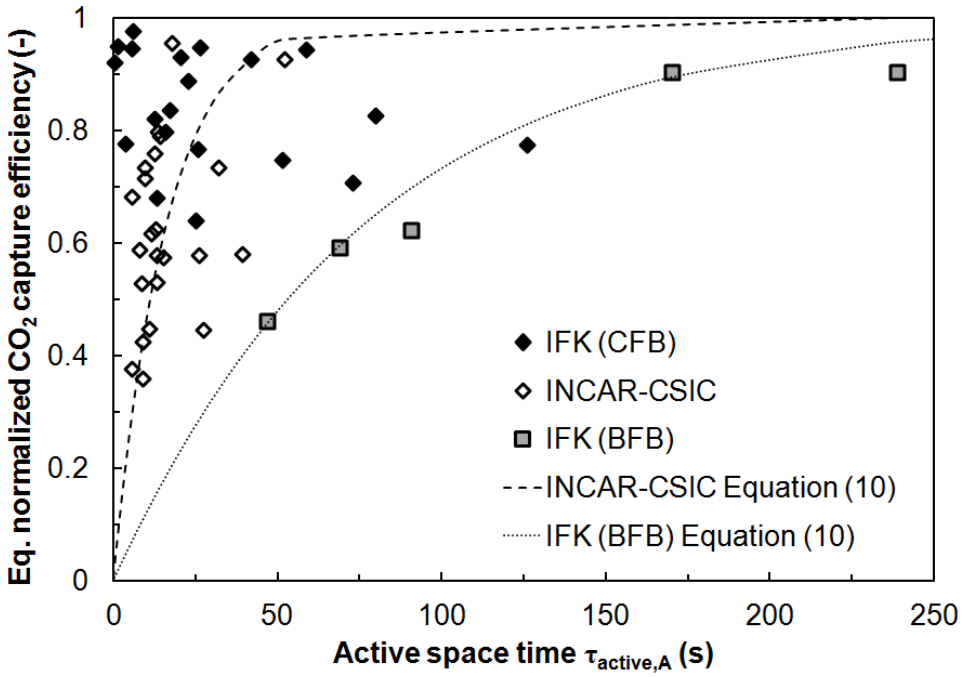

Figure 4.20: Comparison of IFK and INCAR-CSIC experimental equilibrium normalized capture efficiencies against the active space time expression of approach A, given in Equation (11)

The $\tau_{active,A}$ correlates well to the equilibrium normalized CO_2 capture efficiency for the INCAR-CSIC and IFK (BFB) data sets. The respective model lines shown in Figure 4.20 are produced with use of Equation (10) in the following manner. The active space time corresponding to a given CO_2 capture efficiency is calculated by (i) calculating the logarithmic mean of the CO_2 concentration within the carbonator reactor (since the inlet CO_2 concenration is known and the outlet concentration can be calculated based on the given CO_2 capture efficiency), (ii) by calculating the equilibrium CO_2 concentration through Equation (1) for a given temperature, (iii) by calculating the the apparent reaction rate ($k_{sB}\varphi$) as the fitting factor for each data set (iv) by using Equation (10) to calculate the active space time since all other parameters are known. Naturally, the obtained value of active space time can be attained through any combination of the parameters τ, $X_{max,ave}$ and X_{carb}. In addition, it is interesting to note that the curved shape of the model line based on that the average CO_2 concentration decreases with increasing CO_2 capture efficiency. Therefore, the slope of the curves corresponding to Equation (10) in Figure 4.20 decreases with incraasing $\tau_{active,A}$ and E_{carb}. Moreover, model lines produced with application of Equation (10) fit both these data sets well. In the case of INCAR-CSIC and the IFK (BFB) data sets the $(k_s\varphi)_A$ have been found equal to 0.370 s^{-1} and 0.085 s^{-1}, respectively. The large difference between the apparent kinetic constants can be explained mainly due to the poor gas-solid contacting quality exhibited by a BFB in comparison to a CFB reactor. This is explained based on that part of the gas is able to by-pass the sorbent bed in the form of bubbles in the case of the BFB carbonator. Furthermore, it is important to note that in the case of these IFK (BFB) and INCAR-CSIC data sets, carbonator residence times are low, i.e. in the range of ca 1.5 min. Since the IFK (CFB) carbonator data set exhibits unacceptable scatter, no model line is given for this data set. The reason for this discrepancy can be explored in that the expression of $\tau_{active,A}$, given in Equation (10), is proportional to the difference of the average maximum carbonation conversion ($X_{max,ave}$) and the actual average carbonation conversion (X_{carb}). As noted, this difference ($X_{max,ave}$-X_{carb}) is derived through TG analysis of a sample that is assumed to be representative of the whole carbonator bed. Many samples removed from the IFK riser carbonator exhibited very low values (even negative values-respective points not included in Figure 4.20) of the difference ($X_{max,ave}$-X_{carb}), thus explaining the scattering of the experimental points for this particular data set in Figure 4.20. The main reason leading to such ($X_{max,ave}$-X_{carb}) values, which are not encountered for the other two data sets, is that the IFK riser carbonator can accommodate high solid bed inventories leading to large average solid residence time in the reactor, i.e. in the range of 3 min, which in turn result to X_{carb} values close to $X_{max,ave}$. Finally, it can be concluded that approach A, with its corresponding simplified mass balance (Equation (10)) and active space time expression (Equation (11)), is

suitable to fit carbonator data in the case where the X_{carb} is not close to the $X_{max,ave}$. This is the case for carbonator reactors operating with low average particle residence times or with particles that exhibit high values of $X_{max,ave}$, i.e. relatively fresh particles.

4.5.2 Approach B: Data fitting to Equation (12)

Approach B fits all three experimental data sets well. This becomes apparent through the quality of the fit between the experimental data and the model expression of Equation (12), which is presented in Figure 4.21.

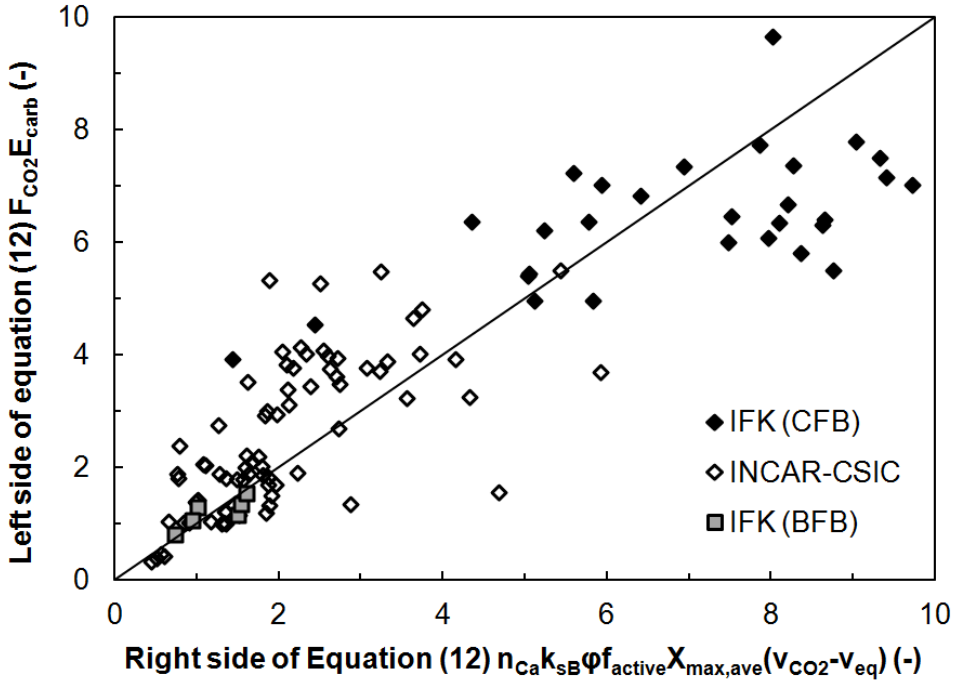

Figure 4.21: Closure of the mass balance/ carbonator model of Equation (12), i.e. comparison of the CO_2 molar flow removed from gas phase with the CO_2 molar flow reacting with CaO in the bed of the carbonator reactor for all experimental runs.

The y-axis and x-axis of this figure represent the left and right hand side of Equation (12), respectively. Also in this approach, the apparent reaction rate constants ($k_{sB}\varphi$) have been used as the fitting constant. Hence, the $k_{sB}\varphi$ values derived were equal to 0.43 s^{-1}, 0.20 s^{-1} and 0.05 s^{-1} for the INCAR-CSIC, IFK (CFB) and IFK (BFB) data sets, respectively. It has to be noted that for the INCAR-CSIC data, the fitted $k_{sB}\varphi$ was found to be insensitive (sum of square error changes<5%) to changes of the apparent reaction rates between 0.30 and 0.60 s^{-1}. Since, most of the points are close to the 45° line in Figure 4.21, Equation (12) is fulfilled to a satisfactory extent and the obtained fitting constants are considered valid. This adds significant confidence regarding the correctness of approach B and validates Equation (12) as a simple yet

efficient carbonator model. In addition, the gas-solid contacting factor φ is calculated for both installations, as the ratio of the apparent reaction rate constant ($k_{sB}\varphi$) derived from fitting the experimental data to Equation (12) and the reaction rate constant k_{sB} derived from the TG experiments, shown in Figure 4.4. The calculated value of φ is equal to 1.3, 0.8 and 0.2 for the INCAR-CSIC, IFK (CFB) and IFK (BFB) data sets, respectively. At this point it has to be noted that φ is the effective fitting constant of the experimental data and model Equation (12), since k_{sB} has been derived from the TG experimentation. As a result, the derivation of φ is burdened by the accumulation of the error of all measurements conducted during experimentation, i.e. gas, solid flow, temperature, pressure drop and TG measurements. Therefore, this justifies that the value of φ is slightly above 1 in the INCAR-CSIC case. However, what has to be pointed out is that both INCAR-CSIC and IFK (CFB) φ values obtained are close to 1 and that this is evidence of the excellent gas-solid contacting encountered in both CFB carbonator reactors. Moreover, this is despite the fact that the two carbonators are operating in different fluidization regimes, i.e. the turbulent and fast fluidization regime. Hence, both regimes can be considered for application in larger scale units. These neighboring regimes could be also combined in one carbonator unit. Consequently, the carbonator can operate in the fast or the turbulent fluidization regime when the original power plant is operating at full or partial load, respectively. However, the DFB design must be able to accommodate such a feature [35]. The very low φ factor in the case of the IFK (BFB) data set has been explained based on the noted poor gas-solid contacting explained by bubble formation. Hence, by application of a gas-solid effectiveness factor (φ) of around 1 in the case of a turbulent or fast fluidized CFB carbonator and of around 0.2 when considering a BFB carbonator, the simplified mass balance expression of Equation (12) can be used directly as a simple carbonator model. The only necessary action before doing so is the determination of the reaction constant k_{sB} from a simple TG experiment, as shown in Figure 4.4, or in the absence of this information, the adoption of a k_{sB} value of around 0.3 s^{-1}.

Having acquired the k_{sB} and φ values for the calculation of $\tau_{active,B}$ as presented in Equations (13-15), the E_{carb}/E_{eq} is plotted against $\tau_{active,B}$ in Figure 4.22.

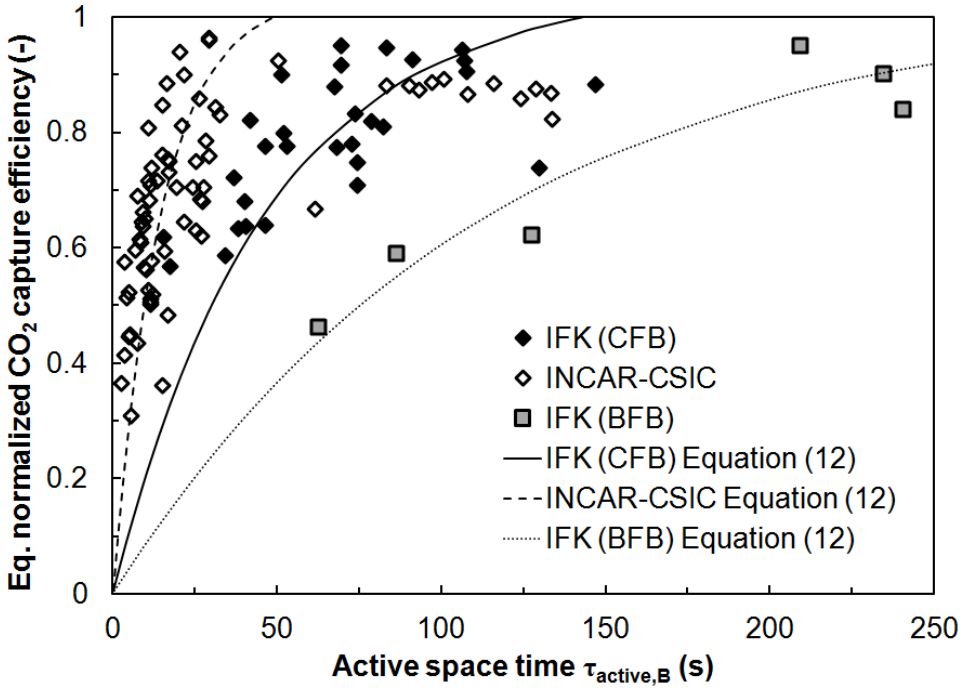

Figure 4.22: Comparison of IFK and INCAR-CSIC experimental equilibrium normalized capture efficiencies against the active space time expression of approach B, given in Equation (15)

The active space time ($\tau_{active,B}$) correlates well with the E_{carb}/E_{eq} for all IFK (CFB), IFK (BFB) and INCAR-CSIC data sets thus proving to be the characteristic carbonator parameter. In addition, the solid model lines obtained through Equation (12) for each data set fit the experimental data to a satisfying extent. The derivation of the model line curves of Figure 4.22 is similar to that of Figure 4.20, while their shape can also be explained on the basis that the average CO_2 concentration decreases with increasing E_{carb}. The solid model lines, corresponding to different data sets, of Figure 4.22 are quantitatively different. Firstly, because of the different apparent reaction rate constant and secondly because most of the INCAR-CSIC experiments were conducted with an inlet CO_2 vol.-% of 16.5 %, considerably higher than the 11.4 % used in the IFK (CFB) experiments and slightly higher than the 15 % used in the IFK (BFB) experiments. However, it must be noted that in the case of INCAR-CSIC only, approach A provides a marginally better fit of the experimental data. This means that the fit of the E_{carb}/E_{eq} with the active space time expression of Equation (11) of approach A, shown in Figure 4.20, is slightly better than with Equation (15) of approach B, presented in Figure 4.22. Despite this fact, it is recognized that the approach B is more general, directly links the active fraction of the bed inventory with average residence time of the solids in the reactor and seems to give a reasonable quality fit for all data coming from both INCAR-CSIC and IFK installations. From Figure 4.22, a critical value of the engineering variable of active space time can be obtained, in order for the E_{carb}/E_{eq} to be greater than 0.9, which can be used to follow a

carbonator design procedure [89]. This value is shown to be 30 s for the INCAR-CSIC case, 92 s for the IFK (CFB) case and greater than 200 s for the IFK (BFB) case. The difference, as noted, is mainly due to the different value of the fitted apparent reaction rate constant ($k_{sB}\varphi$) of the three data sets and the difference between the inlet CO_2 vol.-% applied during experimentation. Furthermore, it has to be pointed out that the active space time values are rather close for the INCAR-CSIC and IFK (CFB) carbonators despite further differences in operating conditions reported in Tables 4.1 and 4.2. Moreover, they are close to the respective critical active space time value of 54 s, i.e. 0.015 h, reported when applying the fitting procedure described in approach A [83].

4.5.2.1 Improvement potential

The carbonator reactor model of Equation (12) and the active space time expression of Equation (15), which have been validated by all IFK and INCAR-CSIC data sets, allow for both optimized design and operation of larger scale units. This has been the case with regard to the design of the next generation pilot scale systems included in Table 2.2, i.e. the 200 kW_{th} IFK DFB pilot [35, 89] and the 1.7 MW_{th} pilot located in La Pereda, Spain [38]. However, the model of Equation (12) can be further developed and the active space time expression of Equation (15) can be further improved. For example, the effect of sulfation [70] and steam presence [109] on the reaction constant k_{sB} can be incorporated in the future. Moreover, the CO_2 absorption taking place from the particle fraction ($1-f_{active}$), which is reacting in the diffusion regime, may also be taken into account thus obtaining a more "complete" form of Equation (12) and a more accurate active space time expression than that of Equation (15). The reaction rate of the diffusion regime in the vicinity of the $X_{max,ave}$ is generally two to three orders of magnitude lower than in the fast reaction regime (see for example Figures 2.3, 2.6 and 4.4), but the average ($1-f_{active}$) bed fraction can be one order of magnitude higher than the active fraction f_{active} . Therefore, it can be claimed that the active space time has been slightly underestimated in the previous analysis. Furthermore, a decisive development with regard to in depth carbonator modeling may come through the discretization of Equation (12) and its application to different regions or cells of the reactor. Such an approach would require coupling of Equation (12) with a semi-empirical [102] or more detailed CFD hydrodynamic model [111, 112]. Such a model would allow the calculation of the local gas-solid effectiveness factors thus improving model accuracy and allowing for the calculation of a global φ factor. Being able to estimate the global φ would allow a more objective assessment of the closure of Equation (12) with use of experimental data, since no parameter would have to be used as a fitting factor. However, despite the simplifications which have been met in the derivation of the model expression of

Equation (12) and the active space time expression of Equation (15), these equations have two striking advantages, i.e. they are simple to apply and fit the experimental data sets. Hence, the equations and general results reported here can be used with greater confidence to carry out first full simulations [66] of the future industrial scale designs.

4.6 Conclusions of the reactor performance analysis

Reactor performance analysis has studied interactions between dependent variables, examined their behavior, and validated two simple yet efficient carbonator models and respective expressions for the key carbonator engineering variable of active space time. Therefore, experiments have been carried out with use of the 10 kW_{th} IFK DFB facility (utilizing its riser or BFB as the carbonator), while results from the 30 kW_{th} INCAR-CSIC DFB facility (respective work has been conducted outside the scope of this thesis) have been utilized. Steady state operation of all three experimental settings has proved to be straightforward as a result of the process fluidized bed nature. Firstly, the good closure of the carbonator mass balances confirmed the quality of respective measurements. This has been particularly important since these were diverse, i.e. included gas-analysis, temperature, pressure drop and manual measurements. Furthermore, the mass balance closure demonstrated that in order to capture a certain molar flow of CO_2, a slightly over-stoichiometric flow of active Ca is necessary. In addition, investigating the behavior of individual variables aided the validation, from the carbonator mass balance, of the two carbonator models and respective active space time expressions mentioned above. The outcome of these investigations is summarized below.

Starting with the dependent variable behavior the following can be concluded. The average maximum carbonation conversion ($X_{max,ave}$) has been noted to decay with increasing theoretical cycle number. The experienced decay starts from values that are smaller than expected from TG tests and ends at values of residual activity close to those expected from these tests, i.e. 0.07-0.1. The carbonation conversion of solids exiting the regenerator (X_{calc}) affects both the active flow of Ca entering the carbonator and its active space time, therefore having an impact on the CO_2 capture efficiency as well. The extent of solids calcination within the regenerator has been shown to be dependent to the ratio of solids residence time within the regenerator (t_{reg}) and the carbonation conversion in/after the carbonator (X_{carb}). An adequate value of the ratio t_{reg}/X_{carb}, for conditions corresponding to an air-fired regenerator and in order for almost complete sorbent calcination to be achieved, is approximately 0.4 h. In addition, the solid flow structure of the CFB carbonator is shown to be of the dense

bed, lean-core annulus and exit region type. This is in accordance with respective scaled cold model predictions of the 10 kW_{th} IFK DFB facility. Agreement between the 10 kW_{th} IFK DFB facility and its cold model has been also noted with regard to the Total Solid Inventory, carbonator velocity range required for facility operation, the functionality of the cone valve as a solid flow control device, the effect of mass availability and velocity on the carbonator riser pressure profile. On the other hand, two discrepancies are also noted, i.e. that the riser entrainment was predicted to be higher during cold model experimentation and that the latter did not predict the "disturbing" slip-stick flow phenomenon observed in the upper standpipe of the actual 10 kW_{th} IFK DFB facility. Furthermore, attrition was found to be moderate. This statement is justified since the mean particle size change has been measured to be only 40 μm after BFB pre-calcination and 8 h of experimentation while the attrition rate was 2 wt.-%/h. The better experimental results recorded in comparison to other Calcium looping facilities is based on that BFB pre-calcination reduces primary fragmentation, due to that mechanical forces are of lesser magnitude than in a CFB, and that pre-calcination partially sinters and therefore strengthens the particles. Hence, it is suggested that the "classical" Calcium looping flow sheet may be improved by adding a BFB pre-calciner reactor in order to calcine the fresh $CaCO_3$ up-steam of the main regenerator of the DFB Calcium looping system.

The two theoretical approaches validated within this thesis, i.e. A and B, combine dependent Calcium looping variables into a respective model and active space time expression. The first (approach A) assumed that all the particles in the carbonator bed react in the fast reaction regime and that their reaction rate is proportional to the difference between their average maximum carbonation conversion ($X_{max,ave}$) and their actual carbonate content (X_{carb}). The second (approach B) assumed that a fraction of the particles react in the fast reaction regime (f_{active}) which is dependent on a simple residence time distribution in the carbonator riser. Moreover, the reaction rate of this approach was considered to be proportional of the particles $X_{max,ave}$ value only, provided that ($X_{carb}<X_{max,ave}$) for a specific particle. The two theoretical approaches enabled the description of the influence of individual dependent variables on the carbonator CO_2 capture efficiency. Hence, the effect of temperature (T_{carb}) is explained based on that it affects the carbonation rate through its impact on the equilibrium CO_2 vol.-% (ν_{eq}), as shown within both approaches. A carbonator temperature window of 600-660 °C was found to be suitable for CO_2 capture efficiency above 90 % and to drive a state of the art steam cycle for the Calcium looping system. Moreover, increasing the Ca looping ratio (F_{Ca}/F_{CO2}) increases the CO_2 capture efficiency. Based on approach A this occurs due to the increment of the reaction rate of the Ca inventory of the carbonator bed. On the other hand, approach B

explains this trend based on that the active fraction of the carbonator inventory (i.e. the one reacting at a constant reaction rate) increases. The range of the F_{Ca}/F_{CO2} variable, when assuming a maximum carbonation conversion range of 0.07-0.3 and a CO_2 capture efficiency close to equilibrium, is 3-13 for a CFB carbonator. The effect of space time (τ) on the CO_2 capture efficiency is explained based on the larger amount of sorbent available to capture a given amount of CO_2 in both approaches. A carbonator space time value greater than 0.5 h may be considered feasible in order to minimize the Ca looping ratio and make-up flow needs of the Calcium looping system and maintain a CO_2 capture efficiency close to the equilibrium.

With regard to the degree that the carbonator models of approach A and B are in accordance with the experimental data the following can be noted. Approach A has shown to fit the INCAR-CSIC and IFK (BFB) data sets well, while it has given unacceptable results for the IFK (CFB) data set. The main reason for this is the large residence time of solids in the IFK riser carbonator, leading to carbonate contents that are very close to the maximum carbonation conversion of a particle. Approach B fits the data sets of all experimental setting well (i.e. always provides closure of the carbonator mass balance) and is considered more general, since it links the CO_2 capture efficiency with a particle residence time distribution of particles in the carbonator. Hence, the active space time expression of approach B ($\tau_{activeB}$) can be claimed to be the critical engineering variable for a given carbonator. However, caution has to be taken when comparing active space time values from different carbonators. In such a case the reactor operating at the lowest active space time for a given E_{carb} value is the one operating in the most favorable conditions, i.e. with a limestone exhibiting a higher reaction rate constant (k_s), at fluid-dynamic conditions allowing for a better (φ), with a higher inlet CO_2 vol.-% (higher reaction driving force) or at a lower temperature. Based on their respective conditions, the active space time values ($\tau_{active,\,B}$) attained with use of approach B for an E_{carb}/E_{eq} of 0.9 to be achieved is 30 s for the INCAR-CSIC carbonator, 92 s for the IFK riser carbonator and above 200 s for the IFK (BFB) carbonator. The respective values for approach A had been found to be 54 s for the INCAR-CSIC riser carbonator and 180 s for the IFK BFB carbonator and are therefore similar to those attained from approach B. Returning to approach B, the apparent reaction constants ($k_{sB}\varphi$) have been found equal to 0.43 s^{-1} for the INCAR-CSIC riser, 0.20 s^{-1} for the IFK riser and 0.05 s^{-1} for the IFK BFB carbonator. Therefore, the gas-solid contacting factor φ has been found to be close to 1 for both CFB carbonators while it has shown to be as low as 0.2 for the IFK BFB carbonator, This demonstrates the excellent gas-solid contacting of the CFB carbonator reactor and denotes its superiority over the BFB where part of the flue gas escapes the bed in the form of bubbles.

5 Outlook

The future of the Calcium looping process seems promising, should humanity pursue the goal set by the Copenhagen accord, i.e. to limit the world temperature increase to 2°C or at least keep moving towards that direction. In this effort, a manifold of technologies are to be deployed and CCS technologies, as shown by the WEO 2010, are expected to be one of the key solutions. Calcium looping has a realistic chance to play an important role within post-combustion CO_2 capture applications since it reduces the cost of amine scrubbing and chilled ammonia processes significantly, while being very competitive to oxy-combustion and pre-combustion capture as well. This is justified since far less O_2 is consumed in comparison to oxy-combustion and since availability issues, which are present in IGCC plants, are not expected. The competitiveness of the Calcium looping process is justified based on its main attributes, i.e. it utilizes a cheap and widely geographically distributed Ca sorbent, standard fluidized bed technology and has wide process integration potential. Prime examples with regard to the latter attribute include: steam cycle integration to produce additional electricity, utilizing the carbonator as a flue gas desulfurization unit and CaO purge utilization for in-situ fluidized bed combustor desulfurization or utilization in the cement industry to produce clinker. The Calcium looping process has come a long way from 1999 when it was first presented. Sorbent chemistry tests in thermo-gravimetric analyzers, batch fluidized bed carbonation/calcination tests, steam cycle and economic feasibility studies paved the way for the first continuous Calcium looping lab-scale systems in 2008 which led to the pilot scale rigs in the order of up to a few MW_e. Based on the results of the above experimental units, it is seems that no obvious obstacle exists for the process to proceed to the demo-plant scale (50-100 MW_e) on the road to commercialization by 2020.

The characterization of the process presented within this thesis, through the study and analysis of fluid-dynamic and reactor performance interactions standing between the facility designer/operator and the CO_2 capture efficiency has helped and are expected to be of further help with regard to process development. First of all the conclusions, parameter ranges, reactor models and active space time expressions presented or/and validated here, attained from lab-scale experimentation, provide a basis for analyzing data sets produced within the pilot plant units of today and for the design of further pilot scale and demo-scale plants. In addition, they can serve as a baseline when conducting experimentation that lifts simplifications included within

this work, i.e. when including sulfation in the carbonator/regenerator, utilizing oxy-fuel conditions within the regenerator, including steam in the carbonator, utilizing a continuous make-up flow or when researching the merit of a given pre-treated or synthetic Ca sorbent within the Calcium looping system. The work at hand may also aid thermodynamic (steam cycle) and reactor modeling approaches. Hence, the carbonator model equations may easily be integrated in calculation sheets looking at the process heat, mass balance and electric efficiency penalties. Since more detailed reactor modeling is required, e.g. through empirical fluid-dynamic models or CFD modeling, fluid-dynamic and reactor performance experimental data are presented in tabular form within the annex in order to allow for their use of any independent researcher. In addition, the data also aids economical feasibility studies, since the validated carbonator model equations and regenerator data allow for rather realistic Calcium looping system design, equipment sizing, fuel consumption and therefore to more realistic cost estimates. Finally, the work may also benefit, from a reactor engineering point of view any Dual Fluidized Bed process such as the gasification Calcium looping processes, e.g. Absorption Enhanced Reforming (AER) and the Limestone Enhanced GaSification (LEGS) processes as well as Chemical Looping Combustion (CLC) and Reforming (CLR).

Annex A: cold model dimensions and tabular data

Geometrical details of the cold model riser are presented here in order to aid fluid-dynamic modeling. In Figure A.1 the positions of the loop seal return legs and the dimensions of the riser exit are noted. Details related to the loop seal are also present. Tables A.1 and A.2 contain all data related to cold model experimental runs and are to be used in conjunction with Figure 3.1 and the equations of Chapter 3. Table A.1 and A.2 refer to experiments conducted with a mean particle size of 142 μm and 230 μm, respectively.

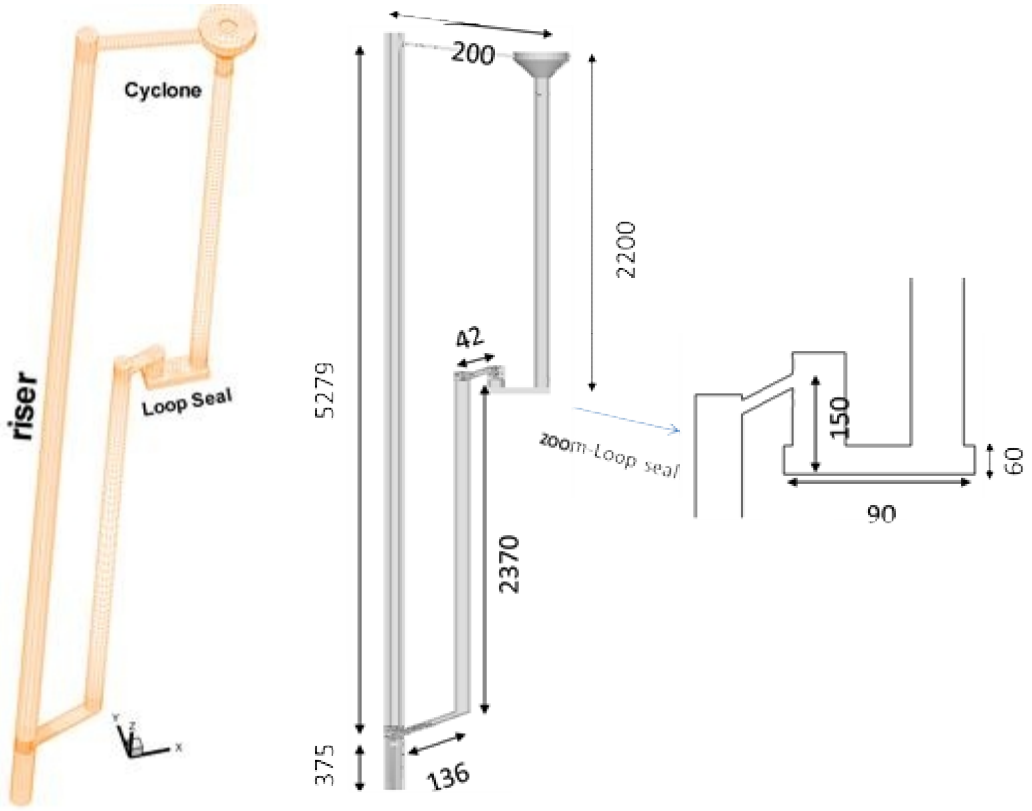

Figure A.1: Cold model riser l geometrical details sketch [65]

Table A.1 – Sheet 1: Tabular presentation of cold model data (Figure 3.1) utilizing ZrO_2 with a median particle size of 142µm

Run no.	TSI (kg)	riser u_0 (m/s)	double exit ls u_0 (m/s)	double exit ls u_0 side (m/s)	Lower ls u_0 (m/s)	P_{BFB} (mbar)	A_{cv} (mm^2)	$\Delta P_{0\text{-}333mm}$ (mbar)	$\Delta P_{333\text{-}2621mm}$ (mbar)	$\Delta P_{2621\text{-}4328mm}$ (mbar)	$\Delta P_{4328\text{-}5090mm}$ (mbar)	$\Delta P_{riser\ total}$ (mbar)	$\Delta P_{upper\ st}$ (mbar)	$\Delta P_{cyclone}$ (mbar)	$\Delta Pr_{iser\ top}$ (mbar)	$\Delta P_{double\ ls}$ (mbar)	$\Delta P_{lower\ st}$ (mbar)	$P_{cyclone}$ (mbar)	$\Delta P_{lower\ ls}$ (mbar)	ΔP_{cv} (mbar)	Upper st height (m)	lower st height (m)	upper/lower standpipe status	$G_{s\ entrainment}$ (kh/m^2s)	$G_{s\ cv}$ (kg/m^2s)
1	2.24	2.31	0.060	0.013	0.073	0.0	7.3	27.5	9.9	7.7	5.5	51.3	28.2	2.0	23.1	0.0	36.4	-	6.8	27.5	15.0		-	26.0	25.7
2	2.24	2.45	0.063	0.033	0.049	0.0	5.8	19.8	9.5	7.9	6.1	44.2	32.7	1.7	23.5	19.2	40.7	-	14.9	44.4	18.5	19.0	-	36.8	23.9
3	2.24	2.54	0.070	0.034	0.049	0.0	5.8	12.6	8.1	9.4	7.2	38.1	39.8	2.2	24.6	18.2	42.4	-	14.8	45.1	19.5	22.0	-	47.2	35.7
4	2.24	2.54	0.066	0.044	0.047	20.0	5.8	23.2	11.0	8.4	6.4	49.9	-	1.9	25.8	17.8	25.0	-	15.0	27.2	24.0	11.0	-	42.4	23.9
5	2.24	2.53	0.066	0.044	0.073	20.0	7.3	27.5	11.2	8.7	6.7	55.0	40.0	1.7	26.7	10.1	25.4	-	15.2	19.8	20.0	11.5	-	36.8	35.5
6	2.24	2.76	0.086	0.034	0.056	0.0	5.8	4.9	6.7	12.1	11.4	35.1	50.8	2.9	30.1	19.8	47.0	-	12.6	53.9	28.0	21.0	-	40.2	28.5
7	2.24	2.76	0.093	0.009	0.073	20.0	5.8	7.4	11.2	13.5	11.5	43.5	55.5	2.4	36.1	19.6	31.0	-	13.4	37.0	29.0	14.5	-	44.8	28.3
8	2.24	2.76	0.091	0.005	0.077	20.0	7.3	14.5	12.6	13.1	10.9	51.1	44.5	2.5	36.6	8.2	37.1	-	13.9	31.2	-	--	-	46.0	46.0
9	2.24	2.98	0.080	0.002	0.056	20.0	7.3	2.1	6.8	15.5	15.0	39.3	59.6	3.8	37.3	21.6	37.1	-	15.1	43.1	33.0	-	-	58.7	43.4
10	2.24	2.98	0.105	0.002	0.083	20.0	8.2	1.0	5.8	13.7	17.4	37.7	59.3	4.4	36.8	20.8	35.0	-	14.2	41.3	30.0	18.0	-	78.3	55.9
11	2.64	2.43	0.070	0.044	0.065	0.0	5.8	37.5	24.0	9.2	8.9	78.6	50.1	1.8	42.1	9.8	46.8	-	5.2	53.0	26.0	25.0	-	30.0	36.1
12	2.64	2.43	0.063	0.019	0.073	20.0	5.8	39.5	31.0	8.8	8.7	87.1	49.5	1.3	48.6	5.0	27.1	-	3.5	30.2	30.0	15.0	-	34.0	27.3
13	2.64	2.43	0.063	0.019	0.038	25.0	5.8	37.7	19.4	8.1	8.3	72.2	44.4	1.1	35.8	10.5	21.5	-	9.9	22.9	27.0	16.0	-	31.3	25.8
14	2.64	2.54	0.077	0.009	0.039	25.0	5.8	35.5	17.7	10.1	9.9	72.3	51.0	1.6	37.7	14.6	24.4	-	11.4	27.7	28.0	20.0	-	47.5	22.9
15	2.64	2.70	0.077	0.002	0.004	40.0	5.8	31.6	15.7	10.9	10.1	67.5	53.1	2.1	36.7	17.3	14.4	-	13.2	18.5	28.0	18.5	-	49.0	25.3
16	2.64	2.78	0.085	0.009	0.004	40.0	5.8	31.3	17.3	12.9	11.8	72.7	58.8	2.3	41.9	17.7	18.6	-	13.5	22.6	31.5	9.0	-	60.3	22.1
17	2.64	3.05	0.077	0.009	0.004	40.0	8.2	12.0	10.9	16.5	19.9	59.1	70.4	6.7	47.3	19.1	31.7	-	12.6	38.1	-	-	-	-	-
18	2.64	3.05	0.049	0.055	0.041	60.0	5.8	5.1	12.7	17.5	16.4	51.7	66.4	3.7	46.6	19.2	6.0	-	14.4	10.6	35-45	16-20	-	64.8	15.9
19	2.64	3.05	0.049	0.034	0.047	72.0	5.8	9.8	13.3	16.6	15.7	55.3	64.8	3.6	45.6	18.8	0.1	-	15.0	2.6	35-40	10-21	-	77.8	-
20	2.64	3.21	0.063	0.034	0.044	35.0	8.2	1.4	5.3	7.2	17.9	31.5	52.4	5.0	30.3	18.6	18.9	-	15.4	21.9	61.0	15.0	-	85.6	35.7
21	2.94	2.50	0.080	0.000	0.040	60.0	5.8	40.7	37.3	10.3	8.4	96.8	59.3	2.7	56.1	4.1	6.3	-	4.1	8.3	29.0	32.0	-	35.7	5.8
22	2.94	2.50	0.077	0.000	0.041	50.0	5.8	40.2	47.6	10.4	8.0	106.1	61.8	1.9	65.9	1.4	19.7	-	3.9	17.1	21.0	27.0	-	42.4	8.7

Table A.1 – Sheet 2: Tabular presentation of cold model data (Figure 3.1) utilizing ZrO_2 with a median particle size of 142µm

Run no.	TSI (kg)	riser u_0 (m/s)	double exit ls u_0 (m/s)	double exit ls u_0 side (m/s)	Lower ls u_0 (m/s)	P_{BFB} (mbar)	A_{cv} (mm^2)	$\Delta P_{0\text{-}333mm}$ (mbar)	$\Delta P_{333\text{-}2621mm}$ (mbar)	$\Delta P_{2621\text{-}4328mm}$ (mbar)	$\Delta P_{4328\text{-}5090mm}$ (mbar)	$\Delta P_{riser\ total}$ (mbar)	$\Delta P_{upper\ st}$ (mbar)	$\Delta P_{cyclone}$ (mbar)	$\Delta P_{riser\ top}$ (mbar)	$\Delta P_{double\ ls}$ (mbar)	$\Delta P_{lower\ st}$ (mbar)	$P_{cyclone}$ (mbar)	$\Delta P_{lower\ ls}$ (mbar)	ΔP_{cv} (mbar)	Upper st height (m)	lower st height (m)	upper/lower standpipe status	$G_{s\ entrainment}$ (kh/m^2s)	$G_{s\ cv}$ (kg/m^2s)
23	2.94	2.76	0.091	0.000	0.041	60.0	5.8	35.5	30.4	15.4	12.3	93.7	69.9	2.8	58.2	10.5	16.1	-	8.3	19.0	36.0	13.5	-	52.2	22.6
24	2.94	2.76	0.094	0.000	0.041	50.0	5.8	37.0	32.7	13.9	11.6	95.1	67.5	2.6	58.2	8.5	20.7	-	6.8	23.5	36.0	13.5	-	56.0	18.8
25	2.94	2.87	0.108	0.000	0.049	50.0	5.8	23.8	19.6	20.1	18.3	81.8	81.1	4.5	58.0	19.8	30.7	-	13.6	37.2	40.5	17.0	-	65.7	30.8
26	2.94	2.87	0.106	0.000	0.071	40.0	5.8	26.8	20.9	20.4	19.7	87.8	85.0	5.0	61.0	20.1	40.5	-	12.2	48.6	46.0	17.0	-	63.6	49.3
27	2.94	2.98	0.105	0.018	0.064	50.0	5.8	22.4	16.3	17.1	24.2	80.1	84.1	9.0	57.7	18.5	34.4	-	13.1	40.1	47.0	19.0	-	127.6	44.6
28	2.94	2.98	0.105	0.000	0.065	65.0	5.8	23.3	17.2	17.8	23.7	82.1	84.6	9.1	58.8	17.8	24.2	-	12.8	29.5	45.0	13.5	-	117.5	38.1
29	2.94	3.09	0.094	0.000	0.047	70.0	5.8	14.9	11.8	14.2	21.7	62.6	74.5	9.5	47.7	17.8	14.3	-	14.8	17.6	32-39	13.5	-	127.3	30.9
30	2.94	3.09	0.105	0.000	0.059	10.0	5.8	3.8	6.1	7.5	16.5	33.9	58.4	8.4	30.1	21.1	44.5	-	14.3	51.5	50.0	13.5	-	121.8	78.8
31	2.94	3.20	0.091	0.024	0.059	30.0	8.2	6.4	7.4	8.8	18.7	41.3	60.3	8.0	34.9	18.7	35.1	-	15.5	38.2	50-62	30.0	-	114.2	31.1
32	3.24	-	0.056	0.000	0.041	65.0	5.8	37.7	24.0	11.0	10.1	82.8	56.8	1.6	45.0	11.7	0.8	-	8.0	1.1	41.0	42.0	-	53.9	1.1
33	3.24	2.76	0.070	0.000	0.043	65.0	5.8	37.1	46.2	16.7	14.7	114.7	76.5	1.9	77.6	2.9	22.8	-	4.8	19.2	36.0	16.0	-	57.1	36.3
34	3.24	2.87	0.088	0.000	0.044	70.0	5.8	33.3	27.1	20.2	19.1	99.7	82.6	3.1	66.4	14.9	19.4	-	11.3	23.0	43.0	21.5	-	65.3	40.1
35	3.24	2.98	0.094	0.000	0.049	70.0	5.8	29.6	21.8	19.7	24.7	95.8	88.5	6.9	66.2	17.2	20.7	-	12.3	25.6	50.0	18.5	-	89.7	40.4
36	3.24	3.03	0.095	0.007	0.062	52.0	5.8	23.1	18.5	18.2	25.9	85.8	85.7	7.2	62.7	18.6	34.4	-	12.6	40.0	53.0	18.0	-	117.0	54.8
37	3.24	3.12	0.095	0.007	0.062	62.0	5.8	26.5	20.1	17.1	27.8	91.6	88.1	9.2	65.0	16.2	30.7	-	11.8	34.6	54.0	22.0	-	162.9	48.7
38	3.24	3.20	0.098	0.007	0.065	65.0	5.8	26.3	19.6	15.8	28.3	89.9	87.3	9.9	63.7	15.0	29.9	-	11.5	32.9	51.0	20.0	-	243.7	42.6
39	3.24	3.32	0.098	0.007	0.071	50.0	8.2	19.0	14.9	12.3	24.3	70.6	78.9	10.0	51.6	16.0	37.6	-	12.3	40.7	42-62	20.0	-	-	72.4
40	3.64	2.98	0.096	0.000	0.041	70.0	5.8	33.5	33.4	21.3	23.7	111.9	93.2	5.8	78.4	11.1	29.1	-	9.1	31.0	60.0	41.0	-	92.8	59.0
41	3.64	2.98	0.099	0.000	0.041	70.0	5.8	35.1	37.9	21.4	23.8	118.1	95.1	5.5	83.1	9.2	29.8	-	7.9	30.8	56.0	41.0	-	92.8	54.8
42	3.64	3.09	0.101	0.000	0.041	75.0	5.8	31.6	29.3	19.8	28.4	109.1	94.9	7.3	77.5	12.2	27.9	-	10.6	29.5	56.0	41.0	-	123.3	64.0
43	3.64	3.09	0.106	0.000	0.049	65.0	8.2	30.2	25.3	18.4	25.1	99.0	93.4	9.9	68.8	14.5	34.3	-	11.4	37.3	66.0	31.0	-	123.3	73.2
44	3.64	3.20	-	-	-	-	-	30.3	29.2	19.0	27.2	105.7	96.4	9.9	75.4	11.7	33.6	-	10.6	34.5	-	-	-	139.0	73.5
45	3.64	3.20	-	-	-	-	-	30.5	29.0	19.2	25.5	104.2	97.0	10.0	73.7	11.6	30.5	-	9.4	32.5	-	-	-	141.7	58.4
46	3.64	3.32	-	-	-	-	-	26.3	22.9	16.7	27.9	93.8	92.7	13.8	67.5	10.0	39.2	-	10.0	41.8	-	-	-	-	-

Table A.2 – Sheet 1: Tabular presentation of cold model data (Figure 3.1) utilizing ZrO_2 with a median particle size of 230 µm

Run no.	TSI (kg)	riser u_0 (m/s)	double exit ls u_0 (m/s)	double exit ls u_0 side (m/s)	Lower ls u_0 (m/s)	P_{BFB} (mbar)	A_{cv} (mm^2)	$\Delta P_{0\text{-}333mm}$ (mbar)	$\Delta P_{333\text{-}2621mm}$ (mbar)	$\Delta P_{2621\text{-}4328mm}$ (mbar)	$\Delta P_{4328\text{-}5090mm}$ (mbar)	$\Delta P_{riser\ total}$ (mbar)	$\Delta P_{upper\ st}$ (mbar)	$\Delta P_{cyclone}$ (mbar)	$\Delta P_{riser\ top}$ (mbar)	$\Delta P_{double\ ls}$ (mbar)	$\Delta P_{lower\ st}$ (mbar)	$P_{cyclone}$ (mbar)	$\Delta P_{lower\ ls}$ (mbar)	ΔP_{cv} (mbar)	Upper st height (m)	lower st height (m)	upper/lower standpipe status	$G_{s\ entrainment}$ (kh/m^2s)	$G_{s\ cv}$ (kg/m^2s)
47	3.00	2.72	0.237	0.000	0.059	25.6	5.3	11.7	6.4	11.2	9.9	39.2	50.9	6.0	27.5	14.1	26.8	2.5	13.7	27.9	56.0	12.5	mov/ mov	56.4	35.3
48	3.00	2.87	0.244	0.000	0.053	33.6	5.3	13.7	7.8	9.9	11.5	42.8	52.3	9.0	29.2	11.1	23.1	3.1	13.1	21.7	52.0	16.5	mov/ mov	73.4	20.5
49	3.00	2.65	0.206	0.000	0.047	40.4	5.3	9.6	6.2	10.5	7.4	33.6	46.2	4.0	29.5	15.6	4.9	2.6	13.4	8.3	75.0	2.0	mov/ mov	36.9	17.9
50	3.00	2.65	0.212	0.000	0.047	39.3	5.3	8.9	7.1	10.9	7.3	34.3	48.4	4.0	27.5	16.4	7.2	2.6	13.2	11.5	69.0	2.0	mov/ mov	39.0	-
51	3.00	2.65	0.223	0.000	0.053	34.8	5.3	8.5	6.9	11.5	7.9	34.8	48.6	4.2	28.4	15.3	12.7	2.7	12.7	16.3	66.0	10.0	mov/ mov	43.4	30.6
52	3.00	2.54	0.220	0.000	0.049	34.8	5.3	17.6	10.5	10.1	6.7	44.9	47.5	3.7	29.2	13.9	12.7	2.5	12.6	14.9	52.0	13.0	mov/ mov	36.6	24.2
53	3.00	2.54	0.230	0.000	0.049	36.0	5.3	21.6	11.9	10.7	6.9	51.2	48.7	3.8	32.0	12.5	13.8	2.5	12.3	14.9	50.0	17.0	mov/ mov	42.8	-
54	-	2.54	0.230	0.000	0.049	36.8	5.3	32.3	17.7	10.3	6.7	66.9	50.0	3.7	36.7	9.1	14.2	2.2	9.1	15.1	34.0	13.0	mov/ mov	-	-
55	3.00	2.43	0.188	0.000	0.047	36.3	5.3	22.8	8.8	7.9	5.2	44.7	42.5	3.0	24.4	14.6	4.4	1.8	12.0	8.2	43.0	19.0	mov/ mov	30.0	21.6
56	3.00	2.43	0.202	0.000	0.047	37.4	5.3	26.2	12.5	8.1	5.4	52.1	44.0	3.1	28.5	12.4	5.6	1.7	10.5	8.7	-	-	bub/ mov	-	-
57	3.00	2.32	0.195	0.000	0.044	36.2	5.3	29.0	9.4	7.2	4.9	50.5	41.1	2.8	23.6	13.9	1.4	1.5	9.7	6.7	61.0	0.0	mov/ bub	29.9	7.9
58	3.00	2.65	0.223	0.000	0.047	44.8	5.3	26.9	13.4	10.8	7.2	58.3	52.6	4.0	33.9	14.0	7.5	2.0	12.9	9.7	51.0	3.0	mov/ bub	39.9	24.9
59	3.00	2.65	0.230	0.000	0.047	46.7	5.3	32.5	20.0	11.1	7.3	70.9	54.2	4.1	41.5	8.5	8.9	2.0	9.1	9.4	32.0	3.0	mov/ bub	43.7	23.8
60	2.94	2.76	0.209	0.000	0.041	46.8	5.3	11.6	8.3	8.8	9.5	38.2	46.6	6.2	29.5	10.1	1.0	2.4	10.1	2.9	70.0	0.0	mov/ bub	48.2	6.7
61	2.94	2.50	0.209	0.000	0.041	27.6	5.3	27.0	12.9	8.5	6.1	54.6	40.0	2.7	30.3	7.0	18.0	1.6	11.1	14.7	19.5	17.0	bub/ mov	32.1	37.8
62	3.25	2.54	0.216	0.000	0.022	29.4	5.3	18.0	9.4	10.4	7.8	45.6	46.5	3.0	30.7	12.3	18.4	1.8	12.2	19.5	31.5	22.0	mov/ mov	35.3	9.9

Table A.2 – Sheet 2: Tabular presentation of cold model data (Figure 3.1) utilizing ZrO_2 with a median particle size of 230 µm

Run no.	TSI (kg)	riser u_0 (m/s)	double exit ls u_0 (m/s)	double exit ls u_0 side (m/s)	Lower ls u_0 (m/s)	P_{BFB} (mbar)	A_{cv} (mm^2)	$\Delta P_{0\text{-}333mm}$ (mbar)	$\Delta P_{333\text{-}2621mm}$ (mbar)	$\Delta P_{2621\text{-}4328mm}$ (mbar)	$\Delta P_{4328\text{-}5090mm}$ (mbar)	$\Delta P_{riser\ total}$ (mbar)	$\Delta P_{upper\ st}$ (mbar)	$\Delta P_{cyclone}$ (mbar)	$\Delta P_{riser\ top}$ (mbar)	$\Delta P_{double\ ls}$ (mbar)	$\Delta P_{lower\ st}$ (mbar)	$P_{cyclone}$ (mbar)	$\Delta P_{lower\ ls}$ (mbar)	ΔP_{cv} (mbar)	Upper st height (m)	lower st height (m)	upper/lower standpipe status	$G_{s\ entrainment}$ (kh/m^2s)	$G_{s\ cv}$ (kg/m^2s)
63	3.25	2.65	0.236	0.000	0.047	37.6	5.3	33.1	27.8	12.2	8.8	81.9	59.8	4.2	52.1	4.0	23.2	1.8	4.7	23.8	40.0	9.0	mov/ bub	43.9	13.1
64	3.25	2.76	0.258	0.000	0.047	31.9	5.3	22.3	14.2	14.6	12.2	63.3	62.7	7.1	44.4	10.1	33.6	2.0	11.8	32.7	47.0	17.0	mov/ mov	59.2	22.6
65	3.25	2.87	0.279	0.000	0.071	36.5	5.3	19.9	12.6	13.3	15.8	61.5	65.3	9.8	45.4	8.6	33.6	2.4	11.9	31.1	49.5	16.0	mov/ bub	-	21.2
66	3.25	2.98	0.282	0.000	0.059	35.3	5.3	16.9	13.8	12.2	16.0	59.0	66.6	9.9	45.8	7.6	37.2	2.6	11.8	33.8	41.0	17.5	mov/ mov	-	30.3
67	3.25	3.09	0.282	0.000	0.059	34.5	5.3	13.3	12.9	9.5	16.8	52.5	64.3	12.7	42.8	7.5	37.2	2.9	12.6	32.8	46.0	14.0	not stable	-	40.8
68	3.65	2.76	0.216	0.000	0.047	31.6	5.3	10.7	6.8	11.7	8.2	37.4	49.6	4.4	29.3	14.8	18.2	2.0	13.8	20.3	66.0	19.0	mov/ mov	41.2	27.2
69	3.65	2.87	0.230	0.000	0.047	38.8	5.3	13.2	7.4	11.1	11.9	43.6	53.4	6.6	33.4	12.2	16.8	2.2	13.2	16.9	50.5	20.8	not stable	-	-
70	3.65	2.87	0.258	0.000	0.084	36.5	5.3	17.2	11.8	15.0	13.3	57.3	64.1	7.5	43.5	11.9	29.7	2.3	12.9	29.6	64.0	12.0	mov/ bub	82.9	35.7
71	3.65	2.87	0.272	0.000	0.084	36.0	5.3	29.2	19.7	15.8	13.0	77.6	69.2	6.9	52.3	9.3	35.6	2.2	10.6	34.9	42.0	16.0	mov / bub	75.0	36.0
72	3.65	2.87	0.286	0.000	0.084	38.2	5.3	31.9	29.6	16.2	13.0	90.7	72.7	6.8	62.8	3.0	38.7	2.3	5.7	36.3	31.5	17.5	bub/ bub	69.4	37.9
73	3.65	2.98	0.314	0.000	0.090	39.9	5.3	27.7	17.7	16.9	19.8	82.1	76.4	9.9	58.6	6.3	42.4	2.7	10.7	38.6	39.0	18.5	bub/ bub	78.3	48.1
74	3.65	3.09	0.314	0.000	0.071	38.5	5.3	23.7	16.7	15.7	19.4	75.5	73.5	12.7	56.0	6.3	41.7	2.7	11.3	37.3	36.0	19.0	bub/ bub	84.4	41.4
75	3.65	3.20	0.317	0.000	0.071	39.4	5.3	17.8	17.2	12.4	21.1	68.6	72.4	16.4	54.8	5.0	41.4	3.1	11.1	35.9	35.0	17.5	bub/ bub	123.3	32.2
76	3.95	2.98	0.346	0.000	0.071	28.0	5.3	25.5	31.0	19.0	21.2	96.7	89.3	9.9	75.7	1.9	72.2	4.0	14.6	64.0	43.5	40.0	bub/ mov	88.9	67.6
77	3.95	3.09	0.377	0.000	0.078	46.4	5.3	28.7	38.0	20.2	22.2	109.1	93.6	12.7	84.8	0.3	60.8	3.4	6.3	49.0	45.0	23.0	bub/ bub	85.8	-
78	3.95	3.20	0.390	0.000	0.084	28.7	5.3	24.9	35.2	16.5	21.5	98.1	91.9	16.4	77.4	0.2	77.8	3.5	6.7	65.5	47.0	25.0	bub/ bub	103.5	43.8

Table A.2 – Sheet 3: Tabular presentation of cold model data (Figure 3.1) utilizing ZrO_2 with a median particle size of 230 μm

Run no.	TSI [kg]	riser u_0 [m/s]	double exit ls u_0 [m/s]	double exit ls u_0 side [m/s]	Lower ls u_0 (m/s)	P_{BFB} (mbar)	A_{cv} (mm^2)	$\Delta P_{0\text{-}333mm}$ (mbar)	$\Delta P_{333\text{-}2621mm}$ (mbar)	$\Delta P_{2621\text{-}4328mm}$ (mbar)	$\Delta P_{4328\text{-}5090mm}$ (mbar)	$\Delta P_{riser\ total}$ (mbar)	$\Delta P_{upper\ st}$ (mbar)	$\Delta P_{cyclone}$ (mbar)	$\Delta P_{riser\ top}$ (mbar)	$\Delta P_{double\ ls}$ (mbar)	$\Delta P_{lower\ st}$ (mbar)	$P_{cyclone}$ (mbar)	$\Delta P_{lower\ ls}$ (mbar)	ΔP_{cv} (mbar)	Upper st height (m)	lower st height (m)	upper/lower standpipe status	$G_{s\ entrainment}$ (kh/m^2s)	$G_{s\ cv}$ (kg/m^2s)
79	3.95	3.32	0.411	0.000	0.084	28.0	5.3	18.6	28.8	14.2	21.4	83.0	89.6	21.2	68.4	0.3	78.1	4.8	8.5	65.5	50.0	25.0	bub/ bub	101.0	96.2
80	3.95	3.43	0.443	0.000	0.081	29.0	5.3	10.0	29.9	14.0	20.2	74.1	92.5	27.4	68.0	0.4	80.9	4.9	9.0	67.5	52.0	35.0	bub/ bub	142.9	106.7
81	3.95	3.54	0.460	0.000	0.094	29.4	5.3	1.3	29.6	13.2	20.0	64.1	94.4	35.4	66.3	0.7	82.2	5.3	9.4	69.4	0.0	0.0	bub/ bub	-	-
82	3.95	3.54	0.460	0.094	0.094	30.2	5.3	0.2	31.6	13.9	19.4	65.2	96.9	35.4	66.8	0.5	83.6	5.3	8.7	71.1	59.0	40.0	bub/ bub	109.8	-
83	2.24	2.54	0.146	0.024	0.059	38.7	5.3	22.5	9.7	8.4	5.6	46.2	47.5	3.1	25.9	17.5	5.0	1.7	13.2	10.4	25.0	0.0	bub/ bub	51.5	26.2
84	2.24	2.65	0.209	0.024	0.071	38.6	5.3	19.2	11.8	11.7	7.6	50.3	51.5	4.1	33.7	13.2	14.9	1.9	14.1	15.0	40.0	27.0	bub/ bub	32.4	26.7
85	2.24	2.76	0.230	0.024	0.071	36.2	5.3	12.8	8.0	13.7	10.1	44.6	53.5	7.1	34.5	11.1	22.2	2.2	14.4	19.8	20.0	9.0	bub/ bub	40.0	32.5
86	2.24	2.87	0.244	0.024	0.071	35.9	5.3	15.3	6.8	10.0	12.7	44.8	50.8	8.2	32.5	9.4	21.8	2.5	14.4	17.8	14.0	9.0	bub/ bub	50.0	23.4
87	2.24	2.98	0.258	0.024	0.084	35.0	5.3	17.0	8.7	8.4	15.6	49.7	53.1	9.4	35.9	6.5	26.7	2.9	13.0	20.9	20.0	10.0	bub/ bub	98.0	32.7
88	2.64	2.76	0.314	0.000	0.071	39.1	5.3	27.3	17.8	16.8	14.3	76.1	66.1	7.4	52.2	6.0	34.3	2.8	11.5	29.3	29.0	13.5	bub/ bub	41.4	47.1
89	2.64	2.87	0.328	0.000	0.084	39.9	5.3	25.7	13.7	13.7	17.9	71.1	63.7	9.4	49.0	4.9	33.3	3.1	11.9	26.7	36.0	15.0	bub/ bub	44.5	45.8
90	2.64	2.98	0.349	0.000	0.084	34.7	5.3	24.1	13.6	10.7	19.3	67.8	62.5	9.9	47.3	4.1	38.8	3.5	11.7	31.3	29.0	13.0	bub/ bub	50.9	46.5
91	2.64	3.09	0.356	0.000	0.090	36.1	5.3	23.0	14.7	9.7	19.4	66.9	63.2	12.7	47.4	3.3	38.6	3.7	11.0	30.7	35.0	21.0	bub/ bub	50.0	53.4
92	2.64	3.20	0.363	0.000	0.090	35.9	5.3	20.0	14.6	8.5	19.8	62.9	63.7	16.4	46.5	3.1	40.1	4.0	11.3	31.9	28.0	18.0	bub/ bub	66.6	45.9

Annex B: 10 kW_{th} IFK DFB facility (stand 2010) dimensions

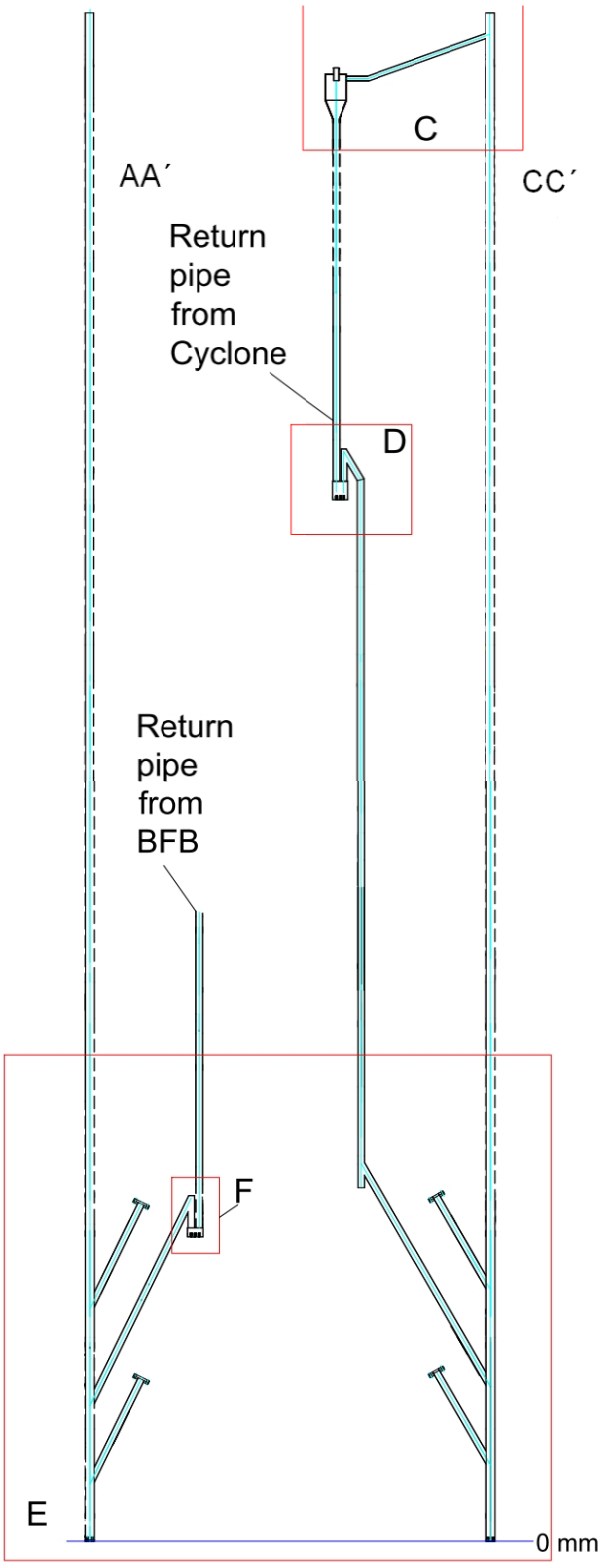

Figure B.1: Geomertical details of riser components

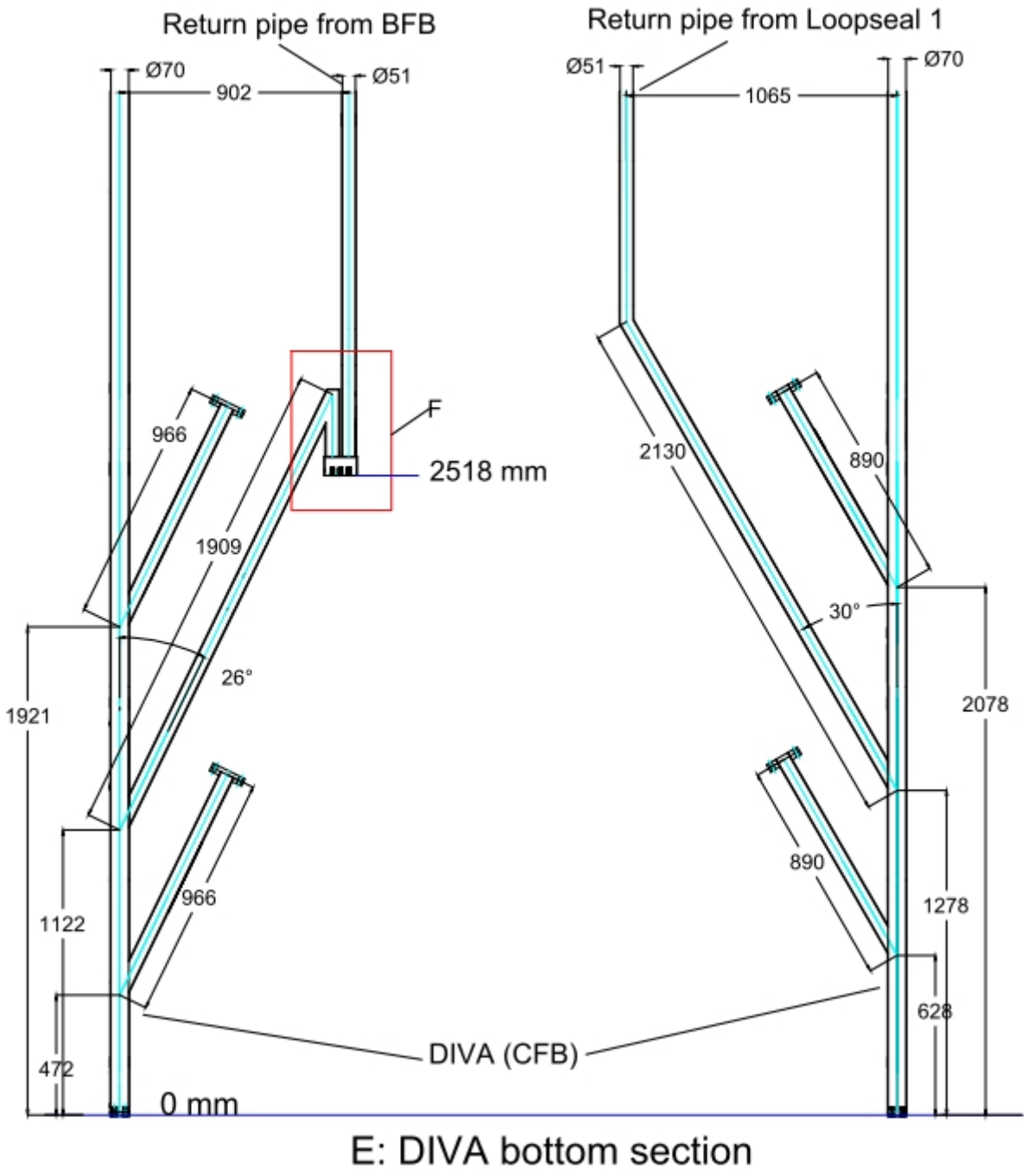

Figure B.2: Details of loop seal return legs

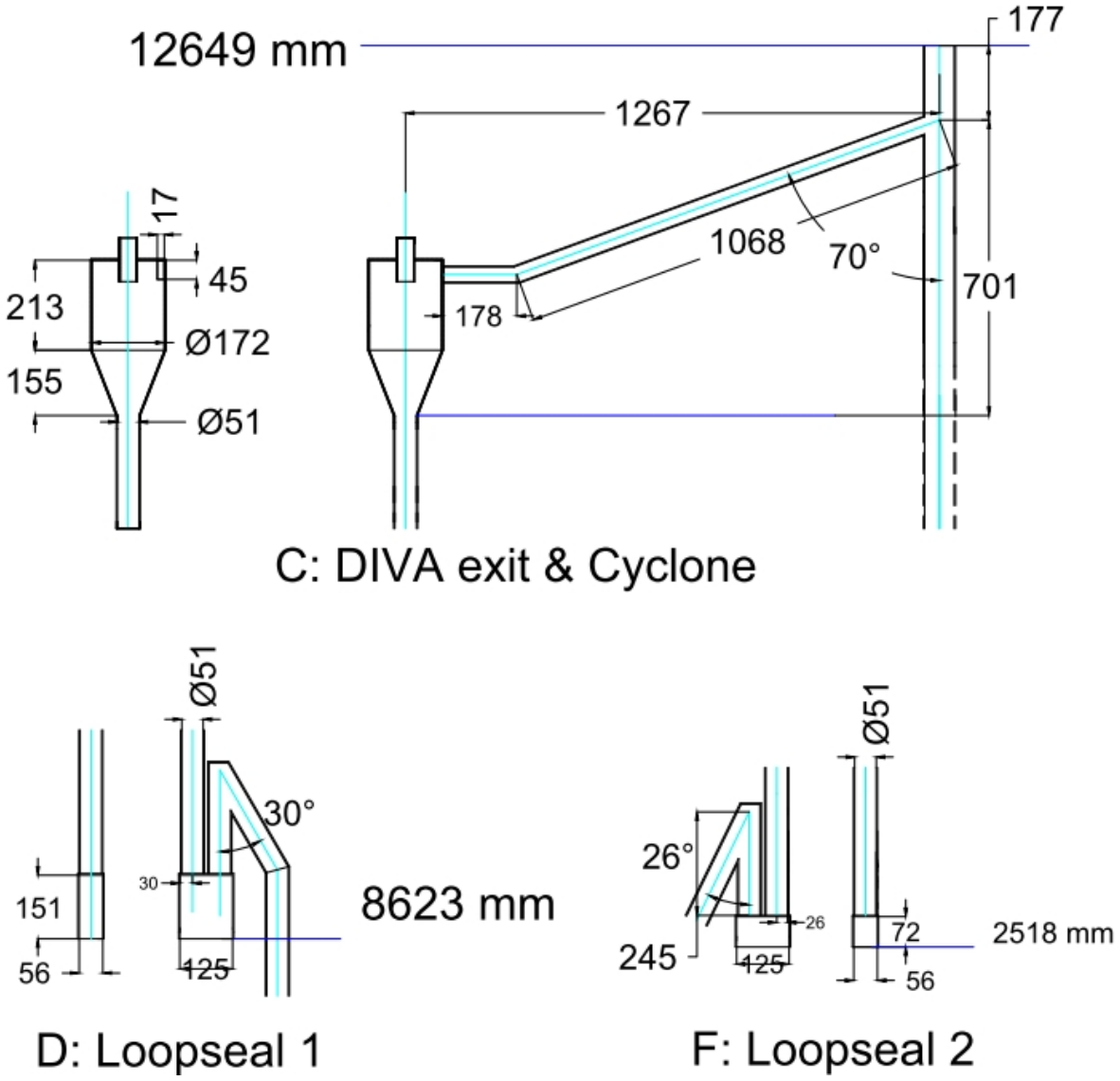

Figure B.3: Details of riser exits, cyclones and loop seals

Annex C Tabular result presentation of the IFK(CFB) setting

Run no.	V_{N2} (m_N^3/h)	V_{CO2} (m_N^3/h)	ν_{CO2} (%)	carbonator u_0 (m/s)	dp_{50} (µm)	T_{carb} (°C)	$\Delta P_{riser\ total}$ (mbar)	F_{CO2} (mol/h)	E_{eq} (%)	$\nu_{CO2,out}$ (%)	E_{carb} (%)	$E_{carb\ 730mm}/E_{carb}$ (-)	E_{carb}/E_{eq} (-)	τ (h)	F_{Ca}/F_{CO2} (mol_{Ca}/mol_{CO2})	X_{carb} (mol_{CaCO3}/mol_{Ca})	X_{calc} (mol_{CaCO3}/mol_{Ca})	$X_{max,ave}$ (mol_{CaCO3}/mol_{Ca})	t*(s)	f_{active} (-)	$\tau_{active,B}$ (s)	$t_{reg}/X_{carb\ meas}$.(h)	$t_{reg}/X_{carb\ calc}$.(h)
1	15.29	1.97	11.4	4.1	170	651	58	87.8	90.2	1.26	88.13	-	97.66	0.46	-	15.91	12.04	15.94	20.6	-	-	-	0.08
2	21.01	2.68	11.3	5.6	350	648	61	119.5	90.7	1.51	86.29	-	95.11	0.36	5.57	15.74	0.51	13.01	123.2	0.41	69.3	0.28	0.28
3	21.50	2.74	11.3	5.8	350	650	100	122.3	90.3	1.55	85.57	91.8	94.76	0.57	17.40	9.93	5.28	10.05	60.8	0.40	83.3	0.21	0.20
4	15.99	2.06	11.4	4.3	170	651	68	91.9	90.2	1.75	83.98	-	93.14	0.52	-	10.43	-	12.10	121.5	-	-	-	-
5	21.50	2.74	11.3	5.8	350	651	59	122.3	90.3	1.80	83.42	-	92.42	0.35	14.64	7.48	0.70	11.63	112.9	0.73	107.0	0.30	0.36
6	15.99	2.06	11.4	4.3	170	651	66	91.9	90.2	1.84	83.04	-	92.05	0.50	-	13.22	11.18	12.97	16.4	-	-	-	0.06
7	21.01	2.68	11.3	5.6	350	646	69	119.5	91.3	1.79	83.68	-	91.69	0.40	5.57	27.37	1.74	14.56	103.6	0.33	69.3	0.15	0.26
8	21.51	2.74	11.3	5.8	350	651	92	122.3	90.2	1.94	81.83	89.5	90.68	0.53	18.76	5.15	0.36	8.49	111.4	0.67	107.5	0.37	0.40
9	21.50	2.74	11.3	5.8	350	650	56	122.3	90.4	2.24	79.51	-	88.00	0.33	11.96	8.99	1.53	9.45	91.2	0.60	67.4	0.28	0.32
10	21.50	2.74	11.3	5.8	350	650	60	122.3	90.3	2.71	75.33	-	83.39	0.35	8.61	10.06	0.34	12.02	97.1	0.48	73.6	0.33	0.37
11	15.29	1.97	11.4	4.1	170	650	56	87.8	90.4	2.73	74.34	-	82.24	0.44	-	15.66	5.11	13.88	62.5	-	-	-	0.25
12	21.50	2.74	11.3	5.8	350	650	107	122.3	90.4	2.82	74.25	82.1	82.15	0.41	13.07	9.54	5.94	9.79	38.6	0.29	41.9	0.23	0.14
13	21.51	2.74	11.3	5.8	350	650	78	122.3	90.3	2.76	74.05	90.6	81.99	0.44	13.81	5.58	0.21	8.68	96.7	0.57	78.6	0.43	0.44
14	21.50	2.74	11.3	5.7	350	648	71	122.3	90.7	2.91	73.53	-	81.05	0.41	7.41	14.23	0.50	14.98	92.8	0.37	82.2	0.24	0.33
15	21.52	2.81	11.6	5.8	350	650	49	125.5	90.5	3.04	72.30	99.7	79.86	0.27	12.71	9.74	3.16	9.55	62.5	0.56	52.1	0.23	0.27
16	21.49	2.74	11.3	5.7	350	648	62	122.3	90.7	3.23	70.81	-	78.05	0.36	8.83	10.95	0.65	12.61	86.8	0.45	72.8	0.28	0.36
17	21.52	2.81	11.6	5.8	350	649	57	125.5	90.8	3.19	70.56	100.9	77.68	0.32	6.71	13.99	3.14	12.32	67.6	0.33	46.3	0.26	0.27

Run no.	V_{N2} (m_N^3/h)	V_{CO2} (m_N^3/h)	ν_{CO2} (%)	carbonator u_0 (m/s)	dp_{50} (µm)	T_{carb} (°C)	$\Delta P_{riser\ total}$ (mbar)	F_{CO2} (mol/h)	E_{eq} (%)	$\nu_{CO2,out}$ (%)	E_{carb} (%)	$E_{carb\ 730mm}/E_{carb}$ (-)	E_{carb}/E_{eq} (-)	τ (h)	F_{Ca}/ F_{CO2} mol_{Ca}/mol_{CO2})	X_{carb} (mol_{CaCO3}/ mol_{Ca})	X_{calc} (mol_{CaCO3}/ mol_{Ca})	$X_{max,ave}$ (mol_{CaCO3}/ mol_{Ca})	t*(s)	f_{active} (-)	$\tau_{active,B}$ (s)	$t_{reg}/X_{carb\ meas.}$(h)	$t_{reg}/X_{carb\ calc.}$(h)
18	21.50	2.74	11.3	5.8	350	650	95	122.3	90.4	3.26	69.97	84.4	77.43	0.55	12.00	7.46	2.52	10.09	68.8	0.41	68.1	0.34	0.29
19	15.99	2.06	11.4	4.3	170	651	57	91.8	90.1	3.81	69.25	-	76.82	0.43		9.63	0.79	11.67	79.4	-	-	-	0.45
20	21.51	2.74	11.3	5.8	350	650	66	122.3	90.4	3.45	67.62	95.2	74.82	0.38	15.46	5.51	1.51	9.50	75.1	0.57	74.4	0.37	0.34
21	21.51	2.74	11.3	5.8	350	650	93	122.3	90.4	3.88	64.01	86.2	70.84	0.54	11.96	8.05	0.30	9.68	81.8	0.40	74.3	0.29	0.42
22	21.52	2.81	11.6	5.8	350	650	59	125.5	90.6	4.19	61.78	104.0	68.16	0.33	10.36	11.17	3.71	9.64	49.3	0.35	39.9	0.22	0.27
23	21.50	2.74	11.3	5.7	350	650	90	122.3	90.5	4.51	57.88	87.6	63.98	0.52	7.89	7.71	0.23	9.02	76.4	0.28	46.5	0.45	0.45
24	21.49	2.74	11.3	5.7	350	648	60	122.2	90.9	4.62	57.91	-	63.72	0.35	5.88	11.87	0.20	10.77	75.6	0.30	40.3	0.38	0.45
25	21.52	2.81	11.6	5.8	350	649	66	125.5	90.7	5.26	51.62	103.8	56.90	0.37	4.82	11.08	4.51	9.94	39.1	0.13	17.5	0.42	0.26
26	15.29	1.97	11.4	4.1	170	650	76	87.8	90.4	2.75	74.80	-	82.76	0.60	-	-	11.18	13.21	15.2	-	-	-	-
27	21.52	2.81	11.6	5.8	350	648	69	125.5	91.0	1.44	86.38	96.1	94.97	0.39	8.41	15.22	17.36	12.32	-	-	-	0.19	-
28	15.99	2.06	11.4	4.3	170	652	63	91.9	90.1	2.19	80.01	-	88.79	0.48	-	9.34	-	11.93	110.2	-	-	-	-
29	15.99	2.06	11.4	4.3	170	652	78	91.9	90.1	1.61	85.31	-	94.66	0.59	-	8.78	-	11.81	126.2	-	-	0.62	-
30	15.99	2.06	11.4	4.3	170	652	70	91.8	90.1	3.07	75.38	-	83.67	0.53	-	12.35	-	11.52	94.4	-	-	-	-
31	21.52	2.81	11.6	5.8	350	652	74	125.4	90.0	1.77	83.58	92.4	92.62	0.42	18.12	7.64	3.34	9.87	79.3	0.62	91.1	-	-
32	21.52	2.81	11.6	5.8	350	652	85	125.5	90.0	1.60	85.13	92.9	94.33	0.48	19.92	7.30	3.75	10.28	79.5	0.60	106.3	0.26	-
33	21.51	2.74	11.3	5.8	350	650	85	122.3	90.0	2.49	76.92	88.0	85.11	0.49	15.46	8.18	0.25	-	-	-	-	-	0.42
34	20.01	2.56	11.3	5.3	350	645	82	114.2	91.4	3.19	69.80	-	76.40	0.50	-	7.16	1.10	11.86	82.4	-	-	-	-
35	20.51	2.64	11.4	5.5	350	648	80	117.8	90.8	2.74	74.34	-	81.89	0.47	-	5.80	0.30	8.99	94.9	-	-	-	-
36	21.02	2.66	11.2	5.6	350	650	87	118.8	90.2	1.81	82.94	-	91.95	0.51	-	5.19	0.22	8.84	117.4	-	-	-	-
37	22.01	2.79	11.2	5.9	350	649	82	124.4	90.4	1.70	84.29	-	93.22	0.46	-	5.33	0.28	8.78	119.1	-	-	-	-
38	20.00	3.73	15.7	5.6	350	649	87	166.3	93.5	7.26	54.92	-	58.72	0.37	6.80	10.90	0.82	12.04	47.1	0.21	34.2	-	-
39	19.69	3.67	15.7	5.5	350	650	91	163.7	93.3	5.07	67.33	-	72.13	0.39	7.48	10.41	0.48	9.98	57.0	0.26	36.7	-	-
40	21.00	3.61	14.7	5.8	350	649	101	161.2	93.1	5.84	59.01	-	63.41	0.44	4.32	8.83	0.93	17.28	55.2	0.14	38.2	-	-

Run no.	V_{N2} (m_N^3/h)	V_{CO2} (m_N^3/h)	ν_{CO2} (%)	carbonator u_0 (m/s)	dp_{50} (µm)	T_{carb} (°C)	$\Delta P_{riser\ total}$ (mbar)	F_{CO2} (mol/h)	E_{eq} (%)	$\nu_{CO2,out}$ (%)	E_{carb} (%)	$E_{carb\ 730mm}/E_{carb}$ (-)	E_{carb}/E_{eq} (-)	τ (h)	F_{Ca}/ F_{CO2} mol_{Ca}/mol_{CO2})	X_{carb} (mol_{CaCO3}/ mol_{Ca})	X_{calc} (mol_{CaCO3}/ mol_{Ca})	$X_{max,ave}$ (mol_{CaCO3}/ mol_{Ca})	t*(s)	f_{active} (-)	$\tau_{active,B}$ (s)	$t_{reg}/X_{carb\ meas}$.(h)	$t_{reg}/X_{carb\ calc}$.(h)
41	21.49	3.70	14.7	6.0	350	651	92	165.0	92.7	2.45	83.45	-	90.01	0.40	6.43	11.20	0.50	11.51	82.6	0.31	51.2	-	-
42	20.50	3.46	14.4	5.7	350	650	93	154.3	92.7	3.82	72.00	-	77.67	0.42	7.05	10.96	0.51	12.67	69.1	0.27	52.8	-	-
43	19.49	2.26	10.4	5.1	350	648	81	100.7	89.8	4.07	55.54	-	61.82	0.56	7.52	19.26	15.00	17.40	12.0	0.04	15.3	-	-
44	19.49	2.25	10.4	5.2	350	649	69	100.6	89.6	3.05	66.26	-	73.96	0.48	13.45	11.21	0.52	14.22	96.5	0.53	129.8	-	-
45	19.49	2.33	10.7	5.2	350	650	84	104.0	89.8	1.94	79.28	-	88.30	0.56	15.48	8.04	0.30	12.17	118.1	0.59	146.7	-	-

-

Notice: Gray shaded lines correspond to experimental runs where the pressure might have been underestimated by up to 30 mbar due to problems in the pressure transducer connections. This error propagates to some calculated values that use the carbonator pressure drop ($\Delta P_{riser\ total}$).

Annex D: Tabular result presentation of the IFK (BFB) setting

Run no.	V_{N2} (m_N^3/h)	V_{CO2} (m_N^3/h)	ν_{CO2} (%)	carbonator u_0 (m/s)	dp_{50} (µm)	T_{carb} (°C)	$\Delta P_{BFB\ total}$ (mbar)	F_{CO2} (mol/h)	E_{eq} (%)	$\nu_{CO2,out}$ (%)	E_{carb} (%)	E_{carb}/E_{eq} (-)	τ (h)	F_{Ca}/F_{CO2} (mol_{Ca}/mol_{CO2})	X_{carb} (mol_{CaCO3}/ mol_{Ca})	X_{calc} (mol_{CaCO3}/ mol_{Ca})	$X_{max,ave}$ (mol_{CaCO3}/ mol_{Ca})	t*(s)	f_{active} (-)	$\tau_{active,B}$ (s)
1	4.23	0.80	15.8	0.5	350	659	27	35.5	91.7	0.86	93.43	101.88	1.41	16.92	7.55	2.96	-	-	-	-
2	6.95	1.29	15.7	0.8	350	663	24	57.7	91.2	1.47	85.42	93.72	0.61	15.37	9.18	0.61	-	-	-	-
3	6.97	1.22	14.9	0.8	350	662	23	54.5	90.8	2.68	80.72	88.87	0.64	-	13.81	0.21	-	-	-	-
4	6.97	1.22	14.9	0.8	350	661	23	54.5	91.0	3.45	75.28	82.73	0.74	6.25	12.51	-	-	-	-	-
5	6.97	1.22	14.9	0.8	350	662	25	54.5	90.6	1.67	88.05	97.20	0.76	10.03	8.04	-	-	-	-	-
6	6.99	1.22	14.9	0.8	350	661	25	54.7	91.1	1.88	86.63	95.13	0.71	5.76	5.14/9.10	2.72	18.5	282.4	0.47	222.33
7	6.98	1.23	14.9	0.8	350	660	25	54.8	91.3	3.25	76.81	84.13	0.72	5.65	11.98/11.60	0.34	23.2	255.2	0.43	256.20
8	6.98	1.23	14.9	0.8	350	660	24	54.8	91.2	4.52	67.45	73.96	0.68	5.64	11.82/11.5	0.00	-	-	-	-
9	6.98	1.23	14.9	0.8	350	658	23	54.8	91.6	6.33	54.22	59.17	0.64	4.02	11.74/11.3	0.00	14.3	188.6	0.28	92.31
10	6.98	1.23	14.9	0.8	350	660	25	54.8	91.2	2.28	84.00	92.07	0.71	10.87	10.23/9.40	0.00	34.2	303.3	0.72	635.55
11	8.98	1.55	14.7	1.0	350	662	21	69.2	90.6	2.63	81.86	90.32	0.45	7.18	13.25/10.50	0.72	20.9	281.2	0.71	242.43
12	8.99	1.67	15.7	1.0	350	658	22	74.7	92.1	1.57	90.07	97.82	0.44	14.30	5.64	-	-	-	-	-
13	8.98	1.70	15.9	1.0	350	657	21	75.7	92.3	4.78	68.88	74.64	0.41	5.64	10.47	-	-	-	-	-
14	8.98	1.70	15.9	1.0	350	657	20	76.1	92.4	7.26	50.91	55.09	0.38	3.80	11.80/12.20	-	-	-	-	-
15	11.97	2.03	14.5	1.3	350	656	19	90.5	91.7	1.86	87.03	94.93	0.45	16.38	5.64	0.58	-	-	-	-
16	11.97	1.79	13.0	1.3	350	655	20	79.9	90.7	2.10	83.54	92.09	0.57	17.95	-	-	-	-	-	-
17	11.97	2.12	15.0	1.3	350	654	19	94.6	92.4	3.46	76.53	82.83	0.43	12.46	7.24	-	-	-	-	-

Run no.	V_{N2} (m_N^3/h)	V_{CO2} (m_N^3/h)	ν_{CO2} (%)	carbonator u_0 (m/s)	dp_{50} (µm)	T_{carb} (°C)	$\Delta P_{BFB\ total}$ (mbar)	F_{CO2} (mol/h)	E_{eq} (%)	$\nu_{CO2,out}$ (%)	E_{carb} (%)	E_{carb}/E_{eq} (-)	τ (h)	F_{Ca}/F_{CO2} mol_{Ca}/mol_{CO2})	X_{carb} (mol_{CaCO3}/mol_{Ca})	X_{calc} (mol_{CaCO3}/mol_{Ca})	$X_{max,ave}$ (mol_{CaCO3}/mol_{Ca})	t*(s)	f_{active} (-)	$\tau_{active,B}$ (s)
18	11.97	1.92	13.8	1.3	350	651	18	85.8	92.3	5.57	57.57	62.36	0.41	8.46	7.63/7.00	0.54	11.8	196.9	0.68	118.01
19	11.97	2.02	14.4	1.3	350	651	18	90.0	92.6	7.68	42.80	46.23	0.47	4.79	8.4/7.10	0.21	20.9	170.4	0.38	135.29
20	6.96	1.33	16.0	0.8	350	654	22	59.3	92.9	1.06	90.86	97.82	0.54	34.49	6.32	-	-	-	-	-
21	6.97	1.34	16.1	0.7	350	628	23	59.7	96.1	1.06	92.90	96.65	0.55	13.61	6.42	-	-	-	-	-
22	6.97	1.33	16.0	0.8	350	747	20	59.4	49.5	5.70	59.61	120.44	0.49	21.02	3.34	-	-	-	-	-
23	6.97	1.20	14.7	0.8	350	703	21	53.6	77.5	2.19	76.86	99.21	0.57	27.90	4.17	-	-	-	-	-
24	6.97	1.20	14.7	0.8	350	747	22	53.6	44.5	5.79	54.74	123.13	0.58	27.78	2.65	-	-	-	-	-
25	4.98	2.12	29.9	0.7	350	667	25	94.6	95.8	1.95	93.95	98.08	0.43	-	13.12	2.94	-	-	-	-
26	4.99	2.12	29.8	0.7	350	665	25	94.6	96.0	2.09	93.84	97.77	0.42	-	13.18	-	-	-	-	-
27	4.99	1.99	28.6	0.6	350	659	25	88.9	96.2	7.52	74.63	77.57	0.46	4.43	14.50	-	-	-	-	-
28	4.98	2.12	29.9	0.7	350	656	26	94.7	96.7	12.37	58.28	60.26	0.43	2.40	16.28	-	-	-	-	-
29	4.98	1.29	20.6	0.6	350	658	26	57.6	94.4	1.21	94.03	99.66	0.76	-	9.02	1.00	-	-	-	-
30	4.98	0.95	16.1	0.5	350	655	26	42.6	92.7	1.00	93.35	100.65	0.99	10.74	6.32	-	-	-	-	-
31	4.98	0.88	15.0	0.5	350	656	26	39.2	92.0	1.22	91.24	99.17	1.06	8.48	-	-	-	-	-	-
32	4.98	0.99	16.5	0.6	350	655	25	44.0	93.1	4.25	71.64	76.96	0.93	2.44	14.45	-	-	-	-	-
33	4.98	0.97	16.4	0.6	350	655	26	43.5	92.9	5.38	66.12	71.16	1.01	2.46	-	-	-	-	-	-
34	1.48	2.20	59.8	0.3	350	675	39	98.4	98.5	0.26	99.58	101.05	0.73	-	21.05	4.84	-	-	-	-
35	1.49	1.80	54.7	0.3	350	731	36	80.1	94.3	1.80	96.77	102.61	0.82	10.51	9.20	-	-	-	-	-
36	1.49	2.17	59.4	0.4	350	743	36	97.1	93.9	3.12	95.66	101.79	0.68	8.79	12.89	2.00	-	-	-	-
37	1.49	2.16	59.2	0.4	350	786	34	96.3	85.3	7.20	89.47	104.94	0.64	13.45	7.91	1.26	-	-	-	-

Literature

[1] Intergovernmental Panel on Climate Change (IPCC): Climate Change 2007: Impacts, Adaptation and Vulnerability. Cambridge, United Kingdom: Cambridge University Press, 2007

[2] International Energy Agency (IEA): World Energy Outlook 2010 (WEO 2010). Paris, France: 2010

[3] Khatib, H.: IEA World Energy Outlook–A comment. Energy Policy 39 (2011) 5, p. 2507-2511

[4] Florin, N.; Fennell, P.: Carbon Capture Technology: future fossil fuel use and mitigating climate change. Grantham Institute for climate change 3 (2010), p. 1-20

[5] European Commission. on-line content (2011), website: http://ec.europa.eu/research/energy/eu/research/ccs/background/index_en.htm

[6] Scheffknecht, G.: Combustion & Firing Systems I (Course material). Stuttgart, Germany: University of Stuttgart, 2011

[7] Brechtel, K.; Schäffer, A.; Scheffknecht, G.: Experimental Investigations of Amine Solvents in a Laboratory Column for CO_2-Scrubbing from Flue Gases of Power Plants. Achema, Frankfurt am Main, Germany: 2009

[8] Kemper, J.; Ewert, G.; Grünewald, M.: Absorption and regeneration performance of novel reactive amine solvents for post-combustion CO_2 capture. Energy Procedia 4 (2011), p. 232-239

[9] Kozak, F.; Petig, A.; Morris Ed.; Rhudy, R.; Thimsen, D.: Chilled ammonia process for CO_2 capture. Energy Procedia 1 (2009) 1, p. 1419-1426

[10] Gal, E.: Ultra cleaning combustion gas including the removal of CO_2. World Intellectual Property (2010), Patent WO 2006022885

[11] Shimizu, T.; Hirama, T.; Hosoda, H.; Kitano, K.; Inagaki, M.; Tejima, K.: A twin fluid-bed reactor for removal of CO_2 from combustion processes. Trans. IChemE 77 (1999) 1, p. 62- 68

[12] Abanades, J.C.; Anthony, E.J.; Wang, J.; Oakey, J.E.: Fluidized Bed Combustion Systems Integrating CO_2 Capture with CaO. Environ. Sci. Technol. 39 (2005) 8, p. 2861-2866

[13] Park, Y.C.; Sung-Ho, J.; Ryu, C.K.; Yi, C.K.: Demonstration of pilot scale carbon dioxide capture system using dry regenerable sorbents to the real coal-fired power plant in Korea. Energy Procedia 4 (2011), p. 1508-1512

[14] Harrison, D.: The role of solids in CO_2 capture: a mini review. Proceedings of the 7th International Conference on Greenhouse Gas Control Technologies. Vancouver, Canada: 2007

[15] Karg, J.: IGCC experience and further developments to meet CCS market needs (Siemens presentation). COAL-GEN, Katowice, Poland: 2009

[16] Weimer, T.; Berger, R.; Hawthorne, C.; Abanades, J.C.: Lime enhanced gasification of solids fuels: examination of a process for simultaneous hydrogen production and CO_2 capture. Fuel 87 (2008) 8-9, p. 1678-1686

[17] Gao, L.; Paterson, N.; Fennell, P.; Dugwell, D; Kandiyoti, R.: The Zero-Emission Carbon Concept (ZECA): extents of reaction with different coals in steam/hydrogen, tar formation and residual char reactivity. Energy & Fuels 22 (2008) 4, p. 2504-2511

[18] Paelnick, P.: PCC and oxy-combustion hold greatest promise in carbon capture (Q & A article). PEi 19 (2011) 5, p. 90-94

[19] MacDowell, N.; Florin, N.; Buchard, A.; Hallett, J.; Galindo, A.; Jackson, G.; Adjiman, C.S.; Williams, C.K.; Shah, N.; Fennell, P.: An overview of CO_2 capture technologies. Environ. Sci. Technol. 3 (2010), p. 1645-1669

[20] Jensen, H.: Carbon Dioxide Capture and Storage (RWE presentation). Energy & Environmental Management Group (EEMG) meeting. Avon and Somerset, UK: 2010

[21] Communiqué Endesa: Endesa starts up first plant to capture CO_2 by chemical absorption in

Spain. Press release (2010), website: http://www.euro-energie.com/endesa-starts-up-first-plant-to-capture-co2-by-chemical-absorption-in-spain--n-2047

[22] EON and TNO: Cato CO_2 Catcher- A CO_2 capture plant treating real flue gas. Brochure (2008), website: www.tno.nl/co2-capture

[23] Moser, P.; Schmidt, S.; Sieder, G.; Garcia, H.; Stoffregen, T.; Stamatov, V.: The post-combustion capture pilot plant Niederaussem – Results of the first half of the testing programme. Energy Procedia 4 (2011), p.1310-1316

[24] Knudsen, J.N; Jensen, J.N.; Vilhelmsen, P-J.; Biede, O.: First year operation experience with a 1 t/h CO_2 absorption pilot plant at Esbjerg coal-fired power plant. Proceedings of European Congress of Chemical Engineering (ECCE-6). Copenhagen, Denmark: 2007

[25] Barbucci, P.:CO_2 Capture and Storage – A utility view. 3rd International Symposium on Capture and geological storage of CO_2. Paris , France: 2009

[26] Jockenhövel, T.; Schneider, R.: Towards Commercial Application of a Second-Generation Post-Combustion Capture Technology – Pilot Plant Validation of the Siemens Capture Process and Implementation of a First Demonstration Case. Energy Procedia 4 (2011), p.1451-1458

[27] Telikapalli, V.; Kozak, F.; Sherrick, B.; Black, J.; Muraskin, D.; Cage, M.; Hammond, M.; Spitznogle, G.: CCS with the Alstom Chilled Ammonia Process Development Program – Field Pilot Results. Energy Procedia 4 (2011), p. 273-281

[28] Scheffknecht, G.; Al-Makhadmeh, L.; Schnell, U.; Maier, J.: Oxy-fuel coal combustion – A review of the current state-of-the-art. Int. J. Greenh. Gas Con. 5S (2010) Supplement 1, p. S16-S35

[29] Anonymous: Will China overtake Europe in the race for CCS?. PEi 19 (2011) 5, p. 22-26

[30] Jopp, K.: CCS Technologien der Zweiten Generation – Effizienzeinbußen mindestens halbiert (in German language). BWK 3 (2011), p. 25-27

[31] Lu, D.Y.; Hughes, R.W.; Anthony, E.J.: Ca-based sorbent looping combustion for CO_2 capture in pilot-scale dual fluidized beds. Fuel Process. Technol. 89 (2008) 12, p. 1386-1395

[32] Fang, F.; Li, Z.; Cai, N.: Continuous CO_2 capture from flue gases using a dual fluidized bed reactor with calcium based sorbent. Ind. Eng. Chem. Res. 48 (2009) 24 , p. 11140-11147

[33] Charitos, A.; Hawthorne, C.; Bidwe, A. R.; Sivalingam, S.; Schuster, A.; Spliethoff, H.; Scheffknecht, G.: Parametric investigation of the calcium looping process for CO_2 capture in a 10 kW_{th} dual fluidized bed. Int. J. Greenh. Gas Con. 4 (2010) 5, p. 776-784

[34] Rodríguez, N.; Alonso, M.; Abanades, J.C.: Experimental investigation of a circulating fluidized bed-reactor to capture CO_2 with CaO. AiChe J. 57 (2011) 5, p. 1356-1366

[35] Hawthorne, C.; Dieter, H.; Holz, H.; Eder, T.; Zieba, M.; Scheffknecht, G.: High Temperature CO_2 Capture with CaO in a 200 kW_{th} Dual Fluidized Bed Pilot Facility. Proceedings of the 2nd International Conference on Energy Process Engineering-Efficient Carbon Capture for Coal Power Plants. Frankfurt am Main, Germany: 2011

[36] Dieter, H.; Hawthorne, C.: Pilot Plant Results for Calcium Looping Processes: Hydrogen Production from Biomass and CO_2 Capture from Fossil Fuel Power Plants (IFK-University of Stuttgart presentation). 3rd High Temperature Solid Looping Cycles Network Meeting. Vienna, Austria: 2011

[37] Ströhle J.; Galloy, A.; Kremer, J.; Plötz, S.; Bayrak, A.; Wieczorek, M.; Epple, B.: First Results from a 1 MW_{th} Carbonate Looping Plant for carbonate and chemical looping (EST-TU Darmstadt presentation). 3rd High Temperature Solid Looping Cycles Network Meeting. Vienna, Austria: 2011

[38] Sánchez-Biezma, A.; Diaz, L.; López, J.; Arias, B.; Paniagua, J.; de Zárraga, E.; Álvarez, J.; Abanades, J.C.: La Pereda CO_2: A 1.7 MW pilot to test post-combustion CO_2 capture with CaO. Proceedings of the 21st International Fluidized Bed Combustion Conference. Napoli, Italy: 2012

[39] Koblitsch, P.; Pröll, T.; Bohlar-Nordenkampf, J.; Hofbauer, M.: Operating experience with chemical looping combustion in a 120 kW dual circulating fluidized bed (DCFB) unit. Energy Procedia 1 (2009) 1, p. 1465-1472

[40] Anthony, E.J.: Solid Looping Cycles: A New Technology for Coal Converson. Ind. Eng.

Chem. Res. 47 (2008) 6, p.1747-1754

[41] Berguerand, N.; Lyngfelt, A.: Design and operation of a 10 kW_{th} chemical-looping combustor for solid fuels – Testing with South African coal. Fuel 87 (2008) 12, p. 2713-2726

[42] Rubin, E.S.; Mantripragada, H.; Marks, A.; Versteeg, P.; Kitchin, J.: The outlook for improved carbon capture technology. Progress Energy Combust. Sci. 38 (2012) 5, p. 630-671

[43] Berstad, D.; Arasto, A.; Jordal, K.; Haugen, G.: Parametric study and benchmarking of NGCC, coal and biomass power cycles integrated with MEA-based post-combustion CO_2 capture. Energy Procedia 4 (2011), p. 1737-1744

[44] Ystad, P.A.M.; Bolland, O.; Hillestad, M.: NGCC and Hard-Coal Power Plant with CO_2 Capture Based on Absorption. Energy Procedia 23 (2012), p. 33-44

[45] Stöver, B.; Bergins, C.; Klebes, J.: Optimized post combustion carbon capturing on coal fired power plants. Energy Procedia 4 (2011), p. 1637-1643

[46] Jilvero, H.; Normann, F.; Andersson, K.; Johnsson, F.: Thermal integration and modelling of the chilled ammonia process. Energy Procedia 4 (2011), p. 1713-1720

[47] Cormos, C.-C.: Integrated assessment of IGCC power generation technology with carbon capture and storage (CCS). Energy, Volume 42 (2012) 1, p. 434-445

[48] Castillo, R.:Thermodynamic evaluation of membrane based oxyfuel power plants with 700 °C technology. Energy Procedia 4 (2011), p. 1026-1034

[49] Hawthorne, C.; Trossmann, M.; Galindo Cifre, P.; Schuster, A.; Scheffknecht, G.: Simulation of the carbonate looping power cycle. Energy Procedia. 1 (2009) 1, p. 1387-1394

[50] Romano M.C.; Martínez, I.; Murillo, R.; Arstad, B.; Blom, R.; Ozcan C.D.; Ahn, H.; Brandani, B. Guidelines for modelling and simulation of Ca-looping processes. EERA website, in press

[51] Romeo, L.M.; Abanades, J.C.; Escosa, J.M.; Paño, J.; Giménez, A.; Sánchez-Biezma, A.; Ballesteros, J.C.: Oxyfuel carbonation/calcination cycle for low cost CO_2 capture in existing power plants. Energy Convers. Manage. 49 (2008) 10, p. 2809-2814

[52] Martínez, I.; Murillo, R.; Grasa, G.; Abanades, J.C.: Integration of a Ca looping system for CO_2 capture in existing power plants. AIChE J. 57 (2011) 9, p. 2599-2607

[53] Abanades, J.C.; Grasa, G.; Alonso, M.; Rodriguez, N.; Anthony, E.J.; Romeo, L.M.: Cost structure of a postcombustion CO_2 capture system using CaO. Sci. Technol. 41 (2007) 15, p. 5523-5527.

[54] Intergovernmental Panel on Climate Change (IPCC): Special report on carbon dioxide capture and storage. Cambridge, United Kingdom: Cambridge University Press, 2005

[55] Poboß, N.; Schuster, A.; Scheffknecht, G.: Machbarkeitsstudie für das Carbonate Looping Verfahren zur CO_2 Abscheidung Kraftwerksabgasen (English: Feasability study of the Carbonate Looping process for removal of CO_2 from power plant flue gases) (Cooretec Final Report FKZ 0327771B). Stuttgart, Germany: University of Stuttgart, 2008

[56] Alvarez, D.; Abanades, J.C.: Pore-size and shape effects on the recarbonation performance of calcium oxide submitted to repeated calcination/recarbonation cycles. Energy Fuels. 19 (2005) 1, p. 270-278

[57] Curran, G. P.; Fink, C. E.; Gorin, E.: CO_2 acceptor gasification process. Studies of acceptor properties. Adv. Chem. Ser. 69 (1967), p. 141

[58] Marquard.Möllenstedt, T.; Zuberbühler, U.; Sichler, P.; Specht, M.; Michel, M.; Berger, R.: H_2-reiches Synthesegas aus Biomasse. Der AER Prozess (in German language), Special edition. FOEST e.V. (Fördergemeinschaft Ökologische Stoffverwertung e.V.), 2003

[59] Koppatz, S.; Pfeifer, C.; Rauch, R.; Hofbauer, H.; Marquard-Moellenstedt, T.; Specht, M.: H_2 rich product gas by steam gasification of biomass with in situ CO_2 absorption in a dual fluidized bed system of 8 MW fuel input. Fuel Process Technol. 90 (2009) 7-8, p. 914-921

[60] Abanades, J.C.; Alvarez, D.; Conversion Limits in the reaction of CO_2 with lime. Energy Fuels 17 (2003) 2, p. 308-315

[61] Abanades, J.C.; Anthony, E.J.; Alvarez, D.; Lu, D.Y.; Salvador, C.: Capture of CO_2 from combustion flue gases in a fluidized bed of CaO. AIChE J. 50 (2004) 7, p. 1614-1622

[62] Christodoulou C.:Determination of operational parameters on the kinetics of carbonation and reactor performance in a small bubbling fluidized bed (diploma thesis). Stuttgart, Germany: University of Stuttgart, 2008

[63] Kronberger, B.; Lyngfelt, A.; Löffler, G.; Hofbauer, H.: Design and fluid dynamic analysis of a bench-scale combustion system with CO_2 separation-Chemical-Looping Combustion. Ind. Eng. Chem. Res. 44 (2005) 3, p. 546-556

[64] Hofbauer, H.: Scale up of fluidized bed gasifiers from laboratory scale to commercial plants: Steam gasification of solid biomass in a Dual Fluidized Bed system. Proceedings of the 19th international conference on fluidized bed combustion. Vienna, Austria: 2006

[65] Nikolopoulos, A.; Nikolopoulos, N.; Charitos, A.; Grammelis, P.; Kakaras, E.: 3-D TFM Full – Loop CFD simulation of CFBs. Addressing Proper Simulation of the Dense Flow within Pneumatic valves. Proceedings of the 21st International Fluidized Bed Combustion Conference. Napoli, Italy: 2012

[66] Romano, M.C.: Modelling the carbonator of a Ca-looping process for CO_2 capture from power plant flue gas. Chem. Eng. Sci. 69 (2011) 1, p. 257-269

[67] Manovic, V; Anthony, E.J.: Lime Based Sorbents for High-Temperature CO_2 capture – A review of Sorbent Modifications Methods. Int. J. Environ. Res. Public Health 7 (2010) 8, p. 3129-3140

[68] Abanades, J. C.; Rubin, E. S.; Anthony, E. J.: Sorbent cost and performance in CO_2 capture systems. Ind. Eng. Chem. Res. 43 (2004) 13, p. 3462-3466

[69] Rodríguez, N.; Alonso, M.; Abanades J.C.; Grasa, G.; Murillo, R.: Analysis of a process to capture the CO_2 resulting from the pre-calcination of the limestone feed to a cement plant. Energy Procedia 1 (2009) 1, p. 141-148

[70] Grasa, G.; Alonso, M.; Abanades, J.C.: Sulfation of CaO particles in a carbonation/ calcination loop to capture CO_2. Ind. Eng. Chem. Res. 47 (2008) 5, p. 1630-1635

[71] Anthony, E.J.: Ca looping technology: current status, developments and future directions. Greenhouse Gases: Sci. Technol. 1 (2011) 1, p. 36–47

[72] Charitos, A.; Hawthorne, C.; Bidwe, A.R.; Schuster, A.; Scheffknecht, G.: Hydrodynamic analysis of a 10 kW_{th} Calcium Looping Dual Fluidized Bed for post-combustion CO_2 capture. Powder Technol. 200 (2010) 3, p 117-127

[73] Hotta, A.; Kuivalainen, R.; Eriksson, T; Lupion, M.; Cortes, V.; Sánchez-Biezma Sacristán, A.; Martínez Jupitero, M.; Ballesteros, J.C.: Development and demonstration of oxy-fuel CFB technology. Proceedings of the Industrial Fluidization of South Africa Conference. Glenburn Lodge, South Africa: 2011

[74] Basu, P.: Combustion and gasification in fluidized beds. Halifax, Nova Scotia, Canada: Taylor and Francis group, 2006

[75] Arias, B.; Cordero, J.M.; Alonso, M.; Abanades J.C.: Sulfation rates of cycled CaO particles in the carbonator of a Ca-looping cycle for post-combustion CO_2 capture. AIChe 58 (2011) 7, p. 2262-2269

[76] Ryu, H. J.; Grace, J. R.; Lim, C.J.: Simultaneous CO_2/SO_2 capture characteristics of three limestones in a Fluidized-Bed reactor. Energy Fuels 20 (2006) 4, p. 1621-1628

[77] Martínez, I.; Murillo, R.; Grasa, G.; Rodríguez, N., Abanades, J.C.: Conceptual design of a three fluidized beds combustion system capturing CO_2 with CaO. Int. J. Greenh. Gas Con. 5 (2011) 3, p.498-504

[78] Poboß, N.; Swiecki, K; Charitos, A.; Hawthorne, C.; Schuster, A; Scheffknecht, G.: Experimental investigation of the absorption enhanced reforming of biomass in a 20 kW_{th} dual fluidized bed system. Proceedings of the 23rd ECOS Concerence. Lausanne, Switzerland: 2010

[79] Bidwe, A.; Mayer, F.; Hawthorne, C.; Charitos, A.; Schuster, A.; Scheffknecht, G.: Use of ilmenite as oxygen carrier in Chemical Looping Combustion-Batch and continuous dual fluidized bed investigation. Energy Procedia 4 (2011), p. 441-448

[80] Shimizu, T.; Takahashi, T.; Narisawa, H.; Murakami, Y.; Li, L.; Kim, H.: CaO looping Cycle for CO_2 separation. Proceedings of the 10th international conference on circulating fluidized beds combustion. Oregon, USA: 2011

[81] Dominguez Mendoza.: Cold model investigations of a biomass-to-hydrogen gasification

process and CO_2 capture in a dual fluidized bed system (diploma thesis). Stuttgart, Germany: University of Stuttgart, 2008

[82] Bidwe, A.; Hawthorne, C.; Charitos, A.; Dominguez, M.; Dieter, H.; Schuster, A.; Scheffknecht, G.: Cold model investigations of a high temperature looping process in a dual circulating fluidized bed. Proceedings of the 10th international conference on circulating fluidized beds combustion, p.137-147. Oregon, USA: 2011

[83] Rodríguez, N.; Alonso, M.; Abanades, J. C.; Charitos, A.; Hawthorne, C.; Scheffknecht, G.; Lu, D. Y.; Anthony, E. J.: Comparison of experimental results from three dual fluidized bed test facilities capturing CO_2 with CaO. Energy Procedia, 4 (2011), p.393-401

[84] Charitos, A.; Rodríguez, N.; Hawthorne, C.; Alonso, M.; Zieba, M.; Arias, B.; Kopanakis, G.; Scheffknecht, G.; Abanades, J.C.: Experimental validation of the Calcium Looping CO_2 capture process with two circulating fluidized bed carbonators. Ind. Eng. Chem. Res. 50 (2011) 16, p. 9685–9695

[85] Sivalingam, S.; Gleis, S.; Spliethoff, H.; Hawthorne, C.; Charitos, A.; Scheffknecht, G.: Analysis and comparison of reactivity and CO_2 capture capacity of fresh calcium-based sorbents and samples from a lab-scale dual fluidized bed calcium looping facility. J. Eng. Gas Turbines Power 133 (2011) 7

[86] González, B.; Alonso, M.; Abanades, J.C.: Sorbent attrition in a carbonation/calcination pilot plant for capturing CO_2 from flue gases. Fuel 89 (2010) 10, p. 2918-2924

[87] Manovic, V.; Lu, D.; Anthony, E.J.: Steam hydration of sorbents from a dual fluidized bed CO_2 looping cycle reactor. Fuel 87 (2008) 15-16, p. 3344-3352

[88] Manovic, V.; Lu, D.; Anthony, E.J.:Sulphation and carbonation properties of hydrated sorbents from a fluidized bed CO_2 looping cycle reactor. Fuel 87 (2008) 13-14, p. 2923-2931

[89] Hawthorne, C.; Dieter, H.; Bidwe, A.; Schuster, A.; Scheffknecht, G.; Unterberger, S.; Käß, M.: CO_2 capture with CaO in a 200 kW_{th} dual fluidized bed pilot plant. Energy Procedia 4 (2011), p. 441-448

[90] Galloy, A. et al.: CO_2 capture in a 1 MW_{th} fluidized bed reactor in batch mode operation Fifth International Conference on Clean Coal Technologies (CCT). Zaragoza, Spain: 2011

[91] Grasa, G.; Abanades, J.C.: CO_2 capture capacity of CaO in long series of carbonation/ calcination cycles. Ind. Eng. Chem. Res. 45 (2006) 26, p. 8846-8851

[92] Grasa, G. S.; Abanades, J. C.; Alonso, M.; Gonzalez, B.: Reactivity of highly cycled particles of CaO in a carbonation/calcination loop. Chem Eng J. 137 (2008) 3, p. 561-567

[93] Scala, F.; Montagnaro, F.; Salatino, P.: Attrition of dolomite during fluidized bed calcination and sulphation. Proceedings of the XXII Meeting of the Italian Section of the Combustion Institute, p. 47-50. Firenze, Italy: 1999

[94] Alvarez, D.; Abanades, J.C.: Determination of the Critical Product Layer Thickness in the Reaction of CaO with CO_2. Ind. Eng. Chem. Res. 44 (2005) 15, p. 5608-5615

[95] Grasa, G.; Murillo, R.; Alonso, M.; Abanades, J. C.: Application of the random pore model to the carbonation cyclic reaction. AIChE J. 55(2009) 5, p. 1246-1255

[96] Lysikov, I.; Salanov, N.; Okunev, G.: Change of CO_2 carrying capacity in isothermal recarbonation-decomposition cycles. Ind. Eng. Chem. Res 46 (2007) 13, p. 4633-4638

[97] Alonso, M.; Rodríguez, N.; Grasa, G.; Abanades, J. C., Modelling of a fluidized bed carbonator reactor to capture CO_2 from a combustion flue gas. Chem Eng Sci. 64 (2009) 5, p. 883-891

[98] Scala, F.; Salatino, P.; Boerefijn, R.; Ghadiri, M.: Attrition of sorbents during fluidized bed calcination and sulphation. Powder Technol. 107 (2000) 1-2 , p. 153-167

[99] Blamey, J.; Anthony, E. J.; Wang, J.; Fennell, P. S.: The calcium looping cycle for large-scale CO_2 capture. Progress Energy Combust. Sci. 36 (2010) 2, p. 260-279

[100] Jia, L.; Hughes, R.; Lu, D.; Anthony, E.J.; Lau, I.: Attrition of calcining limestones in Circulating Fluidized Bed systems. Ind. Eng. Chem. Res. 46 (2007) 15 , p. 5199- 5209

[101] Scala, F.; Cammarota, A.; Chirone, R.; Salatino, P.: Comminution of limestone during batch fluidized-bed calcination and sulfation. AIChe J. 43 (1997), p. 363-373

[102] Hawthorne, C.; Charitos, A.; Perez-Pulido, C. A.; Bing, Z.; Scheffknecht, G.: Design of a dual fluidised bed system for the post-combustion removal of CO_2 using CaO. Part I: CFB

carbonator reactor model. 9th International Conference on Circulating Fluidized Beds, pp. 759-764 Hamburg, Germany: 2008

[103] Rodríguez, N.; Alonso, M.; Abanades, J. C.: Average activity of CaO particles in a calcium looping system. Chem Eng J. 156 (2010) 2, p. 388-394

[104] Rodríguez, N.; Alonso, M.; Grasa, G.; Abanades, J.C.: Heat requirements in a calciner of $CaCO_3$ integrated in a CO_2 capture system using CaO. Chem. Eng. J. 138 (2008) 1-3, p. 148-154

[105] Manovic, V; Charland, J. P.; Blamey, J.; Fennell, P. S.; Lu, D. Y.; Anthony, E. J.: Influence of calcination conditions on carrying capacity of CaO-based sorbent in CO_2 looping cycles. Fuel 88 (2009) 10, p. 1893-1900.

[106] Gonzalez, B.; Grasa, G. S.; Alonso, M.; Abanades, J. C.: Modeling of the Deactivation of CaO in a Carbonate Loop at High Temperatures of Calcination. Ind. Eng. Chem. Res. 47 (2008) 23, p. 9256-9262.

[107] Charitos, A.; Rodríguez, N.; Hawthorne, C.; Alonso, M.; Zieba, M.; Arias, B.; Kopanakis, G.; Scheffknecht, G.; Abanades, J.C.: Validation of a carbonator model for the Ca-looping postcombustion CO_2 capture process. Proceedings of the 21st International Fluidized Bed Combustion Conference. Napoli, Italy: 2012

[108] Alonso, M.; Arias, B.; Rodríguez, N.; Abanades, J.C.: Circulating fluidized bed carbonator reactor model with experimental data from post-combustion capture of CO_2 with CaO. Proceedings of the 5th international conference on clean coal technologies (CCT2011). Zaragoza, Spain: 2011

[109] Manovic, V.; Anthony, E.J.: Carbonation of CaO-based sorbent enhanced by steam addition. Ind. Eng. Chem. Res. 49 (2010) 9, p. 9105-9110

[110] Pugsley, T.S.; Berutti, F.: A predictive hydrodynamic model for circulating fluidized bed risers. Powder Technol. 89 (1996) 1, p. 57-69

[111] Nikolopoulos, A.; Papafotiou, D.; Nikolopoulos, N.; Grammelis, P.; Kakaras, E.: An advanced EMMS scheme for the prediction of drag coefficient under a 1.2 MW_{th} CFBC isothermal flow--Part I: Numerical formulation. Chem Eng Sci. 65 (2010) 1, p. 4080-4088

[112] Nikolopoulos, A.; Atsonios, K.; Nikolopoulos, N.; Grammelis, P.; Kakaras, E.: An advanced EMMS scheme for the prediction of drag coefficient under a 1.2 MW_{th} CFBC isothermal flow--Part II: Numerical implementation. Chem Eng Sci. 65 (2010) 1, p. 4089-4099

[113] Glicksman, L.R.; Hyre, M.; Woloshun, K.: Simplified scaling relationships for fluidized beds. Powder Technol. 77 (1993) 2, p. 177-199

[114] Chang, H.; Louge, M.: Simplified Fluid dynamic similarity in fluidized beds. Powder Technol. 70 (1992) 3, p. 259-270

[115] Foscolo, P.U.; Germanà, A.; Jand, N.; Rapagnà, S.: Design and cold model testing of a biomass gasifier consisting of two interconnected fluidized beds. Powder Technol. 173 (2007) 3, p. 179-188

[116] Kronberger, B.; Lyngfelt, A.; Adanez, J.; Hofbauer, H.: Circulating fluidized bed reactor systems for Chemical Looping combustion. Proceedings of the 19th international conference on fluidized bed combustion. Vienna, Austria: 2006

[117] Pröll, T.; Rupanovits, K.; Koblitsch, P.; Bohlàr-Nordenkampf, J.; Hofbauer, H.: Cold flow model study on a Dual Circulating Fluidized Bed (DCFB) System for Chemical Looping Processes. Chem. Eng. Technol. 32 (2009) 3, p. 418-424

[118] Johansson, E.; Lyngfelt, A.; Mattisson, T.; Johnsson, F.: Gas leakage measurements in a cold model of an interconnected fluidized bed for chemical-looping combustion. Powder Technol. 134 (2003) 3, p. 210-217.

[119] Pfeifer, C.; Kreuzeder, A.; Hofbauer, H.: Fluid-dynamic investigations in a cold model for a dual fluidized bed steam gasifier: solids circulation and fuel residence time. 9th International Conference on Circulating Fluidized Beds, p. 123-128. Hamburg, Germany: 2008

[120] Kotik, J.; Pröll, T.; Hofbauer, H.: Advanced Concept for a “next generation” biomass gasification CHP plant-Basic engineering and cold flow model results. 9th International Conference on Circulating Fluidized Beds, p. 697-702. Hamburg, Germany: 2008

[121] Löffler, G.; Kaiser, S.; Bosch, K.; Hofbauer, H.: Hydrodynamics of a dual fluidized bed

gasifier-Part I: simulation of a riser with gas injection and diffuser. Chem. Eng. Sci. 58 (2003) 18, p. 4197-4213

[122] Kaiser, S.; Löffler, G.; Bosch, K.; Hofbauer, H.: Hydrodynamics of a dual fluidized bed gasifier-Part II: simulation of solid circulation rate, pressure loop and stability. Chem. Eng. Sci. 58 (2003) 18, p. 4215-4223

[123] Gupta, S.K.; Berruti, F.: Evaluation of the gas-solid suspension density in CFB risers with exit effects. Powder Technol. 108 (2000) 1, p. 21-31

[124] Nikolopoulos, A.: Hydrodynamic study and design of solid circulation devices and configurations for dual fluidised bed system for CO_2 capture (diploma thesis). Stuttgart, Germany: University of Stuttgart, 2006

[125] Reddy Karri, S.B.; Knowlton, T.M.: Comparison of group A and group B solids flow in underflow standpipe, Fluidization VII, p.345-352. New York, USA: Engineering foundation, 1992

[126] Stairmand, C.J.: Pressure drop in cyclone separators. Engineering.168 (1949), p. 409-412

[127] Yang, S.; Yang, H.; Zhang, H.; Li, S.; Yue, G.: A transient method to study the pressure drop characteristics of the cyclone in a CFB system. Powder Technol. 192 (2009) 1, p. 105-109

[128] Basu, P.; Cheng, L.: An analysis of loop seal operations in a circulating fluidized bed TransIChemE. 78 (2000) 7, p. 991-998

[129] Leung, L.S.; Jones, P.; Knowlton, T.M.: An analysis of moving-bed flow of solids down standpipes and slide valves. Powder Technol. 19 (1978) 1, p. 7-15

[130] Jones, D. R. M.; Davidson, J.F.: The flow of particles from a fluidised bed through an orifice. Rheologica Acta. 4 (1965) 3, p. 180-192

[131] Werther, J.: Fluid mechanics of large-scale CFB units. Proceedings of the 4th international conference on circulating fluidized beds, p. 1-14. Pennsylvania, USA: 1993

[132] Arnaldos, J.; Casal, J.: Prediction of transition velocities and hydrodynamical regimes in fluidized beds. Powder Technol. 86 (1996) 3, p. 285-298

[133] Smolders, K.; Baeyens, J.: Gas fluidized beds operating at high velocities: a critical review of occurring regimes. Powder Technol. 119 (2001) 8, p. 269-291

[134] Rhodes, M.J.: Turbulent fluidization: myth or reality? Proceedings of the fifth international conference on circulating fluidized bed technology, p.338-343. Beijing, P.R. China: Science press, 1996

[135] Hu, N.; Zhang, H.; Yang, H.; Yang, S.; Yue, G.; Lu, J.; Liu, Q.: Effects of riser height and total solid inventory on the gas-solids in an ultra tall CFB riser. Powder Technol. 196 (2009) 1, p. 8-13

[136] Namkung, W.; Kim, S.W.; Kim, S.D.: Flow regimes and axial pressure profiles in a circulating fluidized bed. Chem. Eng. J. 72 (1999) 3, p. 245-252

[137] Patience, G.S.; Chaouki, J.; Grandjean, B.P.A.: Solids flow metering from pressure drop measurement in circulating fluidized beds. Powder Technol. 61 (1990) 1, p. 95-99

[138] Alonso, M.; Rodríguez, N.; González, B.; Grasa, G.; Murillo, R.; Abanades, J. C.: Carbon dioxide capture from combustion flue gases with a calcium oxide chemical loop. Experimental results and process development. Int. J. Greenh. Gas Con. 4 (2010) 2, p. 167-173

[139] Abanades, J.C.; Alonso, M.; Rodríguez, N.; González, B.; Grasa, G.; Murillo, R.: Capturing CO_2 from combustion flue gases with a carbonation calcination loop. Experimental results and process development. Energy Procedia 1 (2009) 1, p. 1147-1154

[140] Bi, H. T.; Grace, J. R.: Flow regime diagrams for gas-solid fluidization and upward transport. Int. J. Multiphase Flow. 21(1995) 6, p. 1229-1236

[141] Bidwe, A.; Charitos, A.; Dieter, H.; Wei, A.; Zieba, M.; Scheffknecht, G.: A Study of Standpipe and Loop Seal Behavior in a Circulating Fluidized Bed for Geldart B Particles. Proceedings of the 10th international conference on circulating fluidized beds combustion, p. 641-648. Oregon, USA: 2011

[142] Grieco, E.; Marmo, L.: Predicting the pressure drop across the solids flow rate control device for a circulating fluidized bed. Powder Technol. 161 (2006) 2, p. 89-97